



# Energy Management System for Automated Driving

DISSERTATION  
zur Erlangung des Grades eines Doktors  
der Ingenieurwissenschaften

vorgelegt von  
Dipl.-Ing. Kirill Gorelik

eingereicht bei der Naturwissenschaftlich-Technischen Fakultät  
der Universität Siegen  
Siegen 2019

*Gedruckt auf alterungsbeständigem holz- und säurefreiem Papier.*

Betreuer und erster Gutachter  
Prof. Dr. Roman Obermaisser  
Universität Siegen

Zweiter Gutachter  
Prof. Dr. Kristof Van Laerhoven  
Universität Siegen

Industriebetreuer  
Dr. Ahmet Kilic  
Robert Bosch GmbH

Tag der mündlichen Prüfung  
19.06.2019



# Acknowledgements

I would like to express my deepest gratitude to my doctoral advisor Prof. Dr. Roman Obermaisser for his continuous guidance, support and encouragement throughout the research and writing of this thesis. His advices, constructive criticism and motivation were essential for this dissertation.

I would also like to express my warmest gratitude to my supervisor Dr. Ahmet Kilic at Robert Bosch GmbH for his valuable support and motivation. His constant guidance, advices and patience were a great help for me.

Special thanks to Dr. Norbert Müller and Dr. Achim Henkel for giving me the possibility to carry out this work at the Corporate Sector Research and Advance Engineering at Robert Bosch GmbH in Renningen. Also I want to thank Dr. Andreas Schönknecht for his valuable comments on the thesis. Thanks to my colleagues at Robert Bosch GmbH and especially to Dr. Christian Thulfaut for our passionate discussions.

I am grateful to my family, to Eszter and to all my friends, in particular to Benjamin and Philipp, supporting and motivating me throughout my studies. And finally, I would especially like to thank my parents for their love, patience and support during this period of my life.



# Abstract

With increasing levels of driving automation, the responsibility for the vehicle control and passengers' safety is shifted from the driver towards the automation system. This results in increased reliability and safety requirements for the subsystems involved in the automated vehicle motion. In case of a safety-critical failure, an automated transition to a vehicle standstill must be executed without any driver interaction and supervision for high and full driving automation. Therefore, in addition to the functionality of the safety-critical subsystems, also their reliable power supply for the duration of the transition to the standstill must be guaranteed by the vehicle powernet.

According to the functional safety norm ISO 26262, all safety-critical subsystems must be designed with an appropriate automotive safety integrity level (ASIL). Since reliable power supply is one of the prerequisites for their correct functionality, it becomes safety-critical itself. The need for new fail-operational powernet topologies and appropriate control strategies fulfilling the increased reliability and availability requirements arises. The work presented in this dissertation proposes a new generic energy management system for the safety-based range extension, supporting the optimization of the powernet and powertrain control for arrival at the safest possible location for the passengers.

The key element of the proposed energy management system is the online energy distribution optimization with an integrated degradation concept. Using the predicted values for the available energy resources and for the energy required to complete a driving mission, the control strategy automatically adapts the energy flows within the vehicle powernet. Furthermore, it estimates appropriate degradation step for the comfort loads, driving profile and driving destination with the goal to reach the safest destination with a maximum of comfort in a minimum of time under consideration of the available energy resources. With this approach, also the fault reactions of the functional safety concept, required by ISO 26262 for all safety-critical functions, are automated and optimized. In this way, the energy management system finds autonomously the best suited fault reactions for achieving the defined control goal.

The energy demand required for the completion of a driving mission depends on the ve-

---

locity profile, road slope and stops on the way to the destination. Using the electronic horizon, a driving trajectory from the current vehicle position to the destination is approximated online, which is then used for the route based estimation of the required propulsion energy. In powertrain topologies with multiple traction motors, the overall driving efficiency and hereby also the driving range can be increased significantly with an appropriate strategy for the torque distribution between individual motors. Therefore, a torque distribution profile is estimated online based on the theory of optimal control for the entire driving mission, enabling an accurate and realistic prediction of the propulsion energy required for the safety based range extension. In addition to the driving efficiency increase also symmetrical discharge of independent traction batteries, required for approximately the same driving range in case of a breakdown of one battery, is incorporated in the control strategy. Furthermore, also the balancing of the energy losses in powertrain components is considered for the torque distribution, which is required to avoid their overheating possibly leading to faster aging and wear.

The application of the generic framework for the energy management system is exemplified on two different powernet and powertrain topologies with a single and multiple traction motors. The benefits are verified using simulation results for both, fault-free and failure case operation. With the proposed torque distribution strategy a decrease in the energy losses of up to 12% for the given use case was achieved. Also the optimization of the fault reactions shows the ability of the energy management system to achieve the control goals despite multiple faults. In addition to the concepts presented in this dissertation, also runtime optimized algorithms are proposed, implemented and validated by means of simulation. By enhancing the reliability of the power supply and fail-operability of the powertrain, the work presented in this dissertation contributes to the establishment of the evolving automated driving technology and provides a generic framework for model predictive energy management for future implementation in automated vehicles.



# Zusammenfassung

Mit dem steigenden Grad der Fahrautomatisierung geht die Zuständigkeit für die Fahrzeugführung und Sicherheit der Passagiere immer mehr vom Fahrer auf das Automatisierungssystem über. Dies führt zu erhöhten Anforderungen an die Zuverlässigkeit und Verfügbarkeit der Teilsysteme, die in die automatisierte Fahrzeugführung eingebunden sind. Beim Auftritt eines sicherheitskritischen Fehlers muss ein hoch- und vollautomatisiertes Fahrzeug ohne jeglichen Eingriff und Überwachung des Fahrers in den Stillstand überführt werden. Daher muss zusätzlich zu der eigentlichen Funktionalität dieser Teilsysteme auch deren zuverlässige Energieversorgung für die Dauer des Übergangs in den Stillstand von dem Energiebordnetz eines Fahrzeugs sichergestellt werden.

Entsprechend der Norm ISO 26262 für die funktionale Sicherheit müssen alle sicherheitskritische Teilsysteme mit einem entsprechenden Grad der Ausfallsicherheit (ASIL) entwickelt werden. Da zuverlässige Energieversorgung eine der Grundvoraussetzung für deren Funktionalität ist, wird es selbst sicherheitskritisch. Zur Erfüllung dieser erhöhten Zuverlässigkeits- und Verfügbarkeitsanforderungen werden daher neue fehlertolerante Bordnetze und zugehörige Betriebsstrategien benötigt. Die vorliegende Dissertation stellt ein neuartiges und generisches Energiemanagementkonzept für sicherheitsbasierte Reichweitensteigerung vor. Eine Optimierung der Steuerung vom Bordnetz und Antriebsstrang zur Ankunft an einem für die Passagiere sichersten Ort liegt diesem Konzept zugrunde.

Den Kern des vorgeschlagenen Energiemanagementsystems bildet eine zur Laufzeit ausgeführte Optimierung der Energieverteilung mit einem integrierten Degradationskonzept. Anhand prädiktiv ermittelter Werte für die verfügbaren Energieressourcen sowie den bis zum Ende der Fahrt benötigten Energieverbrauch passt die Betriebsstrategie die Energieflüsse an den Zustand des Bordnetzes an. Das Hauptziel der Steuerung ist dabei die Ankunft an einem aus der Sicht der Passagiere möglichst sicheren Ort zu ermöglichen. Zusätzlich wird unter Berücksichtigung der verfügbaren Ressourcen eine entsprechende Degradationsstufe für die Komfortlasten, das Fahrprofil sowie das Fahrziel festgelegt, mit dem Ziel an einem möglichst sicheren Ort mit Maximum an Komfort und Minimum an Fahrzeit anzukommen. Mit diesem Ansatz können auch die Fehlerreaktionen von dem funktionalen Sicherheitskonzept, das von der ISO 26262 für alle sicherheitskritischen Teil-

---

systeme geforderte wird, automatisiert und optimiert werden. Auf diese Weise findet das Energiemanagementsystem automatisch die geeignetsten Fehlerreaktionen zum Erreichen des definierten Steuerungsziels.

Der zum Durchführen einer Fahrt benötigte Energieverbrauch hängt stark von dem Geschwindigkeitsprofil, Straßensteigung sowie den Haltepunkten auf dem Weg zum Fahrtziel ab. Mithilfe des elektronischen Horizonts kann eine Fahrtrajektorie ausgehend von der aktuellen Fahrzeugposition bis zum Fahrtziel zur Laufzeit approximiert werden und anschließend zur streckenbasierten Prädiktion der benötigten Antriebsenergie verwendet werden. In Antriebsstrangtopologien mit mehreren Traktionsmotoren kann die Gesamtfahreffizienz und somit auch die Reichweite mit einer geeigneten Betriebsstrategie zur Drehmomentverteilung zwischen den einzelnen Motoren signifikant erhöht werden. Aus diesem Grund wird zur Laufzeit ein Profil der Drehmomentverteilung unter Anwendung der Theorie der optimalen Steuerung berechnet. Dadurch wird eine präzise und realistische Prädiktion der Antriebsenergie ermöglicht, was wiederum für die sicherheitsbasierte Reichweitensteigerung notwendig ist. Zusätzlich zur Steigerung der Fahreffizienz berücksichtigt die Strategie zur Drehmomentverteilung auch das symmetrische Entladen der unabhängigen Traktionsbatterien, was zur Sicherstellung einer nahezu gleichen Reichweite trotz des Ausfalls einer Batterie notwendig ist. Des Weiteren werden die Energieverluste in den Komponenten des Antriebsstranges ausbalanciert, sodass deren Überhitzen und somit eine mögliche schnellere Alterung und Abnutzung vermieden wird.

Die Anwendung des generischen Energiemanagementsystems wird anhand zwei unterschiedlicher Bordnetz- und Antriebsstrangtopologien mit jeweils einem und mehreren Traktionsmotoren veranschaulicht. Der Nutzen wird mithilfe der Simulationsergebnisse im fehlerfreien und fehlerbehafteten Zustand aufgezeigt. Mit der vorgeschlagenen Strategie zur Drehmomentverteilung konnte eine Verkleinerung der Energieverluste um ca. 12% im gegebenen Anwendungsfall erreicht werden. Auch die Optimierung der Fehlerreaktionen zeigt die Fähigkeit des Energiemanagementsystems die Steuerziele trotz mehrerer Fehler zu erreichen. Neben den in dieser Dissertation vorgestellten Konzepten werden auch Implementierungsalgorithmen vorgeschlagen, die für Laufzeitausführung optimiert wurden. Durch die Steigerung der Zuverlässigkeit der Energieversorgung sowie der Funktionsfähigkeit des Antriebsstranges auch im Fehlerfall trägt diese Arbeit zur Etablierung der ständig wachsenden Technologie für automatisiertes Fahren bei und schlägt ein generisches modellprädiktives Energiemanagementsystem zur Implementierung in künftigen automatisierten Fahrzeugen vor.

# Contents

<b>List of Figures</b>	<b>XV</b>
<b>List of Tables</b>	<b>XVII</b>
<b>List of Acronyms</b>	<b>XIX</b>
<b>1 Introduction</b>	<b>1</b>
1.1 Motivation and Research Contributions of Thesis . . . . .	2
1.2 Thesis Overview . . . . .	4
<b>2 Basic Concepts</b>	<b>7</b>
2.1 Driving Automation . . . . .	7
2.2 Aspects of Fault-Tolerant System Design . . . . .	9
2.3 Functional Safety for Road Vehicles . . . . .	10
2.4 Powernet System . . . . .	11
2.5 Powertrain System . . . . .	12
2.6 Classification of Control Strategies . . . . .	13
2.7 Electronic Horizon . . . . .	15
<b>3 State of the Art in Energy Management Systems</b>	<b>17</b>
3.1 Classification of Energy Management Systems . . . . .	17
3.2 Powernet Energy Management . . . . .	20
3.3 Complete Vehicle Energy Management . . . . .	22
3.4 Powertrain Energy Management . . . . .	23
3.5 Trip-Based Energy Management . . . . .	27
3.6 Research Gap in Energy Management for Automated Driving . . . . .	29
<b>4 Energy Management for Safety-Based Range Extension</b>	<b>31</b>
4.1 Safety-Based Range Extension . . . . .	32
4.2 Requirements for Energy Management System . . . . .	36
4.2.1 Requirements for Energy Distribution Optimization . . . . .	37
4.2.2 Requirements for Remaining Energy Prediction . . . . .	38
4.2.3 Requirements for Driving Trajectory Prediction . . . . .	39
4.2.4 Requirements for Propulsion Energy Prediction . . . . .	39
<b>5 Energy Distribution Optimization</b>	<b>41</b>
5.1 Definition of Mixed-Integer Optimization Problem for Energy Distribution	42
5.1.1 Mathematical Model of Fail-Operational Powernet . . . . .	42
5.1.2 Failure Modes of Powernet Components . . . . .	45

5.1.3	Energy Distribution with Optimal Path Selection . . . . .	48
5.1.4	Energy Distribution with Optimal Multiple Battery Discharge . . . . .	51
5.2	Algorithm for Online Mixed-Integer Energy Distribution Optimization . . . . .	55
5.2.1	Continuous Energy Distribution Optimization (Version 1) . . . . .	58
5.2.2	Continuous Energy Distribution Optimization (Version 2) . . . . .	59
5.2.3	Integer Parameter Variation with Feasibility Check . . . . .	60
5.3	Solving Continuous Energy Distribution Optimization . . . . .	69
5.3.1	Energy Distribution (Version 1) with Nonlinear Programming . . . . .	72
5.3.2	Energy Distribution (Version 1) with Linear Programming . . . . .	74
5.3.3	Energy Distribution (Version 2) with Nonlinear Programming . . . . .	78
5.3.4	Energy Distribution (Version 2) with Linear Programming . . . . .	80
5.4	Modeling of Powerlink Components . . . . .	83
5.4.1	Generic Behavioral Description of Powerlinks . . . . .	83
5.4.2	Examples for Behavioral Powerlink Model . . . . .	85
5.5	Prediction of Battery Remaining Discharge Energy . . . . .	90
5.5.1	Battery Model for Prediction of Remaining Discharge Energy . . . . .	91
5.5.2	Prediction with Constant Discharge Power . . . . .	93
5.5.3	Approximation as a Function of Discharge Power . . . . .	95
5.6	Simulation Results for Battery Remaining Discharge Energy Prediction . . . . .	97
5.6.1	Examples for Prediction with Constant Discharge Power . . . . .	97
5.6.2	Examples for Approximation as a Function of Discharge Power . . . . .	101
5.7	Simulation Results for Energy Distribution . . . . .	106
5.7.1	Example for Continuous Energy Distribution . . . . .	106
5.7.2	Example for Mixed-Integer Energy Distribution Optimization . . . . .	113
<b>6</b>	<b>Powertrain Control and Propulsion Energy Prediction</b>	<b>119</b>
6.1	Powertrain Model . . . . .	120
6.1.1	Failure Modes of Powertrain Components . . . . .	120
6.1.2	Vehicle Model . . . . .	121
6.1.3	Gearbox Model . . . . .	123
6.1.4	Electric Motor Model . . . . .	124
6.1.5	Traction Battery Model . . . . .	126
6.2	Driving Trajectory Prediction . . . . .	127
6.2.1	Concept for Driving Trajectory Prediction . . . . .	128
6.2.2	Algorithm for Online Driving Trajectory Prediction . . . . .	130
6.3	Prediction for Powertrain with Single Motor . . . . .	135
6.3.1	Online Propulsion Energy Prediction . . . . .	136
6.3.2	Simulation Results for Powertrain with Single Motor . . . . .	138
6.4	Prediction for Fail-Operational Powertrain with Multiple Motors . . . . .	141
6.4.1	Optimal Control Strategy for Fail-Operational Powertrain . . . . .	143
6.4.2	Propulsion Energy Prediction for Fail-Operational Powertrain . . . . .	149
6.4.3	Algorithm for Online Torque Distribution Optimization . . . . .	151
6.4.4	Simulation Results for Fault-Free Operation . . . . .	159
6.4.5	Simulation Results for Failure Case Operation . . . . .	166
<b>7</b>	<b>Model Predictive Energy Management</b>	<b>173</b>
7.1	Energy Management Architecture for Powertrain with Single Motor . . . . .	174

7.1.1	System Architecture for Powertrain with Single Motor . . . . .	175
7.1.2	Simulation Results for Powertrain with Single Motor . . . . .	178
7.2	Energy Management Architecture for Powertrain with Multiple Motors . .	185
7.2.1	System Architecture for Powertrain with Multiple Motors . . . . .	185
7.2.2	Simulation Results for Powertrain with Multiple Motors . . . . .	188
<b>8</b>	<b>Conclusion</b>	<b>195</b>
	<b>Appendices</b>	<b>199</b>
<b>A</b>	<b>Definition of Use Case 1</b>	<b>201</b>
<b>B</b>	<b>Definition of Use Case 2</b>	<b>207</b>
	<b>List of Symbols and Notations</b>	<b>209</b>
	<b>List of Publications</b>	<b>219</b>
	<b>Bibliography</b>	<b>221</b>



# List of Figures

4.1	Prioritization of safe stop locations. . . . .	32
4.2	Three-level-degradation concept. . . . .	35
4.3	Architecture of generic energy management system. . . . .	36
5.1	Circuit diagram of subpowernet $k$ . . . . .	43
5.2	Energy flows of subpowernet $k$ . . . . .	43
5.3	Block diagram of the two-stage solving algorithm. . . . .	56
5.4	Flow chart of algorithm solving the mixed-integer energy distribution. . . . .	61
5.5	Exemplary powernet line topology and solution feasibility check. . . . .	63
5.6	Nassi-Shneiderman diagram for solution feasibility check. . . . .	64
5.7	Exemplary powernet ring topology and solution feasibility check. . . . .	65
5.8	Exemplary powernet energy demand as a function of degradation step. . . . .	66
5.9	Extended flow chart of algorithm solving mixed-integer energy distribution. . . . .	68
5.10	Model of powernet efficiency matrix. . . . .	83
5.11	Model of valid powerlink operating mode combinations. . . . .	84
5.12	Model of energy flow activation matrix. . . . .	84
5.13	Behavioral block diagram of DC/DC converter, toggle and single switch. . . . .	86
5.14	Battery model used for the prediction of remaining discharge energy. . . . .	91
5.15	Prediction of remaining discharge energy at constant output power. . . . .	94
5.16	Prediction of remaining discharge energy as a function of output power. . . . .	95
5.17	Fail-operational powernet topology with 48V (red) and 12V (blue). . . . .	106
5.18	Balancing of batteries remaining discharge energy. . . . .	113
5.19	Fail-operational powernet topology with HV (red) and 12V (blue). . . . .	114
5.20	Example of mixed-integer energy distribution optimization. . . . .	115
5.21	Simulation results for energy distribution with fault injection. . . . .	117
6.1	Overview of system architecture for connected energy management. . . . .	128
6.2	Electronic horizon profiles used for connected energy management. . . . .	130
6.3	Preprocessing of electronic horizon profiles. . . . .	131
6.4	Estimation of velocity bounds for driving trajectory segments. . . . .	132
6.5	Estimation of velocity profile. . . . .	133
6.6	Format of predicted driving trajectory. . . . .	135
6.7	Topology of electric powertrain with single motor. . . . .	137
6.8	Model of electric powertrain with single motor. . . . .	137
6.9	Simulation results for powertrain with single motor. . . . .	139
6.10	Topology of fail-operational electric powertrain with multiple motors. . . . .	142
6.11	Model of fail-operational electric powertrain with multiple motors. . . . .	145
6.12	Format of predicted driving and torque distribution trajectory. . . . .	150
6.13	Overview of propulsion energy prediction and powertrain control. . . . .	151

6.14	Flow chart of algorithm for dynamic torque distribution optimization. . . . .	153
6.15	Driving trajectory for torque distribution optimization. . . . .	159
6.16	Normal operation with $\beta_1 = 1$ , $\beta_2 = 0.1$ , $\beta_{3/4} = 0$ and $\beta_5 = 0$ . . . . .	161
6.17	Normal operation with $\beta_1 = 1$ , $\beta_2 = 0.1$ , $\beta_{3/4} = 0.25$ and $\beta_5 = 0$ . . . . .	164
6.18	State of charge balancing with $\beta_1 = 1$ , $\beta_2 = 0.1$ , $\beta_{3/4} = 0.25$ and $\beta_5 = 0$ . . . . .	167
6.19	Motor fault injection with $\beta_1 = 1$ , $\beta_2 = 0.1$ , $\beta_{3/4} = 0.25$ and $\beta_5 = 0$ . . . . .	169
6.20	Battery fault injection with $\beta_1 = 1$ , $\beta_2 = 0.1$ , $\beta_{3/4} = 0.25$ and $\beta_5 = 0$ . . . . .	170
6.21	Battery fault injection with $\beta_1 = 1$ , $\beta_2 = 0.1$ , $\beta_{3/4} = 0.25$ and $\beta_5 = 5$ . . . . .	172
7.1	Energy management architecture for powertrain with single motor. . . . .	176
7.2	Exemplary powernet topology with single motor. . . . .	179
7.3	Simulation results for a powernet topology with single motor (part 1). . . . .	181
7.4	Simulation results for a powernet topology with single motor (part 2). . . . .	182
7.5	Energy management architecture for powertrain with multiple motors. . . . .	187
7.6	Exemplary powernet topology with multiple motors. . . . .	188
7.7	Simulation results for a powernet topology with multiple motors (part 1). . . . .	190
7.8	Simulation results for a powernet topology with multiple motors (part 2). . . . .	191



# List of Tables

5.1	Estimation of $E_{rde}$ with quasistatic approach for HV battery. . . . .	98
5.2	Accuracy of prediction for $E_{rde}$ for HV battery. . . . .	98
5.3	Calculation time required for prediction of $E_{rde}$ for HV battery. . . . .	99
5.4	Estimation of $E_{rde}$ with quasistatic approach for 48V battery. . . . .	99
5.5	Accuracy of prediction for $E_{rde}$ for 48V battery. . . . .	99
5.6	Calculation time required for prediction of $E_{rde}$ for 48V battery. . . . .	100
5.7	Estimation of $E_{rde}$ with quasistatic approach for 12V battery. . . . .	100
5.8	Accuracy of prediction for $E_{rde}$ for 12V battery. . . . .	101
5.9	Calculation time required for prediction of $E_{rde}$ for 12V battery. . . . .	101
5.10	$R^2$ for linear approximation of $E_{rde}$ for HV battery. . . . .	102
5.11	Calculation time for linear approximation of $E_{rde}$ for HV battery. . . . .	103
5.12	$R^2$ for linear approximation of $E_{rde}$ for 48V battery. . . . .	104
5.13	Calculation time for linear approximation of $E_{rde}$ for 48V battery. . . . .	104
5.14	$R^2$ for linear approximation of $E_{rde}$ for 12V battery. . . . .	105
5.15	Calculation time for linear approximation of $E_{rde}$ for 12V battery. . . . .	105
5.16	Continuous energy distribution (Version 1) for fault-free operation. . . . .	108
5.17	Continuous energy distribution (Version 2) for fault-free operation. . . . .	109
5.18	Continuous energy distribution (Version 1) for failure case operation. . . . .	110
5.19	Continuous energy distribution (Version 2) for failure case operation. . . . .	111
5.20	State of charge of batteries $B^{\{1\}}$ and $B^{\{2\}}$ at the end of driving mission. . . . .	113
6.1	Simulation results using quasistatic approach. . . . .	140
6.2	Deviation of predicted values for $d_{pdv} = d_{pda} = 25\%$ . . . . .	140
6.3	Deviation of predicted values for $d_{pdv} = d_{pda} = 75\%$ . . . . .	141
6.4	Predicted average battery discharge $dSoC_{avg}$ in [%] for Example 1. . . . .	162
6.5	Predicted increase of energy efficiency $d\eta_{SoC}$ in [%] for Example 1. . . . .	162
6.6	Predicted battery state of charge delta $dSoC_{fr}$ in [‰] for Example 1. . . . .	162
6.7	Average calculation time $dT_{eval}$ in [ms] for Example 1. . . . .	163
6.8	Predicted average battery discharge $dSoC_{avg}$ in [%] for Example 2. . . . .	165
6.9	Predicted increase of energy efficiency $d\eta_{SoC}$ in [%] for Example 2. . . . .	165
6.10	Predicted battery state of charge delta $dSoC_{fr}$ in [‰] for Example 2. . . . .	165
6.11	Average calculation time $dT_{eval}$ in [ms] for Example 2. . . . .	165
6.12	Predicted losses ratio of front left to right motor ( $R_{emflr.loss}$ ) for Example 2. . . . .	166
6.13	Predicted losses ratio of rear left to right motor ( $R_{emrlr.loss}$ ) for Example 2. . . . .	166
6.14	Predicted losses ratio of front to rear axle motors ( $R_{emfr.loss}$ ) for Example 2. . . . .	166
A.1	Vehicle parameters used in simulation for use case 1. . . . .	201
A.2	Velocity/acceleration limits profile used in simulation for use case 1. . . . .	201
A.3	Slope profile used in simulation for use case 1. . . . .	203

A.4	Stops profile used in simulation for use case 1. . . . .	206
B.1	Vehicle parameters used in simulation for use case 2. . . . .	207
B.2	Velocity/acceleration limits profile used in simulation for use case 2. . . . .	207
B.3	Slope profile used in simulation for use case 2. . . . .	207
B.4	Stops profile used in simulation for use case 2. . . . .	208

# List of Acronyms

ADAS	<u>A</u> dvanced <u>D</u> river <u>A</u> ssistance <u>S</u> ystem
ASIL	<u>A</u> utomotive <u>S</u> afety <u>I</u> ntegrity <u>L</u> evel
BEV	<u>B</u> attery <u>E</u> lectric <u>V</u> ehicle
BMS	<u>B</u> attery <u>M</u> anagement <u>S</u> ystem
CCU	<u>C</u> onnectivity <u>C</u> ontrol <u>U</u> nit
CVEM	<u>C</u> omplete <u>V</u> ehicle <u>E</u> nergy <u>M</u> anagement
DOT	<u>D</u> eartment <u>O</u> f <u>T</u> ransportation
DP	<u>D</u> ynamic <u>P</u> rogramming
dpda	<u>d</u> riving <u>p</u> rofile <u>d</u> egradation <u>a</u> cceleration
dpdv	<u>d</u> riving <u>p</u> rofile <u>d</u> egradation <u>v</u> elocity
E/E	<u>E</u> lectric/ <u>E</u> lectronic
ECU	<u>E</u> lectronic <u>C</u> ontrol <u>U</u> nit
edo	<u>e</u> nergy <u>d</u> istribution <u>o</u> ptimization
EM	<u>E</u> lectric <u>M</u> otor
EMS	<u>E</u> nergy <u>M</u> anagement <u>S</u> ystem
EV	<u>E</u> lectric <u>V</u> ehicle
FCEV	<u>F</u> uel- <u>C</u> ell <u>E</u> lectric <u>V</u> ehicle
FCHEV	<u>F</u> uel- <u>C</u> ell <u>H</u> ybrid <u>E</u> lectric <u>V</u> ehicle
FCR	<u>F</u> ault- <u>C</u> ontainment <u>R</u> egion
FIT	<u>F</u> ailures <u>I</u> n <u>T</u> ime
fr	<u>f</u> ront/ <u>r</u> ear
HARA	<u>H</u> azard <u>A</u> nalysis and <u>R</u> isk <u>A</u> ssessment
HEV	<u>H</u> ybrid <u>E</u> lectric <u>V</u> ehicle
HSE	<u>H</u> igh <u>S</u> pecific <u>E</u> nergy
HSP	<u>H</u> igh <u>S</u> pecific <u>P</u> ower
HV	<u>H</u> igh <u>V</u> oltage
ICE	<u>I</u> nternal <u>C</u> ombustion <u>E</u> ngine
LP	<u>L</u> inear <u>P</u> rogramming
lr	<u>l</u> eft/ <u>r</u> ight
LUT	<u>L</u> ook- <u>U</u> p- <u>T</u> able

MCM	<u>M</u> odular <u>C</u> ascade <u>M</u> achine
MILP	<u>M</u> ixed- <u>I</u> nteger <u>L</u> inear <u>P</u> rogramming
MPC	<u>M</u> odel <u>P</u> redictive <u>C</u> ontrol
MPP	<u>M</u> ost <u>P</u> robable <u>P</u> ath
NEDC	<u>N</u> ew <u>E</u> uropean <u>D</u> riving <u>C</u> ycle
NHTSA	<u>N</u> ational <u>H</u> ighway <u>T</u> raffic <u>S</u> afety <u>A</u> dministration
nlc	<u>n</u> onlinear <u>c</u> onstraint
NLP	<u>N</u> on <u>L</u> inear <u>P</u> rogramming
PHEV	<u>P</u> lug-In <u>H</u> ybrid <u>E</u> lectric <u>V</u> ehicle
PSO	<u>P</u> article <u>S</u> warm <u>O</u> ptimization
PWM	<u>P</u> ulse <u>W</u> idth <u>M</u> odulation
QP	<u>Q</u> uadratic <u>P</u> rogramming
SAE	<u>S</u> ociety of <u>A</u> utomotive <u>E</u> ngineers
SoC	<u>S</u> tate <u>o</u> f <u>C</u> harge
SoH	<u>S</u> tate <u>o</u> f <u>H</u> ealth
spn	<u>s</u> ub <u>p</u> ow <u>e</u> r <u>n</u> ets
SSL	<u>S</u> afe <u>S</u> top <u>L</u> ocations
UDDS	<u>U</u> rban <u>D</u> ynanometer <u>D</u> riving <u>S</u> chedule

# Chapter 1.

## Introduction

The mobility of the future is expected to undergo a major shift from the individual mobility towards shared solutions. According to a study published by Roland Berger [1], the amount of the worldwide driven kilometers with privately and commercially owned vehicles will be reduced by approx. 28 % in 2030 compared to 2015. In the same period, it is expected that the amount of kilometers driven by robocabs will increase to approx. 27 % [1]. For enabling this shift, the automotive industry is currently working on new technologies following the three main trends for electrification, driving automation and connectivity [2, 3]. The advantages of using these new technologies are very promising. In urban areas for example, the road congestion might be reduced and the air quality as well as the road safety increased [3]. Also in rural areas, a better public transport could be established enhancing the social aspects of the people living outside the cities [4].

Depending on the area of usage determining the driving situations which must be covered by the driving automation system, e.g. urban [5, 3] or rural [4], robocabs and automated shuttles used for the shared mobility solutions and intended for the operation without a driver require high or full driving automation. According to the levels of automation introduced by the **S**ociety of **A**utomotive **E**ngineers (SAE), the automated driving system must be able to execute a fallback driving task also without any driver interaction [6] starting with highly automated driving. For this, the functionality of the safety-critical functions required for the automated transition to a standstill must be ensured also in case of a failure. In addition, it is also recommended by the U.S. **D**eartment **O**f **T**ransportation (DOT) and by the **N**ational **H**ighway **T**raffic **S**afety **A**dministration (NHTSA) to design automated driving systems in a way allowing to bring a vehicle to a safe stop outside of the active traffic [7].

For the fulfillment of these new requirements arising with the introduction of automated driving, a disruptive change in the state of the art vehicle **E**lectric/**E**lectronic (E/E)

architecture is required [8]. Besides the increased reliability and safety requirements for the functions involved in the automated vehicle motion and transition to a safe state in case of a failure, e.g. braking, steering, environment sensing and motion control, which highly impact their design, also care must be taken for the establishment of their reliable power supply. New fault-tolerant powernet topologies with redundant supply for these safety-critical functions are required [8]. Several powernet topologies for different voltage levels, e.g. 12 V, 48 V and **H**igh **V**oltage (HV), were developed and proposed in [8, 9].

Following the voluntary guidance of DOT and NHTSA for safely stopping the vehicle outside of active traffic [7], also a fail-operational powertrain design is required for the use cases, where a coasting to a safe stop by means of kinetic vehicle energy only is not possible. A fail-operational powertrain will additionally increase the availability of the automated driving systems, leading also to their higher acceptance. Compared to the state of the art of manually driven vehicles, automated driving in combination with electrification provides new challenges for the design of the vehicle powernet and powertrain topologies. The redundancy required for their fail-operability brings on the other side new degrees of freedom for the control strategies, enabling to enhance the safety and comfort for the passengers, to increase the overall driving efficiency and to reduce the overstress of the powernet and powertrain subsystems. Also by taking the human driver out of the control loop and by using the telematic data made available through the vehicle connectivity, further enhancements in powernet and powertrain control can be achieved.

## 1.1. Motivation and Research Contributions of Thesis

As shown previously, with the introduction of automated driving new requirements for the reliable power supply of safety-critical functions arise. According to the functional safety norm ISO 26262-3 [10], all safety-critical subsystems must be designed with the appropriate **A**utomotive **S**afety **I**ntegrity **L**evel (ASIL), defining the maximum tolerated failure rate as the output of the **H**azard **A**nalysis and **R**isk **A**ssessment (HARA). Since reliable power supply is one of the prerequisites for their functionality, it becomes safety-critical itself. The main task of the energy management system is therefore to allocate sufficient energy and power resources for the supply of the safety-critical subsystems for the duration of the entire transition to a safe state. As required by ISO 26262-3 [10], a functional safety concept must be developed for a safety-critical subsystem ensuring the fulfillment of the safety requirements also in case of a failure. For a powernet topology, approx. 30 failure classes can be identified at the system level, leading to approx. 900 possible failure combinations [11], which should be considered in the safety analysis [12].

As a consequence of this complexity for the design of a functional safety concept for fail-

operational powernets, it is aimed by the work in this dissertation to automate the fault reactions by applying the theory of optimal control. The main goal hereby is to enable a completion of a driving mission at the safest possible location with minimized risks for the passengers. For the automation of fault reactions, the concept of the safety-based range extension is modeled in an optimization problem, which is then used for the control of the energy flows within the vehicle. A generic framework for a model predictive and adaptive energy management system for the safety-based range extension covering both, normal and failure case operation is the main contribution of this dissertation.

For a given vehicle destination, the driving duration as well as the energy required for completing the driving mission can be predicted. The powernet loads can be supplied reliably only if the overall energy demand does not exceed the available resources. In a fail-operational powernet topology also redundant paths for the supply of the loads must exist. Therefore, by allocating the available energy resources for the supply of the loads, also losses due to the energy distribution must be minimized. A mixed-integer energy distribution optimization is proposed in this dissertation for predictive allocation of the energy resources to the powernet loads and for automated selection of the energy flow paths with a minimum of losses. In this way, the control of the powerlink components, e.g. DC/DC converter, as well as the discharge of powernet batteries is automated and adapted to the current state of the powernet components.

Accurate prediction of the energy demand required for the completion of a driving mission as well as of the available energy resources is of high importance for the energy distribution optimization. The overall energy demand can be divided into two parts: (1) energy required for vehicle propulsion and (2) energy required for the supply of safety-critical loads and powernet auxiliaries. If the remaining driving time is known, the energy demand of the safety-critical loads and powernet auxiliaries can be estimated assuming an average power consumption. For accurate estimation of the propulsion energy, knowledge about the velocity and slope profile is required. Also stops on the way to the destination influence the overall energy demand. For gaining these necessary input, a concept and runtime optimized algorithm for the prediction of the driving destination from the current vehicle position to the destination is proposed in this work. Relying on the electronic horizon providing the information about the road ahead [13, 14], the driving trajectory to the destination is predicted online and approximated in a format suitable for runtime optimized prediction of the propulsion energy.

Using a model predictive approach, a profile of the mechanical power required for following a given driving trajectory can be estimated. In a powertrain topology with a single traction motor, this mechanical power can be only provided by this motor. With an appropriate

powertrain model, the corresponding electrical power is estimated considering also the current state of the powertrain components. By integrating this electrical power profile, the energy required for vehicle propulsion can be accurately estimated. In this way, also external environmental factors impacting the propulsion energy demand, e.g. traffic jams, can be considered. By using this input in the energy distribution optimization, also the adaptation of powernet and powertrain control to the environmental factors is realized.

In powertrain topologies with multiple motors several sources for providing mechanical power required for vehicle traction exist. Depending on motor characteristics, the overall driving efficiency can be increased by an appropriate torque distribution strategy, shifting the operating points of the individual motors to regions with higher efficiency [15, 16]. Since the torque distribution strategy strongly impacts the overall energy demand, a torque distribution profile is predicted based on the theory of optimal control. In this way, the overall powertrain losses can be minimized and fault reactions to possible powertrain failures can be automated, maximizing so the driving range also in case of a failure. In addition to the increase of the driving efficiency also further control goals enhancing the availability of a fail-operational powertrain are incorporated in the torque distribution optimization.

In case the energy required for completing a given driving mission exceeds the available energy resources, a three level degradation concept is embedded into the energy distribution optimization, considering the degradation of the load profile, driving profile and driving destination. In this way, the proposed energy management system estimates from the energetic point of view feasible settings for the driving mission enabling a safe transition to the standstill at the safest possible location for the passengers. In addition, the degradation of the powernet auxiliaries and of the velocity profile is minimized.

## 1.2. Thesis Overview

This dissertation is organized as follows. In Chapter 2, basic concepts used in this work are summarized. The different levels of driving automation, their impact on the design of the vehicle E/E architecture as well as aspects of fault-tolerant system design are discussed. A brief overview of the functional safety analysis process for road vehicles according to the norm ISO 26262, which is used for the derivation of safety requirements is given. The functionality of the vehicle powernet and powertrain are explained and the variables for their control are described. The concepts behind the theory of optimal control and telematic information provided by the electronic horizon are explained.

In Chapter 3, state of the art in energy management systems is described. Starting with



the general classification and an overview of related work, each class is then further detailed covering energy management systems designed for the control of a vehicle powernet, vehicle powertrain as well as approaches for the energy management in the entire vehicle. A brief review of the trip based energy management approaches is provided. The research gap in energy management systems for automated driving covering both, normal and failure case operation is concluded.

In Chapter 4, the concept of safety-based range extension meaning the optimization of powernet and powertrain control in a way allowing to arrive at the safest possible location for the passengers is introduced. This concept is proposed as the main control paradigm for the energy management in automated vehicles. In the second part of this chapter, requirements for the energy management system are derived and defined covering four main submodules, namely (1) energy distribution optimization, (2) prediction of remaining discharge energy of a battery, (3) battery's remaining discharge energy prediction and (4) propulsion energy prediction.

In Chapter 5, the first two submodules of the proposed energy manager, namely energy distribution optimization and battery's remaining discharge energy prediction are covered. Starting with a generic model of a fail-operational powernet, a mixed-integer optimization problem used for its control is derived. By solving this optimization problem, the fault reactions enhancing the reliability of the power supply are automated and the overall powernet efficiency is increased. Runtime optimized algorithms for solving the mixed-integer optimization problem are proposed as well as concepts and algorithms for accurate prediction of the battery's remaining discharge energy. The functionality of the proposed concepts and algorithms is exemplified on various examples and verified using simulation results for both, fault-free and failure case operation by means of fault injection.

In Chapter 6, the remaining two submodules of the proposed energy manager, namely driving trajectory and propulsion energy prediction are covered. First, a powertrain model used for the prediction of the propulsion energy required for completing a given driving mission is introduced. For the accurate runtime prediction of the propulsion energy, a concept and the corresponding algorithm for the prediction of the remaining driving trajectory based on the electronic horizon are presented. For the prediction of the propulsion energy two generic approaches are introduced covering both, powertrain topologies with a single traction motor as well as fail-operational topologies with multiple traction motors. Due to its impact on the overall driving efficiency and therefore on the required propulsion energy, additionally predictive estimation of the torque distribution between individual motors is proposed for the latter approach. Simulation results for both, fault-free and failure case operation are provided using two different powertrain topologies exemplify-

ing the functionality and verifying the benefits of the proposed model predictive control concepts and algorithms.

In Chapter 7, the four submodules of the proposed model predictive energy manager are combined to a system architecture covering two different types of powernet and powertrain topologies. For the first type, a fail-operational powernet providing reliable power supply for safety-critical functions, e.g. braking and steering, as well as a powertrain with a single motor are assumed. For the second type, in addition to the fail-operational powernet, also a powertrain with multiple traction motors enabling degraded driving in case of a failure is assumed. The generic energy management system architecture for each type as well as the benefits of the safety-based range extension are exemplified using simulation results in normal and failure case operation. The main results and contributions of this dissertation are summarized and concluded in Chapter 8.

# Chapter 2.

## Basic Concepts

In this chapter, basic concepts and terms used in this thesis are briefly summarized. An overview of driving automation levels and their impact on vehicle E/E-architecture is given in Section 2.1. The terms and aspects of fault-tolerant system design are provided in Section 2.2. A brief overview of the functional safety norm ISO 26262 as well as of risk-based method for the estimation of safety requirements is given in Section 2.3. The functionality of the main components of a vehicle powernet and powertrain is summarized in Section 2.4 and 2.5. The strategies for their control are classified considering their causality and optimality in Section 2.6. A brief description of the electronic horizon concept providing the necessary input for the implementation of predictive control strategies concludes this chapter.

### 2.1. Driving Automation

Driving automation is a challenging and continuously evolving technology, promising to bring numerous advantages [17]. Commuting problems like traffic jams or lack of parking are expected to be mitigated [17], traffic congestion and air pollution to be reduced and road safety increased, all this leading not only to social, but also to financial benefits [17]. For driving automation, all tasks currently executed by the driver must be stepwise transferred to the automation system. The environment must be sensed, decisions must be taken and the actuators must be controlled [17, 18]. Depending on the task split between a driver and automation system, different levels of driving automation can be defined, whereby the responsibilities of a driver are decreased with the increasing automation level. In this dissertation, the definition of the levels introduced by SAE is used [6].

In total five levels of driving automation are differentiated (level 1 to 5) while the case of "no driving automation" is defined as **level 0**. Four aspects are considered for the definition of automation levels [6]: (1) execution of the longitudinal and lateral vehicle

motion, (2) object and event detection and corresponding reactions, (3) execution of a fallback driving task and (4) constraints for the operation. **Level 1** of driving automation ("Driver Assistance" [6]) foresees solely the execution of either longitudinal or lateral vehicle motion by the system. Object and event detection and appropriate reactions are in the responsibility of the driver as well as the execution of a fallback driving task in case of any abnormalities. The operation of the automated driver assistance is also limited to defined use cases and situations (e.g. area of usage, whether conditions, velocity limits etc.). Due to permanent mandatory supervision by the driver, a fail-safe behavior is required for the subsystems executing either longitudinal or lateral vehicle motion. In case of a failure, a driver intervention is mandatory.

**Level 2** of driving automation ("Partial Driving Automation" [6]) requires both, the execution of the longitudinal and lateral vehicle motion by the system in constrained operating conditions. Equivalent to level 1, the responsibility for object and event detection with appropriate reactions, execution of a fallback driving task and permanent supervision lies with the driver. Therefore, also for level 2 a fail-safe behavior of the subsystems incorporated into the longitudinal and lateral vehicle motion is required.

Starting with **level 3** ("Conditional Driving Automation" [6]), the automated system takes over the control for the entire execution of the driving task in constrained operating conditions, consisting of lateral and longitudinal motion as well as object and event detection. The presence of the driver is required for taking over the control within a defined period of time after a request by the automation system in case of a failure or abnormalities in system behavior. For subsystems involved in the execution of the driving task, a degraded functionality for the duration of the handover of the vehicle control to the driver is required in case of a failure.

For **level 4** ("High Driving Automation" [6]) and **level 5** ("Full Driving Automation" [6]) the entire responsibility for the execution of a driving task as well as of a fallback driving task lies with the automation system. The presence of a driver as well as any kind of supervision or intervention is not required. The main difference between level 4 and level 5 lies in the definition of the operating conditions. While the operation of level 4 systems is limited to a defined set of use cases, e.g. driving on a highway or in a restricted area, no limitations exist for level 5. For the introduction of highly and fully automated driving systems, several challenges considering object detection and recognition, decision-making and execution of a safe stop in case of a failure must be mastered [18]. For the latter point, fault-tolerant designs for subsystems involved in the automated transition of a vehicle to a standstill are required. In the next section, general aspects of fault-tolerant system design are briefly discussed.

## 2.2. Aspects of Fault-Tolerant System Design

Fault tolerance is a field of designing a system, while accepting the existence of faults, in a way that a required functionality is still provided despite these faults [19]. For this, in general redundancy is required, foreseeing more resources than necessary for providing an intended functionality [19]. Faults can be classified in three categories [19]: (1) permanent, (2) transient and (3) intermittent. A **permanent** fault impacts the intended operation until a system is repaired or maintained. A **transient** fault impacts the functionality of a system for a given (normally short) duration of time and disappears afterwards. An **intermittent** fault occurs and disappears steadily resulting in an alternating functionality and non-functionality of a system.

Considering the functionality of a system after a fault, the systems can be classified in three categories [20]: (1) fail-silent, (2) fail-safe and (3) fail-operational. A **fail-silent** system switches off after a failure and does not influence the functionality of other systems [20]. A **fail-safe** system transits quickly to a safe state, either passively or actively through external measures, after a failure and has no impact on the functionality of other systems in this state [21, 20]. If no safe state is directly available after a failure, a certain minimum level of functionality must be provided by a **fail-operational** system for the period of time required for the transition to a safe state [21, 20].

It can be further differentiated between fault, error and failure [21, 22]. A **fault** is defined to be the cause for an error leading to an unintended state of a system, which is defined as an **error** [21, 22]. An error then finally can lead to a **failure** resulting in an unintended functionality or service provided by this system [21, 22]. While designing highly reliable systems, care must be taken by partitioning the functionality [22]. For avoiding **single points of failure**, meaning that a single fault can lead to a breakdown of a safety-critical system, appropriate system partitioning in independent **F**ault-**C**ontainment **R**egions (FCR) is required [22]. A **fault-containment region** defines a set of subsystems which might be impacted at once by one single fault [22]. For ensuring that a fault within one FCR does not impact the functionality of subsystems located in other FCRs, appropriate fault detection mechanisms are required at the boundaries of the FCR containing the fault [22]. A set of FCRs capable of fault detection and avoiding error propagation builds an **error-containment region** [22].

Depending on the application, different requirements considering the safety integrity might be needed. For its quantification, a functional safety norm ISO 26262 was introduced for the design of automotive applications, defining a process for the derivation of safety requirements, definition of corresponding safety integrity level as well as neces-

sary methods verifying the fulfillment of these requirements. A brief introduction to the functional safety for road vehicles is given in the next section.

## 2.3. Functional Safety for Road Vehicles

The functional safety norm ISO 26262 describes all activities required for the design of safety-related systems consisting of electrical, electronic and software components within road vehicles [10]. The main goal of the norm is to provide a framework of processes covering the entire safety life cycle of a system and enabling to design and to validate safety-related systems in a way that unreasonable residual risk is avoided and an acceptable level of safety is achieved [10]. The norm consists of 10 parts systematically structuring the required activities. Part 1 of the norm ("Vocabulary") defines the terms and definitions used in the norm [10, 23]. Part 2 ("Management of functional safety") describes general and project specific management activities during the concept and development phase as well as after start of series production [10, 23]. The actual engineering process is covered by four parts divided into "Concept Phase" (Part 3), "Product development at the system level" (Part 4), "Product development at the hardware level" (Part 5) and "Product development at the software level" (Part 6) [10, 23]. Part 7 of the norm ("Production and operation") defines the requirements for production, service and decommissioning [10, 23]. "Supporting processes" which are applicable throughout the safety life cycle are provided in Part 8 [10, 23]. The description of "ASIL-oriented and safety oriented analyses" covering the system tailoring and co-existence aspects as well as failure and safety analysis aspects are described in Part 9 [10, 23]. A "Guideline on ISO 26262" helping to understand the norm requirements is provided in Part 10 [10, 23].

For the development of a safety-related system first the corresponding safety requirements must be derived. For this, a systematic approach for HARA is provided in Part 3 of the norm helping to derive the safety goals and the corresponding ASILs. Before starting with the HARA, a precise definition of the system (or array of systems) implementing the intended functionality at vehicle level is required [10]. This item definition [24] contains besides the functional requirements also the definition of interfaces and interactions with other items, relevant legal requirements, operating conditions as well as possible external measures for risk mitigation [10, 23]. In the first step, possible system malfunctions and resulting hazards as well as relevant driving situations must be analyzed [10, 23]. In the next step, each hazard must be evaluated for relevant driving situations with three parameters [10, 23]: (1) **exposure** describing the relative probability of the hazardous situation in five classes (from E0 for "Incredible" to E4 for "High probability" [10]), (2) **severity** of potential harm in four classes (from S0 for "No injuries" to S3 for "Life-threatening injuries

(survival uncertain), fatal injuries" [10]) and (3) **controllability** rating the capability of the driver or other persons potentially at risk to handle the hazardous situation in four classes (from C0 for "Controllable in general" to C3 for "Difficult to control or uncontrollable" [10]). The required ASIL can be then estimated as a function of these parameters and a **safety goal** meaning a top-level safety requirement [24] for mitigation of the potential hazard must be defined [10, 23]. Depending on the definition of the ASIL, which can vary from ASIL A (lowest) to ASIL D (highest), different development processes must be followed and different residual failure rates measured in **F**ailures **I**n **T**ime (FIT) must be achieved (e.g. 10 FIT for ASIL D with 1 FIT equal to 1 failure in  $10^9$  h).

The defined safety goals with the corresponding ASILs are then used for the derivation of functional safety requirements for each subsystem which could lead to the violation of the safety goal in case of a possible malfunction [10, 23]. The functional safety requirements are then summarized in the functional safety concept containing also the measures for fault detection, definition of a safe state as well as fault reactions required for the transition to this safe state [10, 23]. As already discussed in Chapter 1, a reliable power supply of the safety-critical functions is one of the prerequisites for their correct functionality. Therefore, according to the norm ISO 26262, also a functional safety concept ensuring the reliability of the power supply must be developed. In the next section, a brief overview of powernet functionality is given.

## 2.4. Powernet System

The ongoing electrification of mechanical components, the increasing number of comfort loads and of computationally intensive **A**dvanced **D**river **A**ssistance **S**ystem (ADAS) applications in a vehicle are the cause for the increase of the overall power demand within the vehicle powernet [25]. For ensuring the reliable power supply of these components, new measures and powernet topologies are required. The basic task of a vehicle powernet is to distribute the energy to electrical components [26]. The powernet components can be classified in four main categories [27, 9]: (1) **energy generation** components which are responsible for the conversion of for example mechanical to electrical energy, (2) **energy storage** components responsible for the conversion of electrical to chemical energy and vice versa, (3) electrical loads with either dynamic or rather constant power demand and (4) corresponding **connecting elements**. In powernet topologies with multiple voltage levels (e.g. 12 V and HV), in addition **powerlink components** (e.g. DC/DC converter) converting the voltage levels and enabling the energy flow between subpowernets are required.

As discussed in the previous section, with the introduction of ADAS and automated

driving systems, new safety requirements for reliability of power supply arise, which must be considered for the design of a powernet. In addition to the safety requirements, also various regulative requirements must be fulfilled [9]. For example, in case the braking force depends exclusively on the use of an energy reserve, at least two independent energy reserves are required by the norm ECE R13-H [28, 9]. It is also expected that automated steering will have to provide at least the same performance without the driver interaction as in the case of conventional steering with a driver as a mechanical fallback, resulting in the requirement for redundant design of the steering functionality and power supply [9].

Considering the requirements above, the state of the art powernet of a conventional vehicle with an **I**nternal **C**ombustion **E**ngine (ICE) consisting of a generator and a 12V lead-acid battery must be extended for fail-operability. Several topologies are known from the current research and development activities covering multiple voltage level topologies, ring and tree topologies. A summary of currently known approaches as well as design aspects of fail-operational powernets for automated driving can be found in [9]. A behavioral model of the relevant powernet components is provided in Section 5.1.1, 5.4 and 5.5.1.

## 2.5. Powertrain System

Powertrain systems can be categorized considering the technology of the drivetrain used for the propulsion. A powertrain system of a conventional vehicle consists of an ICE, a gear box, clutches and torque converters with fossil fuel as the main energy carrier [29]. The drivetrain of an **E**lectric **V**ehicle (EV) contains an **E**lectric **M**otor (EM) as a single source for traction power and generally a gear box with a fixed 1-speed transmission. In a **B**attery **E**lectric **V**ehicle (BEV) the main energy carrier is electricity stored in a traction battery in form of chemical energy. The electrical propulsion system can be either centralized containing one EM only or also distributed containing multiple EMs [30]. By distributing the requested torque in a powertrain with multiple EMs which could be disengaged from the shaft by corresponding clutches, the driving efficiency can be increased [15]. Also powertrain topologies with a 2-speed transmission are investigated and turned out to be promising for the increase of the overall driving efficiency [31]. A clear advantage of the BEVs is their zero local emissions, but due to the low energy density of the batteries the driving range of the BEVs is rather limited and also long battery recharging times must be accepted [29].

The electrical energy for the EM can be also provided by a fuel-cell, which is an electrochemical device converting chemical energy in form of e.g. hydrogen into electrical energy [29]. The powertrain topology of a **F**uel-**C**ell **E**lectric **V**ehicle (FCEV) contains an electric drivetrain in combination with a fuel-cell.



Another possibility for the electrification of the powertrain is the combination of an ICE and an EM resulting in a **H**ybrid **E**lectric **V**ehicle (HEV), which can be divided into three main classes [29]: (1) parallel HEV, (2) series HEV and (3) series-parallel HEV. In a **parallel** HEV the driving power can be provided to the shaft by both, ICE and EM [29]. In a **series** HEV, the driving power is provided by the electric motor only, while a battery and an ICE are used for the generation of electrical energy [29]. In a **series-parallel** HEV both variants are combined [29]. A HEV is normally operated in a charge-sustaining mode, since it is not foreseen to recharge the battery from a grid and the fossil fuel remains the main energy carrier. In a **Plug-In Hybrid Electric Vehicle** (PHEV), the battery can be recharged from the grid enabling also the charge-depleting operation [29]. An overview and discussion of powertrain systems with multiple motors for HEVs and EVs can be found in [30].

## 2.6. Classification of Control Strategies

The task of a control strategy for a system is to find the most reasonable operating points according to the defined superimposed control goals and to control it [32]. For the control of a vehicle powernet and powertrain it can be differentiated between energy management and power management. **Energy management** defines the long term control strategy [33, 34] and can be used for example for the overall energy efficiency increase by optimizing the energy flows within the powertrain and powernet. **Power management** defines the medium term control strategy [33, 34] and can be used for example for voltage stabilization within a powernet by optimizing the power split between multiple power sources.

Control strategies can be classified considering their causality and control optimality [29]. A control strategy is **causal** if it is based on the knowledge about the current and previous system states only [29]. **Non-causal** control strategies require in addition also the knowledge about the future system states for the control [29]. Considering the control optimality a differentiation into heuristic and optimal control strategies is possible [29]. A **heuristic** control strategy finds the most reasonable operating points based on intuitive rules [29] which can be derived from system analysis and corresponding observations. An **optimal** control strategy makes the control decisions based on the theory of optimal control [29]. For this, a mathematical model of the system is required for the formulation of the objective function describing the control goals as well as for the definition of optimization constraints describing the system limitations.

The classification of the control strategies can be exemplified on the torque split between an ICE and an EM in a HEV. For the operation of a HEV, four different operating modes can be identified [29]: (1) ICE only driving mode, (2) EM only driving mode, (3)

power assist mode using both ICE and EM as well as (4) battery recharge mode. For the selection of the appropriate operating modes intuitive rules can be defined. The EM only driving mode can be activated below a certain wheel speed and torque request [29]. The battery can be recharged while operating the engine within medium torque requests [29]. In case the power request exceeds the maximum ICE power, the EM can be used for power assist mode [29]. In the regions above the battery recharge mode and below power assist mode, the ICE only driving mode can be activated [29]. A detailed description of this rule-based control strategy for the power split between an ICE and EM in a HEV can be found in [29].

Rule-based strategies are easy to implement for the online control of a HEV with for example a finite state machine or a **L**ook-**U**p-**T**able (LUT), but the optimality of the control cannot be guaranteed [29]. For further improvement of the control, a static optimization problem finding the best instantaneous power split between an ICE and EM based on the instantaneous system state can be applied. In general, a static optimization problem can be defined as [35]:

$$\min_{\underline{x}} f(\underline{x}) \quad \text{s.t.} \quad \begin{cases} \underline{c}(\underline{x}) = \underline{0} \\ \underline{h}(\underline{x}) \leq \underline{0} \end{cases} \quad \text{with} \quad \underline{x} \in \mathbb{R}^n, \underline{c} \in \mathbb{R}^m, \underline{h} \in \mathbb{R}^q \quad (2.1)$$

The objective function  $f(\underline{x})$  models the control goals as a function of the actuating variables vector  $\underline{x}$ . For the minimization of  $f(\underline{x})$ , the equality constraints  $\underline{c}(\underline{x})$  and inequality constraints  $\underline{h}(\underline{x})$  must be considered. The objective function can be defined for example as the instantaneous power losses of the powertrain as a function of the power split between an ICE and EM. By appropriate formulation of the constraints  $\underline{c}$  and  $\underline{h}$  an operation of the powertrain within defined system limits can be achieved. An example of an online control strategy for the power split between the ICE and EM of a HEV can be found in [36]. Depending on the complexity of the objective function and constraints, various analytical and numerical methods can be used for solving the optimization problem. Some examples of numerical solvers are the linear programming solver *linprog*, quadratic programming solver *quadprog* and nonlinear programming solver *fmincon* in MATLAB [37].

Since only the knowledge about the current system state is used for finding the optimal operating point of a system, also for static optimization the optimality of the control cannot be guaranteed. For achieving the global optimality, the knowledge about the future states of a system is required, which can then be used for the dynamic optimization finding the optimal trajectory of the control variables for the entire driving cycle. In general, a dynamic optimal control problem of a system can be defined as [35]:

$$\begin{aligned} \min_{\underline{u}(t)} \quad & J(\underline{x}(t), \underline{u}(t), t_e) = \vartheta(\underline{x}(t_e), t_e) + \int_{t_0}^{t_e} \phi(\underline{x}(t), \underline{u}(t), t) dt \\ \text{s.t.} \quad & \begin{cases} \dot{\underline{x}}(t) = \underline{f}(\underline{x}(t), \underline{u}(t), t) \\ \underline{x}(t_0) = \underline{x}_0 \\ \underline{g}(\underline{x}(t_e), t_e) = \underline{0} \\ \underline{h}(\underline{x}(t), \underline{u}(t), t) \leq \underline{0} \quad \forall t \in [t_0, t_e] \end{cases} \end{aligned} \quad (2.2)$$

The main goal of the dynamic optimization is to find an optimal trajectory for the control vector  $\underline{u}(t)$  minimizing the cost function  $J(\underline{x}(t), \underline{u}(t), t_e)$  defined in the Bolza-form in (2.2) and the corresponding trajectory for the system state vector  $\underline{x}(t)$  [35]. The dynamic behavior of a system is considered by the first equality constraint in (2.2) [35]. The second and the third constraints in (2.2) define the initial system state  $\underline{x}_0$  at the beginning of the optimization ( $t = t_0$ ) and the required final system state at the end of the trajectory ( $t = t_e$ ) [35]. Possible system limits are considered by the inequality constraint  $\underline{h}(\underline{x}(t), \underline{u}(t), t)$  in (2.2).

In the example of dynamic optimization of the power split between an ICE and EM of a HEV, the objective function can be defined as the integral of the fuel mass consumed over a given driving mission, but could be also extended for the inclusion of the pollutant emissions [29]. For the final state, a given battery **S**tate **o**f **C**harge (SoC) might be required for ensuring the charge balance over the driving cycle [29]. The dynamic optimization resulting in the optimal control trajectory can be estimated only offline for an assumed driving cycle, since it requires the exact and a priori knowledge of the future driving states. For enabling the online dynamic optimization, future system states can be predicted and then further processed in the optimization. Control strategies based on this approach can be classified under **M**odel **P**redictive **C**ontrol (MPC) strategies [29, 38]. Due to possible inaccuracy in the prediction, MPC approaches are also suboptimal [29].

## 2.7. Electronic Horizon

As presented in the previous section, for the MPC a prediction of future system states is required. If a driving cycle is known a priori, the optimal control law fulfilling the control goals can be estimated [29]. For the prediction of the future system state, the concept of electronic horizon can be applied [13, 14, 39]. The main goal of the electronic horizon is to provide accurate knowledge about the route coming ahead based on the digital map data to ADAS applications [13, 14, 39]. Depending on the usage of the map data, the ADAS applications can be classified in three categories [40]: (1) **non-map** ADAS applications do not require any data for their functionality, (2) **map-enhanced** ADAS applications can be improved in their functionality by utilizing the map data and (3) **map-enabled**

ADAS applications require the electronic horizon as basic input for their functionality. Different protocols for the transmission of static and dynamic map data to the ADAS applications were developed (e.g. ADASISv2 [14], ADASISv3 [41] or ETSI LDM [42]). In the following, the basic functionality of the ADASIS protocol is explained.

The transmission of the map data via the in-vehicle communication network foresees an ADAS Horizon Provider building the interface to the control unit containing the map data as well as an ADAS Horizon Reconstructor building the interface of the ADAS application receiving the data [14]. For the representation of the data, the main entity used in the ADASISv2 protocol is a PATH consisting of STUBs defining the connection points to other PATH entities as well as SEGMENTS characterizing a part of a PATH entity [14]. The position of the relevant changes or events on the PATH entity is specified by means of path indices and offsets [14]. The definition of a **M**ost **P**robable **P**ath (MPP) is used for the description of the path to be most likely driven in the future [14]. Three types of messages providing the data about current vehicle position (POSITION message), attributes along the path (SEGMENT, STUB, PROFILE and ATTACHMENT messages) and general meta data (META-DATA message) are used in the ADASISv2 protocol [14]. A SEGMENT message provides the most important characteristics of a segment, e.g. current speed limit, number of lanes or route type [14]. A STUB message describes the crossing of the MPP with other paths, containing the most important characteristics, e.g. offset of the crossing, turn angle, route type or number of lanes [14]. A PROFILE message contains the profile type (e.g. slope, curvature, speed limits), numeric value of profile spots as well as the interpolation type between the spots (e.g. discrete values, linear or higher order interpolation) [14]. An ATTACHMENT message provides specifications of a 0-dimensional path entity, e.g. of a speed sign [14].

Depending on the information needed by an ADAS application, the ADAS Horizon Provider can be configured for sending different types of messages. Examples of the map-enhanced applications are curve speed warnings identifying dangerous driving situations and warning the driver in advance [43], lane keeping support helping to enhance the lane detection in difficult situations [43], adaptive cruise control with improved effectiveness and quality of the driver assistance due to the usage of map data [43] and hybrid vehicle support enabling to increase the overall driving efficiency based on the knowledge about the road ahead [43].

# Chapter 3.

## State of the Art in Energy Management Systems

In this chapter, a brief review of the state of the art in **E**nergy **M**anagement **S**ystem (EMS) for a vehicle powernet and powertrain is given. A functional classification of different control strategies for the energy management in a vehicle is carried out in Section 3.1. Examples of the EMS for the control of energy distribution within a vehicle powernet are given in Section 3.2 and for the complete vehicle energy management in Section 3.3. An overview of supervisory algorithms for the control of the vehicle drivetrain is provided in Section 3.4. A survey of trip-based approaches for the powertrain control is presented in Section 3.5. A brief discussion of the research gap in energy management for automated driving in Section 3.6 concludes this chapter.

### 3.1. Classification of Energy Management Systems

The progressing electrification of mechanical components in a vehicle results in the increase of the overall electrical power demand and in high power peak load requests impacting the voltage stability in a powernet [25]. For tackling these problems several approaches for the power management in a vehicle powernet with the main goal to establish the voltage stability despite the increasing electrical power demand and load dynamics [25, 44] were developed. Some examples and the main ideas of related control strategies are briefly summarized in Section 3.2.

In a conventional powertrain with an ICE there is basically one single source for the generation of the mechanical power required for the vehicle propulsion. Therefore, no degrees of freedom are available for the split of mechanical power between multiple mechanical power sources as for example in a HEV between the ICE and EM. One way to improve the fuel economy of an ICE-based vehicle is to optimize the power generation of an alternator

by temporarily charging and recharging the 12V lead-acid battery, which is generally used for the establishment of the voltage stability in a vehicle powernet, shifting so the operating point of the ICE in regions with higher efficiency [45]. A further improvement of the fuel economy can be achieved by introducing electrical loads with a flexible and controllable power demand [46, 47]. With appropriate powernet control also the lifetime of the battery can be extended by reducing its wear in a trade-off with fuel economy [46, 47]. The focus of the mentioned approaches lies basically on the energy generation and distribution to the electrical loads in a vehicle with a conventional drivetrain. Some examples and main ideas of powernet control strategies in an ICE-based vehicle are briefly summarized in Section 3.2.

In an EV with one EM also no degrees of freedom exist for the split of mechanical power required for the propulsion. By using multiple energy sources with different specifications and properties, e.g. with **H**igh **S**pecific **E**nergy (HSE) or **H**igh **S**pecific **P**ower (HSP) [48], a better overall performance of the power supply can be achieved. A battery can be designed either for HSE or HSP, while a supercapacitor can provide HSP only [49]. Motivated by this, powernet topologies with hybrid approaches for the supply of the electric drivetrain in an EV combining both, batteries with HSE and supercapacitors with HSP, were investigated and corresponding EMS controlling the power split between both energy sources implemented, e.g. in [33, 34, 49, 48, 50, 51, 52]. The goals aimed by this approach are for example the minimization of the overall losses and therefore extension of the driving range, better performance during high peak power driving situations (e.g. accelerating or decelerating), extension of the battery lifetime [33, 34, 49, 48, 50, 51, 52] as well as the reduction of components size avoiding overdimensioned powernet designs [48]. But also approaches using multiple energy sources with similar characteristics enabling a better and more reliable performance are investigated, e.g. in [53, 54]. These approaches can be summarized in the category powernet energy management, since they focus only on the power distribution between the energy sources and do not consider the control of the drivetrain. Some examples and main ideas of the related control approaches for the power split between multiple energy sources in an EV drivetrain with a single EM are briefly summarized in Section 3.2.

Energy management systems covering all energy flows within a vehicle considering also different energy domains (e.g. mechanical, electrical, chemical or thermal) and aiming at an optimized control of powernet auxiliaries as well as of drivetrain are defined as the **C**omplete **V**ehicle **E**nergy **M**anagement (CVEM) [55, 56]. Several offline (e.g. [57, 58, 59, 60]) and online (e.g. [61, 62, 63]) approaches were proposed in the literature, which are briefly presented in Section 3.3.

A lot of research is carried out on the EMS for a HEV and a PHEV. Due to the availability of more than one source for mechanical power generation, the ICE and EM, the fuel consumption and pollutant emissions can be reduced with appropriate control strategies for the power split between both mechanical power sources [64]. This additional degree of freedom for the control of a HEV and a PHEV results also in increased complexity of the required control algorithms [65]. The main difference between a HEV and a PHEV is that no battery recharge from the grid is foreseen for a HEV, which is charged either by the ICE and alternator or during regenerative braking phases [66]. Therefore, for the control of a HEV the SoC of the battery is generally kept within a narrow operation range during the entire driving cycle (charge sustaining mode) [67] with the fossil fuel remaining the main energy carrier for the vehicle operation [29]. In contrast, due to the possibility to charge the battery at the end of a driving cycle, it becomes more energy efficient for the control of a PHEV to fully deplete the battery (charge depleting mode) during a trip [67]. In this way, the usage of the fossil fuel is combined with the electricity from the grid as an additional energy carrier for the vehicle operation.

Various approaches for the control of the power split between the ICE and EM in a HEV are known in the state of the art, e.g. [36, 38, 68, 69, 70, 71, 72]. The main goals hereby are the increase of the fuel economy (e.g. in [36, 38, 68, 69, 72, 70]), reduction of the pollutant emissions, increase of the driving performance and drivability (e.g. in [68, 69]) or reduction of component stress (e.g. in [69]). The usage of a traction battery with higher capacity in a PHEV and the possibility to recharge it from a grid provide new degrees of freedom for the control. Therefore, control strategies designed for a charge sustaining operation of a HEV must be adapted. New control strategies utilizing the ability of the charge depleting mode for PHEVs were investigated and numerous examples can be found in the literature, e.g. [66, 73, 74, 75, 67, 76, 70]. The main goals of the related control approaches are the reduction of the fuel consumption (e.g. in [66, 73, 74, 67, 76, 70]), reduction of directly and indirectly produced CO<sub>2</sub> (e.g. in [75]) and of component stress (e.g. in [73]). Various approaches and their main ideas are briefly summarized in Section 3.4.

The goal of the control strategies mentioned above was mainly to optimize the energy flows within the vehicle powernet and drivetrain for a given driving cycle. In addition to the energy flow optimization as a main task of an EMS, also the driving strategy determining the velocity profile can be optimized with the goal to increase the driving comfort (e.g. in [70]), driving safety (e.g. in [77]) and energy efficiency under consideration of the driving time [77, 70, 78, 79]. Examples of these ADAS combining both, the predictive optimization of the powertrain energy flows and optimization of the driving strategy (velocity profile), can be found e.g. in [77] for a conventional ICE-based vehicle, for a HEV and a PHEV in [70] and for an EV with a single EM in [78, 79].

A promising technique in the design of an EV drivetrain is the usage of decentralized propulsion systems consisting of multiple EMs [30] or of the so called **M**odular **C**ascade **M**achine (MCM) systems [80] instead of a centralized propulsion system with one EM only [30]. In EV drivetrains with multiple EMs the overall efficiency of the propulsion system can be increased especially in regions of low torque requests and high torque and low speed requests [80]. In addition, also better availability and reliability of such drivetrains tolerating a breakdown of one EM and still providing a degraded propulsion functionality can be achieved. With this new degree of freedom allowing to split the requested mechanical power between the EMs, a need for new control strategies arises. Several approaches for the optimal torque split between the EMs were investigated, e.g. for an axle-individually driven EV in [81, 15, 82, 16], wheel-individually driven EV in [83, 84, 85] and for an EV drivetrain with three EMs of mixed technology [86]. Examples and main ideas of related approaches are presented in Section 3.4.

The control strategies for the energy management in powernet and powertrain mentioned above are either heuristic or based on the theory of optimal control. Offline optimization based on **D**ynamic **P**rogramming (DP) obtaining a global optimum for a given driving cycle was generally used as a baseline for the performance evaluation of algorithms for the online implementation in an **E**lectronic **C**ontrol **U**nit (ECU). Also predictive approaches for the online implementation of EMS based on the MPC and prediction of the future driving states over a given horizon were proposed. The state of the art also includes online control strategies considering the entire driving cycle starting from the current vehicle position to the destination based on the MPC. Examples and the main ideas of these trip-based EMS can be found in Section 3.5.

## 3.2. Powernet Energy Management

In conventional drivetrain topologies with an ICE or in EVs with a single EM only one source for generation of mechanical power required for vehicle propulsion exists with no need to optimize the power split between multiple sources for mechanical power as for example in a HEV. The focus of the control strategies for these drivetrain topologies lies mainly in the optimization of the power supply for the loads. In this section several examples of related control strategies for a conventional drivetrain with an ICE and for EVs with multiple energy sources are provided.

### **Powernet Control Strategies for a Conventional Drivetrain with an ICE**

Besides progressing replacement of mechanical and hydraulic components with electrical ones, also more comfort and performance is expected in a vehicle, leading to the increased



power demand in a vehicle powernet [45] as well as to short-term power peaks affecting the voltage stability [25]. For mitigation of these issues, the authors of [25, 44] propose a predictive balancing of power distribution based on a cybernetic approach by introducing a layered hierarchical control structure consisting of objects and corresponding management layers generating the control targets. Short-term degradation of the loads' power demand, smoothing of superimposed power peaks or increased power generation are some examples of possible measures which can be initiated for voltage stabilization when a critical and highly dynamic driving situation is predicted [44].

The authors of [45] propose a control strategy for the alternator in a conventional ICE-based drivetrain reducing the fuel consumption and emissions while maintaining the same drivability. The main idea is to minimize the losses in the engine, alternator and battery by finding an optimal control sequence for alternator output power set points [45]. First, an optimization problem is established for offline optimization with DP, which is then further simplified for the use with **Q**uadratic **P**rogramming (QP) [45]. For the use in online applications, a combination of DP or QP with a limited prediction horizon is proposed for the MPC. This approach is further extended by the authors of [46, 47] by additionally incorporating electric loads with flexible and controllable power demand in the optimization problem. The flexibility in the adaptation of the power demand of the loads is used to achieve a balance with the power provided by the alternator, avoiding so unnecessary charging or discharge losses in the battery [46, 47].

### **Control of Multiple Energy Sources**

Various approaches for the power and energy management of EVs with multiple energy sources are known, e.g. [33, 34, 87, 49, 48, 50, 51]. By applying causal control strategies the power split between a battery and an ultracapacitor pack can be optimized [33, 34]. With prediction of future power demand trajectories further enhancement can be achieved with non-causal approaches maximizing the battery SoC at the end of the prediction horizon [33, 34]. For example, the authors of [33, 34] investigate a power and energy management system controlling the power split between a battery and ultracapacitors by dividing the control in three shells. The energy management shell defines the long-term strategy (range of seconds), power management shell defines the medium-term policy (range of milliseconds) and power electronic shell is used for immediate-term control of power electronics (range of microseconds) [33, 34]. Rule-based power management is applied for mitigating peak power demands from the battery, while the maximum allowed battery power is provided by the superimposed energy management system based on the fuzzy logic control ensuring appropriate SoC of the ultracapacitors for covering the peak power demands [33, 34]. The authors of [87] also investigate a rule-based control

strategy for the power split between a battery and a supercapacitor pack for an EV bus. An approach combining both, the limitation of the battery current as well as the speed dependent SoC control of the supercapacitors is applied [87].

Similarly to [33, 34], also the authors of [49, 48, 50] use a multi-level approach for the optimization of the power split between a battery and a supercapacitor pack. For the long-term strategy with decision intervals of 1 s, a rule-based approach derived from expert knowledge is applied setting the upper and lower bounds for the discharge power of the energy sources [49, 48, 50]. The short-term strategy with decision intervals of 10 ms is based on an optimization problem minimizing the delta between power demand and power provided by the sources by means of simulated annealing [49, 48, 50]. The output is then used for the very short-term control of the power electronic converters [49, 48, 50]. The proposed control strategy is compared with a power management strategy based on the frequency disaggregation of the power demand by means of a high pass filter verifying the advantages in efficiency and components sizing in [48]. An algorithm for the real-time implementation based on the **P**article **S**warm **O**ptimization (PSO) is proposed in [50]. In [51], a power split control between a battery and a supercapacitor pack for a three-wheel EV is implemented with a comprehensive fuzzy logic controller increasing the global efficiency and performance while additionally enhancing the battery lifetime.

The authors of [53, 54] propose an EMS for the control of two independent traction batteries with different nominal voltage values and corresponding DC/DC converters connecting them to the HV-DC link, which is then used for the supply of three traction motors. The main functions of the proposed EMS are the calculation of the maximum available power for both, acceleration and regenerative braking, which is further processed by the vehicle dynamics manager, power distribution and batteries charge control [53, 54]. The goal for the power split between the batteries is to balance the SoC as well as the available power for the following time period [53, 54]. Three factors for the power split are taken into consideration enabling equal current distribution, SoC balancing and equalization of the predicted maximum power for both batteries [53, 54]. Also for the case of a fault in one battery the control strategy switches the power supply to the functional one assuming that the required power can be provided by this battery only [53, 54].

### **3.3. Complete Vehicle Energy Management**

A CVEM system considering all powerflows within a vehicle was envisioned in [55]. For reducing the complexity in development of EMS for different vehicle configurations, the authors aim to achieve a plug & play functionality for powernet auxiliaries while maximizing the energy efficiency of the vehicle powernet [55]. A price-based strategy is foreseen

for the control of a smart powernet with programmable auxiliaries [55]. Also the authors of [56] point out the necessity for the vehicle energy management to reduce the overall energy demand and CO<sub>2</sub> emissions. Freewheeling, energy recuperation and advanced stop/start systems in a conventional ICE-based vehicle are the key elements of the proposed rule-based control strategy [56].

A control strategy based on game theory in combination with MPC is proposed for the control of electrified auxiliaries with the main goal to improve the global vehicle energy consumption and to increase the lifetime of a HV battery in HEV/PHEV [57]. Also the authors of [61] use a game-theoretic approach for the implementation of a CVEM for a hybrid heavy-duty truck with the main goal to reduce the global fuel consumption. The control problem is modeled as a two-level single-leader (driver) and multi-follower (auxiliaries) game [61]. For enabling the online control, the first level of the game (sequential game between the leader and each follower) is played offline, while the second level (simultaneous game between the leader and all followers) is played online [61]. This game-theoretic approach for the CVEM is further extended for adaptivity to various drive cycles and driver behaviors by using different probability distribution functions for drive patterns in [62]. For the online implementation of this adaptive game-theoretic CVEM a two stage approach is applied, designing the control strategy for different drive patterns offline and by using an online classification for its appropriate selection [62].

Another approach for the offline CVEM for a hybrid heavy-duty vehicle is proposed by the authors of [58]. For solving the large-scale optimization problem of the CVEM, a dual decomposition method dividing the entire optimization in several smaller optimization problems is applied [58]. This approach is further extended for handling also CVEM optimization over large horizons in [59]. An offline control strategy solving a convex approximation of the CVEM problem for a heavy-duty truck based on the distributed optimization is investigated by the authors of [60]. Methods for the real-time implementation of a distributed economic model predictive control for CVEM of a heavy-duty truck are investigated in [63].

### **3.4. Powertrain Energy Management**

In drivetrain topologies with multiple sources for the generation of mechanical power required for vehicle propulsion, an EMS defining the appropriate power split between these sources is required. In this section, examples and the main ideas of control strategies for the optimal power split between the ICE and EM in a HEV and PHEV as well as between multiple EMs of an EV are presented.

### **Drivetrain Control Strategies for a HEV**

The author of [36] proposes an offline optimization for the control of a parallel HEV with the main goal to minimize the power losses of the drivetrain and therefore to increase the fuel economy. A trajectory for the optimal power split between the ICE and EM is estimated for a given driving cycle under consideration of the required SoC balance at the end of the driving cycle [36]. For runtime implementation, the proposed control strategy is then simplified for online minimization of the instantaneous power losses while ensuring the operation of the battery within a small SoC range [36]. For this, an additional term for the battery charge and discharge power scaled with a factor estimated as a function of SoC is used in the definition of the objective function [36].

Also in [38] a control strategy for the control of the power split between the ICE and EM of a parallel HEV under consideration of the charge and discharge balance of the traction battery is investigated. By incorporating the map data for the prediction of the velocity profile, a MPC with a sliding horizon based on the adapted version of DP with reduced calculation time is proposed [38]. For the approximation of the velocity profile, constant acceleration and deceleration values are assumed [38]. The reduction of the computational time of DP is basically achieved through appropriate reduction of the relevant system state space based on the limitation of the control variables and required final system state [38].

In [68], the author proposes a rule-based adaptive and predictive control strategy for the power split between the ICE and EM of a parallel HEV. The main goals of the EMS are to increase the fuel economy and driving performance, to ensure the intended functionality by avoiding acoustic and optic anomalies and to enhance the driving experience. By avoiding computationally extensive optimizations, a control strategy based on a finite state machine in combination with feedback control is provided for runtime implementation in a vehicle ECU. For the prediction of future driving situations in the range of several kilometers, information from various onboard sensors, e.g. camera or radar, in combination with the map data from navigation system is used [68].

The author of [69] proposes an online control strategy for a parallel-series HEV based on the static optimization with the main goal to reduce the fuel consumption, to increase the driving performance and to reduce the component stress. Due to high computational complexity of online optimization, a rule-based control strategy is derived by using the results from online optimization [69]. Also in [72] online optimization is considered to be not very suitable for runtime implementation in an ECU. Therefore, offline optimization is used for the generation of a map-based control strategy for power split between an ICE and EM of a parallel HEV for online implementation in an ECU [72].

### Drivetrain Control Strategies for a PHEV

The authors of [66] propose a rule-based EMS for the control of the power split between the ICE and EM of a parallel PHEV comparing charge depletion and charge sustaining strategies with the electric assist strategy. Also in [73], a rule-based EMS for a series PHEV implemented by means of fuzzy logic is proposed with the main goal to ensure the operation of the ICE in regions with the maximum fuel efficiency and to avoid a possible battery overdischarge leading potentially to its damage. The basic concept of the EMS is to operate the battery in the charge depleting mode until the lowest permissible battery SoC is achieved with ICE assisting the EM [73]. The battery is then further operated in the charge sustaining mode and is used for the coverage of peak power demands [73].

In [74], an EMS for the optimal power split between two EMs and one ICE of a series-parallel PHEV based on the stochastic DP with the main goal to increase the overall fuel economy is studied. For the trade off between the fuel and electricity consumption additionally the relative fuel to electricity prices are incorporated into the objective function [74]. Due to the stochastic drive cycle model used for the optimization, no a priori knowledge about the future drive cycle is required in this approach and an optimal solution in the average sense is achieved [74]. In [75], an EMS for a PHEV is introduced with the main goal to minimize the total CO<sub>2</sub> emissions produced directly by the ICE and indirectly considering the primary energy required for the electricity taken from the grid. The general structure of the algorithm based on the Pontryagin's minimum principle can be adapted for the control of series, parallel and series-parallel PHEVs [75].

Due to the computational complexity of optimal control strategies based on DP, various EMS approaches were studied enabling the runtime implementation in a vehicle ECU. For example, the authors of [76] investigate the usage of neural networks for the control of a series-parallel PHEV with the main objective to increase the fuel economy. Two different versions of neural networks for the usage with and without given trip length and duration are trained based on the simulation data obtained by means of DP for various driving cycles [76]. As input for the neural network eleven variables containing the trip information, powertrain state and power request are used for the first version and seven variables neglecting the trip information are used for the second version of the neural network, both estimating the battery output current [76].

The author of [70] investigates an ADAS combining both the EMS and the optimal driving strategy for a parallel HEV and PHEV with the main goal to increase the fuel economy, driving comfort and to optimize the driving time. For this, the entire driving cycle to the destination is considered in the MPC based on the DP extended with iterative, heuristic and approximated methods speeding up the calculation time for the runtime execution

[70]. Three levels of prediction and optimization with various time periods for long range, mid range and short range control are used in parallel [70]. Further examples and an extensive literature review on EMS for a PHEV can be found in [88, 89].

### **Drivetrain Control Strategies for an EV with Multiple EMs**

The authors of [81, 15] investigate a torque distribution strategy for a front and rear axle driven EV with one EM per axle and a common traction battery with the main goal to increase the overall driving efficiency by shifting the operating point of the identical EMs into the regions with higher efficiency. It was pointed out that in regions with low torque requests it becomes more energy efficient to decouple one EM via the corresponding clutch and to operate both EMs in regions with high torque requests [81, 15]. This result is used in the online control strategy which differentiates between two cases [81, 15]. For torque requests higher than a defined threshold, both EMs are operated and the requested torque is equally distributed between the EMs [81, 15]. If the torque request does not exceed the defined threshold, power losses are calculated for both, the operation of one EM only providing the entire torque and for the operation of both EMs with equally distributed torque [81, 15]. The case with the minimum of power losses is then used in the control achieving in this way an improvement of drivetrain efficiency by approx. 4% over the **N**ew **E**uropean **D**riving **C**ycle (NEDC) [81, 15].

Also the authors of [82, 16] investigate a torque distribution strategy for an EV drivetrain with two identical EMs and one common traction battery. An optimal torque distribution factor is estimated by solving a non-convex optimization problem minimizing the overall drivetrain losses [82, 16]. Due to high computational effort the optimal torque distribution factors are estimated offline and stored in a LUT as a function of requested torque and speed [82, 16]. Similar to the results presented in [81, 15], the operation of one EM in case of a low torque request and equal torque distribution for a high torque request is estimated to be optimal in most of the cases [82, 16]. The LUT for the optimal torque distribution factor is then used online for the control of the drivetrain [82, 16]. By optimizing the torque distribution considering the energy efficiency only, frequent switching of the clutches can occur if the torque request oscillates at the threshold between the states for optimal operation with either one or both EMs, resulting in increased wear of the components and driving discomfort [82, 16]. For tackling this problem, the basic torque distribution control strategy is extended to MPC under consideration of a penalty for frequent switching in the objective function [16]. As output of the optimization, torque distribution and clutch operation vectors are estimated with DP for the finite prediction horizon [16]. Simulation and experimental results show an efficiency increase by up to 12% compared to equal torque distribution [16].

The authors of [83] investigate a control strategy for an EV drivetrain with four in-wheel motors and one common traction battery. For the estimation of the optimal torque distribution, minimization of the drivetrain power losses as a function of speed, longitudinal force and yaw moment resulting in a non-convex multi-parametric optimization problem is proposed [83]. Under the assumption of strictly monotonically increasing drivetrain losses, an analytical solution for the optimization problem is derived and parametrized as a function of the vehicle speed [83]. The authors conclude that the operation of a single axle is optimal in low torque regions and equal torque distribution is optimal in high torque regions [83]. For the estimation of the torque demand threshold separating the low and high torque regions, the derived analytical formula is used [83]. Further examples of the control strategies for an EV with four in-wheel motors can be found e.g. in [84, 85].

A comparison of the energy efficiency of an EV drivetrain based on an MCM propulsion system, which is basically a system of EMs with adapted shafts and covers, with a single EM drivetrain is investigated in [80]. For the control of the MCM an optimal torque distribution is estimated based on the maximization of the overall efficiency solved with a sequential search algorithm [80]. By using two different EMs in the MCM with total rated power equal to the rated power of the single EM, the authors show that the high efficiency area can be significantly increased compared to the efficiency map of the single EM, especially considering the low torque area as well as high torque and low speed area [80]. Simulation results show an improvement of approx. 11.8% over the Urban Dynanometer Driving Schedule (UDDS) [80].

The authors of [86] propose a real-time control strategy for torque distribution in an EV drivetrain consisting of one indirectly driven brushless DC motor at the front axle and two in-wheel permanent magnet motors based on the PSO algorithm. The results of the optimal torque distribution estimated with the algorithm based on the PSO are compared to the results obtained by means of DP over a NEDC proving the accuracy of the PSO based EMS [86]. Furthermore, the authors compare the driving efficiency of different multi-kind (various types of EMs) and single-kind (one type of EM) drivetrain configurations and conclude that up to 10% of efficiency increase can be obtained with appropriate dimensioning of multi-kind drivetrain configurations [86].

### 3.5. Trip-Based Energy Management

In [90, 91], a trip-based power management for a PHEV estimating the optimal battery charge and depletion curve over the entire driving cycle for the minimization of the fuel consumption is proposed. Based on the real-time traffic information and historical traffic data, a simplified driving cycle is approximated assuming constant acceleration and de-

celeration values and by dividing the route into segments with a given speed limit and bounded by two consecutive stops, for which an average waiting time is assumed [90, 91]. A similar approach of a simplified driving cycle assuming constant acceleration and deceleration values can be also found in [38]. For this simplified driving cycle an optimal charge and depletion curve is then estimated by means of dynamic programming [90, 91]. For reducing the calculation time, the dynamic programming is divided into two optimization levels, resulting in a two-scale optimization in [92]. A macro scale global optimization is first executed offline for the entire trip estimating the global optimal SoC reference curve, which is then used for setting the end SoC value for micro scale optimization executed online for short segments [92]. Further examples for the trip-based power management of a PHEV can be found e.g. in [93, 67, 94, 95].

The authors of [96, 97] propose a trip-based energy management system for an EV helping to ensure that the driver can safely reach the driving destination with the current battery SoC. For this, a supervisory trip management utilizing the electronic horizon and based on a real-time dynamic programming approach used for the estimation of recommended maximal driving velocity profile and acceleration limits under consideration of all electric loads is applied [96, 97]. The estimation of the velocity profile is executed online by dividing the entire trip into segments with constant velocity limits and slope values, while the calculation of optimal acceleration and recuperation limits is optimized offline and stored in look-up tables for different changes in velocity [96, 97]. A similar approach dividing the route in segments with constant values for factors influencing the power losses was also proposed in [98]. For the recalculation of the recommended velocity profile due to external unexpected changes a calculation time of approx. 1 min is reported [96, 97].

The author of [99] proposes a modular functional architecture for the EMS of an EV with the goal to solve optimally the trade off between driving range, driving dynamics and comfort. Under consideration of all relevant energy sources and sinks, the energy flows are optimized for achieving extended range by temporarily shifting thermal and comfort requirements [99]. The proposed architecture consists basically of three main modules for the energy management, drivetrain management and driving range estimation under consideration of route preview [99] and covers both, driving missions with and without set destination. The goal of the energy management is to control and to prioritize the energy flows for the trade off between driving range, driving dynamics and comfort [99]. The drivetrain management is responsible for the execution of the driver power requests by considering also the optimal and online torque distribution in EV drivetrain topologies with multiple EMs. For the extension of the driving range an iterative temporal and situational degradation of the loads is foreseen, which are classified in groups with different priorities according to their criticality and functionality [99]. For the prediction of



the average propulsion energy, the mechanical power demand at the wheels based on the driving profile is predicted and integrated [99]. The remaining driving range is then estimated considering the current battery SoC, nominal battery energy and average energy consumption per kilometer for propulsion, climatization and loads in low voltage subpowernet [99]. In case the set destination is given, a velocity profile is predicted based on the velocity limitations, slope profile and cornering velocities [99]. In phases with constant velocity, a velocity dependent fluctuation is superimposed [99]. For the extension of the driving range, basically four measures are identified [99]: (1) degradation of the maximum power and torque for the propulsion, (2) degradation of maximum power for climatization, (3) reduction of battery losses by appropriate control of loads for temporarily increasing and decreasing of power demand in recuperation and propulsion phases similar to [55], and (4) optimal torque split between the multiple EMs for minimization of power losses.

### **3.6. Research Gap in Energy Management for Automated Driving**

As shown in the previous sections, numerous approaches for the control of the powernet and powertrain were carried out for various drivetrain topologies of an ICE-based vehicle, a HEV, a PHEV or an EV. Also multiple approaches for the enhancement of the voltage supply and voltage stability in a powernet were proposed. However, the focus of the EMS in the state of the art is to increase the driving efficiency of a vehicle in a fault-free operation, while the control of the vehicle powernet and powertrain in case of a failure is not addressed. With the introduction of highly and fully automated driving, tightly bounded with the release of the driver from his responsibility for the control of the vehicle and passenger safety, the main goal in the control of the vehicle powernet and powertrain changes. Since the automated vehicle (level 4 and 5) must be able to execute a fall back driving task without any driver interaction and supervision also in case of a failure, the main control goal for the EMS for automated driving can be considered to establish reliable power supply for the duration of the entire driving mission in both, fault-free and failure case operation.

This gap is addressed by the work presented in this thesis. For the control of fail-operational powernet topologies additional degrees of freedom arise for the energy distribution due to the redundancy of the energy flow paths required for the supply of safety-critical loads (e.g. braking or steering). A generic approach for the control of a fail-operational powernet takes advantage of these additional degrees of freedom for the enhancement of the power supply and increase of overall energy efficiency under consideration of possible failure states. Furthermore, by incorporating the failure models of the

powernet components into the optimization problem used for the MPC with the main goal to establish reliable power supply for the entire driving mission and to arrive at the safest possible location for the passengers, also required fault reactions are automated. For the fault reactions on system level, degradation of powernet loads, of driving profile and of driving destination is foreseen and embedded in the mixed-integer optimization problem used for the control of the vehicle powernet.

With a fail-operational design of the vehicle drivetrain, enabling a degraded propulsion functionality also in case of one failure, vehicle breakdown at hazardous locations, e.g. on the highway within the active traffic, can be avoided and therefore the acceptance of automated driving systems increased. For the control of fail-operational powertrain topologies, generally consisting of multiple motors and independent traction batteries, also new control strategies for normal and failure case operation are required, which are also not addressed in the state of the art. This work provides new concepts and algorithms for the control of the drivetrain in automated EVs with multiple traction motors and independent traction batteries. As already shown in Section 3.2, with appropriate torque distribution between the EMs, the overall driving efficiency can be significantly increased, resulting in the extension of the available driving range. Therefore, for accurate prediction of the remaining driving range, a trip-based prediction of the torque distribution profile considering also possible failure states of the powernet components is required, which is also not addressed in this form in the state of the art for the drivetrain control in an EV with fail-operational powertrain. The work presented in this dissertation closes this gap.

## Chapter 4.

# Energy Management for Safety-Based Range Extension

With increasing levels of driving automation also reliability and availability requirements for subsystems responsible for vehicle motion increase. According to the classification of driving automation levels defined by SAE [6], which are briefly summarized in Section 2.1, an automated vehicle should be able to execute a fallback driving task in case of a failure without any driver interaction starting with highly automated driving (SAE level 4). While fully automated driving (SAE level 5) has no restrictions, the operation of a highly automated vehicle is restricted to a set of defined use cases and driving situations in accordance with the intended system design. Therefore, for a highly automated driving system, the presence of a driver is not required if a vehicle is operated only within the intended restricted area.

For a fully automated driving system the absence of a driver must be assumed, meaning that in case of safety-critical faults leading to a possible vehicle breakdown, no person with required qualification would be available for securing the vehicle and ensuring the passengers' safety. For manual driving, these tasks are currently in the responsibility of a driver. Fail-operability of an automated vehicle can help to prevent an unsecured vehicle breakdown endangering passengers and the environment and will additionally lead to a higher acceptance of driving automation. This work proposes the concept of safety-based range extension, meaning the adaption of vehicle control allowing to arrive at the safest possible location for the passengers. It will be explained in detail in Section 4.1.

For driving automation, three main tasks must be executed: (1) sensing the environment, (2) actuating the braking, steering and propulsion subsystems as well as (3) controlling the vehicle motion. Depending on the definition of the use cases and the required stop location to be reached in case of a failure, the subsystems executing these tasks must be




































symbol	destination	prio	name	energy demand	drive	brake	steer
	driving home	1	SSL A				
	parking area	2	SSL B				
	emergency stop bay	3	SSL C				
	emergency lane	4	SSL D				
	rightmost lane	5	SSL E				
	current lane	6	SSL F				
	emergency braking	7	SSL G				

Figure 4.1.: Prioritization of safe stop locations.

designed with corresponding ASILs in accordance with the functional safety norm ISO 26262-3 [10]. For the intended functionality of these subsystems, a reliable power supply for the entire duration of a driving mission in normal and failure case operation must be established. The power supply is considered to be reliable if subsystems can be operated within the specified voltage range and sufficient energy for their operation can be provided. An energy management system based on the theory of optimal control with automated fault reactions increasing the overall powertrain and powertrain efficiency is proposed in this work. Basic requirements for the energy management system are discussed and specified in Section 4.2.

## 4.1. Safety-Based Range Extension

An automated driving system can be considered to be in a safe state if it comes to a standstill. Therefore, also in case of a failure, an automated transition to a standstill must be guaranteed. Depending on the location at which a vehicle comes to a standstill, different risks and hazards may arise for both, passengers of a vehicle and persons in its surrounding. For example, if in case of a failure an immediate emergency braking is executed, a vehicle comes to a stop in the same driving lane. In this situation, due to the active traffic, risks and hazards for the passengers are higher than if a vehicle continues the operation and comes to a standstill for example at the next emergency stop bay. A possible rear end collision or traffic obstruction could be avoided in this case. Therefore, possible locations for a vehicle stop, **S**afe **S**top **L**ocations (SSL), can be rated in terms of risks and hazards arising for the passengers and persons in the surroundings, if an automated driving system comes to a standstill at this location.

Such a possible rating of safe stop locations is depicted in Fig. 4.1. The destination set by the passengers (SSL A, "driving home") is considered to be the safest location. If it is not possible to arrive at this destination, the next coming parking area (SSL B) is considered to be the safest location, since a vehicle can be taken off the road and the passengers could get off the vehicle with minimized risks. A standstill in the current driving lane after an emergency braking (SSL G) is considered to be the worst case scenario with the maximum of risks and hazards for the passengers and the persons in the surroundings. The difference between a standstill in current lane (SSL F) or after an emergency braking (SSL G) lies in the transition time. While for SSL G an immediate braking with full available performance is executed, a more comfortable stop is intended for SSL F, resulting in a longer distance to be covered before coming to a standstill and also in longer time available for driver or system reactions in subsequent vehicles.

A definition of the safe stop location, that must be reached in case of a failure, is user defined and must be selected after an appropriate analysis of risks and hazards for a given use case and considering the required system availability. It has a huge impact on the design of the vehicle powertrain and powernet topology and affects also the required fail-operational behavior of the subsystems responsible for the automated transition to a safe state, which is discussed later in this section. A fail-operational system remains functional also in case of one fault [100] and it can be in general achieved with a redundant design. If, for example, the "driving home" is required also in case of a failure, fail-operability for the functions drive, steer and brake is required, which is indicated by a green box in the corresponding columns in Fig. 4.1. Also for driving to the next parking area, to emergency stop bay or for stopping in the emergency lane, the fail-operability of drive, steer and brake functionality is required, since due to the distance to be covered, it cannot be guaranteed that the safe stop location can be reached by means of coasting in case of a failure in the propulsion system. The correct service of the safety-critical subsystems after a fault must be provided for the duration required for the automated transition to a safe state location, which depends on the road environment and can be estimated for a given use case.

For stopping at the rightmost lane, fail-operational steering and braking subsystems are required. Assuming no uphill driving and no traffic jam, stopping at the rightmost lane could be executed without a fail-operational propulsion system by means of coasting using the kinetic energy of a vehicle, which is indicated by an orange box in the corresponding columns in Fig. 4.1. Also for stopping in the current lane, propulsion and steering systems might not be required, assuming additionally a straight road and a short distance to be covered. A functional propulsion system is not required in case of an immediate emergency braking (indicated by a red box). Assuming a straight road, only a fail-operational braking

system is required. Also the amount of energy required for the transition to a safe state is dependent on the definition of the safe stop location. Assuming an increasing distance that should be driven before coming to a standstill, starting with emergency braking and ending with "driving home", the amount of energy required for the transition to a safe state increases with the priority of the safe stop location.

In this work, a concept for safety-based range extension for the control of a vehicle powernet and powertrain is proposed. Independently from the definition of the safe stop location, the energy management system adapts the control strategy to the current powernet and powertrain state and optimizes the energy flow in a way allowing to arrive at a safe stop location with the highest priority. The energy demand required for completing a given driving mission can be divided into two parts: (1) the energy required for the propulsion and (2) for the supply of powernet auxiliaries (safety-critical and driving comfort functions). For a given destination, the energy demand of propulsion loads and powernet auxiliaries as well as the available energy resources can be estimated predictively. If the total energy demand exceeds the available resources, the driving mission to this safe stop location with the current settings cannot be completed. For this case, a three-level-degradation concept is proposed.

The total energy demand can be reduced in three different ways. A load profile describes the power demand of safety-critical and comfort loads. By degrading the load profile, the total required energy can be reduced, resulting in a decreased driving comfort for the sake of extended driving range. A driving profile describes the settings of the driving performance and is defined in terms of maximum velocity and acceleration values used on the way to the destination. By degrading the driving profile, the velocity and acceleration values are decreased. Due to the reduced aerodynamic friction and energy required for vehicle acceleration, the total consumption of propulsion energy required for completing the driving mission is reduced. In this way, the driving range can be extended by degrading the driving profile for the price of longer travel time. Also by degrading the driving destination according to the prioritization as depicted in Fig. 4.1, the total energy demand can be decreased.

For the safety-based range extension in this work, the degradation of the load profile is applied at the first level. The degradation of the driving profile is the second level and the degradation of the driving destination is the third level. The process of the proposed three-level-degradation concept is illustrated in Fig. 4.2. At the beginning, no degradation is active. All comfort loads are turned on, the driving profile is set to normal and the destination to "driving home". For these settings, the energy management system estimates that the energy demand exceeds the available resources, so the driving mission

degradation levels		degradation step		1	...	$n_{lp}$	...	...	...	...	...	...	...	...	...	
1st Level	stepwise degradation of comfort loads	load profile	group 1	■			...	■			■			...	■	
			...		...		...		...		...		...		...	
			group $n_{lp}$			■	...		■			■			...	■
2nd Level	stepwise degradation of driving profile	driving profile	normal (1)	■	...	■					■	...	■			
			...			...								...		
			slow ( $n_{dp}$ )					■	...	■						■
3rd Level	stepwise degradation of safe stop location	destination	SSL A (1)	■	...	■	...	■	...	■						
			SSL B (2)									■	...	■	...	
			...													
			SSL G ( $n_{ssl}$ )													
		valid solution?		✗	...	✗	...	✗	...	✗	✗	...	✗	...	✓	

Figure 4.2.: Three-level-degradation concept.

cannot be completed. Assuming that the powernet loads are divided into  $n_{lp}$  groups, the energy management system tries to find a valid solution first turning off the loads stepwise. If it is not possible to find a valid solution by degradation at the first level, the degradation of the driving profile is applied stepwise as depicted in Fig. 4.2. After each degradation of the driving profile, again all comfort loads are activated and the degradation at the first level is repeated with a slower driving profile. If it is not possible to achieve a valid solution allowing to complete the driving mission by degradation at the first and second level, the driving destination is degraded at the third level in  $n_{ssl}$  steps. Assuming  $n_{dp}$  degradation steps for the driving profile, the driving destination is first degraded after  $n_{lp} \cdot n_{dp}$  steps. In the example depicted in Fig. 4.2, a valid solution allowing to complete the driving mission is found for no degradation of comfort loads, slow driving profile and next parking area (SSL B) as the driving destination.

In the proposed three-level-degradation concept the arrival at the safest possible destination is prioritized over the driving duration and the driving duration is prioritized over the driving comfort. The result of the degradation concept is a combination of parameters allowing to arrive at the safest possible location with the best suited driving profile and maximum of driving comfort based on the current system state. It should be noted that the order for the prioritization of the degradation levels can be easily changed and adapted to the specific requirements for a given use case. The three-level-degradation concept proposed for the safety-based range extension is implemented as a part of the energy management system. In the next section, the requirements for the proposed energy management system are discussed and specified.

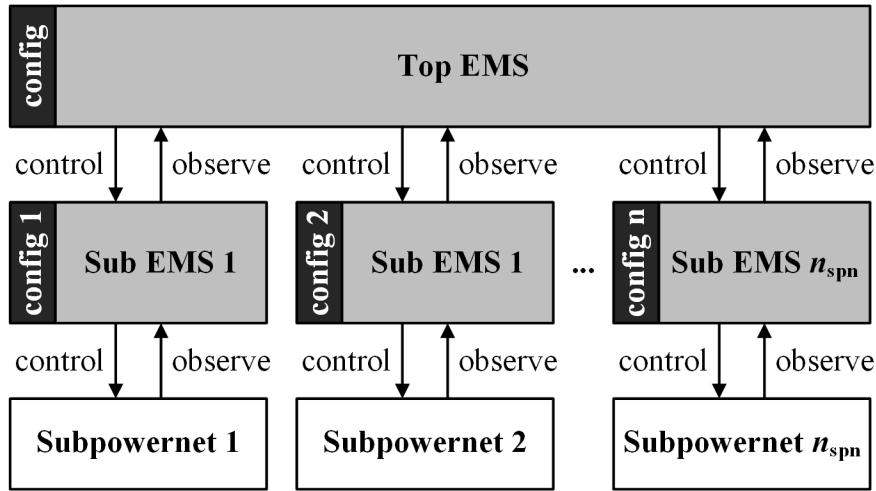


Figure 4.3.: Architecture of generic energy management system.

## 4.2. Requirements for Energy Management System

As already mentioned in the introduction to this chapter, subsystems required for automated vehicle transition to a safe state must be designed with appropriate automotive safety integrity levels in accordance with ISO 26262-3 [10]. Reliable power supply is one of the prerequisites for the operation of safety-critical functions and therefore becomes safety-critical itself. In addition to the design of new fail-operational powernet topologies [8, 9, 11], also new control strategies are required. According to the functional safety norm ISO 26262-3, a functional safety concept must be implemented [10], defining fault reactions for all possible failures violating the functional safety requirements. For the purpose of safety analysis, deductive or inductive methods are strongly recommended for the safety goals classified with ASIL C and D, considering also multiple-point faults [12]. Assuming 30 possible failures within the vehicle powernet [11] and considering double failures, a rule-based functional safety concept would contain  $30 \cdot 30 = 900$  different failure combinations with corresponding fault reactions, making this approach inflexible and time consuming in the design. The fulfillment of the safety requirements using the designed powernet topology in combination with the safety concept must be verified. However, also small changes within the powernet topology or in dimensioning of powernet components (e.g. capacity of a battery or output power of a DC/DC converter) would require a revision of the safety concept. Also the integrity of a rule-based safety concept cannot be guaranteed due to the system complexity leading to numerous system states to be covered. Furthermore, the verification of the intended operation at different conditions (e.g. temperature, aging of the components) is limited.

Besides the powernet and powertrain control in fault-free operation, the main require-



ment for the energy management system proposed in this work is to automate the fault reactions in case of failures for overcoming the limitations of rule-based safety concept as described above. In addition, a generic and topology independent EMS should be developed for avoiding time consuming redesigns of the control strategy in fault-free and failure operation. An overview of the intended energy management architecture for the control of a fail-operational powernet is depicted in Fig. 4.3.

For the sake of generality it is assumed that a fail-operational powernet topology can have up to  $n_{\text{spn}}$  subpowernets. Each subpowernet is observed and controlled by the corresponding sub energy management system  $k$  (Sub EMS  $k$ ) with  $k \in \{1..n_{\text{spn}}\}$ . All relevant subpowernet state variables and diagnostic data observed by the sub energy management systems are transmitted to the top energy management system (Top EMS). While the Sub EMS  $k$  can react to failures and abnormalities within the subpowernet  $k$ , the Top EMS defines the control goals at the system level and is responsible for the superimposed vehicle powernet control. The main goal is the distribution of the available powernet resources to the safety-critical and comfort loads according to the concept of safety-based range extension. For the implementation of the three level degradation concept as presented in Section 4.1 an algorithm for the energy distribution based on the theory of optimal control is proposed. The main requirements for the energy distribution optimization are discussed and summarized in the following subsection.

### 4.2.1. Requirements for Energy Distribution Optimization

The main goal of the energy distribution optimization is to provide sufficient energy resources to the subsystems required for vehicle motion to complete a given driving mission at the safest possible location according to the prioritization defined in Fig. 4.1. In addition, the remaining energy resources should be distributed in a way allowing to complete the driving mission with the most suitable driving profile and comfort according to the prioritization as depicted in Fig. 4.2. For the energy distribution optimization, the completion of a given driving mission with the most suitable driving profile is prioritized over the operation of comfort loads.

Due to the redundancy, several paths for the supply of loads might exist in fail-operational powernets. By selecting the path with the best energy flow efficiency, the powernet losses can be reduced. Therefore, the next requirement for the energy flow optimization is to select the best paths for the energy transport and to minimize the powernet losses. In fail-operational powernet topologies also several energy storage elements, e.g. batteries, might exist. The discharge efficiency of a battery is dependent on the discharge power [101]. In powernet topologies with multiple batteries, the overall discharge efficiency

can be improved by applying an appropriate discharge strategy. Therefore, the next requirement that can be formulated for the energy distribution optimization is to find an optimal discharge strategy for multiple batteries and to minimize the battery losses due to electrochemical energy conversion.

While operating a vehicle, different spontaneous failures in powernet components might occur or their behavior can be changed slowly depending on the operating conditions or due to the aging. In addition to the automated fault reactions based on the three-level-degradation concept, also these component failures or behavioral changes should be considered by the energy distribution optimization. By adapting the control strategy to the current state of the powernet, additional stress can be reduced and the lifetime of powernet components increased. Also the selection of the optimal paths with the best energy flow efficiency must be adapted to the current state of powernet components, minimizing so the overall powernet losses. For enabling fast reactions to the powernet failures and changes in the system, the energy distribution optimization should be executed at runtime and the computational burden should be minimized for enabling the implementation of the energy management system in embedded systems.

The energy distribution optimization is based on the predictive estimation of available energy resources and demands for the comfort, safety-critical and propulsion loads. The basic requirements for the prediction of available energy resources are discussed and summarized in Subsection 4.2.2. For the prediction of energy demands, the knowledge about the driving trajectory as well as the driving duration must be known. Therefore, an algorithm for the prediction of the driving trajectory is required enabling accurate calculation of the input data for the energy distribution optimization. The basic requirements for the prediction of the driving trajectory are discussed and summarized in Subsection 4.2.3.

#### **4.2.2. Requirements for Remaining Energy Prediction**

In a battery electric vehicle, the available energy resources can be divided into two parts. The energy required for propulsion and high voltage loads is stored in the high voltage traction batteries. The energy required for the supply of low voltage loads, e.g. braking or steering system, can be transmitted from the high voltage batteries via corresponding powerlinks, e.g. DC/DC converter. In addition to the traction batteries, also voltage stability batteries might be available in fail-operational powernets. The amount of energy that can be extracted from the batteries depends on the operating conditions and discharge power. Therefore, the main requirement for the remaining energy prediction is to estimate at runtime how much energy can be extracted from a battery for given operating conditions. In addition, for the determination of the optimal discharge strategy for

multiple batteries, the remaining discharge energy should be approximated as a function of the discharge power, which can be influenced by the energy management system.

### 4.2.3. Requirements for Driving Trajectory Prediction

The energy management system proposed in this work optimizes the energy flow within the vehicle powertrain for the entire driving mission, requiring accurate prediction of the energy demand of comfort, safety-critical and propulsion loads. For a given average power demand of the comfort and safety-critical loads with assumed low dynamics in power consumption, the energy demand can be estimated accurately and straightforward for a given driving duration.

The power demand of propulsion components is dynamic and depends on the velocity and slope profile of a driving trajectory. Therefore, for an accurate estimation of the energy demand required for completing a given driving mission, a driving trajectory from the current vehicle position to the destination should be approximated at runtime. The shape of a velocity profile depends on the speed limits on the way to the destination and also on the setting for the driving profile defined by a user, which defines basically set velocity and acceleration values for the entire route. The main requirement for the driving trajectory prediction is therefore to approximate the slope and velocity profile to the destination considering speed limits and driving profile settings.

Additionally, since the driving trajectory is required for the estimation of the input data for the energy flow distribution, it should be estimated at runtime with minimal computational burden. The driving trajectory is then further processed by the energy management system for the prediction of the power demand profile of the propulsion components. Therefore, the driving trajectory should be described and stored in an appropriate format enabling fast and accurate estimation of the power demand profile of the propulsion components. The basic requirements for the propulsion energy prediction are discussed and summarized in the following subsection.

### 4.2.4. Requirements for Propulsion Energy Prediction

The energy required for completing a given driving trajectory is dependent on the topology and the state of the powertrain components. In a powertrain topology with a single motor, the entire driving torque is provided by this motor. The main requirement for the propulsion energy prediction is then to estimate the profile of electrical power required by the motor and the corresponding current profile of the traction battery. By integrating the electrical power profile, the energy required by the traction motor can be estimated,

which is then used as the input for the energy distribution optimization. Therefore, the prediction of propulsion energy at runtime with low computational effort is required for implementing the algorithms in embedded systems.

In powertrain topologies with a single traction motor, the vehicle motion cannot be guaranteed in case of a single point of failure in the traction motor or power supply. Therefore, redundancy in traction actuators, power supply and corresponding control units is required for the fail-operability of powertrain enabling the vehicle motion also in case of a single failure in one of these subsystems. Due to this redundancy, new degrees of freedom arise for the control of powertrain topologies with multiple traction motors. The requested driving torque can be then distributed between the motors. The simplest control strategy is to equally distribute the requested torque between the motors. In this case, similar to the propulsion energy prediction for powertrain topologies with a single traction motor, the electrical power and corresponding current profiles can be estimated for each motor.

An electrical machine converts electrical power to mechanical power in motor mode, and mechanical power to electrical power in generator mode (recuperation). The power losses of an electrical machine depend on the requested torque and rotational speed. By distributing the requested driving torque between multiple electrical machines in an appropriate way, the overall driving efficiency can be increased [15, 16]. Therefore, the propulsion energy required for completing a given driving trajectory as well as the driving range depend on the applied torque distribution strategy. By assuming equal torque distribution between the motors, a pessimistic value for the required propulsion energy is estimated, resulting in an underestimation of the driving range prediction. Therefore, for increasing the prediction accuracy, the torque distribution strategy applied for the control of the powertrain with multiple traction motors should be considered.

For this reason, the algorithm for the prediction of propulsion energy for powertrain topologies with multiple traction motors must first predict the torque distribution profile according to the applied control strategy. In the second step, based on the estimated torque distribution profile, the propulsion energy required for completing a given driving trajectory must be estimated. In addition to the requirements discussed above, also a strategy for the reaction to possible powertrain failures is required and must be considered for the prediction. If, for example, one motor can only be operated with a decreased efficiency, the load of this motor should be reduced by the control strategy for energy efficient driving. Therefore, also the fault reaction strategy for powertrain topologies with multiple motors must be considered by the propulsion energy prediction algorithm.

# Chapter 5.

## Energy Distribution Optimization

With the introduction of automated driving new requirements arise for the powernet of a vehicle. As explained in Section 4, a reliable power supply for safety-critical subsystems required for the automated vehicle transition to a standstill must be established also in case of a single failure in powernet components. The EMS proposed in this work is designed for safety-based range extension as presented in Section 4.1. Based on the current system state, the energy manager adapts the control of the vehicle powernet in a way allowing to arrive at the safest possible location for the passengers. The main requirements for the predictive energy distribution optimization, which is the core of the proposed EMS, were defined in Section 4.2.1. In this chapter, concepts and algorithms for the fulfillment of the defined requirements are presented.

Due to the discrete degradation steps of the three-level-degradation concept, the energy distribution optimization is in general a mixed-integer problem. Starting with generic mathematical modeling of a fail-operational powernet and a definition of failure modes in the powernet components, a mixed-integer energy distribution optimization problem for the selection of optimal energy flow paths and optimal multiple battery discharge is formulated in Section 5.1. Solving a mixed-integer optimization problem is in general time consuming. Since the energy distribution optimization is used for the control of a powernet at runtime, an optimization model and optimization algorithm with low computational burden are required. A two stage optimization algorithm dividing the mixed-integer optimization into a continuous optimization problem and a superimposed variation of integer parameters with feasibility checks is proposed in Section 5.2. For solving the continuous energy distribution optimization problem several solvers exist. In Section 5.3, two different approaches using nonlinear and linear optimization problems are presented. The subpowernets of a fail-operational powernet are interconnected using powerlinks. Depending on the powerlink, different operating modes for the energy transport exist. In Section 5.4, three main powerlink components, namely DC/DC converter, toggle and

single power switches as well as possible component failure modes are modeled for the use in the energy flow optimization.

One of the main goals of the energy flow optimization is to establish reliable power supply for the entire duration of the driving mission. For guaranteeing that sufficient energy resources are available for the supply of powernet loads, accurate prediction of remaining discharge energy of powernet batteries is required. In Section 5.5, two different approaches for the estimation of the remaining discharge energy of a battery are proposed. In the first approach, a model-based algorithm for the estimation of the remaining discharge energy for a given discharge power is presented, which is then extended to the approximation of remaining discharge energy as a function of the discharge power. Simulation results verifying the accuracy of the proposed algorithms and the capability for their execution at runtime are presented in Section 5.6.

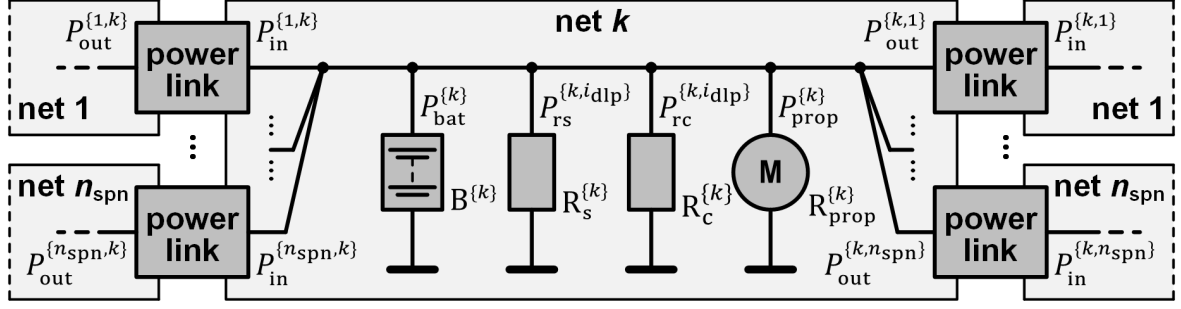
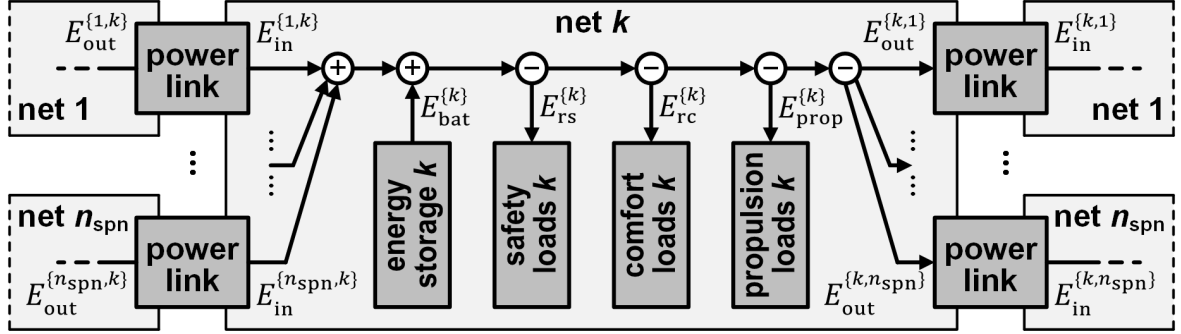
Using two different fail-operational powernet topologies, the basic features of the energy distribution optimization are exemplified in Section 5.7 with simulation results. Different use cases for the application of the proposed energy distribution optimization for the control of powernets at runtime are demonstrated.

## 5.1. Definition of Mixed-Integer Optimization Problem for Energy Distribution

The algorithm proposed for the control of a fail-operational powernet in automated vehicles is based on the theory of optimal control. For the definition of the optimization problem for the energy distribution, a generic mathematical model of a powernet with up to  $n_{\text{spn}}$  subpowernets is presented in Section 5.1.1. Two approaches for energy distribution optimization are proposed. In the first approach, presented in Section 5.1.3, the fault reactions based on degradation as well as the selection of optimal paths for energy transmission are automated. The second approach, presented in Section 5.1.4, additionally automates the optimal discharge of multiple batteries within the vehicle powernet.

### 5.1.1. Mathematical Model of Fail-Operational Powernet

A fail-operational powernet must be able to supply safety-critical loads also in case of a failure. Therefore, a fail-operational powernet topology should contain a certain degree of redundancy, e.g. for energy storage and energy distribution components, resulting so in more than one powernet channel. For ensuring flexibility of the proposed EMS, it is assumed that a fail-operational powernet consists of up to  $n_{\text{spn}}$  subpowernets (spn). A


 Figure 5.1.: Circuit diagram of subpowernet  $k$ .

 Figure 5.2.: Energy flows of subpowernet  $k$ .

circuit diagram of the subpowernet  $k \in \{1..n_{\text{spn}}\}$  is depicted in Fig. 5.1 and the corresponding energy flows in Fig. 5.2. It is further assumed that each subpowernet  $k$  can be connected to up to  $n_{\text{spn}} - 1$  subpowernets at its inputs and to up to  $n_{\text{spn}} - 1$  at its outputs. The amount of energy transferred from the output  $k$  of the subpowernet  $i$  to the input  $i$  of the subpowernet  $k$  is denoted by  $E_{\text{out}}^{\{i,k\}}$ , the corresponding energy flow efficiency by  $\eta_{\text{pl}}^{\{i,k\}}$ , so the available energy at the input  $i$  of the subpowernet  $k$  can be expressed as:

$$E_{\text{in}}^{\{i,k\}} = \eta_{\text{pl}}^{\{i,k\}} E_{\text{out}}^{\{i,k\}} \quad (5.1)$$

Each subpowernet  $k$  can have energy storage components ( $B^{(k)}$ ), safety-critical ( $R_s^{(k)}$ ), comfort ( $R_c^{(k)}$ ) and propulsion ( $R_{\text{prop}}^{(k)}$ ) loads. The remaining discharge energy of the storage components in subpowernet  $k$  is denoted by  $E_{\text{rde}}^{\{k\}}$ , while the energy provided to the loads during a given driving mission is  $E_{\text{bat}}^{\{k\}}$ . The average power demand of the safety-critical and comfort loads is assumed to be scalable in  $n_{\text{lp}}$  discrete steps. The average power demand at the degradation step  $i_{\text{p}}$  of the comfort and safety-critical loads in subpowernet  $k$  is denoted by  $P_{\text{rc}}^{\{k,i_{\text{p}}\}}$  and  $P_{\text{rs}}^{\{k,i_{\text{p}}\}}$ , the total energy demand for a given driving mission by  $E_{\text{rc}}^{\{k\}}$  and  $E_{\text{rs}}^{\{k\}}$ . As shown in Section 4.1, the duration  $dT_{\text{ssl}}$  of the driving mission is dependent on the degradation step of the driving profile and the driving destination. By denoting the current degradation step of the driving profile by  $i_{\text{dp}}$  and of the driving destination by  $i_{\text{ssl}}$ , the energy demand of safety-critical and comfort loads

as a function of integer valued degradation variables in subpowernet  $k$  can be expressed as:

$$\begin{aligned} E_{rc}^{\{k\}}(i_p, i_{dp}, i_{ssl}) &= dT_{ssl}(i_{dp}, i_{ssl}) P_{rc}^{\{k, i_p\}} \\ E_{rs}^{\{k\}}(i_p, i_{dp}, i_{ssl}) &= dT_{ssl}(i_{dp}, i_{ssl}) P_{rs}^{\{k, i_p\}} \end{aligned} \quad (5.2)$$

Using the notation introduced above and assuming the dependency of the energy required by propulsion loads in subpowernet  $k$  on the degradation of the driving profile ( $i_{dp}$ ) and the destination ( $i_{ssl}$ ), the energy demand  $E_{load}^{\{k\}}$  of the subpowernet  $k$  can be expressed as:

$$E_{load}^{\{k\}}(i_p, i_{dp}, i_{ssl}) = E_{rs}^{\{k\}}(i_p, i_{dp}, i_{ssl}) + E_{rc}^{\{k\}}(i_p, i_{dp}, i_{ssl}) + E_{prop}^{\{k\}}(i_{dp}, i_{ssl}) \quad (5.3)$$

The energy flow from subpowernet  $i$  to  $k$  can be either activated or deactivated by controlling the operating mode of the powerlink component connecting both subpowernets. Assuming  $n_{pl}$  powerlink components in total within the vehicle powernet, an integer valued  $n_{pl}$ -by-1 state vector  $\underline{M}_{pl}$  containing the current operating mode of all powerlink components can be introduced. The state variable  $S_{pl}^{\{i, k\}}$  modeling the activation of the energy flow from subpowernet  $i$  to  $k$  as a function of state vector  $\underline{M}_{pl}$  can be defined as:

$$S_{pl}^{\{i, k\}}(\underline{M}_{pl}) = \begin{cases} 0, & E_{out}^{\{i, k\}} = 0 \\ 1, & E_{out}^{\{i, k\}} > 0 \end{cases} \quad \text{with } i \neq k \quad \text{and } i, k \in \{1..n_{spn}\} \quad (5.4)$$

The energy flow from subpowernet  $i$  to  $k$  is only possible if both subpowernets are operational. A subpowernet is considered to be operational if the voltage supply within the specified operating range of the components can be established. This is, for example, not possible in case of a short circuit to ground within the subpowernet. The operational state of the subpowernet  $k$  can be modeled using the state variable  $S_{spn}^{\{k\}}$ :

$$S_{spn}^{\{k\}} = \begin{cases} 0, & \text{subpowernet } k \text{ is operational} \\ 1, & \text{subpowernet } k \text{ is not operational} \end{cases} \quad (5.5)$$

Using the definitions introduced above, the state  $S_{out}^{\{i, k\}}$  of the energy flow  $E_{out}^{\{i, k\}}$  from subpowernet  $i$  to  $k$ , which is set to 1 if the energy flow is activated and both subpowernets are operational, and to 0 otherwise, can be modeled as:

$$S_{out}^{\{i, k\}}(\underline{M}_{pl}) = S_{spn}^{\{i\}} S_{spn}^{\{k\}} S_{pl}^{\{i, k\}}(\underline{M}_{pl}) \quad \text{with } i \neq k \quad \text{and } i, k \in \{1..n_{spn}\} \quad (5.6)$$

Considering all energy flows within the subpowernet  $k$ , the energy balance equation for each subpowernet  $k \in \{1..n_{spn}\}$  can be introduced as:



$$\begin{aligned}
 E_{\text{spn}}^{\{k\}}(\underline{E}_{\text{out}}, \underline{M}_{\text{pl}}, i_{\text{p}}, i_{\text{dp}}, i_{\text{ssl}}) = & \sum_{i=1, i \neq k}^{n_{\text{spn}}} \left( S_{\text{out}}^{\{i,k\}}(\underline{M}_{\text{pl}}) \eta_{\text{pl}}^{\{i,k\}} E_{\text{out}}^{\{i,k\}} - S_{\text{out}}^{\{k,i\}}(\underline{M}_{\text{pl}}) E_{\text{out}}^{\{k,i\}} \right) \\
 & + S_{\text{spn}}^{\{k\}} \left( E_{\text{rde}}^{\{k\}} - E_{\text{load}}^{\{k\}}(i_{\text{p}}, i_{\text{dp}}, i_{\text{ssl}}) \right)
 \end{aligned} \tag{5.7}$$

The first line in (5.7) describes the delta between the amount of energy received at the inputs ( $\eta_{\text{pl}}^{\{i,k\}} E_{\text{out}}^{\{i,k\}}$  with  $i \in \{1..n_{\text{spn}}\} \setminus \{k\}$ ) of the subpowernet  $k$  and the amount of energy provided to other subpowernets via the outputs ( $E_{\text{out}}^{\{k,i\}}$  with  $i \in \{1..n_{\text{spn}}\} \setminus \{k\}$ ). The second line in (5.7) describes the delta between the available energy resources ( $E_{\text{rde}}^{\{k\}}$ ) and the internal energy demand ( $E_{\text{load}}^{\{k\}}$ ) in subpowernet  $k$ . The matrix  $\underline{E}_{\text{out}}$  in (5.7) is used for the notation of all energy flows within the vehicle powernet.

The energy balance value  $E_{\text{spn}}^{\{k\}}$  can be used as one indicator for reliable power supply of the loads in subpowernet  $k$ . The positive energy balance  $E_{\text{spn}}^{\{k\}}$  means that the predicted energy demand  $E_{\text{load}}^{\{k\}}$  of the subpowernet  $k$  can be covered by the energy resources within the entire powernet. As shown in (5.7), the energy balance  $E_{\text{spn}}^{\{k\}}$  of subpowernet  $k$  can be influenced in two ways. The first way is to adapt the distribution of the energy between the subpowernets. This can be controlled by changing the integer valued state vector  $\underline{M}_{\text{pl}}$  describing the operating modes of the powerlink components and by varying the amount of energy  $\underline{E}_{\text{out}}$  exchanged between the subpowernets. The second way is to adapt the energy demand of the loads in subpowernet  $k$ , which can be controlled by changing the degradation step  $i_{\text{p}}$  for the load profile,  $i_{\text{dp}}$  for the driving profile and  $i_{\text{ssl}}$  for the driving destination. As presented in Section 4.2.1, one of the goals for the energy distribution optimization is to automate the reactions to possible faults in powernet components. In the next subsection, the failure modes of powernet components considered in this work and the corresponding FCRs are defined.

### 5.1.2. Failure Modes of Powernet Components

A fail-operational powernet must provide reliable power supply for safety-critical subsystems also in case of a single fault. It should be avoided by design that a failure resulting from a single fault in a component can propagate and impact the functionality of the other subsystems [22]. For this, a safety-critical system can be divided into independent FCRs, which define the boundaries for fault detection and fault isolation [22]. The model of a fail-operation powernet as presented in Section 5.1.1 contains three subsystems: (1) powerlink components, (2) energy storage components and (3) powernet load components. For the further analysis in this work it is assumed that each powernet component (subsystem) builds a FCR. In the following, the failure modes considered in this work for these three types of subsystems of a fail-operational powernet are defined.

## Powerlink Components

A powerlink connects two or more subpowernets and enables the energy transport between the subpowernets in the defined operating modes. Five failure modes with impact on the energy transport between the subpowernets are considered by the EMS in this work. The first failure mode considers faults resulting in a *decreased energy flow efficiency* from the powerlink input to the output. This fault can be either transient (e.g. due to a temporal overheating) or permanent (e.g. due to a damaged semiconductor switch). The operation of a powerlink in this failure mode leads to a faster discharge of energy storages and to a higher heating of the powerlink.

The second failure mode considers faults resulting in a *loss of operating mode control* of the powerlink. This fault can be either transient or permanent (e.g. due to a fault in the embedded microcontroller). The operation of a powerlink in this failure mode can lead to an unintended energy transport between the subpowernets.

The third failure mode considers faults resulting in *no energy transport* from the powerlink input to the output. This fault can be either transient (e.g. due to a temporally activated overcurrent protection) or permanent (e.g. due to a damaged semiconductor switch). An alternative path for the supply of the loads connected to the output of this faulty powerlink must be used in this failure mode.

The fourth failure mode considers faults resulting in a *short circuit between the powerlink inputs and the outputs*. This fault can be either transient (e.g. due to a temporal wiring problem) or permanent (e.g. due to a damaged semiconductor switch). This failure mode can lead to an unintended energy transport between the subpowernets.

The fifth failure mode considers faults resulting in a *short circuit to ground* either at the powerlink input or output. This fault can be either transient (e.g. due to a temporal wiring problem) or permanent (e.g. due to a permanent short circuit to ground within external component). For the short circuit to ground at the output it is assumed that the overcurrent protection disables the energy transport. In case of a short circuit to ground at the input, it is assumed that no reverse energy flow is possible. It is also assumed that an internal short circuit to ground is detected and disconnected within the powerlink.

## Energy Storage Components

An energy storage component provides the energy for the powernet loads. Three failure modes with impact on the power supply of the powernet loads are considered by the EMS in this work. The first failure mode considers faults resulting in a *decreased capacity* of the energy storage. This failure can be either transient (e.g. due to a faulty diagnostic of

a short circuit to ground within a battery branch leading to the shutdown of this branch) or permanent (e.g. due to a persistent short circuit to ground within a battery branch leading to the shutdown of this branch). In this failure mode, no energy can be depleted from the energy storage component.

The second failure mode considers faults resulting in an *increased internal resistance* of the energy storage. This failure can be either transient (e.g. due to a transient overheating) or permanent (e.g. due to the aging effects). In this failure mode, a reduced amount of energy due to higher internal losses can be depleted from the energy storage. Furthermore, for avoiding the undervoltage condition within the subpowernet with faulty energy storage, the maximum output power of the energy storage is reduced in this failure mode. The third failure mode considers faults resulting in a *internal short circuit to ground* of the energy storage. This failure can be either transient (e.g. with active disconnection) or permanent (e.g. without active disconnection).

### **Powernet Load Components**

For a powernet load an average power consumption required for correct functionality is assumed. Three failure modes with impact on the energy distribution within the powernet are considered by the EMS in this work. The first failure mode considers faults resulting in an *increased average power consumption* of a powernet load. This failure can be either transient (e.g. due to a wiring problem with a parallel branch) or permanent (e.g. due to a faulty load control unit). The operation of a powernet load in this failure mode leads to a faster discharge of energy storages.

The second failure mode considers faults resulting in a *loss of load control*. This failure can be either transient (e.g. due to a temporally faulty control interface) or permanent (e.g. due to a permanent fault in a load control unit). The operation of a powernet load in this failure mode can result in no degradation of the powernet load leading also to a faster discharge of energy storages. The third failure mode considers faults resulting in a *internal short circuit to ground* of the powernet load. This failure can be either transient (e.g. with active disconnection) or permanent (e.g. without active disconnection).

The task of the EMS is to predict accurately the energy demand and available resources for each subpowernet and to find the optimal operating point for the powernet ensuring the positive energy balance for each operational subpowernet  $k$ . The theory of optimal control is used for the estimation of the best suited operating point fulfilling the control requirements of the vehicle powernet. The optimization problem used for the optimal energy flow distribution is presented in the next subsection.

### 5.1.3. Energy Distribution with Optimal Path Selection

The main control goal of the concept for safety-based range extension is to utilize the available powernet resources in a way allowing to arrive at the safest possible location for the passengers. Additionally, the best suited driving profile out of user defined and prioritized profiles should be selected. For increasing the driving comfort also the operation of comfort loads at the lowest possible degradation step should be enabled.

By applying the theory of optimal control, each of these goals can be modeled as a part of the cost function of a multi-objective optimization problem, taking its solution for the energy flow control. By using the integer valued degradation variables  $i_{\text{ssl}}$  for driving destination,  $i_{\text{dp}}$  for driving profile and  $i_{\text{lp}}$  for load profile and by denoting the corresponding maximum degradation step by  $n_{\text{ssl}}$ ,  $n_{\text{dp}}$  and  $n_{\text{lp}}$ , the following objectives for the energy distribution optimization (edo) can be defined:

$$f_{\text{edo,ssl}}(i_{\text{ssl}}) = n_{\text{ssl}} - i_{\text{ssl}}, \quad i_{\text{ssl}} \in \{1..n_{\text{ssl}}\} \quad (5.8a)$$

$$f_{\text{edo,dp}}(i_{\text{dp}}) = n_{\text{dp}} - i_{\text{dp}}, \quad i_{\text{dp}} \in \{1..n_{\text{dp}}\} \quad (5.8b)$$

$$f_{\text{edo,lp}}(i_{\text{lp}}) = n_{\text{lp}} - i_{\text{lp}}, \quad i_{\text{lp}} \in \{1..n_{\text{lp}}\} \quad (5.8c)$$

Equations (5.8a) to (5.8c) define the difference between the current and last degradation step. By maximizing the objectives, the lowest possible degradation step will be taken. As it will be shown later, the prioritization between degradation levels (destination, driving and load profile) can be achieved by appropriate selection of the weighting factors.

The energy balance value  $E_{\text{spn}}^{\{k\}}$  as defined in (5.7) indicates the remaining energy resources in subpowernet  $k$  after completing a given driving mission. Due to the possible redundancies within a fail-operational powernet, several energy flow paths to each load may exist. By transmitting the energy via the paths with the best efficiencies, the energy losses can be minimized. As the result, the remaining energy resources after completing the driving mission will be maximized. Therefore, a further objective can be incorporated into the energy distribution optimization problem:

$$f_{\text{edo.loss.pl}}(\underline{E}_{\text{out}}, \underline{M}_{\text{pl}}, i_{\text{lp}}, i_{\text{dp}}, i_{\text{ssl}}) = \sum_{k=1}^{n_{\text{spn}}} E_{\text{spn}}^{\{k\}}(\underline{E}_{\text{out}}, \underline{M}_{\text{pl}}, i_{\text{lp}}, i_{\text{dp}}, i_{\text{ssl}}) \quad (5.9)$$

By maximizing the sum of the energy balance values, the selection of the optimal energy flow paths with minimum of losses can be automated. Taking into account the diagnostic information about the current efficiencies of powerlinks, also the fault reactions to possible failures resulting in decrease of energy flow efficiencies are automated. If, for example, two

redundant energy flow paths exist, the path with higher efficiency would be automatically selected for the energy transport, minimizing so the energy losses on the one hand. On the other hand, it might lead to undesirable effects, e.g. to overheating of the powerlinks on this path. Therefore, a penalty function for each output of the powerlinks can be introduced for avoiding the selection of the paths considering the energy efficiency only:

$$f_{\text{edo.pen.pl}}(\underline{E}_{\text{out}}, \underline{M}_{\text{pl}}) = \sum_{i=1, i \neq k}^{n_{\text{spn}}} \beta_{\text{pl}}^{\{i,k\}}(t) S_{\text{out}}^{\{i,k\}}(\underline{M}_{\text{pl}}) E_{\text{out}}^{\{i,k\}} \quad (5.10)$$

The penalty factor  $\beta_{\text{pl}}^{\{i,k\}}$  can be changed during the runtime depending on user requirements for the control of powerlinks. If, for example, an overheating of a powerlink transmitting the energy from subpowernet  $i$  to  $k$  should be avoided, denoting the powerlink junction temperature by  $T_{\text{jun.pl}}^{\{i,k\}}$  and the desired nominal temperature by  $T_{\text{nom.pl}}^{\{i,k\}}$ , the time dependent penalty factor could be defined as:

$$\beta_{\text{pl}}^{\{i,k\}}(t) = \begin{cases} \frac{\gamma_{\text{temp}}}{dT_{\text{ssl}}(i_{\text{dp}}, i_{\text{ssl}})} \left( T_{\text{jun.pl}}^{\{i,k\}}(t) - T_{\text{nom.pl}}^{\{i,k\}} \right), & T_{\text{jun.pl}}^{\{i,k\}}(t) > T_{\text{nom.pl}}^{\{i,k\}} \\ 0, & T_{\text{jun.pl}}^{\{i,k\}}(t) \leq T_{\text{nom.pl}}^{\{i,k\}} \end{cases} \quad (5.11)$$

If the junction temperature of the powerlink is greater than desired, the temperature delta scaled with the factor  $\gamma_{\text{temp}}$  can be used as a penalty factor. The higher the junction temperature, the more costly becomes the energy transport via this powerlink output. Since the penalty function defined in (5.11) is a function of the entire output energy to be transmitted via the powerlinks while driving, which decreases with decreasing remaining driving time  $dT_{\text{ssl}}$ , a division by  $dT_{\text{ssl}}$  is required to keep the weight of the penalty function approximately constant. Depending on the control requirements, also other definitions of the penalty factor can be used. The objective function for the automated selection of the optimal paths for the energy transport can be then defined as:

$$f_{\text{edo.path}}(\underline{E}_{\text{out}}, \underline{M}_{\text{pl}}, i_{\text{p}}, i_{\text{dp}}, i_{\text{ssl}}) = f_{\text{edo.loss.pl}}(\underline{E}_{\text{out}}, \underline{M}_{\text{pl}}, i_{\text{p}}, i_{\text{dp}}, i_{\text{ssl}}) - f_{\text{edo.pen.pl}}(\underline{E}_{\text{out}}, \underline{M}_{\text{pl}}) \quad (5.12)$$

With the objectives introduced above, the cost function for the energy distribution optimization can be defined as:

$$f_{\text{edo}}(\underline{E}_{\text{out}}, \underline{M}_{\text{pl}}, i_{\text{p}}, i_{\text{dp}}, i_{\text{ssl}}) = \begin{bmatrix} \beta_{\text{edo.path}} \\ \beta_{\text{edo.ssl}} \\ \beta_{\text{edo.dp}} \\ \beta_{\text{edo.lp}} \end{bmatrix}^{\text{T}} \cdot \begin{bmatrix} f_{\text{edo.path}}(\underline{E}_{\text{out}}, \underline{M}_{\text{pl}}, i_{\text{p}}, i_{\text{dp}}, i_{\text{ssl}}) \\ f_{\text{edo.ssl}}(i_{\text{ssl}}) \\ f_{\text{edo.dp}}(i_{\text{dp}}) \\ f_{\text{edo.lp}}(i_{\text{p}}) \end{bmatrix} \quad (5.13)$$

By maximizing the objective function  $f_{\text{edo}}$  it should be ensured that the total energy demand does not exceed the available powernet resources for the duration of the driving mission. This is the case if the energy balance  $E_{\text{spn}}^{\{k\}}$  is positive or equal to zero for all operational subpowernets, which can be achieved by adding the corresponding constraint to the optimization problem.

According to the model of a fail-operational powernet presented in Section 5.1.1, the energy flow between subpowernet  $i$  and  $k$  is modeled by two variables:  $E_{\text{out}}^{\{i,k\}}$  denoting the energy flow from subpowernet  $i$  to  $k$  and  $E_{\text{out}}^{\{k,i\}}$  for the opposite direction. Due to this definition, each energy flow  $E_{\text{out}}^{\{i,k\}}$  is therefore positive or equal zero. The energy  $\eta_{\text{pl}}^{\{i,k\}} E_{\text{out}}^{\{i,k\}}$  at the input  $i$  of the subpowernet  $k$  is limited by the powerlink specifications defining the maximum allowed output power  $P_{\text{pl.max}}^{\{i,k\}}$ . The maximum amount of energy  $E_{\text{out.max}}^{\{i,k\}}$  which can be transferred from subpowernet  $i$  to  $k$  during the driving time  $dT_{\text{ssl}}$  with the efficiency  $\eta_{\text{pl}}^{\{i,k\}}$  can be therefore calculated as:

$$E_{\text{out.max}}^{\{i,k\}}(i_{\text{dp}}, i_{\text{ssl}}) = \frac{P_{\text{pl.max}}^{\{i,k\}}}{\eta_{\text{pl}}^{\{i,k\}}} dT_{\text{ssl}}(i_{\text{dp}}, i_{\text{ssl}}) \quad (5.14)$$

In the following definition of the optimization problem, the matrix  $\underline{E}_{\text{out.max}}$  is used for the notation of all output energy limits and the vector  $\underline{E}_{\text{spn}}$  for all energy balance values. A matrix or vector with all elements equal to zero is denoted by  $\underline{0}$ . Using the definitions above, the mixed-integer energy distribution optimization problem can be formulated as:

$$\begin{aligned} \max_{(\cdot)} \quad & f_{\text{edo}}(\underline{E}_{\text{out}}, \underline{M}_{\text{pl}}, i_{\text{p}}, i_{\text{dp}}, i_{\text{ssl}}) \\ \text{s.t.} \quad & \begin{cases} \underline{0} \leq \underline{E}_{\text{spn}}(\underline{E}_{\text{out}}, \underline{M}_{\text{pl}}, i_{\text{p}}, i_{\text{dp}}, i_{\text{ssl}}) \\ \underline{0} \leq \underline{E}_{\text{out}} \leq \underline{E}_{\text{out.max}}(i_{\text{dp}}, i_{\text{ssl}}) \\ 1 \leq i_{\text{p}} \leq n_{\text{lp}} \\ 1 \leq i_{\text{dp}} \leq n_{\text{dp}} \\ 1 \leq i_{\text{ssl}} \leq n_{\text{ssl}} \end{cases} \end{aligned} \quad (5.15)$$

The objective  $f_{\text{edo.path}}$  used for the automation of energy flow path selection is opposite to the objectives  $f_{\text{edo.ssl}}$ ,  $f_{\text{edo.dp}}$  and  $f_{\text{edo.lp}}$  modeling the degradation concept. By increasing the degradation step, the total energy demand is reduced and the remaining energy resources after completing the driving mission are maximized. Therefore, for ensuring the degradation only in case the energy demand exceeds the available resources, a proper selection of the weighting factors  $\beta_{\text{edo.path}}$ ,  $\beta_{\text{edo.lp}}$ ,  $\beta_{\text{edo.dp}}$  and  $\beta_{\text{edo.ssl}}$  is required. The weighting factors for the degradation objectives should be selected greater than the weighted absolute maximum of the objective  $f_{\text{edo.path}}$ , which corresponds to the sum of the remaining discharge energies  $E_{\text{rde0}}^{\{k\}}$  of the energy storage components  $B^{\{k\}}$  at the beginning of a driving mission:

$$\beta_{\text{edo.lp}}, \beta_{\text{edo.dp}}, \beta_{\text{edo.ssl}} > \beta_{\text{edo.path}} \sum_{k=1}^{n_{\text{spn}}} S_{\text{spn}}^{\{k\}} E_{\text{rde0}}^{\{k\}}(t_0) \quad (5.16)$$

Similarly, the order of the degradation levels for the load profile, driving profile and destination can be established by selecting the proper weighting factors for the degradation objectives. Assuming the order of degradation levels as presented in Section 4.1, degrading load profile at the first level, driving profile at the second and destination at the third level, the following conditions should be fulfilled by selecting the weighting factors:

$$\begin{aligned} \beta_{\text{edo.dp}} &\geq n_{\text{lp}} \beta_{\text{edo.lp}}, \\ \beta_{\text{edo.ssl}} &\geq n_{\text{dp}} \beta_{\text{edo.dp}} \end{aligned} \quad (5.17)$$

By solving the mixed-integer optimization problem as defined in (5.15), the energy flow within a powernet can be controlled. The optimal operating mode for powerlinks is automatically selected and the amount of energy to be exchanged between the subpowernets is estimated. Additionally, using the powernet runtime diagnostics, the fault reactions are automated by applying the degradation concept for safety-based range extension.

According to the definition of the energy balance  $E_{\text{spn}}^{\{k\}}$  in (5.7), the available energy  $E_{\text{rde}}^{\{k\}}$  in the subpowernet  $k$  can be extracted without energy losses. Considering the case of a full battery electric vehicle with multiple batteries, this assumption is justified when the battery internal resistance is low and almost the same for all batteries. In a case of a battery with low discharge efficiency in subpowernet  $k$ , it might be more energy efficient not to utilize the internal energy resources for the supply of the loads in subpowernet  $k$ , but instead to transfer the required energy from other subpowernets despite the additional losses in powerlink components. By incorporating the battery discharge efficiency into the optimization problem, which is presented in the next subsection, also the optimal discharge of multiple batteries can be achieved.

#### 5.1.4. Energy Distribution with Optimal Multiple Battery Discharge

The available discharge energy is dependent on the battery discharge power [101] due to the battery internal losses. Therefore, for the energy flow distribution optimization the remaining discharge energy  $E_{\text{rde}}^{\{k\}}$  of the battery  $B^{\{k\}}$  in subpowernet  $k$  can be modeled as a function of the average battery output power  $P_{\text{bat}}^{\{k\}}$ . Using linear approximation, the battery's remaining discharge energy can be defined as:

$$E_{\text{rde}}^{\{k\}}(P_{\text{bat}}^{\{k\}}) = E_{\text{rde0}}^{\{k\}} - a_{\text{rde}}^{\{k\}} P_{\text{bat}}^{\{k\}} \quad (5.18)$$

The parameter  $E_{\text{rde0}}^{\{k\}}$  models the electrochemical energy of the battery ( $E_{\text{rde0}}^{\{k\}} > 0$ ) and  $a_{\text{rde}}^{\{k\}}$  the battery internal losses as a function of the average discharge power ( $a_{\text{rde}}^{\{k\}} > 0$ ). Depending on the battery state, the parameters  $E_{\text{rde0}}^{\{k\}}$  and  $a_{\text{rde}}^{\{k\}}$  may vary over time. The energy losses  $a_{\text{rde}}^{\{k\}} P_{\text{bat}}^{\{k\}}$  correspond to the total losses of the battery discharge from the current state of charge  $SoC_0^{\{k\}}$  to the minimum allowed discharge threshold  $SoC_{\text{min}}^{\{k\}}$ . The algorithm for their estimation is presented in Section 5.5.3. By denoting the maximum discharge power with  $P_{\text{bat.max}}^{\{k\}}$  and the corresponding minimum discharge time with  $dT_{\text{dcha.min}}$ , the maximum average discharge power losses  $P_{\text{bat.loss.max}}^{\{k\}}$  can be defined as:

$$P_{\text{bat.loss.max}}^{\{k\}} = \frac{a_{\text{rde}}^{\{k\}} P_{\text{bat.max}}^{\{k\}}}{dT_{\text{dcha.min}}} \quad \text{with} \quad dT_{\text{dcha.min}} = \frac{E_{\text{rde0}}^{\{k\}} - a_{\text{rde}}^{\{k\}} P_{\text{bat.max}}^{\{k\}}}{P_{\text{bat.max}}^{\{k\}}} \quad (5.19)$$

For the estimation of the battery losses dissipated during the driving time  $dT_{\text{ssl}}$ , the average discharge power losses  $P_{\text{bat.loss}}^{\{k\}}$  can be approximated as a function of the average discharge power  $P_{\text{bat}}^{\{k\}}$ . For the sake of simplicity, the nonlinear battery power losses  $P_{\text{bat.loss}}^{\{k\}}$  are linearly approximated as a function of the battery discharge power using (5.19) as:

$$P_{\text{bat.loss}}^{\{k\}} = dp_{\text{bat}}^{\{k\}} P_{\text{bat}}^{\{k\}} \quad \text{with} \quad dp_{\text{bat}}^{\{k\}} = \frac{P_{\text{bat.loss.max}}^{\{k\}}}{P_{\text{bat.max}}^{\{k\}}} \quad (5.20)$$

With (5.20), the losses  $E_{\text{bat.loss}}^{\{k\}}$  can be calculated as a function of the battery energy  $E_{\text{bat}}^{\{k\}}$ :

$$E_{\text{bat.loss}}^{\{k\}} = P_{\text{bat.loss}}^{\{k\}} dT_{\text{ssl}}(i_{\text{dp}}, i_{\text{ssl}}) = dp_{\text{bat}}^{\{k\}} E_{\text{bat}}^{\{k\}} \quad (5.21)$$

By considering the subpowernet  $k$  as an energy junction and by using the powernet model as presented in Section 5.1.1, for each functional subpowernet  $k$  the following equation, requiring that the sum of energy flows entering the junction is equal to the sum of energy flows leaving the junction, is valid:

$$\begin{aligned} & \sum_{i=1, i \neq k}^{n_{\text{spn}}} S_{\text{out}}^{\{i,k\}}(\underline{M}_{\text{pl}}) \eta_{\text{pl}}^{\{i,k\}} E_{\text{out}}^{\{i,k\}} + S_{\text{spn}}^{\{k\}} E_{\text{bat}}^{\{k\}} \\ & - \sum_{i=1, i \neq k}^{n_{\text{spn}}} S_{\text{out}}^{\{k,i\}}(\underline{M}_{\text{pl}}) E_{\text{out}}^{\{k,i\}} - S_{\text{spn}}^{\{k\}} E_{\text{load}}^{\{k\}}(i_{\text{p}}, i_{\text{dp}}, i_{\text{ssl}}) = 0 \end{aligned} \quad (5.22)$$

Using (5.22), the battery discharge energy in subpowernet  $k$  can be calculated as:

$$\begin{aligned} E_{\text{bat}}^{\{k\}}(E_{\text{out}}, \underline{M}_{\text{pl}}, i_{\text{p}}, i_{\text{dp}}, i_{\text{ssl}}) &= \sum_{i=1, i \neq k}^{n_{\text{spn}}} S_{\text{spn}}^{\{i\}} S_{\text{pl}}^{\{k,i\}}(\underline{M}_{\text{pl}}) E_{\text{out}}^{\{k,i\}} + E_{\text{load}}^{\{k\}}(i_{\text{p}}, i_{\text{dp}}, i_{\text{ssl}}) \\ &- \sum_{i=1, i \neq k}^{n_{\text{spn}}} S_{\text{spn}}^{\{i\}} S_{\text{pl}}^{\{i,k\}}(\underline{M}_{\text{pl}}) \eta_{\text{pl}}^{\{i,k\}} E_{\text{out}}^{\{i,k\}} \end{aligned} \quad (5.23)$$



The corresponding average discharge power for a given driving time  $dT_{\text{ssl}}$  is defined as:

$$P_{\text{bat}}^{\{k\}}(\underline{E}_{\text{out}}, \underline{M}_{\text{pl}}, i_{\text{p}}, i_{\text{dp}}, i_{\text{ssl}}) = \frac{E_{\text{bat}}^{\{k\}}(\underline{E}_{\text{out}}, \underline{M}_{\text{pl}}, i_{\text{p}}, i_{\text{dp}}, i_{\text{ssl}})}{dT_{\text{ssl}}(i_{\text{dp}}, i_{\text{ssl}})} \quad (5.24)$$

By substituting the battery's remaining discharge energy  $E_{\text{rde}}^{\{k\}}$  in (5.7) with the electrochemical energy  $E_{\text{rde0}}^{\{k\}}$  and by subtracting the battery losses  $E_{\text{bat.loss}}^{\{k\}}$  as defined in (5.21), the energy balance equation for the subpowernet  $k$  can be reformulated as:

$$\begin{aligned} E_{\text{spn.opt}}^{\{k\}}(\underline{E}_{\text{out}}, \underline{M}_{\text{pl}}, i_{\text{p}}, i_{\text{dp}}, i_{\text{ssl}}) &= \left[1 + dp_{\text{bat}}^{\{k\}}\right] \sum_{i=1, i \neq k}^{n_{\text{spn}}} S_{\text{out}}^{\{i,k\}}(\underline{M}_{\text{pl}}) \eta_{\text{pl}}^{\{i,k\}} E_{\text{out}}^{\{i,k\}} \\ &\quad - \left[1 + dp_{\text{bat}}^{\{k\}}\right] \sum_{i=1, i \neq k}^{n_{\text{spn}}} S_{\text{out}}^{\{k,i\}}(\underline{M}_{\text{pl}}) E_{\text{out}}^{\{k,i\}} \\ &\quad - \left[1 + dp_{\text{bat}}^{\{k\}}\right] S_{\text{spn}}^{\{k\}} E_{\text{load}}^{\{k\}} + S_{\text{spn}}^{\{k\}} E_{\text{rde0}}^{\{k\}} \end{aligned} \quad (5.25)$$

The objective function  $f_{\text{edo.loss.pl}}$  as defined in (5.9) is used for the minimization of the energy distribution losses considering the efficiency of the powerlinks only. By maximizing the sum of the energy balance values as defined in (5.25), additionally the battery discharge losses can be considered and the optimal discharge strategy can be estimated:

$$f_{\text{edo.loss.opt}}(\underline{E}_{\text{out}}, \underline{M}_{\text{pl}}, i_{\text{p}}, i_{\text{dp}}, i_{\text{ssl}}) = \sum_{k=1}^{n_{\text{spn}}} E_{\text{spn.opt}}^{\{k\}}(\underline{E}_{\text{out}}, \underline{M}_{\text{pl}}, i_{\text{p}}, i_{\text{dp}}, i_{\text{ssl}}) \quad (5.26)$$

Similarly to the definition of the penalty function for the automated selection of the energy flow paths, it might be also beneficial to introduce a penalty function for the discharge control of multiple batteries using the time dependent penalty factors  $\beta_{\text{bat}}^{\{k\}}$ :

$$f_{\text{edo.pen.bat}}(\underline{E}_{\text{out}}, \underline{M}_{\text{pl}}, i_{\text{p}}, i_{\text{dp}}, i_{\text{ssl}}) = \sum_{k=1}^{n_{\text{spn}}} \beta_{\text{bat}}^{\{k\}}(t) S_{\text{spn}}^{\{k\}} E_{\text{bat}}^{\{k\}}(\underline{E}_{\text{out}}, \underline{M}_{\text{pl}}, i_{\text{p}}, i_{\text{dp}}, i_{\text{ssl}}) \quad (5.27)$$

Considering the case of a powernet topology with redundant channels  $i$  and  $k$ , each supplying redundant safety-critical subsystems (e.g. braking or steering), it might be beneficial to balance the battery's remaining discharge energy in these subpowernets. If a failure occurs within one of the supply channels, nearly the same operating duration of the safety-critical subsystems can be guaranteed with the remaining functional powernet channel, since the available energy resources are nearly the same due to the balancing of the remaining discharge energy. The time dependent penalty factor  $\beta_{\text{bat}}^{\{k\}}$  for the subpowernet  $k$  and  $\beta_{\text{bat}}^{\{i\}}$  for subpowernet  $i$  used for the remaining discharge energy balancing is defined as:

$$\beta_{\text{bat}}^{\{k\}}(t) = \begin{cases} \frac{\gamma_{\text{rde}}}{dT_{\text{ssl}}(i_{\text{dp}}, i_{\text{ssl}})} (E_{\text{rde}}^{\{i\}}(t) - E_{\text{rde}}^{\{k\}}(t)), & E_{\text{rde}}^{\{k\}}(t) < E_{\text{rde}}^{\{i\}}(t) \\ 0, & E_{\text{rde}}^{\{k\}}(t) \geq E_{\text{rde}}^{\{i\}}(t) \end{cases} \quad (5.28a)$$

$$\beta_{\text{bat}}^{\{i\}}(t) = \begin{cases} \frac{\gamma_{\text{rde}}}{dT_{\text{ssl}}(i_{\text{dp}}, i_{\text{ssl}})} (E_{\text{rde}}^{\{k\}}(t) - E_{\text{rde}}^{\{i\}}(t)), & E_{\text{rde}}^{\{i\}}(t) < E_{\text{rde}}^{\{k\}}(t) \\ 0, & E_{\text{rde}}^{\{i\}}(t) \geq E_{\text{rde}}^{\{k\}}(t) \end{cases} \quad (5.28b)$$

If the remaining discharge energy of one subpowernet is less than in the other, the further discharge of this battery becomes more costly and the cost increases with the increasing discharge energy delta between the subpowernets scaled with the user defined factor  $\gamma_{\text{rde}}$ , which defines the sensitivity of the cost to the delta remaining discharge energy. Since the penalty function defined in (5.27) is a function of the entire battery energy to be depleted while driving, which decreases with decreasing remaining driving time  $dT_{\text{ssl}}$ , a division by  $dT_{\text{ssl}}$  is required to keep the weight of the penalty function approximately constant.

Using the definition of the objective function  $f_{\text{edo.loss.opt}}$  in (5.26) and penalty functions  $f_{\text{edo.pen.pl}}$  in (5.10) and  $f_{\text{edo.pen.bat}}$  in (5.27), the following objective for the control of the energy flow within a powernet can be defined:

$$\begin{aligned} f_{\text{edo.path.opt}}(\underline{E}_{\text{out}}, \underline{M}_{\text{pl}}, i_{\text{p}}, i_{\text{dp}}, i_{\text{ssl}}) &= f_{\text{edo.loss.opt}}(\underline{E}_{\text{out}}, \underline{M}_{\text{pl}}, i_{\text{p}}, i_{\text{dp}}, i_{\text{ssl}}) \\ &\quad - f_{\text{edo.pen.bat}}(\underline{E}_{\text{out}}, \underline{M}_{\text{pl}}, i_{\text{p}}, i_{\text{dp}}, i_{\text{ssl}}) \\ &\quad - f_{\text{edo.pen.pl}}(\underline{E}_{\text{out}}) \end{aligned} \quad (5.29)$$

Using the definitions above, the objective function for the energy distribution optimization considering additionally the optimal discharge of multiple batteries within a vehicle powernet can be defined as:

$$f_{\text{edo.opt}}(\underline{E}_{\text{out}}, \underline{M}_{\text{pl}}, i_{\text{p}}, i_{\text{dp}}, i_{\text{ssl}}) = \begin{bmatrix} \beta_{\text{edo.path}} \\ \beta_{\text{edo.ssl}} \\ \beta_{\text{edo.dp}} \\ \beta_{\text{edo.lp}} \end{bmatrix}^T \cdot \begin{bmatrix} f_{\text{edo.path.opt}}(\underline{E}_{\text{out}}, \underline{M}_{\text{pl}}, i_{\text{p}}, i_{\text{dp}}, i_{\text{ssl}}) \\ f_{\text{edo.ssl}}(i_{\text{ssl}}) \\ f_{\text{edo.dp}}(i_{\text{dp}}) \\ f_{\text{edo.lp}}(i_{\text{p}}) \end{bmatrix} \quad (5.30)$$

For the weighting factors  $\beta_{\text{edo.path}}$ ,  $\beta_{\text{edo.ssl}}$ ,  $\beta_{\text{edo.dp}}$  and  $\beta_{\text{edo.lp}}$  the same conditions as defined in (5.16) and (5.17) are valid. For batteries discharge also the maximum allowed discharge power  $P_{\text{bat.max}}^{\{k\}}$  according to the battery specifications should be considered. In addition to the constraints of the optimization problem in (5.15), a further constraint defining the upper bound for the battery discharge energy according to (5.24) can be defined, limiting the average battery output power to the corresponding specification. The vectors  $\underline{P}_{\text{bat}}$  and  $\underline{P}_{\text{bat.max}}$  denote the average and maximum possible battery output power. With the definitions above, the energy distribution optimization problem consid-

ering also the discharge strategy for multiple batteries of a powernet can be formulated as:

$$\begin{aligned}
 & \max_{(\cdot)} f_{\text{edo.opt}}(\underline{E}_{\text{out}}, \underline{M}_{\text{pl}}, i_{\text{p}}, i_{\text{dp}}, i_{\text{ssl}}) \\
 & \text{s.t.} \quad \begin{cases} 0 \leq \underline{E}_{\text{spn.opt}}(\underline{E}_{\text{out}}, \underline{M}_{\text{pl}}, i_{\text{p}}, i_{\text{dp}}, i_{\text{ssl}}) \\ 0 \leq \underline{E}_{\text{out}} \leq \underline{E}_{\text{out.max}}(i_{\text{dp}}, i_{\text{ssl}}) \\ 0 \leq \underline{P}_{\text{bat}}(\underline{E}_{\text{out}}, \underline{M}_{\text{pl}}, i_{\text{p}}, i_{\text{dp}}, i_{\text{ssl}}) \leq \underline{P}_{\text{bat.max}} \\ 1 \leq i_{\text{p}} \leq n_{\text{ip}} \\ 1 \leq i_{\text{dp}} \leq n_{\text{dp}} \\ 1 \leq i_{\text{ssl}} \leq n_{\text{ssl}} \end{cases} \quad (5.31)
 \end{aligned}$$

By solving this optimization problem, the selection of the optimal energy flow paths is automated and the optimal discharge strategy for multiple batteries is estimated. Additionally, the fault reactions to possible failures in the vehicle powernet are automated by applying the three level degradation concept. Solving mixed-integer optimization problems is in general NP-hard and not always possible at runtime. A two-stage algorithm developed for the optimization at runtime dividing the mixed-integer optimization problem into a continuous optimization and an appropriate variation of the integer valued variables is presented in the next section of this chapter.

## 5.2. Algorithm for Online Mixed-Integer Energy Distribution Optimization

For solving mixed-integer optimization problems as defined in (5.15) and (5.31) several commercial solvers exist, e.g. IBM CPLEX [102], or MOSEK [103]. Also the free MATLAB toolbox YALMIP can be used for solving small mixed-integer optimization problems based on the internal branch-and-bound framework [104]. The authors of [105] use the IBM CPLEX solver for obtaining energy efficient function partitioning in automotive electric/electronic architectures based on a **M**ixed-**I**nteger **L**inear **P**rogramming (MILP) optimization problem. Also in [106], the CPLEX solver is used for the estimation of the optimal charge-depleting control of the battery in plug-in hybrid electric vehicles for minimization of the total trip fuel consumption based on a MILP problem. In [107], the authors use the CPLEX solver for the minimization of the total annualized cost of residential distributed energy systems based on mixed-integer optimization. The MOSEK solver is used for example in [108] for solving a mixed-integer convex programming problem minimizing the overall operation cost of an electric vehicle with a rental range extender. With the MATLAB toolbox YALMIP the authors of [109] implement an online EMS for a grid connected hybrid energy source for minimization of total operating cost and of

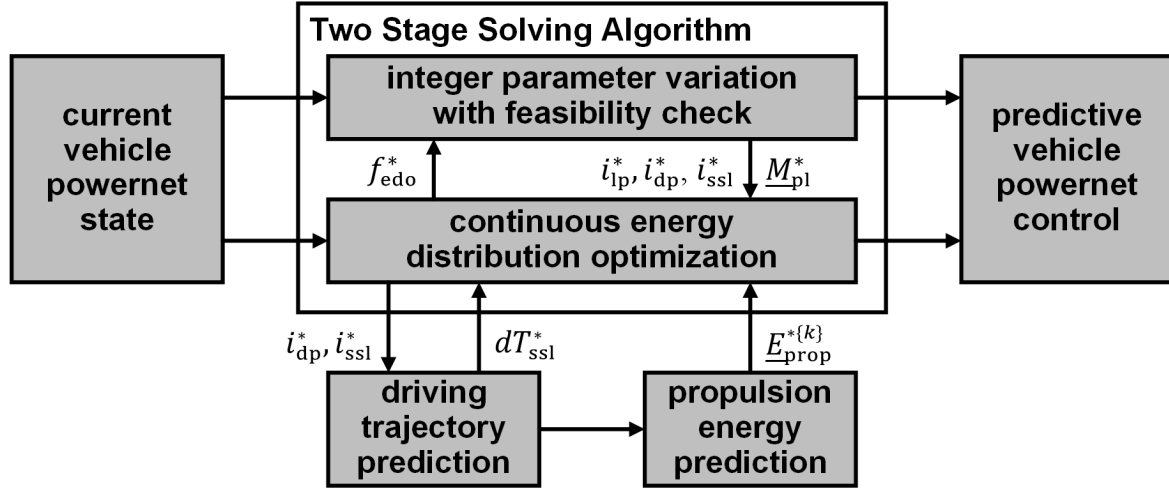


Figure 5.3.: Block diagram of the two-stage solving algorithm.

pollutant gas emissions based on a MILP problem.

Direct solving of mixed-integer control problems is in general computationally intensive and not very well suited for the execution at runtime. Several approaches reducing the computational burden are known. For example, the authors of [110] apply a tailored optimal control solver for a predictive gear shift and cruise controller for heavy duty trucks by dividing the control problem into a continuous optimization and a superimposed discrete parameter variation. In the basic version, the continuous optimization solution is obtained for all possible variations of the discrete parameters, which is then replaced by a heuristic branch and bound search strategy based on the direct multiple shooting method by Bock [110]. A decoupled formulation splitting a complex mixed-integer optimization problem into integer and real decision variables using an iterative optimization strategy is also applied for the reduction of the required computational resources [111, 112]. Examples for the implementation of this approach can be found in [111] for optimal engine on/off control of a serial hybrid electric bus or for cooperative energy management of automated vehicles in [112].

For solving the mixed-integer optimization problem for energy distribution with automated fault reactions in a vehicle powernet as defined in (5.15) and (5.31) at runtime, a two-stage algorithm is proposed. It consists basically of a continuous optimization for energy distribution for a given set of integer variables and a superimposed algorithm for the variation and reduction of all possible combinations for the integer valued optimization variables. As it will be shown in Section 5.3, the continuous optimization problem can be modeled as a **NonLinear Programming** (NLP) problem or by reformulating the objective function and the constraints also as a **Linear Programming** (LP) problem. A block diagram of the algorithm used for solving the mixed-integer energy flow optimiza-

tion is depicted in Fig. 5.3. The output of the integer parameter variation block defines the integer variables for the continuous optimization and is denoted by a star \*. For a given combination of the degradation variables for driving profile ( $i_{dp}^*$ ) and destination ( $i_{ssl}^*$ ), a driving trajectory to the current destination can be approximated as explained in Section 6.2, which is then used for the prediction of the remaining mission time ( $dT_{ssl}^*$ ) and the required propulsion energy ( $E_{prop}^{\{k\}}$ ) for each subpowernet  $k$ :

$$E_{prop}^{\{k\}} = E_{prop}^{\{k\}}(i_{dp}^*, i_{ssl}^*) \quad (5.32a)$$

$$dT_{ssl}^* = dT_{ssl}(i_{dp}^*, i_{ssl}^*) \quad (5.32b)$$

The prediction of the required propulsion energy for a powertrain topology with one and multiple motors is presented in detail in Section 6.3 and 6.4. For the driving time  $dT_{ssl}^*$ , the energy demand of comfort ( $E_{rc}^{\{k\}}$ ) and safety-critical loads ( $E_{rs}^{\{k\}}$ ) in each subpowernet  $k$  for a given degradation step of the load profile ( $i_p^*$ ) is estimated as defined in (5.2):

$$E_{rc}^{\{k\}} = dT_{ssl}^* P_{rc}^{\{k, i_p^*\}} \quad (5.33a)$$

$$E_{rs}^{\{k\}} = dT_{ssl}^* P_{rs}^{\{k, i_p^*\}} \quad (5.33b)$$

The total energy demand of a subpowernet  $k$  as defined in (5.3) is then calculated as:

$$E_{load}^{\{k\}} = E_{rc}^{\{k\}} + E_{rs}^{\{k\}} + E_{prop}^{\{k\}} \quad (5.34)$$

Assuming a given state vector ( $\underline{M}_{pl}^*$ ) storing the operating modes of the powerlink components and considering the current state of the powernet components, the activation state variable ( $S_{pl}^{\{i, k\}}$ ) of the energy flow from subpowernet  $i$  to  $k$  and the corresponding status ( $S_{out}^{\{i, k\}}$ ) can be calculated using (5.4) and (5.6):

$$S_{pl}^{\{i, k\}} = S_{pl}^{\{i, k\}}(\underline{M}_{pl}^*) \quad (5.35a)$$

$$S_{out}^{\{i, k\}} = S_{spn}^{\{i\}} S_{spn}^{\{k\}} S_{pl}^{\{i, k\}} \quad (5.35b)$$

Two different versions of the mixed-integer optimization problem for the energy distribution in the vehicle powernet were defined in Section 5.1.3 and 5.1.4. The energy distribution optimization problem for the automated selection of the optimal paths for energy transport as defined in (5.15) is denoted hereinafter by Version 1. The definition of the continuous energy distribution optimization problem for a given set of mixed-integer variables is presented in Section 5.2.1. Two approaches using nonlinear and linear programming for solving it are proposed in Section 5.3.1 and 5.3.2. The energy distribution optimization problem for the automated selection of optimal paths considering also op-

timal discharge of multiple batteries as defined in (5.31) is denoted in the following by Version 2. The definition of the continuous energy distribution optimization problem for a given set of mixed-integer variables is presented in Section 5.2.2. Two approaches using nonlinear and linear programming for solving it are proposed in Section 5.3.3 and 5.3.4.

The solution  $f_{\text{edo}}^*$  for the continuous energy optimization is provided to the superimposed integer parameter variation algorithm. The combination of the integer variables with maximum  $f_{\text{edo}}^*$  value is considered to be the solution of the mixed-integer optimization problem, which is then used for the control of the vehicle powernet.

### 5.2.1. Continuous Energy Distribution Optimization (Version 1)

With the definitions above, the energy balance equation (5.7) used for the definition of the optimization problem for optimal path selection for a given set of integer valued variables can be simplified to:

$$E_{\text{spn}}^*\{k\}(\underline{E}_{\text{out}}) = \sum_{i=1, i \neq k}^{n_{\text{spn}}} \left( S_{\text{out}}^*\{i,k\} \eta_{\text{pl}}^{\{i,k\}} E_{\text{out}}^{\{i,k\}} - S_{\text{out}}^*\{k,i\} E_{\text{out}}^{\{k,i\}} \right) + S_{\text{spn}}^*\{k\} \left( E_{\text{rde}}^{\{k\}} - E_{\text{load}}^*\{k\} \right) \quad (5.36)$$

The objective for the minimization of energy losses in powerlink components as defined in (5.9) is then simplified to:

$$f_{\text{edo.loss.pl}}^*(\underline{E}_{\text{out}}) = \sum_{k=1}^{n_{\text{spn}}} E_{\text{spn}}^*\{k\}(\underline{E}_{\text{out}}) \quad (5.37)$$

The penalty function for the energy transmission via powerlink outputs as defined in (5.10) is simplified to:

$$f_{\text{edo.pen.pl}}^*(\underline{E}_{\text{out}}) = \sum_{i=1, i \neq k}^{n_{\text{spn}}} \beta_{\text{pl}}^{\{i,k\}}(t) S_{\text{out}}^*\{i,k\} E_{\text{out}}^{\{i,k\}} \quad (5.38)$$

The real valued objective function  $f_{\text{edo}}^*$  for the continuous energy distribution optimization is simplified to  $f_{\text{edo.path}}^*$  and defined as:

$$f_{\text{edo.path}}^*(\underline{E}_{\text{out}}) = f_{\text{edo.loss.pl}}^*(\underline{E}_{\text{out}}) - f_{\text{edo.pen.pl}}^*(\underline{E}_{\text{out}}) \quad (5.39)$$

The maximum allowed output energy  $E_{\text{out.max}}^*\{i,k\}$  at output  $k$  of subpowernet  $i$  as defined in (5.14) is calculated as:

$$E_{\text{out.max}}^*\{i,k\} = \frac{P_{\text{pl.max}}^{\{i,k\}}}{\eta_{\text{pl}}^{\{i,k\}}} dT_{\text{ssl}}^* \quad (5.40)$$

The mixed-integer optimization problem as defined in (5.15) is then simplified for a given set of integer valued variables to a real valued optimization problem:

$$\begin{aligned} \max_{\underline{E}_{\text{out}}} \quad & f_{\text{edo.path}}^*(\underline{E}_{\text{out}}) \\ \text{s.t.} \quad & \begin{cases} 0 \leq \underline{E}_{\text{spn}}^*(\underline{E}_{\text{out}}) \\ 0 \leq \underline{E}_{\text{out}} \leq \underline{E}_{\text{out.max}}^* \end{cases} \end{aligned} \quad (5.41)$$

An appropriate notation of this optimization problem for the use with nonlinear and linear programming solvers is presented in Section 5.3.

### 5.2.2. Continuous Energy Distribution Optimization (Version 2)

For a given set of integer valued variables, the energy balance equation (5.25) used for the definition of the optimization problem for optimal path selection and multiple battery discharge can be simplified to:

$$\begin{aligned} E_{\text{spn.opt}}^*\{\{k\}\}(\underline{E}_{\text{out}}) = & \left[1 + dp_{\text{bat}}^*\{\{k\}\}\right] \sum_{i=1, i \neq k}^{n_{\text{spn}}} \left( S_{\text{out}}^*\{i,k\} \eta_{\text{pl}}^*\{i,k\} E_{\text{out}}^*\{i,k\} - S_{\text{out}}^*\{k,i\} E_{\text{out}}^*\{k,i\} \right) \\ & - \left[1 + dp_{\text{bat}}^*\{\{k\}\}\right] S_{\text{spn}}^*\{k\} E_{\text{load}}^*\{k\} + S_{\text{spn}}^*\{k\} E_{\text{rde0}}^*\{k\} \end{aligned} \quad (5.42)$$

The battery discharge energy  $E_{\text{bat}}^*\{\{k\}\}$  as defined in (5.23) is simplified to:

$$E_{\text{bat}}^*\{\{k\}\}(\underline{E}_{\text{out}}) = \sum_{i=1, i \neq k}^{n_{\text{spn}}} S_{\text{spn}}^*\{i\} \left( S_{\text{pl}}^*\{k,i\} E_{\text{out}}^*\{k,i\} - S_{\text{pl}}^*\{i,k\} \eta_{\text{pl}}^*\{i,k\} E_{\text{out}}^*\{i,k\} \right) + E_{\text{load}}^*\{k\} \quad (5.43)$$

The average battery discharge power  $P_{\text{bat}}^*\{\{k\}\}$  as defined in (5.24) is calculated as:

$$P_{\text{bat}}^*\{\{k\}\}(\underline{E}_{\text{out}}) = \frac{E_{\text{bat}}^*\{\{k\}\}(\underline{E}_{\text{out}})}{dT_{\text{ssl}}^*} \quad (5.44)$$

The objective for the minimization of the energy losses in powerlink and energy storage components as defined in (5.26) is simplified to:

$$f_{\text{edo.loss.opt}}^*(\underline{E}_{\text{out}}) = \sum_{k=1}^{n_{\text{spn}}} E_{\text{spn.opt}}^*\{\{k\}\}(\underline{E}_{\text{out}}) \quad (5.45)$$

The penalty function for the batteries discharge as defined in (5.27) is simplified to:

$$f_{\text{edo.pen.bat}}^*(\underline{E}_{\text{out}}) = \sum_{k=1}^{n_{\text{spn}}} \beta_{\text{bat}}^*\{k\}(t) S_{\text{spn}}^*\{k\} E_{\text{bat}}^*\{\{k\}\}(\underline{E}_{\text{out}}) \quad (5.46)$$

The real valued objective function  $f_{\text{edo.opt}}^*$  for the continuous energy distribution optimization is simplified to  $f_{\text{edo.path.opt}}^*$  and using (5.38) and (5.40) is defined as:

$$f_{\text{edo.path.opt}}^*(\underline{E}_{\text{out}}) = f_{\text{edo.loss.opt}}^*(\underline{E}_{\text{out}}) - f_{\text{edo.pen.pl}}^*(\underline{E}_{\text{out}}) - f_{\text{edo.pen.bat}}^*(\underline{E}_{\text{out}}) \quad (5.47)$$

The mixed-integer optimization problem as defined in (5.31) is then simplified for a given set of integer valued variables to a real valued optimization problem:

$$\begin{aligned} \max_{\underline{E}_{\text{out}}} \quad & f_{\text{edo.path.opt}}^*(\underline{E}_{\text{out}}) \\ \text{s.t.} \quad & \begin{cases} 0 \leq \underline{E}_{\text{spn.opt}}^*(\underline{E}_{\text{out}}) \\ 0 \leq \underline{P}_{\text{bat}}^*(\underline{E}_{\text{out}}) \leq \underline{P}_{\text{bat.max}} \\ 0 \leq \underline{E}_{\text{out}} \leq \underline{E}_{\text{out.max}}^* \end{cases} \end{aligned} \quad (5.48)$$

An appropriate notation of this optimization problem for the use with nonlinear and linear programming solver is presented in Section 5.3.

### 5.2.3. Integer Parameter Variation with Feasibility Check

Optimal energy distribution within a fail-operational powernet depends on the integer valued vector variable  $\underline{M}_{\text{pl}}$  containing the operating mode for each powerlink, and also on the integer valued variables  $i_{\text{lp}}$ ,  $i_{\text{dp}}$  and  $i_{\text{ssl}}$  modeling the stepwise degradation of load profile, driving profile and driving destination. As depicted in Fig. 5.3, the mixed-integer optimization problem used for optimal energy distribution is solved by varying the integer parameters and by solving the continuous optimization problem for each valid parameter combination. By reducing the number of possible combinations for integer variables, the computational effort can be significantly reduced.

Solving the mixed-integer energy distribution optimization problem as presented in Section 5.1.3 and 5.1.4 does not only increase the overall energy efficiency, but also enables automated fault reactions to possible failures within the powernet. Therefore, the optimization problem should be solved online periodically, bounding so the worst case fault reaction time to a maximum of two periods, which should be selected depending on the system requirements. Assuming no unexpected events like faults, the optimal solution is approximately the same during the entire driving mission due to the predictive nature of the energy distribution optimization. Therefore, once a solution is found, it can be used as the starting point for solving the optimization problem in the next cycle.

The flow chart of the algorithm solving the mixed-integer energy distribution optimization problem is depicted in Fig. 5.4. The integer valued optimization variables  $i_{\text{ssl}}$ ,  $i_{\text{dp}}$  and  $i_{\text{lp}}$





are summarized in one degradation step variable  $i_{ds}$ . Using a look-up table, for each  $i_{ds}$  the corresponding combination of  $i_{ssl}$ ,  $i_{dp}$  and  $i_{ip}$  can be assigned. The prioritization of the degradation steps for load profile, driving profile and destination can be defined in any order by appropriate buildup of the look-up table. The degradation step  $i_{ds}$  varies between 1, meaning no degradation, and  $n_{ip} \times n_{dp} \times n_{ssl}$  as the maximum degradation, assuming  $n_{ip}$ ,  $n_{dp}$  and  $n_{ssl}$  steps in total for the degradation of load profile, driving profile and driving destination.

As explained in Section 5.2.1 and 5.2.2, the continuous energy distribution optimization problem is solved for a given degradation step  $i_{ds}^*$  and powerlink operating mode vector  $\underline{M}_{pl}^*$ . At the start of each solving cycle, the optimal degradation step  $i_{ds}$  found in the previous cycle is taken as the initial solution. If, for example, the highest degradation step was estimated as the optimal solution, starting the solver algorithm at the lowest degradation step would result in unnecessary computational burden. To be able to react to transient failures, the degradation step  $i_{ds}^*$ , if not already equal to the minimum, is first decreased. By doing so, it can be checked if the failure causing the previous degradation is still present or not. For this  $i_{ds}^*$ , the energy demand vector  $\underline{E}_{load}^*$  according to (5.34) as well as the remaining discharge energy vector  $\underline{E}_{rde}$ , or alternatively the parameter vectors  $\underline{a}_{rde}$  and  $\underline{E}_{rde0}$  modeling the remaining discharge energy as a function of average discharge power accordingly to (5.18), are estimated.

In the next step, using the powerlinks' diagnostic data, the current energy flow efficiencies are read and the set of possible operating modes  $\underline{PL}_{mod}^{\{i\}}$  for each powerlink  $i$  is estimated. It is assumed that up to  $n_{pl}$  powerlinks are connecting the  $n_{spn}$  subpowernets of a fail-operational powernet topology. By denoting the number of possible operating modes of powerlink  $i$  by  $n_{mod}^{\{i\}}$ , the number  $n_{mod}$  of possible operating mode combinations is then defined as:

$$n_{mod} = \prod_{i=1}^{n_{pl}} n_{mod}^{\{i\}} \quad (5.49)$$

By combining the possible operating modes of each powerlink  $i$ , the set  $\underline{PL}_{mod}$  containing  $n_{mod}$  possible combinations of the  $n_{pl}$ -by-1 operating mode vector variable  $\underline{M}_{pl}$  is estimated. The behavioral modeling of powerlink components as well as the estimation of the sets  $\underline{PL}_{mod}^{\{i\}}$  and  $\underline{PL}_{mod}$  is presented in Section 5.4.

For each operating mode vector  $\underline{M}_{pl}^* \in \underline{PL}_{mod}$  with corresponding counter variable  $i_{mod}$ , the continuous energy distribution optimization problem must be solved. An exemplary powernet line topology is depicted in Fig. 5.5. It consists of five subpowernets and four DC/DC converters with three operating modes each, resulting in  $3 \times 3 \times 3 \times 3 = 81$

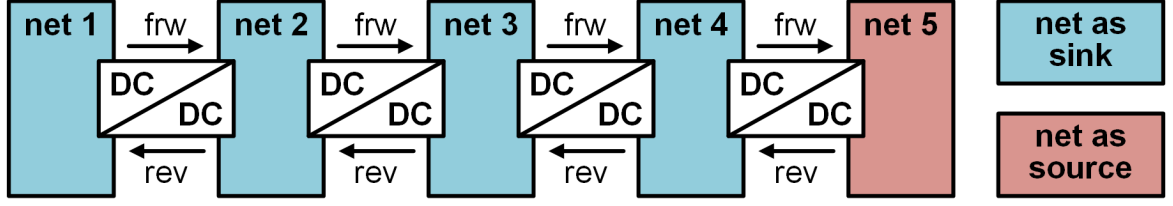


Figure 5.5.: Exemplary powernet line topology and solution feasibility check.

possible operating mode combinations. For a given degradation step  $i_{ds}^*$ , the continuous optimization problems should be solved for each of these combinations, resulting in unnecessary computational burden. Therefore, before solving the continuous optimization problem for a given powerlink operating mode vector  $\underline{M}_{pl}^*$ , a solution feasibility check can be applied using the application specific knowledge. Depending on the available resources and the energy demand, each subpowernet  $k$  can be classified as a source or a sink. In case the available resources are greater than the energy demand, the operational subpowernet  $k$  can be classified as a source, since the surplus energy can be provided to other subpowernets. The set  $SRC$  of all subpowernets classified as a source is then defined as:

$$SRC = \left\{ k \mid (E_{rde}^{\{k\}} > E_{load}^{*\{k\}}) \wedge (S_{spn}^{\{k\}} = 1) \wedge (k \in \{1..n_{spn}\}) \right\} \quad (5.50)$$

In case the energy demand exceeds the available energy resources, the operational subpowernet  $k$  can be classified as a sink, since the lacking energy must be provided from other subpowernets. The set  $SNK$  of all subpowernets classified as a sink is defined as:

$$SNK = \left\{ k \mid (E_{rde}^{\{k\}} \leq E_{load}^{*\{k\}}) \wedge (S_{spn}^{\{k\}} = 1) \wedge (k \in \{1..n_{spn}\}) \right\} \quad (5.51)$$

In case the remaining discharge energy is estimated as a function of the average discharge power, for the classification of the subpowernet  $k$  as a sink or a source,  $E_{rde}^{\{k\}}$  is estimated using the average power of the loads:

$$E_{rde}^{\{k\}} = E_{rde0}^{\{k\}} - dp_{bat}^{\{k\}} \frac{E_{load}^{*\{k\}}}{dT_{ssl}^*} \quad (5.52)$$

For each DC/DC converter depicted in Fig. 5.5, three operating modes are assumed. In the forward (frw) and reverse (rev) mode, the energy flow is enabled in the illustrated direction, in the off (off) mode, the energy flow is disabled. As already mentioned, 81 combinations of powerlink operating modes are possible. Since only the fifth subpowernet is classified as a source, it becomes obvious, that only in case when all DC/DC converters are operating in the reverse mode, a solution for the energy distribution can be obtained. Therefore, by checking if each subpowernet classified as a sink has a direct or indirect

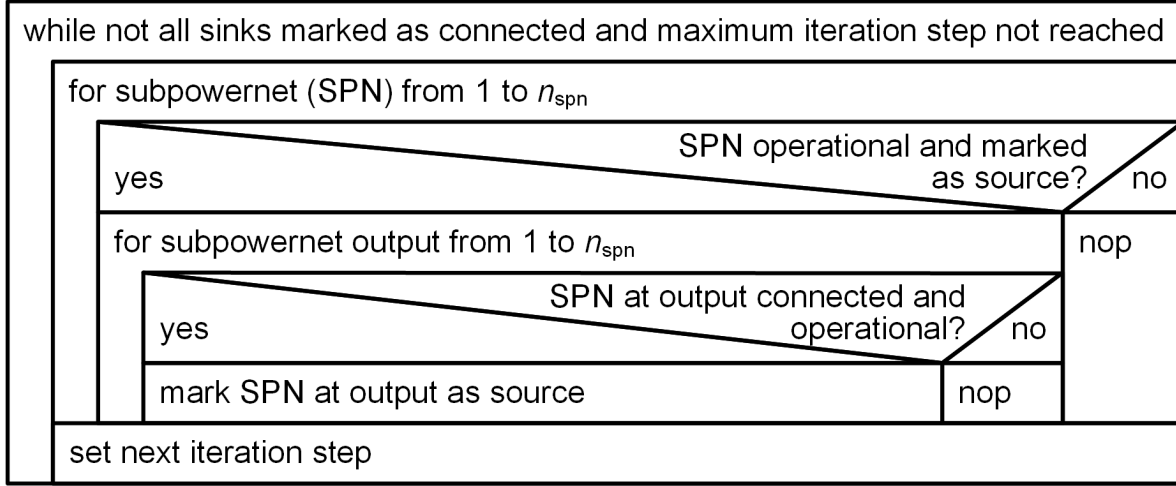


Figure 5.6.: Nassi-Shneiderman diagram for solution feasibility check.

connection to a source, the number of valid powerlink operating mode combinations with feasible solution as well as the computational burden can be significantly reduced.

Based on this consideration, an algorithm verifying the connection of each subpowernet classified as a sink to a source can be applied for each combination  $\underline{M}_{pl}^*$  of powerlink operating modes. Only if for vector  $\underline{M}_{pl}^*$  a solution is feasible, as depicted in the flow diagram in Fig. 5.4, the continuous optimization problem is solved. The Nassi-Shneider diagram of the algorithm proposed for solution feasibility checking is shown in Fig. 5.6. For each subpowernet  $i \in \{1..n_{spn}\}$ , it is checked whether it is operational and marked as a source. If this is true, all operational subpowernets  $k \in \{1..n_{spn}\} \setminus \{i\}$ , which can receive the energy from the subpowernet  $i$  are marked as a source too. This process is repeated iteratively until either all operational subpowernets are marked as a source or the maximum iteration step is reached. In the latter case, the solution of the energy distribution optimization for the combination  $\underline{M}_{pl}^*$  is considered to be not feasible.

Another example for the reduction of the operating mode combinations  $\underline{M}_{pl}^*$  with the solution feasibility check algorithm is presented in Fig. 5.7. Six subpowernets are connected to a ring by six DC/DC converters, enabling the energy transport in both directions. Each DC/DC converter can be again operated in three modes (forward, reverse and off mode), resulting in  $3^6 = 729$  possible combinations. As depicted in the table on the right side of Fig. 5.7, only for 13 combinations the solution of the energy distribution optimization problem is feasible.

The continuous optimization problem is solved for each of the valid combinations  $\underline{M}_{pl}^*$  (refer to Fig. 5.4). The combination  $\underline{M}_{pl}^*$ , for which the objective function is minimal, is considered to be the optimal solution for the current degradation step  $i_{ds}^*$ . If a solution for

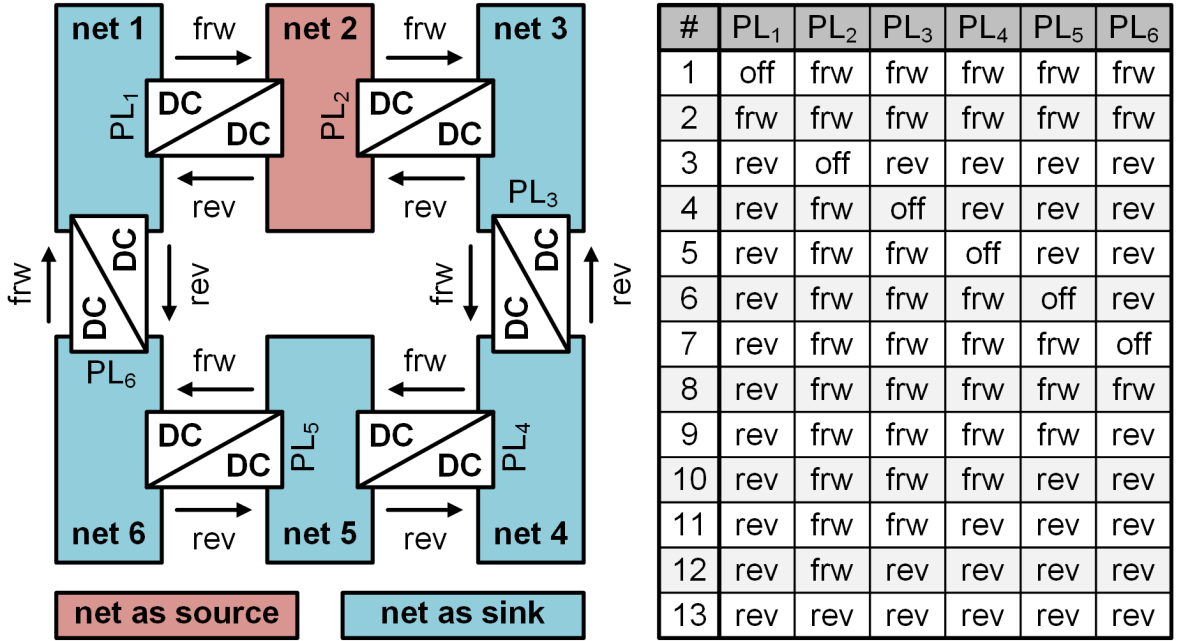


Figure 5.7.: Exemplary powernet ring topology and solution feasibility check.

the continuous optimization problem is found and the degradation step  $i_{ds}^*$  was decreased last,  $i_{ds}^*$  is decreased again until no solution for the continuous optimization problem is found or the degradation of loads is inactive ( $i_{ds}^* = 1$ ). The minimum  $i_{ds}^*$  with an existing solution for the continuous optimization problem is considered to be optimal.

If a solution for the continuous optimization problem is not found for the current degradation step  $i_{ds}^*$  and no solution was saved in the iterations before,  $i_{ds}^*$  is increased until a valid solution for the continuous optimization problem is found or the maximum degradation step is reached ( $i_{ds}^* = n_{ds}$ ). In this case, an immediate stop of the vehicle (emergency braking) is required.

If no failures or unpredicted changes in the system state happen, two iterations of the outer loop of the mixed-integer energy distribution optimization solver according to the flow chart depicted in Fig. 5.4 are required. If degradation is active, in the first outer loop iteration, the algorithm tries to reduce the current degradation step. In the second iteration, it is expected that the algorithm finds the previous solution. In case of a transient failure, the degradation caused by this failure should be deactivated. Using the algorithm as depicted in Fig. 5.4, this can only be guaranteed if the total energy demand of a powernet is a monotonically decreasing function of degradation step  $i_{ds}$ , which is not always the case as it will be shown in the following example.

An exemplary powernet energy demand as a function of the degradation step is illustrated in Fig. 5.8. For the calculation of the energy demand for each degradation step it is

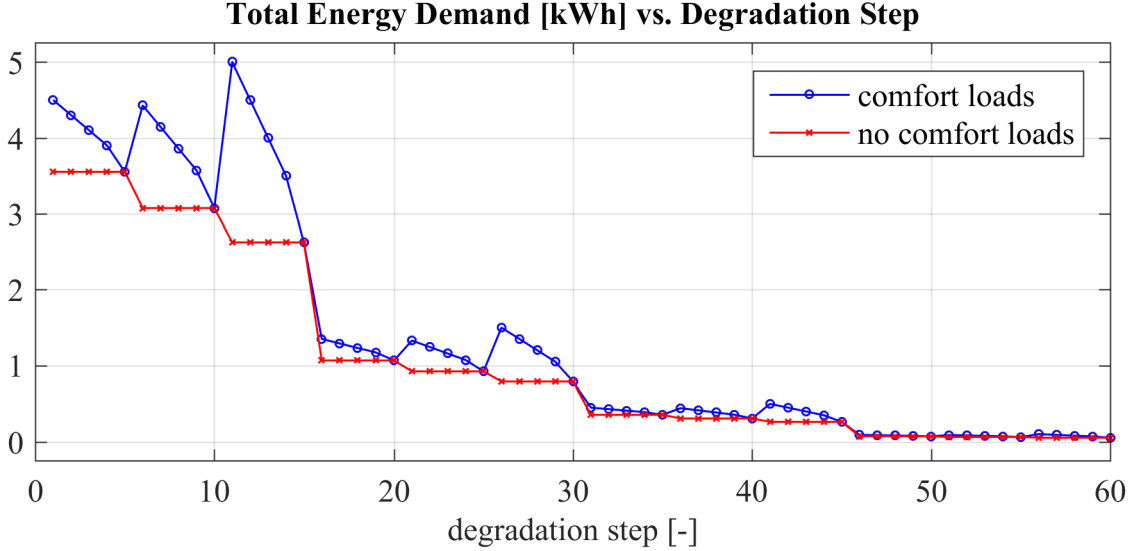


Figure 5.8.: Exemplary powernet energy demand as a function of degradation step.

assumed that the driving destination can be degraded in four steps ( $n_{ssl} = 4$ ). The total distance to be covered is assumed to be 50 km, 15 km, 5 km and 1 km. For the driving profile, three degradation steps ( $n_{dp} = 3$ ) are assumed. By degrading the driving profile, the average driving velocity as well as the propulsion energy needed per 1 km is reduced. The average driving velocity is assumed to be  $50 \frac{\text{km}}{\text{h}}$ ,  $35 \frac{\text{km}}{\text{h}}$  and  $20 \frac{\text{km}}{\text{h}}$ . The corresponding propulsion energy per kilometer is assumed to be  $0.07 \frac{\text{kWh}}{\text{km}}$ ,  $0.06 \frac{\text{kWh}}{\text{km}}$  and  $0.05 \frac{\text{kWh}}{\text{km}}$ . For the degradation of the load profile, five steps ( $n_{lp} = 5$ ) are assumed with the corresponding power demand equal to 1000 W, 800 W, 600 W, 400 W and 50 W.

For these simplified assumptions, the total propulsion energy required at a given degradation step is calculated as the product of driving destination and average propulsion energy per kilometer. The total energy consumed by powernet loads is calculated as a product of the average load power and driving duration, which is obtained with the assumed average velocity. The blue curve (comfort loads) in Fig. 5.8 illustrates the total energy demand for each degradation step estimated using the assumptions above. It can be seen that the energy demand as a function of the degradation step is not monotonically decreasing.

In this example, the total energy required at the first degradation step (no degradation) is equal to 4.5 kWh. A transient failure resulting in a decrease of energy resources from available 4.6 kWh to e.g. 2.0 kWh would cause as a fault reaction the degradation from step 1 to 16. After the failure disappears, again 4.6 kWh would be available. Using the algorithm according to the flow chart in Fig. 5.4, the degradation step would be decreased by 1 until a solution is not found, meaning that the energy demand exceeds the available resources. In this simplified example the degradation step 12 would be identified as

a new solution due to the energy demand peak at step 11. Therefore, for handling the energy demand functions which are not monotonically decreasing, the proposed algorithm illustrated in Fig. 5.4 should be extended.

Degradation of the driving profile reduces the average propulsion energy per kilometer on one side, but also increases the average driving time to the same destination on the other side, which leads to increased energy required by powernet loads. Therefore, if the reduction in the propulsion energy is less than the increase in load energy, the total energy demand as a function of degradation steps becomes not monotonically decreasing. In Fig. 5.8, a second curve (no comfort loads) assuming a constant power demand of powernet loads equal to 50 W (last degradation step of load profile with  $i_p = 5$ ) for all degradation steps is illustrated. Assuming all comfort loads turned off and only safety-critical loads with a low average power demand, also the corresponding total energy demand as a function of degradation step can be assumed monotonically decreasing, which is illustrated in Fig. 5.8 for the simplified assumptions made above. This property is used for the extension of the mixed-integer energy distribution solver for handling the degradation recovery in case of transient failures also for energy demand functions, which are not monotonically decreasing. The extension is illustrated in blue in Fig. 5.9.

The main idea is to branch the jump for decreasing the last valid degradation step  $i_{ds}$  in two parts. At first, the degradation step is iteratively decreased to the next smallest step, at which all comfort loads are in maximum degradation ( $i_p = n_p$ ). After no jumps to the next smallest step with all loads degraded are possible or a solution was not found for the previous jump, the decrease of degradation with a step equal to 1 is tried next.

In the example of the transient failure described above (decrease in energy resources from 4.6 kWh to 2.0 kWh), in the optimization after the failure is recovered, the degradation variable  $i_{ds}^*$  would be set from  $i_{ds} = 16$  to 15. After a solution is found for  $i_{ds}^* = 15$ , the degradation step is set again to the next smallest step with all loads degraded, in this case to  $i_{ds}^* = 10$ . After jumping to  $i_{ds}^* = 5$ , the decrease of degradation is continued with steps equal to 1, until  $i_{ds}^* = 1$  is reached.

If no changes or failures occur, meaning that the degradation step  $i_{ds}$  should not change, the algorithm according to the flow chart depicted in Fig. 5.9 would still try to decrease the degradation step in two iterations, before it gets the current solution. Assuming a valid solution for  $i_{ds} = 14$  in the example above, the algorithm would first try to find a solution for  $i_{ds} = 10$ , then for  $i_{ds} = 13$  and only in the third iteration it will find a valid solution for  $i_{ds} = 14$ . Compared to the algorithm depicted in Fig. 5.4, which would require only two iterations (first for  $i_{ds} = 13$  and then  $i_{ds} = 14$ ), it adds additional computational burden due to the third iteration. Therefore, the algorithm depicted in





Fig. 5.4 is better suited for use cases with monotonically decreasing energy demand as a function of the degradation step due to the reduced average computational effort. Also for non monotonically decreasing energy demand this version of the algorithm can be used by adding additional recalculation cycles at which  $i_{ds}$  is reset to 1. The extended version of the algorithm depicted in Fig. 5.9 shows better convergence by dynamic changes in the system state and for transient failures, covering also use cases with non monotonically decreasing energy demand as a function of the degradation step. Therefore, based on the requirements and system properties, the appropriate version of the algorithm for the optimal energy distribution should be selected.

Summing up the results, it can be stated that by applying application specific knowledge, the number of valid combinations for integer valued optimization variables can be reduced significantly, speeding up in this way the computational time required for solving the mixed-integer energy distribution optimization. The speed up depends on the ratio of valid combinations of discrete variables to the number of all possible combinations. Another important point influencing the execution of the proposed control strategy at runtime is the time required for solving the continuous optimization problem. In the next section, two different approaches using nonlinear and linear programming solvers are presented.

### 5.3. Solving Continuous Energy Distribution Optimization

The continuous optimization problem for the optimal energy distribution in the vehicle powernet as defined in (5.41) and (5.48) is a constrained multivariable optimization problem. Depending on the properties of the objective function and equality and inequality constraints of the optimization problem, different solvers can be used.

For solving an optimization problem with a nonlinear objective function and nonlinear and/or linear equality and/or inequality constraints, for example, the *fmincon* solver available in MATLAB can be used. The optimization problem must be then formulated in the following form [37]:

$$\begin{aligned} \min_{\underline{x}_{nlp}} \quad & f_{obj,nlp}(\underline{x}_{nlp}) \\ \text{s.t.} \quad & \begin{cases} c_{ineq,nlp}(\underline{x}_{nlp}) \leq 0 \\ c_{eq,nlp}(\underline{x}_{nlp}) = 0 \\ A_{ineq,nlp} \cdot \underline{x}_{nlp} \leq b_{ineq,nlp} \\ A_{eq,nlp} \cdot \underline{x}_{nlp} = b_{eq,nlp} \\ \underline{lb}_{nlp} \leq \underline{x}_{nlp} \leq \underline{ub}_{nlp} \end{cases} \end{aligned} \quad (5.53)$$

The optimization variable ( $\underline{x}_{\text{nlp}}$ ), which can be a vector or a matrix, is bounded by lower ( $\underline{lb}_{\text{nlp}}$ ) and upper limits ( $\underline{ub}_{\text{nlp}}$ ). The solution space of the optimization problem can be constrained by defining the nonlinear and/or linear equality and/or inequality constraints. The nonlinear equality and inequality constraints are defined using the functions  $\underline{c}_{\text{ineq.nlp}}$  and  $\underline{c}_{\text{eq.nlp}}$ , both returning a vector or a matrix. The linear equality and inequality constraints can be specified using the matrices  $\underline{A}_{\text{ineq.nlp}}$  and  $\underline{A}_{\text{eq.nlp}}$  and the corresponding vectors  $\underline{b}_{\text{ineq.nlp}}$  and  $\underline{b}_{\text{eq.nlp}}$ .

For solving an optimization problem with linear objective function and linear equality and/or inequality constraints, for example, the *linprog* solver available in MATLAB can be used. The optimization problem must be then formulated in the following form [37]:

$$\begin{aligned} \min_{\underline{x}_{\text{lp}}} \quad & \underline{f}_{\text{obj.lp}}^T \cdot \underline{x}_{\text{lp}} \\ \text{s.t.} \quad & \begin{cases} \underline{A}_{\text{ineq.lp}} \cdot \underline{x}_{\text{lp}} \leq \underline{b}_{\text{ineq.lp}} \\ \underline{A}_{\text{eq.lp}} \cdot \underline{x}_{\text{lp}} = \underline{b}_{\text{eq.lp}} \\ \underline{lb}_{\text{lp}} \leq \underline{x}_{\text{lp}} \leq \underline{ub}_{\text{lp}} \end{cases} \end{aligned} \quad (5.54)$$

The optimization variable ( $\underline{x}_{\text{lp}}$ ) in the form of a vector is bounded by lower ( $\underline{lb}_{\text{lp}}$ ) and upper limits ( $\underline{ub}_{\text{lp}}$ ). The objective of the optimization problem is defined by multiplying the optimization variable with the objective vector  $\underline{f}_{\text{obj.lp}}$  of the same size. The solution space of the optimization problem can be constrained by defining the linear equality and/or inequality constraints. The linear equality and inequality constraints can be specified using the matrices  $\underline{A}_{\text{ineq.lp}}$  and  $\underline{A}_{\text{eq.lp}}$  and the corresponding vectors  $\underline{b}_{\text{ineq.lp}}$  and  $\underline{b}_{\text{eq.lp}}$ . For the formulation of the energy distribution optimization defined in (5.41) and (5.48) in the format as required by *fmincon* and *linprog* solver, an appropriate matrix and vector notation of the system state and optimization variables is introduced in the following.

The  $n_{\text{spn}}$ -by- $n_{\text{spn}}$  matrix  $\underline{E}_{\text{out}}$  is used for the notation of all energy flows within a power-net. The element  $\underline{E}_{\text{out}\{i,k\}}$  in the  $i$ -th row and  $k$ -th column of the matrix  $\underline{E}_{\text{out}}$  is defined as:

$$\underline{E}_{\text{out}\{i,k\}} = \begin{cases} E_{\text{out}}^{\{i,k\}}, & i \neq k \\ 0, & i = k \end{cases} \quad \text{with } i, k \in \{1..n_{\text{spn}}\} \quad (5.55)$$

The  $n_{\text{spn}}$ -by- $n_{\text{spn}}$  matrix  $\underline{E}_{\text{out.max}}^*$  is used for the notation of the output energy transport limit of all powerlink outputs within the vehicle powernet as defined in (5.40). The element  $\underline{E}_{\text{out.max}\{i,k\}}^*$  in the  $i$ -th row and  $k$ -th column of the matrix  $\underline{E}_{\text{out.max}}^*$  is defined as:

$$\underline{E}_{\text{out.max}\{i,k\}}^* = \begin{cases} E_{\text{out.max}}^{*\{i,k\}}, & i \neq k \\ 0, & i = k \end{cases} \quad \text{with } i, k \in \{1..n_{\text{spn}}\} \quad (5.56)$$

Depending on the current powerlink components' state, the efficiency  $\eta_{\text{pl}}^{\{i,k\}}$  of the energy flow from subpowernet  $i$  to  $k$  might vary over time. Also possible powerlink faults resulting in a decreased energy flow efficiency are modeled by the time-dependent  $n_{\text{spn}}$ -by- $n_{\text{spn}}$  matrix  $\underline{\eta}_{\text{pl}}$ , which is used for the notation of all energy flow efficiencies within the powernet. The element  $\underline{\eta}_{\text{pl}\{i,k\}}$  in the  $i$ -th row and  $k$ -th column of the matrix  $\underline{\eta}_{\text{pl}}$  is defined as:

$$\underline{\eta}_{\text{pl}\{i,k\}}(t) = \begin{cases} \eta_{\text{pl}}^{\{i,k\}}(t), & i \neq k \\ 0, & i = k \end{cases} \quad \text{with } i, k \in \{1..n_{\text{spn}}\} \quad (5.57)$$

The time-dependent  $n_{\text{spn}}$ -by- $n_{\text{spn}}$  matrix  $\underline{\beta}_{\text{pl}}$  stores the penalty factors for all powerlink outputs of the powernet. The element  $\underline{\beta}_{\text{pl}\{i,k\}}$  in the  $i$ -th row and  $k$ -th column of the matrix  $\underline{\beta}_{\text{pl}}$  for the penalty factor of the energy flow  $E_{\text{out}}^{\{i,k\}}$  from subpowernet  $i$  to  $j$  is defined as:

$$\underline{\beta}_{\text{pl}\{i,k\}}(t) = \begin{cases} \beta_{\text{pl}}^{\{i,k\}}(t), & i \neq k \\ 0, & i = k \end{cases} \quad \text{with } i, k \in \{1..n_{\text{spn}}\} \quad (5.58)$$

The time-dependent  $n_{\text{spn}}$ -by-1 vector  $\underline{S}_{\text{spn}}$  is used for the notation of operational state as defined in (5.5) for all subpowernets. The  $i$ -th element of the vector  $\underline{S}_{\text{spn}}$  is defined as:

$$\underline{S}_{\text{spn}\{i\}}(t) = S_{\text{spn}}^{\{i\}}(t) \quad \text{with } i \in \{1..n_{\text{spn}}\} \quad (5.59)$$

The  $n_{\text{spn}}$ -by- $n_{\text{spn}}$  matrix  $\underline{S}_{\text{pl}}^*$  is used for the notation of the activation state of all energy flows within the vehicle powernet as defined in (5.35a). The element  $\underline{S}_{\text{pl}\{i,k\}}^*$  in the  $i$ -th row and  $k$ -th column of the matrix  $\underline{S}_{\text{pl}}^*$  is defined as:

$$\underline{S}_{\text{pl}\{i,k\}}^* = \begin{cases} S_{\text{pl}}^{\{i,k\}}, & i \neq k \\ 0, & i = k \end{cases} \quad \text{with } i, k \in \{1..n_{\text{spn}}\} \quad (5.60)$$

The  $n_{\text{spn}}$ -by- $n_{\text{spn}}$  matrix  $\underline{S}_{\text{out}}^*$  with the element  $\underline{S}_{\text{out}\{i,k\}}^*$  in the  $i$ -th row and  $k$ -th column for the status of the energy flow from subpowernet  $i$  to  $k$  as defined in (5.35b) is calculated as:

$$\underline{S}_{\text{out}}^* = \left( \underline{S}_{\text{spn}} \cdot \underline{S}_{\text{spn}}^{\text{T}} \right) \circ \underline{S}_{\text{pl}}^* \quad (5.61)$$

The time-dependent  $n_{\text{spn}}$ -by-1 vectors  $\underline{E}_{\text{rde}}$  and  $\underline{E}_{\text{load}}^*$  are used for the notation of available energy resources and required energy as defined in (5.34) for all subpowernets. The  $i$ -th element of the vectors  $\underline{E}_{\text{rde}}$  and  $\underline{E}_{\text{load}}^*$  is defined as:

$$\underline{E}_{\text{rde}\{i\}}(t) = E_{\text{rde}}^{\{i\}}(t) \quad (5.62a)$$

$$\underline{E}_{\text{load}\{i\}}^*(t) = E_{\text{load}}^{\{i\}*}(t) \quad (5.62b)$$

The time-dependent  $n_{\text{spn}}$ -by-1 vectors  $\underline{E}_{\text{rde0}}$  and  $\underline{dp}_{\text{bat}}$  are used for the notation of parameters approximating the energy resources as a function of the battery output energy. The  $i$ -th element of the vectors  $\underline{E}_{\text{rde0}}$  and  $\underline{dp}_{\text{bat}}$  is defined as:

$$\underline{E}_{\text{rde0}\{i\}}(t) = E_{\text{rde0}}^{\{i\}}(t) \quad (5.63a)$$

$$\underline{dp}_{\text{bat}\{i\}}(t) = dp_{\text{bat}}^{\{i\}}(t) \quad (5.63b)$$

In the following subsections, the multiplication of an  $n$ -by- $m$  matrix  $\underline{a}$  with  $m$ -by- $p$  matrix  $\underline{b}$  is denoted by a dot '.':

$$\underline{c}^{n \times p} = \underline{a}^{n \times m} \cdot \underline{b}^{m \times p} \quad \text{with} \quad c_{\{i,j\}} = \sum_{k=1}^m a_{\{i,k\}} b_{\{k,j\}} \quad \text{and} \quad i \in \{1..n\}, j \in \{1..p\} \quad (5.64)$$

The elementwise multiplication of an  $n$ -by- $m$  matrix  $\underline{a}$  with  $b$  is denoted by a circle 'o':

$$\underline{c}^{n \times m} = \underline{a}^{n \times m} \circ \underline{b}^{n \times m} \quad \text{with} \quad c_{\{i,j\}} = a_{\{i,j\}} b_{\{i,j\}} \quad \text{and} \quad i \in \{1..n\}, j \in \{1..m\} \quad (5.65)$$

The matrix operation *diag* puts the elements of an  $n$ -by-1 column vector  $\underline{b}$  on the diagonal of an  $n$ -by- $n$  matrix  $\underline{c}$  with all other elements equal to zero:

$$\underline{c}^{n \times n} = \text{diag}(\underline{b}^{n \times 1}) \quad \text{with} \quad c_{\{i,j\}} = \begin{cases} b_{\{i\}}, & i = j \\ 0, & i \neq j \end{cases} \quad \text{and} \quad i, j \in \{1..n\} \quad (5.66)$$

Using the notations above, the continuous energy distribution optimization problem as defined in (5.41) is converted to a form required by the nonlinear programming solver (*fmincon*) in Section 5.3.1 and by linear programming solver (*linprog*) in Section 5.3.2. In a similar way, also the extended version of the energy distribution optimization problem defined in (5.48) is converted to a form required by the nonlinear programming solver (*fmincon*) in Section 5.3.3 and by linear programming solver (*linprog*) in Section 5.3.4.

### 5.3.1. Energy Distribution (Version 1) with Nonlinear Programming

A continuous energy distribution problem used for the control of fail-operational power networks with up to  $n_{\text{spn}}$  channels was defined in (5.41). By solving it, an optimal energy output matrix  $\underline{E}_{\text{out}}$  with regard to the minimization of energy losses in powerlink components and user defined criteria is found. The following relationship between the solution  $\underline{x}_{\text{nlp}}$  of the *fmincon* solver and the optimal energy output matrix  $\underline{E}_{\text{out}}$  is valid:

$$\underline{E}_{\text{out}\{i,k\}} = \begin{cases} \underline{x}_{\text{nlp}\{i,k\}}, & i \neq k \\ 0, & i = k \end{cases} \quad \text{with} \quad i, k \in \{1..n_{\text{spn}}\} \quad (5.67)$$

For the estimation of the  $n_{\text{spn}}$ -by-1 vector  $\underline{E}_{\text{spn}}^*$  storing the energy balance value for each subpowernet  $k \in \{1..n_{\text{spn}}\}$  as defined in (5.36), the following matrix notation is used:

$$\underline{E}_{\text{spn}}^*(\underline{E}_{\text{out}}) = \underline{S}_{\text{spn}} \circ \left[ \left( \underline{S}_{\text{pl}}^{*\text{T}} \circ \underline{\eta}_{\text{pl}}^{\text{T}} \circ \underline{E}_{\text{out}}^{\text{T}} - \underline{S}_{\text{pl}}^* \circ \underline{E}_{\text{out}} \right) \cdot \underline{S}_{\text{spn}} + \underline{E}_{\text{rde}} - \underline{E}_{\text{load}}^* \right] \quad (5.68)$$

The objective  $f_{\text{edo.loss.pl}}^*$  for the minimization of the energy losses in powerlink components as defined in (5.37) can be calculated using the following matrix notation:

$$f_{\text{edo.loss.pl}}^*(\underline{E}_{\text{out}}) = \underline{S}_{\text{spn}}^{\text{T}} \cdot \left[ \left( \underline{S}_{\text{pl}}^{*\text{T}} \circ \underline{\eta}_{\text{pl}}^{\text{T}} \circ \underline{E}_{\text{out}}^{\text{T}} - \underline{S}_{\text{pl}}^* \circ \underline{E}_{\text{out}} \right) \cdot \underline{S}_{\text{spn}} + \underline{E}_{\text{rde}} - \underline{E}_{\text{load}}^* \right] \quad (5.69)$$

The penalty function  $f_{\text{edo.pen.pl}}^*$  for adjusting the powerlink output energy as defined in (5.38) can be rewritten as:

$$f_{\text{edo.pen.pl}}^*(\underline{E}_{\text{out}}) = \underline{S}_{\text{spn}}^{\text{T}} \cdot \left( \underline{S}_{\text{pl}}^* \circ \underline{\beta}_{\text{pl}} \circ \underline{E}_{\text{out}} \right) \cdot \underline{S}_{\text{spn}} \quad (5.70)$$

In the formulation of the optimization problem for the *fmincon* solver, the objective function  $f_{\text{obj.nlp}}^{\text{v1}}$  is minimized, which is opposite to the maximization of the objective function  $f_{\text{edo.path}}^*$  in the optimization problem defined in (5.39). Therefore, the objective function  $f_{\text{obj.nlp}}^{\text{v1}}$  must be opposite to  $f_{\text{edo.path}}^*$ . By combining (5.69) with (5.70), the objective function  $f_{\text{obj.nlp}}^{\text{v1}}$  for the *fmincon* solver can be formulated as:

$$\begin{aligned} f_{\text{obj.nlp}}^{\text{v1}}(\underline{x}_{\text{nlp}}) &= \underline{S}_{\text{spn}}^{\text{T}} \cdot \left( \underline{S}_{\text{pl}}^* \circ \left( \underline{\mathbb{1}} + \underline{\beta}_{\text{pl}} \right) \circ \underline{x}_{\text{nlp}} - \underline{S}_{\text{pl}}^{*\text{T}} \circ \underline{\eta}_{\text{pl}}^{\text{T}} \circ \underline{x}_{\text{nlp}}^{\text{T}} \right) \cdot \underline{S}_{\text{spn}} \\ &\quad + \underline{S}_{\text{spn}}^{\text{T}} \cdot \left( \underline{E}_{\text{load}}^* - \underline{E}_{\text{rde}} \right) \end{aligned} \quad (5.71)$$

The first constraint of the optimization problem in (5.41) can be defined for the *fmincon* solver with the nonlinear inequality constraint function  $\underline{c}_{\text{ineq.nlp}}^{\text{v1}}$  as:

$$\underline{c}_{\text{ineq.nlp}}^{\text{v1}}(\underline{x}_{\text{nlp}}) = -\underline{E}_{\text{spn}}^*(\underline{x}_{\text{nlp}}) \quad (5.72)$$

If an energy flow path is deactivated or not operational, the corresponding element of the output state matrix is set to zero and otherwise to one. For forcing these energy flows to zero, the nonlinear equality constraint function  $\underline{c}_{\text{eq.nlp}}$  in (5.53) can be defined by denoting an  $n_{\text{spn}}$ -by- $n_{\text{spn}}$  matrix with all elements equal to one by  $\underline{\mathbb{1}}$  as:

$$\underline{c}_{\text{eq.nlp}}(\underline{E}_{\text{out}}) = \left( \underline{\mathbb{1}} - \underline{S}_{\text{out}}^* \right) \circ \underline{E}_{\text{out}} \quad (5.73)$$

The second constraint of the optimization problem formulated in (5.41) corresponds to the definition of the  $n_{\text{spn}}$ -by- $n_{\text{spn}}$  lower and upper bound matrices  $\underline{lb}_{\text{nlp}}$  and  $\underline{ub}_{\text{nlp}}$  for the

*fmincon* solver as:

$$\begin{aligned}\underline{lb}_{\text{nlp}} &= \underline{0} \\ \underline{ub}_{\text{nlp}} &= \underline{E}_{\text{out.max}}^*\end{aligned}\tag{5.74}$$

A matrix or vector with all elements equal to zero is denoted by  $\underline{0}$ . The linear equality and inequality constraints in (5.53) are not required and set to zero:

$$\begin{aligned}\underline{A}_{\text{ineq.nlp}} &= \underline{A}_{\text{eq.nlp}} = \underline{0} \\ \underline{b}_{\text{ineq.nlp}} &= \underline{b}_{\text{eq.nlp}} = \underline{0}\end{aligned}\tag{5.75}$$

The formulation of the continuous energy distribution optimization problem as defined in (5.41) for the linear programming solver *linprog* with significant lower computation effort is presented in the next subsection.

### 5.3.2. Energy Distribution (Version 1) with Linear Programming

The  $n_{\text{spn}}$ -by- $n_{\text{spn}}$  variable matrix  $\underline{x}_{\text{nlp}}$  used for the notation of the energy distribution optimization problem for the *fmincon* solver is substituted by the  $n_{\text{spn}}^2$ -by-1 variable column vector  $\underline{x}_{\text{lp}}$  for the *linprog* solver. The following relationship between the *linprog* optimal solution  $\underline{x}_{\text{lp}}$  and the optimal energy output  $\underline{E}_{\text{out}}$  in matrix notation according to the format in (5.55) is valid:

$$\underline{E}_{\text{out}\{i,k\}} = \begin{cases} \underline{x}_{\text{lp}\{i+n_{\text{spn}}(k-1)\}}, & i \neq k \\ 0, & i = k \end{cases} \quad \text{with } i, k \in \{1..n_{\text{spn}}\}\tag{5.76}$$

For the definition of the  $n_{\text{spn}}^2$ -by-1 objective column vector  $f_{\text{obj.lp}}^{\text{v1}}$  according to the notation of the optimization problem in *linprog* format, two  $n_{\text{spn}}$ -by- $n_{\text{spn}}^2$  matrices  $\underline{A}_{\text{espn.lp}}$  and  $\underline{A}_{\text{pen.pl.lp}}$  are introduced. The first matrix  $\underline{A}_{\text{espn.lp}}$ , consisting of  $n_{\text{spn}}$  submatrices  $\underline{A}_{\text{espn.lp}\{i\}}$  with  $i \in \{1..n_{\text{spn}}\}$  is defined as:

$$\underline{A}_{\text{espn.lp}} = \left( \underline{A}_{\text{espn.lp}\{1\}} \quad \underline{A}_{\text{espn.lp}\{2\}} \quad \cdots \quad \underline{A}_{\text{espn.lp}\{n_{\text{spn}}\}} \right)\tag{5.77}$$

Denoting the  $i$ -th column of a matrix  $\underline{a}$  by  $\underline{a}^{(i)}$ , the  $i$ -th  $n_{\text{spn}}$ -by- $n_{\text{spn}}$  submatrix  $\underline{A}_{\text{espn.lp}\{i\}}$  can be calculated using the  $n_{\text{spn}}$ -by- $n_{\text{spn}}$  identity matrix  $\underline{I}$  and efficiency matrix  $\underline{\eta}_{\text{pl}}$ :

$$\underline{A}_{\text{espn.lp}\{i\}} = \underline{I} - \underline{I}^{(i)} \cdot (\underline{\eta}_{\text{pl}}^{(i)})^{\text{T}} \quad \text{with } i \in \{1..n_{\text{spn}}\}\tag{5.78}$$

The second matrix  $\underline{A}_{\text{pen.pl.lp}}$  consisting of  $n_{\text{spn}}$  submatrices  $\underline{A}_{\text{pen.pl.lp}\{i\}}$  with  $i \in \{1..n_{\text{spn}}\}$

is defined as:

$$\underline{A}_{\text{pen.pl.lp}} = \left( \underline{A}_{\text{pen.pl.lp}\{1\}} \quad \underline{A}_{\text{pen.pl.lp}\{2\}} \quad \cdots \quad \underline{A}_{\text{pen.pl.lp}\{n_{\text{spn}}\}} \right) \quad (5.79)$$

The  $i$ -th  $n_{\text{spn}}$ -by- $n_{\text{spn}}$  submatrix  $\underline{A}_{\text{pen.pl.lp}\{i\}}$  of  $\underline{A}_{\text{pen.pl.lp}}$  can be calculated using the  $n_{\text{spn}}$ -by- $n_{\text{spn}}$  output energy penalty matrix  $\underline{\beta}_{\text{pl}}$  as:

$$\underline{A}_{\text{pen.pl.lp}\{i\}} = \text{diag}(\underline{\beta}_{\text{pl}}^{(i)}) \quad \text{with} \quad i \in \{1..n_{\text{spn}}\} \quad (5.80)$$

Using (5.77), the energy balance vector  $\underline{E}_{\text{spn.lp}}^*$  for *linprog* solver can be defined as:

$$\underline{E}_{\text{spn.lp}}^*(\underline{x}_{\text{lp}}) = -\underline{A}_{\text{espn.lp}} \cdot \underline{x}_{\text{lp}} \quad (5.81)$$

By denoting the  $n_{\text{spn}}$ -by-1 column vector with all ones by  $\underline{1}$ , the  $n_{\text{spn}}^2$ -by-1 objective vector  $\underline{f}_{\text{edo.loss.pl}}^*$  and function  $f_{\text{edo.loss.pl.lp}}^*$  for the minimization of the energy losses in powerlink components can be defined as:

$$\underline{f}_{\text{edo.loss.pl}}^* = -\left(\underline{1}^T \cdot \underline{A}_{\text{espn.lp}}\right)^T \quad (5.82a)$$

$$f_{\text{edo.loss.pl.lp}}^*(\underline{x}_{\text{lp}}) = \underline{f}_{\text{edo.loss.pl}}^{*\text{T}} \cdot \underline{x}_{\text{lp}} \quad (5.82b)$$

The definition of the energy balance vector  $\underline{E}_{\text{spn.lp}}^*$  and of the objective for minimization of energy losses in powerlink components  $\underline{f}_{\text{edo.loss.pl.lp}}^*$  is not equal to the definition in (5.68) and (5.69), since the calculation of  $\underline{E}_{\text{spn.lp}}^*$  does not consider the energy demand vector  $\underline{E}_{\text{load}}^*$ , remaining discharge energy vector  $\underline{E}_{\text{rde}}$ , subpowernets state vector  $\underline{S}_{\text{spn}}$  and the energy flow activation matrix  $\underline{S}_{\text{pl}}^*$ . The equality between (5.68) and (5.81) as well as between (5.69) and (5.82b) can be achieved, when the following conditions are fulfilled:

$$\underline{x}_{\text{lp}\{i+n_{\text{spn}}(k-1)\}} = \begin{cases} \underline{E}_{\text{load}\{i\}}^* - \underline{E}_{\text{rde}\{i\}}, & i = k \wedge \underline{S}_{\text{spn}\{i\}} = 1 \\ \underline{E}_{\text{out}\{i,k\}}, & i \neq k \wedge \underline{S}_{\text{out}\{i,k\}}^* = 1 \\ 0, & \text{otherwise} \end{cases} \quad \text{with } i, k \in \{1..n_{\text{spn}}\} \quad (5.83)$$

The  $\{i + n_{\text{spn}}(k - 1)\}$ -th element of the vector  $\underline{x}_{\text{lp}}$  with  $i = k$  corresponds to the diagonal element  $\underline{E}_{\text{out}\{i,i\}}$  of the energy output matrix  $\underline{E}_{\text{out}}$  in (5.55), which is by definition equal to zero. By forcing the  $\{i + n_{\text{spn}}(k - 1)\}$ -th element of the vector  $\underline{x}_{\text{lp}}$  to a constant value, which is done by the first condition in (5.83), an offset can be added to the  $i$ -th row of the vector  $\underline{E}_{\text{spn.lp}}^*$ . In this way, the difference between the remaining discharge energy and demand ( $\underline{E}_{\text{rde}\{i\}} - \underline{E}_{\text{load}}^*$ ) (negative in (5.83) due to the minus sign in (5.81)) is added to

the energy balance value of the operational subpowernet  $i$  with  $\underline{S}_{\text{spn}\{i\}} = 1$ .

If the energy flow  $\underline{E}_{\text{out}\{i,k\}}$  from subpowernet  $i$  to  $k$  is deactivated or not possible due to a failure in the corresponding subpowernets, the state variable  $\underline{S}_{\text{out}\{i,k\}}^*$  is set to zero. Since the state variable matrix  $\underline{S}_{\text{out}}^*$  is not considered in (5.81), the energy flows which are deactivated or not possible are forced to zero using the third condition in (5.83).

Using (5.79) and by denoting the  $n_{\text{spn}}$ -by-1 column vector with all ones by  $\underline{1}$ , the  $n_{\text{spn}}^2$ -by-1 objective vector  $\underline{f}_{\text{edo.pen.pl}}^*$  and the penalty function  $f_{\text{edo.pen.pl}}^*$  for the adjustment of the output energy of powerlink components can be defined as:

$$\underline{f}_{\text{edo.pen.pl}}^* = \left( \underline{1}^T \cdot \underline{A}_{\text{pen.pl.lp}} \right)^T \quad (5.84a)$$

$$f_{\text{edo.pen.pl}}^*(\underline{x}_{\text{lp}}) = \underline{f}_{\text{edo.pen.pl}}^{*T} \cdot \underline{x}_{\text{lp}} \quad (5.84b)$$

In the definition of the penalty function, the output state matrix ( $\underline{S}_{\text{out}}^*$ ) is not considered. With the conditions defined in (5.83), also the equality between (5.70) and (5.84b) is established. By solving the energy distribution optimization problem as defined in (5.41), the value of  $\underline{E}_{\text{out}}$  maximizing the objective function is found. This is equal to the minimization of the negative objective function with the *linprog* solver. By combining the objective vector for the minimization of the energy losses in (5.82a) with the penalty function for the energy transport via powerlink outputs in (5.84a), the objective vector  $\underline{f}_{\text{obj.lp}}^{\text{v1}}$  for the *fmincon* solver can be written as:

$$\underline{f}_{\text{obj.lp}}^{\text{v1}} = \left[ \underline{1}^T \cdot \left( \underline{A}_{\text{espn.lp}} + \underline{A}_{\text{pen.pl.lp}} \right) \right]^T \quad (5.85)$$

The first constraint in the optimization problem defined in (5.41) requires a positive energy vector. This can be achieved by applying the conditions defined in (5.83) and by defining the linear inequality constraints matrix  $\underline{A}_{\text{ineq.lp}}$  and vector  $\underline{b}_{\text{ineq.lp}}$  as:

$$\underline{A}_{\text{ineq.lp}}^{\text{v1}} = \underline{A}_{\text{espn.lp}} \quad (5.86a)$$

$$\underline{b}_{\text{ineq.lp}}^{\text{v1}} = \underline{0} \quad (5.86b)$$

The conditions in (5.83) can be fulfilled by using the linear equality constraints defined in (5.54) with the matrix  $\underline{A}_{\text{eq.lp}}$  and vector  $\underline{b}_{\text{eq.lp}}^{\text{v1}}$ . The  $n_{\text{spn}}^2$ -by- $n_{\text{spn}}^2$  matrix  $\underline{A}_{\text{eq.lp}}$  consisting of  $n_{\text{spn}}^2$  submatrices  $\underline{A}_{\text{eq.lp}\{i,k\}}$  with  $i, k \in \{1..n_{\text{spn}}\}$  is defined as:

$$\underline{A}_{\text{eq.lp}} = \begin{pmatrix} \underline{A}_{\text{eq.lp}\{1,1\}} & \cdots & \underline{A}_{\text{eq.lp}\{1,n_{\text{spn}}\}} \\ \vdots & \ddots & \vdots \\ \underline{A}_{\text{eq.lp}\{n_{\text{spn}},1\}} & \cdots & \underline{A}_{\text{eq.lp}\{n_{\text{spn}},n_{\text{spn}}\}} \end{pmatrix} \quad (5.87)$$



The  $n_{\text{spn}}$ -by- $n_{\text{spn}}$  submatrix  $\underline{A}_{\text{eq.lp}\{i,k\}}$  can be calculated using the  $n_{\text{spn}}$ -by- $n_{\text{spn}}$  identity matrix  $\underline{I}$  and energy output state matrix  $\underline{S}_{\text{out}}^*$  as:

$$\underline{A}_{\text{eq.lp}\{i,k\}} = \begin{cases} \underline{0}, & i \neq k \\ \underline{I} - \text{diag}(\underline{S}_{\text{out}}^{*(i)}), & i = k \end{cases} \quad \text{with } i, k \in \{1..n_{\text{spn}}\} \quad (5.88)$$

The  $n_{\text{spn}}^2$ -by-1 vector  $\underline{b}_{\text{eq.lp}}^{\text{v1}}$  consisting of  $n_{\text{spn}}$  subvectors  $\underline{b}_{\text{eq.lp}\{i\}}^{\text{v1}}$  with  $i \in \{1..n_{\text{spn}}\}$  can be defined as:

$$\underline{b}_{\text{eq.lp}}^{\text{v1}} = \left( \underline{b}_{\text{eq.lp}\{1\}}^{\text{v1}} \quad \dots \quad \underline{b}_{\text{eq.lp}\{n_{\text{spn}}\}}^{\text{v1}} \right)^{\text{T}} \quad (5.89)$$

The  $n_{\text{spn}}$ -by-1 subvector  $\underline{b}_{\text{eq.lp}\{i\}}^{\text{v1}}$  can be calculated using the  $n_{\text{spn}}$ -by- $n_{\text{spn}}$  identity matrix  $\underline{I}$ ,  $n_{\text{spn}}$ -by-1 subpowernet state vector  $\underline{S}_{\text{spn}}$ , remaining discharge energy vector  $\underline{E}_{\text{rde}}$  and energy demand vector  $\underline{E}_{\text{load}}^*$  as:

$$\underline{b}_{\text{eq.lp}\{i\}}^{\text{v1}} = \underline{S}_{\text{spn}} \circ \underline{I}^{(i)} \circ (\underline{E}_{\text{load}}^* - \underline{E}_{\text{rde}}) \quad \text{with } i \in \{1..n_{\text{spn}}\} \quad (5.90)$$

The second constraint of the optimization problem in (5.41) restricting the output energy for powerlink components can be defined for the *linprog* solver by specifying the vectors for lower ( $\underline{lb}_{\text{lp}}$ ) and upper ( $\underline{ub}_{\text{lp}}$ ) bounds. The  $n_{\text{spn}}^2$ -by-1 vector  $\underline{b}_{\text{ub.lp}}$  consisting of  $n_{\text{spn}}$  subvectors  $\underline{b}_{\text{ub.lp}\{i\}}$  with  $i \in \{1..n_{\text{spn}}\}$  can be defined as:

$$\underline{b}_{\text{ub.lp}} = \left( \underline{b}_{\text{ub.lp}\{1\}} \quad \dots \quad \underline{b}_{\text{ub.lp}\{n_{\text{spn}}\}} \right)^{\text{T}} \quad (5.91)$$

Using the output energy limit matrix  $\underline{E}_{\text{out.max}}^*$  defined in (5.56), the  $n_{\text{spn}}$ -by-1 subvector  $\underline{b}_{\text{ub.lp}\{i\}}$  can be calculated as:

$$\underline{b}_{\text{ub.lp}\{i\}} = \underline{E}_{\text{out.max}}^{*(i)} \quad \text{with } i \in \{1..n_{\text{spn}}\} \quad (5.92)$$

The  $n_{\text{spn}}^2$ -by-1 lower and upper bounds vectors can be then defined as:

$$\begin{aligned} \underline{lb}_{\text{lp}}^{\text{v1}} &= \underline{0} \\ \underline{ub}_{\text{lp}}^{\text{v1}} &= \underline{b}_{\text{ub.lp}} + \underline{b}_{\text{eq.lp}}^{\text{v1}} \end{aligned} \quad (5.93)$$

In the next two subsections, the transformation of an extended version of the energy distribution optimization problem supporting additionally an optimal multiple battery discharge strategy to the form required by *fmincon* and *linprog* solver is presented.

### 5.3.3. Energy Distribution (Version 2) with Nonlinear Programming

An extended version of a continuous energy distribution problem used for the control of fail-operational powernets with up to  $n_{\text{spn}}$  channels with an optimal multiple battery discharge strategy was defined in (5.48). By solving this optimization problem, an optimal energy output matrix  $\underline{E}_{\text{out}}$  with regard to the minimization of energy losses in powerlink and energy storage components and additional user defined criteria is found. The relationship between the solution  $\underline{x}_{\text{nlp}}$  of the *fmincon* solver and the optimal energy output matrix  $\underline{E}_{\text{out}}$  is equal to the definition in (5.67). For the estimation of the  $n_{\text{spn}}$ -by-1 vector  $\underline{E}_{\text{spn.opt}}^*$  storing the energy balance values for each subpowernet  $k \in \{1..n_{\text{spn}}\}$  as defined in (5.42), the following matrix notation is used:

$$\begin{aligned} \underline{E}_{\text{spn.opt}}^*(\underline{E}_{\text{out}}) = & \underline{S}_{\text{spn}} \circ \left[ \left( \underline{S}_{\text{pl}}^{*\text{T}} \circ \underline{\eta}_{\text{pl}}^{\text{T}} \circ \underline{E}_{\text{out}}^{\text{T}} - \underline{S}_{\text{pl}}^* \circ \underline{E}_{\text{out}} \right) \cdot \underline{S}_{\text{spn}} \circ \left( \underline{1} + \underline{dp}_{\text{bat}} \right) \right. \\ & \left. + \underline{E}_{\text{rde0}} - \left( \underline{1} + \underline{dp}_{\text{bat}} \right) \circ \underline{E}_{\text{load}} \right] \end{aligned} \quad (5.94)$$

The objective  $f_{\text{edo.loss.opt}}^*$  as defined in (5.45) and used for the minimization of the energy losses in both, powerlink components connecting the subpowernets and powernet batteries can be rewritten in matrix notation as:

$$\begin{aligned} f_{\text{edo.loss.opt}}^*(\underline{E}_{\text{out}}) = & \underline{S}_{\text{spn}}^{\text{T}} \cdot \left[ \left( \underline{S}_{\text{pl}}^{*\text{T}} \circ \underline{\eta}_{\text{pl}}^{\text{T}} \circ \underline{E}_{\text{out}}^{\text{T}} - \underline{S}_{\text{pl}}^* \circ \underline{E}_{\text{out}} \right) \cdot \underline{S}_{\text{spn}} \circ \left( \underline{1} + \underline{dp}_{\text{bat}} \right) \right. \\ & \left. + \underline{E}_{\text{rde0}} - \left( \underline{1} + \underline{dp}_{\text{bat}} \right) \circ \underline{E}_{\text{load}} \right] \end{aligned} \quad (5.95)$$

The  $n_{\text{spn}}$ -by-1 vector  $\underline{E}_{\text{bat}}^*$  containing the battery output energy for each subpowernet  $k$  as defined in (5.43) and the  $n_{\text{spn}}$ -by-1 vector  $\underline{P}_{\text{bat}}$  containing the corresponding average discharge power as defined in (5.44) can be rewritten in matrix notation as:

$$\underline{E}_{\text{bat}}^*(\underline{E}_{\text{out}}) = \left( \underline{S}_{\text{pl}}^* \circ \underline{E}_{\text{out}} - \underline{S}_{\text{pl}}^{*\text{T}} \circ \underline{\eta}_{\text{pl}}^{\text{T}} \circ \underline{E}_{\text{out}}^{\text{T}} \right) \cdot \underline{S}_{\text{spn}} + \underline{E}_{\text{load}}^* \quad (5.96a)$$

$$\underline{P}_{\text{bat}}^*(\underline{E}_{\text{out}}) = \frac{\underline{E}_{\text{bat}}^*(\underline{E}_{\text{out}})}{dT_{\text{ssl}}^*} \quad (5.96b)$$

The penalty function  $f_{\text{edo.pen.bat}}^*$  as defined in (5.46) and used for the adjustment of the discharge power of the batteries with appropriate penalty vector  $\underline{\beta}_{\text{bat}}$  can be rewritten in matrix notation as:

$$f_{\text{edo.pen.bat}}^*(\underline{E}_{\text{out}}) = \underline{S}_{\text{spn}}^{\text{T}} \circ \underline{\beta}_{\text{bat}}^{\text{T}} \cdot \left[ \left( \underline{S}_{\text{pl}}^* \circ \underline{E}_{\text{out}} - \underline{S}_{\text{pl}}^{*\text{T}} \circ \underline{\eta}_{\text{pl}}^{\text{T}} \circ \underline{E}_{\text{out}}^{\text{T}} \right) \cdot \underline{S}_{\text{spn}} + \underline{E}_{\text{load}}^* \right] \quad (5.97)$$

By solving the energy distribution optimization problem as defined in (5.48), the value of  $\underline{E}_{\text{out}}$  maximizing the objective function is obtained. This is equal to the minimization of

the negative objective function with the *fmincon* solver. By combining the objective for the minimization of the energy losses in (5.95) with the penalty function for the energy transport via powerlink outputs in (5.70) and for the batteries discharge in (5.97), the objective function  $f_{\text{obj.nlp}}^{v2}$  for the *fmincon* solver, which is negative to  $f_{\text{edo.path.opt}}^*$  defined in (5.47), can be written in matrix notation as:

$$f_{\text{obj.nlp}}^{v2}(\underline{x}_{\text{nlp}}) = \underline{S}_{\text{spn}}^T \cdot \left[ \left( \underline{S}_{\text{pl}}^* \circ \underline{x}_{\text{nlp}} - \underline{S}_{\text{pl}}^{*\text{T}} \circ \underline{\eta}_{\text{pl}}^T \circ \underline{x}_{\text{nlp}}^T \right) \cdot \underline{S}_{\text{spn}} \circ \left( \underline{1} + \underline{dp}_{\text{bat}} + \underline{\beta}_{\text{bat}} \right) \right. \\ \left. + \left( \underline{\beta}_{\text{pl}} \circ \underline{S}_{\text{pl}}^* \circ \underline{x}_{\text{nlp}} \right) \cdot \underline{S}_{\text{spn}} - \underline{E}_{\text{rde0}} + \left( \underline{1} + \underline{dp}_{\text{bat}} + \underline{\beta}_{\text{bat}} \right) \circ \underline{E}_{\text{load}}^* \right] \quad (5.98)$$

Three inequality constraints as well as lower and upper bounds for the optimization variable  $\underline{E}_{\text{out}}$  are defined in (5.48). The inequality constraints requiring positive energy balance and limiting the average battery discharge power can be rewritten as:

$$\begin{aligned} -\underline{E}_{\text{spn.opt}}^*(\underline{x}_{\text{nlp}}) &\leq \underline{0} \\ \underline{P}_{\text{bat}}^*(\underline{x}_{\text{nlp}}) - \underline{P}_{\text{bat.max}} &\leq \underline{0} \\ -\underline{P}_{\text{bat}}^*(\underline{x}_{\text{nlp}}) &\leq \underline{0} \end{aligned} \quad (5.99)$$

By introducing the  $3n_{\text{spn}}$ -by- $n_{\text{spn}}$  matrix  $\underline{C}_{\text{nlc2}}$  and  $3n_{\text{spn}}$ -by-1 vector  $\underline{B}_{\text{nlc2}}$ , the **nonlinear constraint** (nlc) function  $\underline{c}_{\text{ineq.nlp}}^{v2}$  can be defined as:

$$\underline{c}_{\text{ineq.nlp}}^{v2}(\underline{x}_{\text{nlp}}) = \underline{C}_{\text{nlc2}} \cdot \left[ \left( \underline{S}_{\text{pl}}^* \circ \underline{x}_{\text{nlp}} - \underline{S}_{\text{pl}}^{*\text{T}} \circ \underline{\eta}_{\text{pl}}^T \circ \underline{x}_{\text{nlp}}^T \right) \cdot \underline{S}_{\text{spn}} + \underline{E}_{\text{load}}^* \right] - \underline{B}_{\text{nlc2}} \quad (5.100)$$

The corresponding matrix  $\underline{C}_{\text{nlc2}}$  and vector  $\underline{B}_{\text{nlc2}}$  are defined as:

$$\underline{C}_{\text{nlc2}} = \begin{bmatrix} \underline{C}_{\text{nlc2}\{1\}} \\ \underline{C}_{\text{nlc2}\{2\}} \\ \underline{C}_{\text{nlc2}\{3\}} \end{bmatrix} = \begin{bmatrix} \text{diag} \left( \underline{S}_{\text{spn}} \circ \left[ \underline{1} + \underline{dp}_{\text{bat}} \right] \right) \\ \frac{1}{dT_{\text{ssl}}^*} \underline{I} \\ -\frac{1}{dT_{\text{ssl}}^*} \underline{I} \end{bmatrix} \quad (5.101a)$$

$$\underline{B}_{\text{nlc2}} = \begin{bmatrix} \underline{B}_{\text{nlc2}\{1\}} \\ \underline{B}_{\text{nlc2}\{2\}} \\ \underline{B}_{\text{nlc2}\{3\}} \end{bmatrix} = \begin{bmatrix} \underline{S}_{\text{spn}} \circ \underline{E}_{\text{rde0}} \\ \underline{P}_{\text{bat.max}} \\ \underline{0} \end{bmatrix} \quad (5.101b)$$

The  $n_{\text{spn}}$ -by- $n_{\text{spn}}$  identity matrix is denoted by  $\underline{I}$ , the  $n_{\text{spn}}$ -by- $n_{\text{spn}}$  submatrix of  $\underline{C}_{\text{nlc2}}$  by  $\underline{C}_{\text{nlc2}\{i\}}$  and  $n_{\text{spn}}$ -by-1 subvector of  $\underline{B}_{\text{nlc2}}$  by  $\underline{B}_{\text{nlc2}\{i\}}$  with  $i \in \{1..3\}$ . The definition of the equality constraint function  $\underline{c}_{\text{eq.nlp}}$ , lower and upper bounds  $\underline{lb}_{\text{nlp}}$  and  $\underline{ub}_{\text{nlp}}$  as well as of linear equality and inequality constraints  $\underline{A}_{\text{ineq.nlp}}/\underline{b}_{\text{ineq.nlp}}$  and  $\underline{A}_{\text{eq.nlp}}/\underline{b}_{\text{eq.nlp}}$  is equal to the definition in (5.73), (5.74) and (5.75). The formulation of the continuous energy distribution optimization problem as defined in (5.48) for the linear programming solver *linprog* with significant lower computational effort is presented in the next subsection.

### 5.3.4. Energy Distribution (Version 2) with Linear Programming

The relationship between the optimal energy output matrix  $\underline{E}_{\text{out}}$  and the *linprog* solver result  $\underline{x}_{\text{lp}}$  is the same as in (5.76). For the formulation of the  $n_{\text{spn}}^2$ -by-1 objective column vector  $f_{\text{obj.lp}}^{v2}$  according to the notation of the optimization problem in *linprog* format, in addition to the matrices  $\underline{A}_{\text{espn.lp}}$  and  $\underline{A}_{\text{pen.pl.lp}}$  defined in (5.77) and (5.79), a third  $n_{\text{spn}}$ -by- $n_{\text{spn}}^2$  matrix  $\underline{A}_{\text{bat.lp}}$ , consisting of  $n_{\text{spn}}$  submatrices  $\underline{A}_{\text{bat.lp}\{i\}}$  with  $i \in \{1..n_{\text{spn}}\}$  is introduced:

$$\underline{A}_{\text{bat.lp}} = \left( \underline{A}_{\text{bat.lp}\{1\}} \quad \underline{A}_{\text{bat.lp}\{2\}} \quad \dots \quad \underline{A}_{\text{bat.lp}\{n_{\text{spn}}\}} \right) \quad (5.102)$$

For the calculation of the submatrix  $\underline{A}_{\text{bat.lp}\{i\}}$ , the following  $n_{\text{spn}}$ -by-1 vectors  $\underline{c}_{\text{bat}}$  and  $\underline{d}_{\text{bat}}$  are required with the  $i$ -th element defined as:

$$\underline{c}_{\text{bat}\{i\}} = \frac{\underline{E}_{\text{rde0}\{i\}}}{1 + \underline{dp}_{\text{bat}\{i\}}} \quad \text{with } i \in \{1..n_{\text{spn}}\} \quad (5.103a)$$

$$\underline{d}_{\text{bat}\{i\}} = \frac{\underline{c}_{\text{bat}\{i\}}}{\underline{E}_{\text{load}\{i\}}^* - \underline{c}_{\text{bat}\{i\}}} \quad \text{with } i \in \{1..n_{\text{spn}}\} \quad (5.103b)$$

Using the remaining driving time  $dT_{\text{ssl}}^*$  and the vectors  $\underline{a}_{\text{rde}}$  and  $\underline{E}_{\text{rde0}}$  approximating the remaining discharge energy as a function of average battery output power, the submatrix  $\underline{A}_{\text{bat.lp}\{i\}}$  can be calculated as:

$$\underline{A}_{\text{bat.lp}\{i\}} = \underline{I}^{(i)} \cdot \left( \underline{I}^{(i)} \circ \underline{d}_{\text{bat}} \right)^{\text{T}} \quad \text{with } i \in \{1..n_{\text{spn}}\} \quad (5.104)$$

With (5.77), the energy balance vector  $\underline{E}_{\text{spn.opt.lp}}^*$  for *linprog* solver can be defined as:

$$\underline{E}_{\text{spn.opt.lp}}^*(\underline{x}_{\text{lp}}) = -\text{diag} \left( \underline{1} + \underline{dp}_{\text{bat}} \right) \cdot \underline{A}_{\text{espn.lp}} \cdot \underline{x}_{\text{lp}} \quad (5.105)$$

The  $n_{\text{spn}}^2$ -by-1 objective vector  $f_{\text{edo.loss.opt}}^*$  and function  $f_{\text{edo.loss.opt.lp}}^*$  for the minimization of the energy losses in powerlink and energy storage components can be defined as:

$$f_{\text{edo.loss.opt}}^* = - \left[ \left( \underline{1} + \underline{dp}_{\text{bat}} \right)^{\text{T}} \cdot \underline{A}_{\text{espn.lp}} \right]^{\text{T}} \quad (5.106a)$$

$$f_{\text{edo.loss.opt.lp}}^*(\underline{x}_{\text{lp}}) = f_{\text{edo.loss.opt}}^{*\text{T}} \cdot \underline{x}_{\text{lp}} \quad (5.106b)$$

The energy balance vector  $\underline{E}_{\text{spn.opt.lp}}^*$  and the objective for the minimization of energy losses  $f_{\text{edo.loss.opt.lp}}^*$  are not equal to the definition in (5.94) and (5.95), since the calculation of  $\underline{E}_{\text{spn.opt.lp}}^*$  does not consider the energy demand vector  $\underline{E}_{\text{load}}^*$ , the vectors  $\underline{dp}_{\text{bat}}$  and  $\underline{E}_{\text{rde0}}$  used for the approximation of the remaining discharge energy as a function of average bat-

tery output power, subpowernets state vector  $\underline{S}_{\text{spn}}$  and the energy flow activation matrix  $\underline{S}_{\text{pl}}^*$ . The equality between (5.94) and (5.105) as well as between (5.95) and (5.106b) can be achieved, when the following conditions are fulfilled:

$$\underline{x}_{\text{lp}\{i+n_{\text{spn}}(k-1)\}} = \begin{cases} \underline{E}_{\text{load}\{i\}}^* - \underline{c}_{\text{bat}\{i\}}, & i = k \wedge \underline{S}_{\text{spn}\{i\}} = 1 \\ \underline{E}_{\text{out}\{i,k\}}, & i \neq k \wedge \underline{S}_{\text{out}\{i,k\}}^* = 1 \\ 0, & \text{otherwise} \end{cases} \quad \text{with } i, k \in \{1..n_{\text{spn}}\} \quad (5.107)$$

The  $n_{\text{spn}}^2$ -by-1 objective vector  $\underline{f}_{\text{edo.pen.pl}}^*$  and the penalty function  $f_{\text{edo.pen.pl.lp}}$  for the adjustment of the powerlinks output energy is equal to (5.84a) and (5.84b). Using (5.77), (5.102) and  $n_{\text{spn}}$ -by-1 penalty vector  $\underline{\beta}_{\text{bat}}$ , the  $n_{\text{spn}}^2$ -by-1 objective vector  $\underline{f}_{\text{edo.pen.bat}}^*$  and penalty function  $f_{\text{edo.pen.bat.lp}}$  for the adjustment of batteries discharge can be defined as:

$$\underline{f}_{\text{edo.pen.bat}}^* = \left( \underline{\beta}_{\text{bat}}^T \cdot \left( \underline{A}_{\text{espn.lp}} + \underline{A}_{\text{bat.lp}} \right) \right)^T \quad (5.108a)$$

$$f_{\text{edo.pen.bat.lp}}^*(\underline{x}_{\text{lp}}) = \underline{f}_{\text{edo.pen.bat}}^* \cdot \underline{x}_{\text{lp}} \quad (5.108b)$$

The equality between the penalty function  $f_{\text{edo.pen.bat}}^*$  in (5.46) and  $f_{\text{edo.pen.bat.lp}}^*$  in (5.108b) is given if the conditions defined in (5.107) are fulfilled.

By combining the objective vector for the minimization of the energy losses in (5.106a) with the penalty function for the energy transport via powerlink outputs in (5.84a) and for batteries discharge in (5.108b), the objective vector  $\underline{f}_{\text{obj.lp}}^{v2}$  for the *fmincon* solver multiplied by  $\underline{x}_{\text{lp}}$ , which is negative to  $f_{\text{edo.path.opt}}^*$  defined in (5.47), can be written as:

$$\underline{f}_{\text{obj.lp}}^{v2} = \left[ \left( \underline{1} + \underline{dp}_{\text{bat}} + \underline{\beta}_{\text{bat}} \right)^T \cdot \underline{A}_{\text{espn.lp}} + \underline{1}^T \cdot \underline{A}_{\text{pen.pl.lp}} + \underline{\beta}_{\text{bat}}^T \cdot \underline{A}_{\text{bat.lp}} \right]^T \quad (5.109)$$

The first constraint of the optimization problem defined in (5.48) requires a positive energy vector. This is achieved by applying the conditions defined in (5.107) and by defining the linear inequality constraints submatrix  $\underline{A}_{\text{ineq.lp}\{1\}}^{v2}$  and subvector  $\underline{b}_{\text{ineq.lp}\{1\}}^{v2}$  as:

$$\underline{A}_{\text{ineq.lp}\{1\}}^{v2} = \text{diag} \left( \underline{1} + \underline{dp}_{\text{bat}} \right) \cdot \underline{A}_{\text{espn.lp}} \quad (5.110a)$$

$$\underline{b}_{\text{ineq.lp}\{1\}}^{v2} = \underline{0} \quad (5.110b)$$

The second constraint in the optimization problem defined in (5.48) limits the average battery output power to the range between zero (discharge case only) and maximum specified discharge power  $\underline{P}_{\text{bat.max}}$ . This can be achieved by applying the conditions defined in (5.107) and by defining the linear inequality constraints submatrices  $\underline{A}_{\text{ineq.lp}\{2..3\}}^{v2}$

and subvectors  $\underline{b}_{\text{ineq.lp}\{2..3\}}^{v2}$  as:

$$\underline{A}_{\text{ineq.lp}\{2\}}^{v2} = \frac{\underline{A}_{\text{espn.lp}}}{dT_{\text{ssl}}^*} \quad (5.111a)$$

$$\underline{A}_{\text{ineq.lp}\{3\}}^{v2} = -\frac{\underline{A}_{\text{espn.lp}}}{dT_{\text{ssl}}^*} \quad (5.111b)$$

$$\underline{b}_{\text{ineq.lp}\{2\}}^{v2} = \underline{P}_{\text{bat.max}} - \underline{S}_{\text{spn}} \circ \frac{\underline{c}_{\text{bat}}}{dT_{\text{ssl}}^*} \quad (5.111c)$$

$$\underline{b}_{\text{ineq.lp}\{3\}}^{v2} = \underline{S}_{\text{spn}} \circ \frac{\underline{c}_{\text{bat}}}{dT_{\text{ssl}}^*} \quad (5.111d)$$

The  $3n_{\text{spn}}$ -by- $n_{\text{spn}}^2$  linear inequality matrix  $\underline{A}_{\text{ineq.lp}}^{v2}$  and  $3n_{\text{spn}}$ -by-1 vector  $\underline{b}_{\text{ineq.lp}}^{v2}$  according to the format of *linprog* solver are then defined as:

$$\underline{A}_{\text{ineq.lp}}^{v2} = \left( \underline{A}_{\text{ineq.lp}\{1\}}^{v2} \quad \underline{A}_{\text{ineq.lp}\{2\}}^{v2} \quad \underline{A}_{\text{ineq.lp}\{3\}}^{v2} \right)^T \quad (5.112a)$$

$$\underline{b}_{\text{ineq.lp}}^{v2} = \left( \underline{b}_{\text{ineq.lp}\{1\}}^{v2} \quad \underline{b}_{\text{ineq.lp}\{2\}}^{v2} \quad \underline{b}_{\text{ineq.lp}\{3\}}^{v2} \right)^T \quad (5.112b)$$

The conditions in (5.107) can be fulfilled by using the linear equality constraints defined in (5.54) with the matrix  $\underline{A}_{\text{eq.lp}}$  and vector  $\underline{b}_{\text{eq.lp}}^{v2}$ . The  $n_{\text{spn}}^2$ -by- $n_{\text{spn}}^2$  matrix  $\underline{A}_{\text{eq.lp}}$  was already defined in (5.87). The  $n_{\text{spn}}^2$ -by-1 vector  $\underline{b}_{\text{eq.lp}}^{v2}$  consisting of  $n_{\text{spn}}$  subvectors  $\underline{b}_{\text{eq.lp}\{i\}}^{v2}$  with  $i \in \{1..n_{\text{spn}}\}$  can be defined as:

$$\underline{b}_{\text{eq.lp}}^{v2} = \left( \underline{b}_{\text{eq.lp}\{1\}}^{v2} \quad \cdots \quad \underline{b}_{\text{eq.lp}\{n_{\text{spn}}\}}^{v2} \right)^T \quad (5.113)$$

The  $n_{\text{spn}}$ -by-1 subvector  $\underline{b}_{\text{eq.lp}\{i\}}^{v2}$  can be calculated using the  $n_{\text{spn}}$ -by- $n_{\text{spn}}$  identity matrix  $\underline{I}$ ,  $n_{\text{spn}}$ -by-1 subpowernet state vector  $\underline{S}_{\text{spn}}$ , remaining discharge energy vector  $\underline{E}_{\text{rde}}$  and energy demand vector  $\underline{E}_{\text{load}}^*$  as:

$$\underline{b}_{\text{eq.lp}\{i\}}^{v2} = \underline{S}_{\text{spn}} \circ \underline{I}^{(i)} \circ (\underline{E}_{\text{load}}^* - \underline{c}_{\text{bat}}) \quad \text{with } i \in \{1..n_{\text{spn}}\} \quad (5.114)$$

The third constraint of the optimization problem defined in (5.48) is achieved by formulating the  $n_{\text{spn}}^2$ -by-1 lower and upper bound vectors using (5.92) as:

$$\begin{aligned} \underline{lb}_{\text{lp}}^{v2} &= \underline{0} \\ \underline{ub}_{\text{lp}}^{v2} &= \underline{b}_{\text{ub.lp}} + \underline{b}_{\text{eq.lp}}^{v2} \end{aligned} \quad (5.115)$$

For the variation of the integer parameters as presented in Section 5.2.3, an appropriate model of powerlink components in normal and failure case operation is required and is presented in the following section.

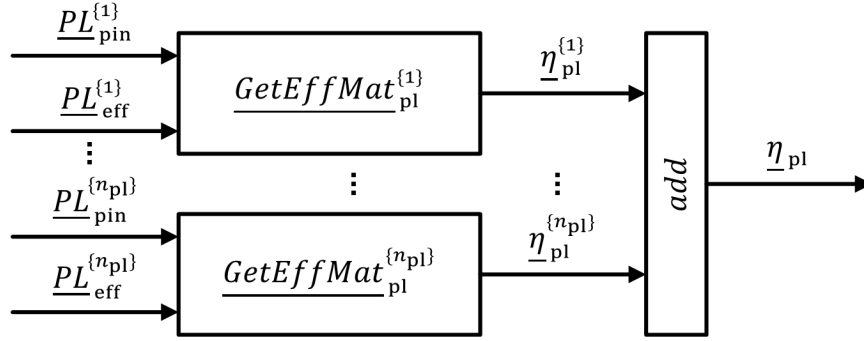


Figure 5.10.: Model of powernet efficiency matrix.

## 5.4. Modeling of Powerlink Components

The energy distribution within the vehicle powernet is dependent on the current state of powerlink components and their operating mode. By solving the mixed-integer energy distribution optimization problem as defined in (5.15) or (5.31), an optimal operating mode for each powerlink reducing the energy losses and establishing reliable power supply in all functional subpowernets is found.

For solving the mixed-integer optimization problem as described in Section 5.1, three inputs from powerlinks are required, namely the efficiency matrix  $\underline{\eta}_{pl}$  containing all current energy flow efficiencies, the set  $\underline{PL}_{mod}$  containing all valid powerlink operating mode combinations  $\underline{M}_{pl}$  as well as the energy flow activation matrix  $\underline{S}_{pl}^*$  containing the activation status for all energy flows within the vehicle powernet for a given operating mode combination  $\underline{M}_{pl}^*$ .

A behavioral model consisting of three functions, namely  $GetEffMat_{pl}^{\{i\}}$ ,  $GetModeVec_{pl}^{\{i\}}$  and  $GetTopMat_{pl}^{\{i\}}$  is proposed for abstracting the information of powerlink  $i$  required for the mixed-integer energy distribution optimization, which is presented in the next subsection.

### 5.4.1. Generic Behavioral Description of Powerlinks

A generic model of a vehicle powernet as presented in Section 5.1.1 consists of up to  $n_{spn}$  subpowernets which can be interconnected by up to  $n_{pl}$  powerlinks. Each subpowernet can receive energy from and also supply up to  $n_{spn} - 1$  subpowernets. Therefore, in total  $n_{spn} \times (n_{spn} - 1)$  energy flows are possible. As defined in (5.57), an  $n_{spn}$ -by- $n_{spn}$  matrix with diagonal elements equal to zero is used for storing the energy flow efficiencies.

For creation of the efficiency matrix  $\underline{\eta}_{pl}$ , a stepwise algorithm as depicted in Fig. 5.10 is proposed. For each powerlink  $i$  ( $i \in \{1..n_{pl}\}$ ), an efficiency matrix  $\underline{\eta}_{pl}^{\{i\}}$  is created using

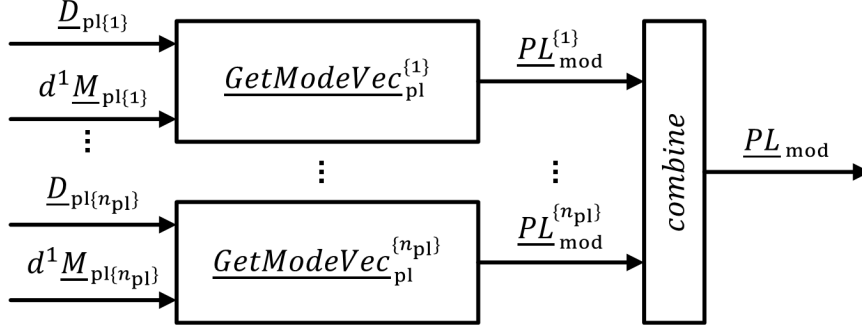


Figure 5.11.: Model of valid powerlink operating mode combinations.

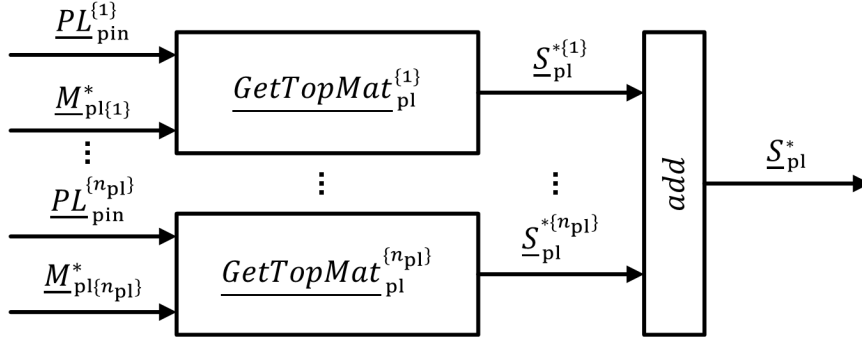


Figure 5.12.: Model of energy flow activation matrix.

the function  $\underline{GetEffMat}_{pl}^{\{i\}}$ . The vector  $\underline{PL}_{pin}^{\{i\}}$  contains the connections of the powerlink  $i$ , describing which pin is connected to which subpowernet. The vector  $\underline{PL}_{eff}^{\{i\}}$  contains the current energy flow efficiencies of all connections of the powerlink  $i$ . By calling the function  $\underline{EffGetMat}_{pl}^{\{i\}}$ , the efficiencies of powerlink  $i$  are written to the corresponding elements of the matrix  $\underline{\eta}_{pl}^{\{i\}}$ , which are basically defined by the vector  $\underline{PL}_{pin}^{\{i\}}$ . After creating the efficiency matrix for each powerlink  $i$ , the total efficiency matrix  $\underline{\eta}_{pl}$  is created by adding the  $n_{pl}$  matrices for each powerlink, with the assumption, that the energy flow  $E_{out}^{\{k,i\}}$  from subpowernet  $k$  to  $i$  (with  $i, k \in \{1..n_{spn}\}$  and  $i \neq k$ ) is only possible via one powerlink.

For creation of the set  $\underline{PL}_{mod}$  containing all valid powerlink operating mode vectors  $\underline{M}_{pl}$ , also a stepwise algorithm as depicted in Fig. 5.11 is proposed. For each powerlink  $i$  ( $i \in \{1..n_{pl}\}$ ), a vector  $\underline{PL}_{mod}^{\{i\}}$  containing all currently possible operating modes for powerlink  $i$  is created by calling the function  $\underline{GetModeVec}_{pl}^{\{i\}}$ . The  $i$ -th element  $\underline{D}_{pl\{i\}}$  of the  $n_{pl}$ -by-1 vector  $\underline{D}_{pl}$  stores the current diagnostic information for the powerlink  $i$ . In the following, the operator  $d^1 a$  is used to describe a value of  $a$  delayed by one sample period ( $d^1 a[n] = a[n - 1]$ ). The  $i$ -th element  $d^1 \underline{M}_{pl\{i\}}$  of the  $n_{pl}$ -by-1 vector  $d^1 \underline{M}_{pl}$  stores the current operating mode (set in the previous optimization cycle) for the powerlink  $i$ , which is required if the current operating mode cannot be changed due to a powerlink failure. The function  $\underline{GetModeVec}_{pl}^{\{i\}}$  evaluates the input data and creates an  $n_{mod}^{\{i\}}$ -by-1 operating



mode vector  $\underline{PL}_{\text{mod}}^{\{i\}}$  for the powerlink  $i$ . After creating operating mode vectors for each powerlink, all possible combinations of  $\underline{M}_{\text{pl}}$  vectors are stored in the  $n_{\text{pl}}$ -by- $n_{\text{mod}}$  matrix  $\underline{PL}_{\text{mod}}$  with  $n_{\text{mod}}$  equal to the definition in (5.49).

The energy flow activation matrix  $\underline{S}_{\text{pl}}^*$  as defined in (5.60) is a function of operating mode vector  $\underline{M}_{\text{pl}}^*$ . For a given operating mode vector  $\underline{M}_{\text{pl}}^*$ , the corresponding  $n_{\text{spn}}$ -by- $n_{\text{spn}}$  energy flow activation matrix  $\underline{S}_{\text{pl}}^*$  can be created stepwise as depicted in Fig. 5.12. By calling the function  $\underline{GetTopMat}_{\text{pl}}^{\{i\}}$ ,  $\underline{S}_{\text{pl}}^{\{i\}}$  matrix for the powerlink  $i$  is created for the requested operating mode  $\underline{M}_{\text{pl}\{i\}}^*$ . For this, the corresponding matrix elements, defined by the pin connection vector  $\underline{PL}_{\text{pin}}^{\{i\}}$  and modeling the active connections in the requested operating mode, are set to 1 and all other elements to 0. After creating the energy flow activation matrix for each powerlink  $i$ , the total energy flow activation matrix  $\underline{S}_{\text{pl}}^*$  can be created by adding the  $n_{\text{pl}}$  energy flow activation matrices for each powerlink, with the assumption, that the energy flow  $E_{\text{out}}^{\{k,i\}}$  from subpowernet  $k$  to  $i$  (with  $i, k \in \{1..n_{\text{spn}}\}$  and  $i \neq k$ ) is only possible via one powerlink. The proposed behavioral model will be exemplified for three types of powerlinks, namely bidirectional DC/DC converter, toggle power switch and single power switch in the next subsection.

### 5.4.2. Examples for Behavioral Powerlink Model

A behavioral block diagram of a bidirectional DC/DC converter, toggle power switch and single power switch is depicted in Fig. 5.13. In the following, the creation of the efficiency matrix, operating mode vector and energy flow activation matrix for these powerlinks using the behavioral model functions as presented in Section 5.4.1 will be exemplified.

#### Bidirectional DC/DC Converter

A bidirectional DC/DC converter connects two subpowernets  $i$  and  $j$ . It can be operated in three modes. In the forward operating mode (frw), the energy is transported from subpowernet  $i$  to  $j$  with the corresponding energy flow efficiency  $\eta_{\text{frw}}$ . In the reverse operating mode (rev), the energy is transported in the reverse direction with the efficiency  $\eta_{\text{rev}}$ . In the off mode (off), no energy flow is active between subpowernets  $i$  and  $j$ . The pin connection vector  $\underline{PL}_{\text{pin}}^{\{\text{dcdc}\}}$  contains two entries with the corresponding number of the subpowernet connected to pin0 and pin1 of the DC/DC converter:

$$\underline{PL}_{\text{pin}}^{\{\text{dcdc}\}} = [i \quad j]^T \quad (5.116)$$

By denoting the current required operating mode with  $M_{\text{pl}}^{\{\text{dcdc}\}}$ , the element  $\underline{S}_{\text{pl}\{i,k\}}^{\{\text{dcdc}\}}$  in the  $i$ -th row and  $k$ -th column of the energy flow activation matrix  $\underline{S}_{\text{pl}}^{\{\text{dcdc}\}}$  with  $i, k \in \{1..n_{\text{spn}}\}$

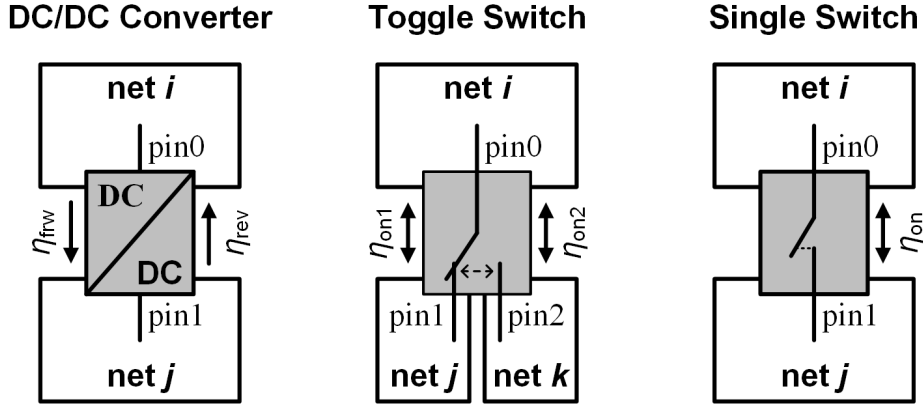


Figure 5.13.: Behavioral block diagram of DC/DC converter, toggle and single switch.

is defined as:

$$S_{pl\{i,k\}}^{*\{dcdc\}} = \begin{cases} 1, & \text{if } i = \underline{PL}_{pin\{1\}}^{\{dcdc\}} \wedge k = \underline{PL}_{pin\{2\}}^{\{dcdc\}} \wedge M_{pl}^{\{dcdc\}} = \text{frw} \\ 1, & \text{if } k = \underline{PL}_{pin\{1\}}^{\{dcdc\}} \wedge i = \underline{PL}_{pin\{2\}}^{\{dcdc\}} \wedge M_{pl}^{\{dcdc\}} = \text{rev} \\ 0, & \text{otherwise} \end{cases} \quad (5.117)$$

The corresponding element  $\eta_{pl\{i,k\}}^{\{dcdc\}}$  in the  $i$ -th row and  $k$ -th column of the efficiency matrix  $\underline{\eta}_{pl}^{\{dcdc\}}$  with  $i, k \in \{1..n_{spn}\}$  is defined as:

$$\eta_{pl\{i,k\}}^{\{dcdc\}} = \begin{cases} \eta_{frw}, & \text{if } i = \underline{PL}_{pin\{1\}}^{\{dcdc\}} \wedge k = \underline{PL}_{pin\{2\}}^{\{dcdc\}} \\ \eta_{rev}, & \text{if } k = \underline{PL}_{pin\{1\}}^{\{dcdc\}} \wedge i = \underline{PL}_{pin\{2\}}^{\{dcdc\}} \\ 0, & \text{otherwise} \end{cases} \quad (5.118)$$

For the evaluation of possible operating modes of a DC/DC converter, three discrete failure states are assumed, which are modeled by the diagnostic state variable  $D_{pl}^{\{dcdc\}}$ . The first state models a fault-free operation of the DC/DC converter ( $D_{pl}^{\{dcdc\}} = \text{no\_fail}$ ). The second state models faults resulting in the loss of the DC/DC converter operating mode control, meaning that the currently set operating mode cannot be changed ( $D_{pl}^{\{dcdc\}} = \text{no\_chng}$ ). The third failure state models faults resulting in no energy transport between pin0 and pin1 in both, forward and reverse direction ( $D_{pl}^{\{dcdc\}} = \text{open}$ ). By denoting the currently set DC/DC operating mode with  $d^1 M_{pl}^{\{dcdc\}}$ , the operating mode vector  $\underline{PL}_{mod}^{\{dcdc\}}$  can be defined as a function of the diagnostic state variable  $D_{pl}^{\{dcdc\}}$ :

$$\underline{PL}_{mod}^{\{dcdc\}} = \begin{cases} \begin{bmatrix} \text{frw} & \text{rev} & \text{off} \end{bmatrix}^T, & \text{if } D_{pl}^{\{dcdc\}} = \text{no\_fail} \\ \begin{bmatrix} d^1 M_{pl}^{\{dcdc\}} \end{bmatrix}^T, & \text{if } D_{pl}^{\{dcdc\}} = \text{no\_chng} \\ \begin{bmatrix} \text{off} \end{bmatrix}^T, & \text{if } D_{pl}^{\{dcdc\}} = \text{open} \end{cases} \quad (5.119)$$

Five failure modes were assumed for powerlink components in Section 5.1.2. Two of them, namely *loss of operating mode control* and *no energy transport* are covered by (5.119). The failure mode *decreased energy flow efficiency* is already considered by the time-dependent energy flow efficiency matrix  $\underline{\eta}_{\text{pl}}^{\{\text{dcdc}\}}$ , which is permanently updated according to the DC/DC diagnostic data. The failure mode *short circuit to ground* at DC/DC input or output (external short circuit to ground) is covered by the time-dependent state variable  $S_{\text{spn}}^{\{k\}}$  modeling the operational state of subpowernet  $k$ , which is set to 0 in case of a short circuit to ground in subpowernet  $k$ . In case of an internal short circuit to ground in the DC/DC converter, it is assumed that the input and output pins are disconnected automatically and no further energy flow is possible (fail safe behavior). This corresponds to the state *no energy transport* ( $D_{\text{pl}}^{\{\text{dcdc}\}} = \text{open}$ ) and is covered by (5.119). Due to possible different voltage levels at DC/DC input and output (e.g. high voltage at input and low voltage at output), the failure mode *short circuit between the DC/DC input and output* must be avoided by design and is not further considered for behavioral model of a DC/DC converter. Using the equations of this subsection, the behavioral model of a DC/DC converter according to the generic description in Section 5.4.1 can be implemented.

### Toggle Power Switch

A toggle power switch connects three subpowernets  $i$ ,  $j$  and  $k$ . It can be operated in four modes. In the first operating mode (on01), the subpowernets  $i$  and  $j$  are connected and the energy transport between these subpowernets is activated with the corresponding energy flow efficiency  $\eta_{\text{on1}}$ . In the second operating mode (on02), the subpowernets  $i$  and  $k$  are connected and the energy transport between these subpowernets is activated with the corresponding energy flow efficiency ( $\eta_{\text{on2}}$ ). The third operating mode (on12), connecting subpowernet  $i$  to  $j$  and to  $k$ , enabling so the energy exchange between all three subpowernets, can be either set if a **P**ulse **W**idth **M**odulation (PWM) operation of the toggle switch is possible or if a short circuit failure between pin1 and pin2 is present. The fourth operating mode (off) models a failure state of the toggle switch in case of an open circuit at pin0, meaning that no energy exchange between the subpowernets is possible. The pin connection vector  $\underline{PL}_{\text{pin}}^{\{\text{tgl}\}}$  contains three entries with the corresponding number of the subpowernet connected to pin0, pin1 and pin2 of the toggle power switch:

$$\underline{PL}_{\text{pin}}^{\{\text{tgl}\}} = [i \quad j \quad k]^T \quad (5.120)$$

By denoting the current required operating mode of the toggle switch with  $M_{\text{pl}}^{\{\text{tgl}\}}$ , the element  $\underline{S}_{\text{pl}\{i,k\}}^{*\{\text{tgl}\}}$  in the  $i$ -th row and  $k$ -th column of the energy flow activation matrix  $\underline{S}_{\text{pl}}^{*\{\text{tgl}\}}$  with  $i, k \in \{1..n_{\text{spn}}\}$  can be defined as:

$$\underline{S}_{pl\{i,k\}}^{*\{tgl\}} = \begin{cases} 1, & \text{if } i = \underline{PL}_{pin\{1\}}^{\{tgl\}} \wedge k = \underline{PL}_{pin\{2\}}^{\{tgl\}} \wedge M_{pl}^{\{tgl\}} = (\text{on01} \vee \text{on12}) \\ 1, & \text{if } k = \underline{PL}_{pin\{1\}}^{\{tgl\}} \wedge i = \underline{PL}_{pin\{2\}}^{\{tgl\}} \wedge M_{pl}^{\{tgl\}} = (\text{on01} \vee \text{on12}) \\ 1, & \text{if } i = \underline{PL}_{pin\{1\}}^{\{tgl\}} \wedge k = \underline{PL}_{pin\{3\}}^{\{tgl\}} \wedge M_{pl}^{\{tgl\}} = (\text{on02} \vee \text{on12}) \\ 1, & \text{if } k = \underline{PL}_{pin\{1\}}^{\{tgl\}} \wedge i = \underline{PL}_{pin\{3\}}^{\{tgl\}} \wedge M_{pl}^{\{tgl\}} = (\text{on02} \vee \text{on12}) \\ 0, & \text{otherwise} \end{cases} \quad (5.121)$$

The corresponding element  $\eta_{pl\{i,k\}}^{\{tgl\}}$  in the  $i$ -th row and  $k$ -th column of the efficiency matrix  $\underline{\eta}_{pl}^{\{tgl\}}$  with  $i, k \in \{1..n_{spn}\}$  is defined as:

$$\underline{\eta}_{pl\{i,k\}}^{\{tgl\}} = \begin{cases} \eta_{on1}, & \text{if } i = \underline{PL}_{pin\{1\}}^{\{tgl\}} \wedge k = \underline{PL}_{pin\{2\}}^{\{tgl\}} \\ \eta_{on1}, & \text{if } k = \underline{PL}_{pin\{1\}}^{\{tgl\}} \wedge i = \underline{PL}_{pin\{2\}}^{\{tgl\}} \\ \eta_{on2}, & \text{if } i = \underline{PL}_{pin\{1\}}^{\{tgl\}} \wedge k = \underline{PL}_{pin\{3\}}^{\{tgl\}} \\ \eta_{on2}, & \text{if } k = \underline{PL}_{pin\{1\}}^{\{tgl\}} \wedge i = \underline{PL}_{pin\{3\}}^{\{tgl\}} \\ 0, & \text{otherwise} \end{cases} \quad (5.122)$$

For the evaluation of possible operating modes of a toggle power switch, eight discrete failure states are assumed, which are modeled by the diagnostic state variable  $D_{pl}^{\{tgl\}}$ . The first state models a fault-free operation ( $D_{pl}^{\{tgl\}} = \text{no\_fail}$ ). The second state models faults resulting in the loss of toggle switch operating mode control, meaning that the currently set operating mode cannot be changed ( $D_{pl}^{\{tgl\}} = \text{no\_chng}$ ). The third, fourth and fifth failure states model faults resulting in a short circuit connection between pin0 and pin1 ( $D_{pl}^{\{tgl\}} = \text{sc01}$ ), between pin0 and pin2 ( $D_{pl}^{\{tgl\}} = \text{sc02}$ ) and between pin1 and pin2 ( $D_{pl}^{\{tgl\}} = \text{sc12}$ ). The sixth, seventh and eighth failure states model faults resulting in the open connection at pin0 ( $D_{pl}^{\{tgl\}} = \text{open0}$ ), at pin1 ( $D_{pl}^{\{tgl\}} = \text{open1}$ ) and at pin2 ( $D_{pl}^{\{tgl\}} = \text{open2}$ ). By denoting the currently set operating mode with  $d^1 M_{pl}^{\{tgl\}}$ , the operating mode vector  $\underline{PL}_{mod}^{\{tgl\}}$  can be defined as a function of the diagnostic state variable  $D_{pl}^{\{tgl\}}$ :

$$\underline{PL}_{mod}^{\{tgl\}} = \begin{cases} [\text{on01} \ \text{on02} \ \text{on12}]^T, & \text{if } D_{pl}^{\{tgl\}} = \text{no\_fail} \\ [d^1 M_{pl}^{\{tgl\}}]^T, & \text{if } D_{pl}^{\{tgl\}} = \text{no\_chng} \\ [\text{on01} \ (\text{on12})]^T, & \text{if } D_{pl}^{\{tgl\}} = \text{sc01} \\ [\text{on02} \ (\text{on12})]^T, & \text{if } D_{pl}^{\{tgl\}} = \text{sc02} \\ [\text{on12}]^T, & \text{if } D_{pl}^{\{tgl\}} = \text{sc12} \\ [\text{off}]^T, & \text{if } D_{pl}^{\{tgl\}} = \text{open0} \\ [\text{off} \ \text{on02}]^T, & \text{if } D_{pl}^{\{tgl\}} = \text{open1} \\ [\text{off} \ \text{on01}]^T, & \text{if } D_{pl}^{\{tgl\}} = \text{open2} \end{cases} \quad (5.123)$$

Five failure modes were assumed for powerlink components in Section 5.1.2. Three of

them, namely *loss of operating mode control*, *no energy transport* and *short circuit between the toggle input and outputs* are covered by (5.123). The operating mode on12 is not possible for the cases sc01 and sc02 if the short circuit connection between the pins is due to a stuck contact (indicated by brackets in (5.123)). Assuming a short circuit connection due to an external wiring problem, the operating mode on12 is theoretically possible for these cases. The failure mode *decreased energy flow efficiency* is already considered by the time-dependent energy flow efficiency matrix  $\underline{\eta}_{\text{pl}}^{\{\text{tgl}\}}$ , which is permanently updated according to the toggle switch diagnostic data. The failure mode *short circuit to ground* at toggle switch input or outputs (external short circuit to ground) is covered by the time-dependent state variable  $S_{\text{spn}}^{\{k\}}$  modeling the operational state of subpowernet  $k$ , which is set to 0 in case of a short circuit to ground in subpowernet  $k$ . Using the equations presented in this subsection the behavioral model of the toggle power switch according to the generic description in Section 5.4.1 can be implemented.

### Single Power Switch

A single power switch connects two subpowernets  $i$  and  $j$ . It can be operated in two modes. In the first operating mode (on), the subpowernets  $i$  and  $j$  are connected and the energy transport between these subpowernets is activated with the corresponding energy flow efficiency  $\eta_{\text{on}}$ . In the second operating mode (off), the subpowernets  $i$  and  $k$  are disconnected. The pin connection vector  $\underline{PL}_{\text{pin}}^{\{\text{sw}\}}$  contains two entries with the corresponding number of the subpowernet connected to pin0 and pin1 of the power switch:

$$\underline{PL}_{\text{pin}}^{\{\text{sw}\}} = [i \quad j]^T \quad (5.124)$$

By denoting the required operating mode of the switch with  $M_{\text{pl}}^{\{\text{sw}\}}$ , the element  $\underline{S}_{\text{pl}\{i,k\}}^{*\{\text{sw}\}}$  in the  $i$ -th row and  $k$ -th column of the energy flow activation matrix  $\underline{S}_{\text{pl}}^{*\{\text{sw}\}}$  with  $i, k \in \{1..n_{\text{spn}}\}$  can be defined as:

$$\underline{S}_{\text{pl}\{i,k\}}^{*\{\text{sw}\}} = \begin{cases} 1, & \text{if } i = \underline{PL}_{\text{pin}\{1\}}^{\{\text{sw}\}} \wedge k = \underline{PL}_{\text{pin}\{2\}}^{\{\text{sw}\}} \wedge M_{\text{pl}}^{\{\text{sw}\}} = \text{on} \\ 1, & \text{if } k = \underline{PL}_{\text{pin}\{1\}}^{\{\text{sw}\}} \wedge i = \underline{PL}_{\text{pin}\{2\}}^{\{\text{sw}\}} \wedge M_{\text{pl}}^{\{\text{sw}\}} = \text{on} \\ 0, & \text{otherwise} \end{cases} \quad (5.125)$$

The corresponding element  $\underline{\eta}_{\text{pl}\{i,k\}}^{\{\text{sw}\}}$  in the  $i$ -th row and  $k$ -th column of the efficiency matrix  $\underline{\eta}_{\text{pl}}^{\{\text{sw}\}}$  with  $i, k \in \{1..n_{\text{spn}}\}$  is defined as:

$$\underline{\eta}_{\text{pl}\{i,k\}}^{\{\text{sw}\}} = \begin{cases} \eta_{\text{on}}, & \text{if } i = \underline{PL}_{\text{pin}\{1\}}^{\{\text{sw}\}} \wedge k = \underline{PL}_{\text{pin}\{2\}}^{\{\text{sw}\}} \\ \eta_{\text{on}}, & \text{if } k = \underline{PL}_{\text{pin}\{1\}}^{\{\text{sw}\}} \wedge i = \underline{PL}_{\text{pin}\{2\}}^{\{\text{sw}\}} \\ 0, & \text{otherwise} \end{cases} \quad (5.126)$$

For the evaluation of possible operating modes of a power switch, three discrete failure states are assumed, which are modeled by the diagnostic state variable  $D_{\text{pl}}^{\{\text{sw}\}}$ . The first state models a fault-free operation of the switch ( $D_{\text{pl}}^{\{\text{sw}\}} = \text{no\_fail}$ ). The second state models failures of the switch resulting in the loss of operating mode control, meaning that the currently set operating mode cannot be changed ( $D_{\text{pl}}^{\{\text{sw}\}} = \text{no\_chng}$ ). The third failure state models failures resulting in the connection loss from pin0 to pin1 ( $D_{\text{pl}}^{\{\text{sw}\}} = \text{open}$ ). By denoting the currently set switch operating mode with  $d^1 M_{\text{pl}}^{\{\text{sw}\}}$ , the operating mode vector  $\underline{PL}_{\text{mod}}^{\{\text{sw}\}}$  can be defined as a function of diagnostic state variable  $D_{\text{pl}}^{\{\text{sw}\}}$ :

$$\underline{PL}_{\text{mod}}^{\{\text{sw}\}} = \begin{cases} \begin{bmatrix} \text{on} & \text{off} \end{bmatrix}^T, & \text{if } D_{\text{pl}}^{\{\text{sw}\}} = \text{no\_fail} \\ \begin{bmatrix} d^1 M_{\text{pl}}^{\{\text{sw}\}} \end{bmatrix}^T, & \text{if } D_{\text{pl}}^{\{\text{sw}\}} = \text{no\_chng} \\ \begin{bmatrix} \text{off} \end{bmatrix}^T, & \text{if } D_{\text{pl}}^{\{\text{sw}\}} = \text{open} \end{cases} \quad (5.127)$$

Five failure modes were assumed for powerlink components in Section 5.1.2. Two of them, namely *loss of operating mode control* and *no energy transport* are covered by (5.127). The failure mode *short circuit between the power switch input and output* corresponds to the case *loss of operating mode control*, since the energy transport cannot be disconnected. The failure mode *decreased energy flow efficiency* is already considered by the time-dependent energy flow efficiency matrix  $\eta_{\text{pl}}^{\{\text{sw}\}}$ , which is permanently updated according to the power switch diagnostic data. The failure mode *short circuit to ground* at power switch input or output (external short circuit to ground) is covered by the time-dependent state variable  $S_{\text{spn}}^{\{k\}}$  modeling the operational state of subpowernet  $k$ , which is set to 0 in case of a short circuit to ground in subpowernet  $k$ . Using the equations presented in this subsection, the behavioral model of a single power switch according to the generic description in Section 5.4.1 can be implemented.

## 5.5. Prediction of Battery Remaining Discharge Energy

One of the main goals for the control of fail-operational powernets is to guarantee reliable power supply for safety-critical functions during the entire driving mission. Based on the predictive estimation of the energy demand and available energy resources, an optimal energy distribution strategy is found by solving the mixed-integer optimization problem as presented in Section 5.1. Accurate prediction of the energy demand and available energy resources is of high importance for the concept of safety-based range extension, meaning the arrival of the vehicle at the safest possible location for the passengers.

Different methods estimating the remaining discharge energy of the battery exist. The energy counting method is based on the estimation of the initial available energy and

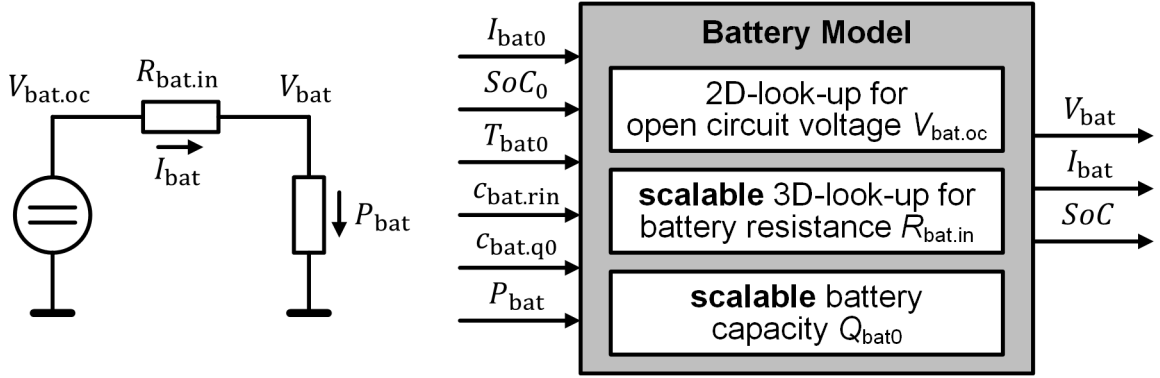


Figure 5.14.: Battery model used for the prediction of remaining discharge energy.

online counting of used energy by digital integration [113]. Due to inaccuracy by accumulating the measurement errors, additional recalibration using a look-up table can be added [113]. The remaining discharge energy is also dependent on the discharge power [101], which adds additional inaccuracy to the energy counting method. The accuracy can be increased by predicting the future battery states, parameters and discharge curve [101, 113]. For the model predictive estimation of the remaining discharge energy, different battery models, e.g. electrochemical, neural network or equivalent circuit models [113] can be used.

The estimation of the remaining discharge energy is required for the solution of the mixed-integer energy distribution optimization used for the control of a fail-operational powernet. Therefore, accurate and fast online estimation with low computational effort is required considering also the possible battery failure states. The battery model used for the prediction is presented in Section 5.5.1. The algorithm for the prediction of the remaining discharge energy for a constant discharge power is explained in Section 5.5.2. The proposed algorithm for the online approximation of the remaining discharge energy as a function of discharge power is presented in Section 5.5.3.

### 5.5.1. Battery Model for Prediction of Remaining Discharge Energy

The prediction of the remaining discharge energy for the control of the powernet is based on an equivalent circuit model consisting of an open circuit voltage source  $V_{\text{bat.oc}}$  and battery internal resistance  $R_{\text{bat.in}}$  as depicted in Fig. 5.14. The battery internal resistance models the sum of the ohmic resistance, charge-transfer and diffusion resistance [29]. For modeling possible battery failures resulting in an increase of the internal resistance, the time-dependent scaling factor  $c_{\text{bat.rin}}$  ( $c_{\text{bat.rin}} > 1$ ) is used, which can be estimated by applying diagnostic methods (e.g. **S**tate of **H**ealth (SoH) monitoring). Using the definitions above and by denoting the battery output current with  $I_{\text{bat}}$ , the battery output

voltage  $V_{\text{bat}}$  can be calculated as:

$$V_{\text{bat}}(t) = V_{\text{bat.oc}}(t) - c_{\text{bat.rin}}(t) R_{\text{bat.in}}(t) I_{\text{bat}}(t) \quad (5.128)$$

As depicted on the right side of Fig. 5.14, the battery parameters  $V_{\text{bat.oc}}$  and  $R_{\text{bat.in}}$  are obtained by using look-up functions. The battery open circuit voltage  $V_{\text{bat.oc}}$  is estimated with a 2D-LUT as a function of current battery state of charge  $SoC_0$  ( $SoC_0 = SoC(t_0)$ ) and battery temperature  $T_{\text{bat}0}$  ( $T_{\text{bat}0} = T_{\text{bat}}(t_0)$ ) as:

$$V_{\text{bat.oc}}(t_0) = LUT_{\text{bat.oc}}(SoC_0, T_{\text{bat}0}) \quad (5.129)$$

The internal resistance  $R_{\text{bat.in}}$  is estimated with a 3D-look-up-table as a function of battery state of charge  $SoC_0$ , temperature  $T_{\text{bat}0}$  and output current  $I_{\text{bat}0}$  ( $I_{\text{bat}0} = I_{\text{bat}}(t_0)$ ) as:

$$R_{\text{bat.in}}(t_0) = LUT_{\text{bat.rin}}(SoC_0, T_{\text{bat}0}, I_{\text{bat}0}) \quad (5.130)$$

Battery discharge or charge power  $P_{\text{bat}}$  is defined as:

$$P_{\text{bat}}(t) = V_{\text{bat}}(t) I_{\text{bat}}(t) \quad (5.131)$$

Using (5.128) and (5.131), the output voltage  $V_{\text{bat}}$  can be expressed as a function of battery output power  $P_{\text{bat}}$  [29]:

$$V_{\text{bat}}(t) = \frac{V_{\text{bat.oc}}(t)}{2} + \frac{\sqrt{V_{\text{bat.oc}}(t)^2 - c_{\text{bat.rin}}(t) R_{\text{bat.in}}(t) P_{\text{bat}}(t)}}{2} \quad (5.132)$$

The corresponding battery output current  $I_{\text{bat}}$  can be then calculated as [29]:

$$I_{\text{bat}}(t) = \frac{V_{\text{bat.oc}}(t) - \sqrt{V_{\text{bat.oc}}(t)^2 - c_{\text{bat.rin}}(t) R_{\text{bat.in}}(t) P_{\text{bat}}(t)}}{2 c_{\text{bat.rin}}(t) R_{\text{bat.in}}(t)} \quad (5.133)$$

Assuming a given state of charge at time instant  $t_0$ , the battery state of charge can be expressed as a function of the output current and battery initial capacity  $Q_{\text{bat}0}$  as [29, 114, 115]:

$$SoC(t) = SoC(t_0) - \frac{1}{c_{\text{bat.q}0}(t) Q_{\text{bat}0}} \int_{t_0}^t I_{\text{bat}}(\tau) d\tau \quad \text{for } c_{\text{bat.q}0} \in (0..1] \quad (5.134)$$

In (5.134), an additional time-dependent scaling factor  $c_{\text{bat.q}0}$  ( $c_{\text{bat.q}0} \in (0..1]$ ) is added for modeling possible battery faults resulting in the decrease of the initial battery capacity  $Q_{\text{bat}0}$ . The failure mode *internal short circuit to ground* is modeled already by the oper-



ational state variable  $S_{\text{spn}}^{\{i\}}$ , which is set to 0 in case of a short circuit in subpowernet  $i$ . Assuming an automated disconnection of the battery in case of a battery internal short circuit to ground, the time-dependent scaling factor  $c_{\text{bat.q0}}$  can be set to 0 and the battery state of charge to the minimum discharge threshold  $SoC_{\text{min}}$ . In this case, as it will be shown in (5.143) and (5.147), the battery remaining discharge energy equals to 0. Using (5.134), the battery current can be also expressed as a function of the state of charge:

$$I_{\text{bat}}(t) = -c_{\text{bat.q0}}(t) Q_{\text{bat0}} \frac{d}{dt} SoC(t) \quad (5.135)$$

The battery remaining discharge energy can be defined as the integral of battery output power starting from  $t_0$  and ending at the time instant  $t_0 + dT_{\text{dcha}}$ , at which the minimum allowed state of charge threshold  $SoC_{\text{min}}$  is reached:

$$E_{\text{rde}} = \int_{t_0}^{t_0+dT_{\text{dcha}}} P_{\text{bat}}(t) dt = \int_{t_0}^{t_0+dT_{\text{dcha}}} V_{\text{bat}}(t) I_{\text{bat}}(t) dt \quad (5.136)$$

Using the battery model as described above, the battery output voltage  $V_{\text{bat}}$  and current  $I_{\text{bat}}$  can be expressed as a function of the battery state of charge  $SoC$ . The equation for estimation of  $E_{\text{rde}}$  can be then rewritten as:

$$E_{\text{rde}} = -c_{\text{bat.q0}}(t) Q_{\text{bat0}} \int_{t_0}^{t_0+dT_{\text{dcha}}} V_{\text{bat}}(SoC(t)) \left( \frac{d}{dt} SoC(t) \right) dt \quad (5.137)$$

By substituting  $SoC(t) = SoC$  and by denoting  $SoC(t_0)$  and  $SoC(t_0 + dT_{\text{dcha}})$  with  $SoC_0$  and  $SoC_{\text{min}}$ , the battery remaining discharge energy can be defined as:

$$E_{\text{rde}} = c_{\text{bat.q0}}(t) Q_{\text{bat0}} \int_{SoC_{\text{min}}}^{SoC_0} V_{\text{bat}}(SoC) dSoC \quad (5.138)$$

An online algorithm for accurate model predictive estimation of  $E_{\text{rde}}$  based on (5.138) is presented in the next subsection.

### 5.5.2. Prediction with Constant Discharge Power

Using the battery model as presented in Section 5.5.1, the battery output voltage  $V_{\text{bat}}$  can be estimated as a function of the state of charge. For a given battery output power  $P_{\text{bat}}$ ,  $V_{\text{bat}}$  can be calculated for the interval between minimum state of charge threshold  $SoC_{\text{min}}$  and the current state of charge value  $SoC_0$ . By assuming  $n_{\text{soc}}$  breakpoints, the  $i$ -th element of the  $n_{\text{soc}}$ -by-1 state of charge column vector  $\underline{SoC}$  can be defined as:

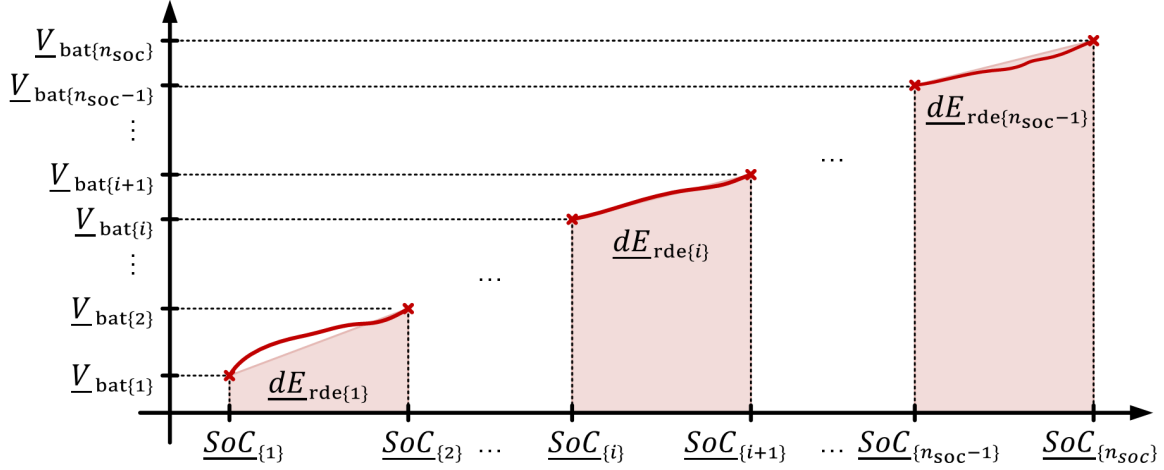


Figure 5.15.: Prediction of remaining discharge energy at constant output power.

$$\underline{SoC}_{\{i\}} = SoC_{\min} + (i - 1) \frac{SoC_0 - SoC_{\min}}{n_{\text{soc}} - 1} \quad \text{with } i \in \{1..n_{\text{soc}}\} \quad (5.139)$$

For each of the state of charge breakpoints, the battery model can be calculated obtaining  $n_{\text{soc}}$ -by-1 column vectors for battery open circuit voltage  $\underline{V}_{\text{bat.oc}}$ , current  $\underline{I}_{\text{bat0}}$ , internal resistance  $\underline{R}_{\text{bat.in}}$  and using (5.132) for battery output voltage  $\underline{V}_{\text{bat}}$  with  $i \in \{1..n_{\text{soc}}\}$ :

$$\underline{V}_{\text{bat.oc}\{i\}} = LUT_{\text{bat.oc}}(\underline{SoC}_{\{i\}}, T_{\text{bat0}}) \quad (5.140a)$$

$$\underline{I}_{\text{bat0}\{i\}} \approx \frac{P_{\text{bat}}}{\underline{V}_{\text{bat.oc}\{i\}}} \quad (5.140b)$$

$$\underline{R}_{\text{bat.in}\{i\}} = LUT_{\text{bat.rin}}(\underline{SoC}_{\{i\}}, T_{\text{bat0}}, \underline{I}_{\text{bat0}\{i\}}) \quad (5.140c)$$

$$\underline{V}_{\text{bat}\{i\}} = \frac{1}{2} \underline{V}_{\text{bat.oc}\{i\}} + \frac{1}{2} \sqrt{\underline{V}_{\text{bat.oc}\{i\}}^2 - \underline{R}_{\text{bat.in}\{i\}} P_{\text{bat}}} \quad (5.140d)$$

Since the battery internal resistance  $R_{\text{bat.in}}$  is a function of the battery current and the battery current is a function of the battery resistance according to (5.133), an iterative calculation for the estimation of the battery current for a given discharge power  $P_{\text{bat}}$  and state of charge would be required. Therefore, by neglecting the battery resistance, the battery current for the look-up of battery resistance is approximated as defined in (5.140c). As depicted in Fig. 5.15, the delta battery discharge energy  $\underline{dE}_{\text{rde}\{i\}}$  in interval  $i$  can be calculated as:

$$\underline{dE}_{\text{rde}\{i\}} = \frac{SoC_0 - SoC_{\min}}{n_{\text{soc}} - 1} \frac{\underline{V}_{\text{bat}\{i\}} + \underline{V}_{\text{bat}\{i+1\}}}{2} \quad \text{with } i \in \{1..n_{\text{soc}} - 1\} \quad (5.141)$$

The energy which can be depleted while discharging the battery from the current state of charge  $SoC_0$  to the minimum discharge threshold  $SoC_{\min}$  for a given constant discharge

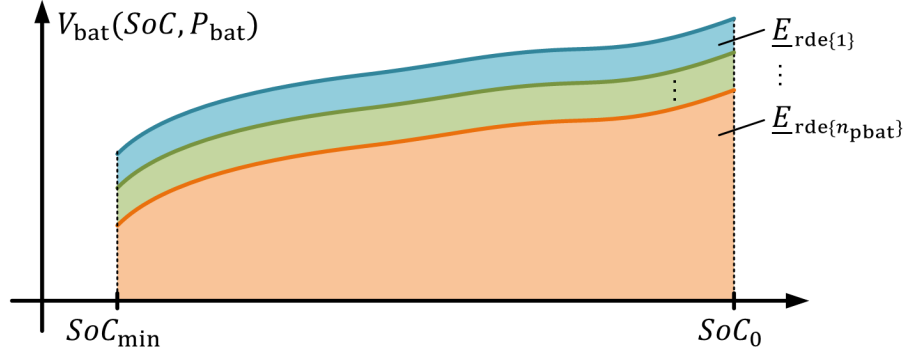


Figure 5.16.: Prediction of remaining discharge energy as a function of output power.

power  $P_{\text{bat}}$  can be then calculated as:

$$E_{\text{rde}}|_{P_{\text{bat}}=\text{const.}} = \sum_{i=1}^{n_{\text{soc}}-1} dE_{\text{rde}\{i\}} = \frac{SoC_0 - SoC_{\text{min}}}{n_{\text{soc}} - 1} \sum_{i=1}^{n_{\text{soc}}-1} \frac{V_{\text{bat}\{i\}} + V_{\text{bat}\{i+1\}}}{2} \quad (5.142)$$

By denoting the 1-by- $n_{\text{soc}}$  row vector with each element equal to 1 by  $\underline{1}$ , the equation for the calculation of the remaining discharge energy  $E_{\text{rde}}$  can be rewritten in the following matrix notation form:

$$E_{\text{rde}}|_{P_{\text{bat}}=\text{const.}} = \frac{SoC_0 - SoC_{\text{min}}}{n_{\text{soc}} - 1} \left( \underline{1} \cdot V_{\text{bat}} - \frac{V_{\text{bat}\{1\}} + V_{\text{bat}\{n_{\text{soc}}\}}}{2} \right) \quad (5.143)$$

Based on the estimation of the battery remaining discharge energy for a constant discharge power, the presented algorithm is extended for the approximation of the remaining discharge energy as a linear function of the discharge power in the next subsection.

### 5.5.3. Approximation as a Function of Discharge Power

Using linear approximation of the remaining discharge energy  $E_{\text{rde}}$  as a function of the battery discharge power  $P_{\text{bat}}$  as proposed in (5.18), an optimal discharge strategy for powernet topologies with multiple batteries can be obtained by solving the energy distribution optimization defined in (5.31). For this, in the first step, the remaining discharge energy can be estimated for a set of different discharge power values using the algorithm presented in Section 5.5.2. In the second step, using the least square minimization, the parameters  $E_{\text{rde}0}$  and  $a_{\text{rde}}$  can be estimated.

For the estimation of the remaining discharge energy for a given discharge power,  $n_{\text{soc}}$  breakpoints stored in the state of charge vector  $\underline{SoC}$  as defined in (5.139) are used. The remaining discharge energy is estimated for  $n_{\text{pbat}}$  linearly distributed breakpoints between the minimum ( $P_{\text{bat.min}}$ ) and maximum ( $P_{\text{bat.max}}$ ) allowed or expected discharge power. The

$j$ -th element of the 1-by- $n_{\text{pbat}}$  discharge power row vector  $P_{\text{bat}}$  can be defined as:

$$\underline{P}_{\text{bat}\{j\}} = P_{\text{bat.min}} + (j - 1) \frac{P_{\text{bat.max}} - P_{\text{bat.min}}}{n_{\text{pbat}} - 1} \quad \text{with } j \in \{1..n_{\text{pbat}}\} \quad (5.144)$$

For each of the state of charge and discharge power breakpoints, the battery model can be calculated obtaining  $n_{\text{soc}}$ -by-1 column vector  $\underline{V}_{\text{bat.oc}}$  for battery open circuit voltage and  $n_{\text{soc}}$ -by- $n_{\text{pbat}}$  matrices for battery current  $\underline{I}_{\text{bat0}}$ , internal resistance  $\underline{R}_{\text{bat.in}}$  and using (5.132) for battery output voltage  $\underline{V}_{\text{bat}}$  with  $i \in \{1..n_{\text{soc}}\}$  and  $j \in \{1..n_{\text{pbat}}\}$ :

$$\underline{V}_{\text{bat.oc}\{i\}} = LUT_{\text{bat.oc}}(\underline{SoC}\{i\}, T_{\text{bat0}}) \quad (5.145a)$$

$$\underline{I}_{\text{bat0}\{i,j\}} \approx \frac{\underline{P}_{\text{bat}\{j\}}}{\underline{V}_{\text{bat.oc}\{i\}}} \quad (5.145b)$$

$$\underline{R}_{\text{bat.in}\{i,j\}} = LUT_{\text{bat.rin}}(\underline{SoC}\{i\}, T_{\text{bat0}}, \underline{I}_{\text{bat0}\{i,j\}}) \quad (5.145c)$$

$$\underline{V}_{\text{bat}\{i,j\}} = \frac{1}{2} \underline{V}_{\text{bat.oc}\{i\}} + \frac{1}{2} \sqrt{\underline{V}_{\text{bat.oc}\{i\}}^2 - \underline{R}_{\text{bat.in}\{i,j\}} \underline{P}_{\text{bat}\{j\}}} \quad (5.145d)$$

The remaining discharge energy  $\underline{E}_{\text{rde}\{j\}}$  for the  $j$ -th breakpoint of  $\underline{P}_{\text{bat}\{j\}}$  is calculated as:

$$\underline{E}_{\text{rde}\{j\}} \Big|_{P_{\text{bat}} = \underline{P}_{\text{bat}\{j\}}} = \frac{SoC_0 - SoC_{\text{min}}}{n_{\text{soc}} - 1} \sum_{i=1}^{n_{\text{soc}}-1} \frac{\underline{V}_{\text{bat}\{i,j\}} + \underline{V}_{\text{bat}\{i+1,j\}}}{2} \quad (5.146)$$

By denoting the 1-by- $n_{\text{soc}}$  row vector with all elements equal to 1 by  $\underline{1}$  and the  $i$ -th row of the  $n_{\text{soc}}$ -by- $n_{\text{pbat}}$  matrix  $\underline{V}_{\text{bat}}$  by  $\underline{V}_{\text{bat}\langle i \rangle}$ , the 1-by- $n_{\text{pbat}}$  remaining discharge energy vector  $\underline{E}_{\text{rde}}$  can be calculated as:

$$\underline{E}_{\text{rde}} = \frac{SoC_0 - SoC_{\text{min}}}{n_{\text{soc}} - 1} \left( \underline{1} \cdot \underline{V}_{\text{bat}} - \frac{\underline{V}_{\text{bat}\langle 1 \rangle} + \underline{V}_{\text{bat}\langle n_{\text{soc}} \rangle}}{2} \right) \quad (5.147)$$

Using the method of least squares, the objective function for the estimation of the parameters  $a_{\text{rde}}$  and  $E_{\text{rde0}}$  for linear approximation can be defined as:

$$f_{\text{bat.lsm}}(E_{\text{rde0}}, a_{\text{rde}}) = \sum_{j=1}^{n_{\text{pbat}}} \left( E_{\text{rde0}} - a_{\text{rde}} \underline{P}_{\text{bat}\{j\}} - \underline{E}_{\text{rde}\{j\}} \right)^2 \quad (5.148)$$

The optimal approximation parameters  $a_{\text{rde}}$  and  $E_{\text{rde0}}$  are obtained by unconstrained minimization of the least squares objective:

$$(E_{\text{rde0}}, a_{\text{rde}}) = \min_{(E_{\text{rde0}}, a_{\text{rde}})} f_{\text{bat.lsm}}(E_{\text{rde0}}, a_{\text{rde}}) \quad (5.149)$$

For online estimation, analytical solution for the least squares minimization can be used:

$$\begin{pmatrix} E_{rde0} & a_{rde} \end{pmatrix}^T = \underline{A}_{\text{ism}}^{-1} \cdot \underline{b}_{\text{ism}} \quad (5.150)$$

By denoting the  $n_{\text{pbat}}$ -by-1 column vector with all elements equal to 1 by  $\underline{1}$ , the corresponding matrix  $\underline{A}_{\text{ism}}$  is defined as:

$$\underline{A}_{\text{ism}} = \begin{pmatrix} n_{\text{pbat}} & -\sum_{j=1}^{n_{\text{pbat}}} P_{\text{bat}\{j\}} \\ -\sum_{j=1}^{n_{\text{pbat}}} P_{\text{bat}\{j\}} & \sum_{j=1}^{n_{\text{pbat}}} (P_{\text{bat}\{j\}})^2 \end{pmatrix} = \begin{pmatrix} n_{\text{pbat}} & -P_{\text{bat}} \cdot \underline{1} \\ -P_{\text{bat}} \cdot \underline{1} & P_{\text{bat}} \cdot P_{\text{bat}}^T \end{pmatrix} \quad (5.151)$$

By denoting the  $n_{\text{pbat}}$ -by-1 column vector with all elements equal to 1 by  $\underline{1}$ , the corresponding vector  $\underline{b}_{\text{ism}}$  is defined as:

$$\underline{b}_{\text{ism}} = \begin{pmatrix} \sum_{j=1}^{n_{\text{pbat}}} E_{rde\{j\}} \\ -\sum_{j=1}^{n_{\text{pbat}}} E_{rde\{j\}} P_{\text{bat}\{j\}} \end{pmatrix} = \begin{pmatrix} E_{rde} \cdot \underline{1} \\ -P_{\text{bat}} \cdot E_{rde}^T \end{pmatrix} \quad (5.152)$$

In the following section, simulation results verifying the accuracy of the proposed algorithm for the prediction of the remaining discharge energy at runtime are presented.

## 5.6. Simulation Results for Battery Remaining Discharge Energy Prediction

For the prediction of the remaining discharge energy of a battery two approaches were proposed in Section 5.5.2 and 5.5.3. In the first approach, the battery remaining discharge energy  $E_{rde}$  is estimated for a constant discharge power  $P_{\text{bat}}$ . In the second approach, the battery remaining discharge energy  $E_{rde}$  is linearly approximated as a function of the discharge power  $P_{\text{bat}}$  using the approximation parameters  $E_{rde0}$  and  $a_{rde}$ . In the following, simulation results verifying the accuracy of the proposed algorithms as well as their capability to be executed at runtime are provided for three different types of batteries, namely for HV and 48 V lithium-ion and for 12 V lead-acid battery.

### 5.6.1. Examples for Prediction with Constant Discharge Power

For each battery type the remaining discharge energy  $E_{rde,qs}$  for a set of different discharge power values  $P_{\text{bat}}$  is estimated using the quasistatic approach with the calculation time step  $dT_{qs} = 0.1$  s. The results are summarized in Tables 5.1, 5.4 and 5.7, which are used as a reference for the estimation of the prediction algorithm accuracy for different numbers  $n_{\text{soc}}$  of state of charge breakpoints as presented in Section 5.5.2. The accuracy of the prediction algorithm is summarized in Tables 5.2, 5.5 and 5.8 and is calculated as a relative deviation of predicted remaining discharge energy  $E_{rde,pred}$  to the value  $E_{rde,qs}$

estimated with the quasistatic approach:

$$\Delta E_{\text{rde}} = \frac{E_{\text{rde.qs}} - E_{\text{rde.pred}}}{E_{\text{rde.qs}}} \quad (5.153)$$

### High Voltage Lithium-Ion Battery

In Table 5.1, the remaining discharge energy  $E_{\text{rde.qs}}^{\text{HV}}$  of a HV lithium-ion battery is calculated for five breakpoints of discharge power  $P_{\text{bat}}^{\text{HV}}$  at temperature  $T_{\text{bat0}}^{\text{HV}} = 25^\circ\text{C}$ . The nominal battery capacity  $Q_{\text{bat0}}^{\text{HV}}$  equals approx. 63 Ah with a nominal voltage of approx. 355 V. The remaining discharge energy is estimated for a battery discharge from the initial state of charge  $\text{SoC}_0^{\text{HV}} = 90\%$  to the minimum user defined threshold  $\text{SoC}_{\text{min}}^{\text{HV}} = 10\%$ .

Table 5.1.: Estimation of  $E_{\text{rde}}$  with quasistatic approach for HV battery.

$P_{\text{bat}}^{\text{HV}}$	10 kW	25 kW	40 kW	55 kW	70 kW
$E_{\text{rde.qs}}^{\text{HV}}$	18.59 kWh	18.30 kWh	17.99 kWh	17.68 kWh	17.35 kWh

As expected, the battery remaining discharge battery  $E_{\text{rde.qs}}^{\text{HV}}$  is decreasing with the increasing discharge power  $P_{\text{bat}}^{\text{HV}}$ . Using different numbers of breakpoints  $n_{\text{soc}}$  for the state of charge vector  $\underline{\text{SoC}}$ , the predicted remaining discharge energy  $E_{\text{rde.pred}}^{\text{HV}}$  is estimated with the algorithm presented in Section 5.5.2. The relative deviation  $\Delta E_{\text{rde}}^{\text{HV}}$  of  $E_{\text{rde.pred}}^{\text{HV}}$  to  $E_{\text{rde.qs}}^{\text{HV}}$  as defined in (5.153) is given in Table 5.2.

Table 5.2.: Accuracy of prediction for  $E_{\text{rde}}$  for HV battery.

$\Delta E_{\text{rde}}^{\text{HV}}$	$P_{\text{bat}}^{\text{HV}} = 10 \text{ kW}$	$P_{\text{bat}}^{\text{HV}} = 25 \text{ kW}$	$P_{\text{bat}}^{\text{HV}} = 40 \text{ kW}$	$P_{\text{bat}}^{\text{HV}} = 55 \text{ kW}$	$P_{\text{bat}}^{\text{HV}} = 70 \text{ kW}$
$n_{\text{soc}} = 10$	0.037 %	0.063 %	0.095 %	0.132 %	0.180 %
$n_{\text{soc}} = 20$	0.050 %	0.073 %	0.099 %	0.127 %	0.161 %
$n_{\text{soc}} = 30$	0.015 %	0.026 %	0.039 %	0.052 %	0.069 %
$n_{\text{soc}} = 40$	0.014 %	0.017 %	0.022 %	0.027 %	0.034 %
$n_{\text{soc}} = 50$	0.002 %	0.005 %	0.008 %	0.011 %	0.016 %

It can be seen that the prediction accuracy of the proposed algorithm is very high and increases with the increasing number of breakpoints for the state of charge vector  $\underline{\text{SoC}}$  almost for all considered values for the battery discharge power  $P_{\text{bat}}^{\text{HV}}$ . The corresponding calculation time  $dT_{\text{eval}}^{\text{HV}}$  required for the prediction is given in Table 5.3. For the estimation of the battery open circuit voltage and internal resistance, a 2D look-up table as a function of state of charge and temperature is used.

The calculation time  $dT_{\text{eval}}^{\text{HV}}$  is estimated using the MATLAB functions *tic* and *toc* as the average out of 1000 runs on an Intel i7 CPU. It can be seen that with increasing number of breakpoints  $n_{\text{soc}}$  for state of charge vector  $\underline{\text{SoC}}$ , also the calculation time  $dT_{\text{eval}}^{\text{HV}}$  slightly

Table 5.3.: Calculation time required for prediction of  $E_{rde}$  for HV battery.

$dT_{eval}^{HV}$	$P_{bat}^{HV} = 10 \text{ kW}$	$P_{bat}^{HV} = 25 \text{ kW}$	$P_{bat}^{HV} = 40 \text{ kW}$	$P_{bat}^{HV} = 55 \text{ kW}$	$P_{bat}^{HV} = 70 \text{ kW}$
$n_{soc} = 10$	39.82 $\mu\text{s}$	39.11 $\mu\text{s}$	38.97 $\mu\text{s}$	38.76 $\mu\text{s}$	38.80 $\mu\text{s}$
$n_{soc} = 20$	40.03 $\mu\text{s}$	39.83 $\mu\text{s}$	39.71 $\mu\text{s}$	39.59 $\mu\text{s}$	39.56 $\mu\text{s}$
$n_{soc} = 30$	40.89 $\mu\text{s}$	40.87 $\mu\text{s}$	40.64 $\mu\text{s}$	40.86 $\mu\text{s}$	40.90 $\mu\text{s}$
$n_{soc} = 40$	43.20 $\mu\text{s}$	42.93 $\mu\text{s}$	42.80 $\mu\text{s}$	42.94 $\mu\text{s}$	42.76 $\mu\text{s}$
$n_{soc} = 50$	44.22 $\mu\text{s}$	44.11 $\mu\text{s}$	44.33 $\mu\text{s}$	44.29 $\mu\text{s}$	44.13 $\mu\text{s}$

increases. For all values for discharge power  $P_{bat}^{HV}$  and number of breakpoints  $n_{soc}$ , a calculation time less than 45  $\mu\text{s}$  is achieved, making the proposed algorithm very well suited for the implementation and execution at runtime in embedded systems.

#### 48V Lithium-Ion Battery

In Table 5.4, the remaining discharge energy  $E_{rde,qs}^{48V}$  of a 48V lithium-ion battery is calculated for five breakpoints of discharge power  $P_{bat}^{48V}$  at temperature  $T_{bat0}^{48V} = 25^\circ\text{C}$ . The nominal battery capacity  $Q_{bat0}^{48V}$  equals approx. 300 Ah with a nominal voltage of approx. 48 V. The remaining discharge energy is estimated for a battery discharge from the initial state of charge  $SoC_0^{48V} = 90\%$  to the minimum user defined threshold  $SoC_{min}^{48V} = 15\%$ .

 Table 5.4.: Estimation of  $E_{rde}$  with quasistatic approach for 48V battery.

$P_{bat}^{48V}$	4 kW	8 kW	12 kW	16 kW	20 kW
$E_{rde,qs}^{48V}$	10.84 kWh	10.63 kWh	10.41 kWh	10.20 kWh	9.99 kWh

Again, the battery remaining discharge energy  $E_{rde,qs}^{48V}$  is decreasing with the increasing discharge power  $P_{bat}^{48V}$ . Using different numbers of breakpoints  $n_{soc}$  for the state of charge vector  $SoC$ , the predicted remaining discharge energy  $E_{rde,pred}^{48V}$  is estimated and the relative deviation  $\Delta E_{rde}^{48V}$  of  $E_{rde,pred}^{48V}$  to  $E_{rde,qs}^{48V}$  as defined in (5.153) is given in Table 5.5.

 Table 5.5.: Accuracy of prediction for  $E_{rde}$  for 48V battery.

$\Delta E_{rde}^{48V}$	$P_{bat}^{48V} = 4 \text{ kW}$	$P_{bat}^{48V} = 8 \text{ kW}$	$P_{bat}^{48V} = 12 \text{ kW}$	$P_{bat}^{48V} = 16 \text{ kW}$	$P_{bat}^{48V} = 20 \text{ kW}$
$n_{soc} = 10$	0.890 %	1.295 %	2.016 %	3.105 %	4.672 %
$n_{soc} = 20$	0.485 %	0.339 %	0.641 %	1.241 %	2.310 %
$n_{soc} = 30$	0.391 %	0.174 %	0.394 %	0.894 %	1.864 %
$n_{soc} = 40$	0.389 %	0.190 %	0.416 %	0.918 %	1.878 %
$n_{soc} = 50$	0.383 %	0.164 %	0.378 %	0.867 %	1.813 %

Also in this example, the prediction accuracy of the proposed algorithm is very high and increases with the increasing number of breakpoints for state of charge vector  $SoC$  almost for all considered values for the discharge power  $P_{bat}^{48V}$ . The corresponding calculation

time  $dT_{\text{eval}}^{48V}$  required for the prediction is given in Table 5.6, which is estimated using the MATLAB functions *tic* and *toc* as the average out of 1000 runs on an Intel i7 CPU. For the estimation of the open circuit voltage, a 2D look-up table as a function of state of charge and temperature is used. For the estimation of the internal resistance, a 3D look-up table as a function of state of charge, temperature and battery current is used.

Table 5.6.: Calculation time required for prediction of  $E_{\text{rde}}$  for 48V battery.

$dT_{\text{eval}}^{48V}$	$P_{\text{bat}}^{48V} = 4 \text{ kW}$	$P_{\text{bat}}^{48V} = 8 \text{ kW}$	$P_{\text{bat}}^{48V} = 12 \text{ kW}$	$P_{\text{bat}}^{48V} = 16 \text{ kW}$	$P_{\text{bat}}^{48V} = 20 \text{ kW}$
$n_{\text{soc}} = 10$	56.51 $\mu\text{s}$	57.09 $\mu\text{s}$	56.84 $\mu\text{s}$	57.21 $\mu\text{s}$	57.73 $\mu\text{s}$
$n_{\text{soc}} = 20$	58.11 $\mu\text{s}$	59.85 $\mu\text{s}$	59.69 $\mu\text{s}$	59.64 $\mu\text{s}$	59.74 $\mu\text{s}$
$n_{\text{soc}} = 30$	59.26 $\mu\text{s}$	60.80 $\mu\text{s}$	61.28 $\mu\text{s}$	62.11 $\mu\text{s}$	62.19 $\mu\text{s}$
$n_{\text{soc}} = 40$	62.65 $\mu\text{s}$	63.90 $\mu\text{s}$	64.75 $\mu\text{s}$	65.49 $\mu\text{s}$	65.34 $\mu\text{s}$
$n_{\text{soc}} = 50$	65.29 $\mu\text{s}$	67.17 $\mu\text{s}$	67.59 $\mu\text{s}$	68.45 $\mu\text{s}$	68.80 $\mu\text{s}$

It can be seen that with increasing number of breakpoints  $n_{\text{soc}}$  for state of charge vector  $\underline{SoC}$ , also the calculation time  $dT_{\text{eval}}^{48V}$  slightly increases. For all values for discharge power  $P_{\text{bat}}^{48V}$  and number of breakpoints  $n_{\text{soc}}$ , a calculation time less than 70  $\mu\text{s}$  is achieved, making the proposed algorithm very well suited for implementation in real-time embedded systems. The higher computational time compared to the HV battery can be explained by the additional dimension in the look-up table for the estimation of battery resistance.

## 12V Lead-Acid Battery

In Table 5.7, the remaining discharge energy  $E_{\text{rde,qs}}^{12V}$  of a 12V lead-acid battery is calculated for five breakpoints of discharge power  $P_{\text{bat}}^{12V}$  at temperature  $T_{\text{bat0}}^{12V} = 25^\circ\text{C}$ . The nominal battery capacity  $Q_{\text{bat0}}^{12V}$  equals approx. 30 Ah with a nominal voltage of approx. 12 V. The remaining discharge energy is estimated for a battery discharge from the initial state of charge  $SoC_0^{12V} = 90\%$  to the minimum user defined threshold  $SoC_{\text{min}}^{12V} = 30\%$ .

Table 5.7.: Estimation of  $E_{\text{rde}}$  with quasistatic approach for 12V battery.

$P_{\text{bat}}^{12V}$	0.2 kW	0.4 kW	0.6 kW	0.8 kW	1.0 kW
$E_{\text{rde,qs}}^{12V}$	0.207 kWh	0.202 kWh	0.198 kWh	0.193 kWh	0.186 kWh

Also in this example, the battery remaining discharge energy  $E_{\text{rde,qs}}^{12V}$  is decreasing with the increasing discharge power  $P_{\text{bat}}^{12V}$ . The relative deviation  $\Delta E_{\text{rde}}^{12V}$  of the predicted discharge energy  $E_{\text{rde,pred}}^{12V}$  to  $E_{\text{rde,qs}}^{12V}$  as defined in (5.153) is given in Table 5.8.

Also in this example, a very high prediction accuracy is achieved. The corresponding calculation time  $dT_{\text{eval}}^{12V}$  required for the prediction is given in Table 5.9, which is estimated using the MATLAB functions *tic* and *toc* as the average out of 1000 runs on an Intel i7 CPU. For the estimation of battery open circuit voltage, a 2D look-up table as a function



Table 5.8.: Accuracy of prediction for  $E_{rde}$  for 12V battery.

$\Delta E_{rde}^{12V}$	$P_{bat} = 0.2 \text{ kW}$	$P_{bat} = 0.4 \text{ kW}$	$P_{bat} = 0.6 \text{ kW}$	$P_{bat} = 0.8 \text{ kW}$	$P_{bat} = 1.0 \text{ kW}$
$n_{soc} = 10$	0.426 ‰	0.913 ‰	1.230 ‰	-0.119 ‰	-0.819 ‰
$n_{soc} = 20$	0.420 ‰	0.887 ‰	1.163 ‰	-0.278 ‰	-1.138 ‰
$n_{soc} = 30$	0.419 ‰	0.880 ‰	1.147 ‰	-0.300 ‰	-1.168 ‰
$n_{soc} = 40$	0.418 ‰	0.878 ‰	1.143 ‰	-0.303 ‰	-1.168 ‰
$n_{soc} = 50$	0.418 ‰	0.878 ‰	1.142 ‰	-0.308 ‰	-1.180 ‰

of state of charge and temperature is used. For the estimation of internal resistance, a 3D look-up table as a function of state of charge, temperature and battery current is used.

 Table 5.9.: Calculation time required for prediction of  $E_{rde}$  for 12V battery.

$dT_{eval}^{12V}$	$P_{bat} = 0.2 \text{ kW}$	$P_{bat} = 0.4 \text{ kW}$	$P_{bat} = 0.6 \text{ kW}$	$P_{bat} = 0.8 \text{ kW}$	$P_{bat} = 1.0 \text{ kW}$
$n_{soc} = 10$	64.75 $\mu\text{s}$	63.35 $\mu\text{s}$	63.23 $\mu\text{s}$	63.95 $\mu\text{s}$	63.41 $\mu\text{s}$
$n_{soc} = 20$	65.76 $\mu\text{s}$	66.10 $\mu\text{s}$	65.98 $\mu\text{s}$	66.50 $\mu\text{s}$	66.33 $\mu\text{s}$
$n_{soc} = 30$	67.77 $\mu\text{s}$	68.66 $\mu\text{s}$	68.51 $\mu\text{s}$	69.37 $\mu\text{s}$	69.29 $\mu\text{s}$
$n_{soc} = 40$	71.71 $\mu\text{s}$	72.65 $\mu\text{s}$	72.75 $\mu\text{s}$	73.79 $\mu\text{s}$	73.87 $\mu\text{s}$
$n_{soc} = 50$	74.71 $\mu\text{s}$	76.23 $\mu\text{s}$	76.27 $\mu\text{s}$	77.69 $\mu\text{s}$	77.51 $\mu\text{s}$

It can be seen that with increasing number of breakpoints  $n_{soc}$  for state of charge vector  $SoC$ , also the calculation time  $dT_{eval}^{12V}$  slightly increases. For all values for discharge power  $P_{bat}^{12V}$  and number of breakpoints  $n_{soc}$ , a calculation time less than 80  $\mu\text{s}$  is achieved. The higher computational time compared to the 48V battery can be explained by the structure and number of breakpoints in the battery current vector for 3D look-up for the estimation of internal resistance and required iterations by the look-up function.

## 5.6.2. Examples for Approximation as a Function of Discharge Power

For the linear approximation of the battery remaining discharge energy  $E_{rde}$  as a function of discharge power  $P_{bat}$  as presented in Section 5.5.3, different values for the number  $n_{soc}$  of breakpoints for state of charge and number  $n_{pbat}$  of breakpoints for discharge power can be used. For the estimation of approximation accuracy, the coefficient of determination  $R^2$  describing the quality of model fit [116] is calculated. With the estimated parameters  $E_{rde0}$  and  $a_{rde}$ , the  $j$ -th element  $\underline{E}_{rde.apprx\{j\}}$  of the approximated battery remaining discharge energy vector  $\underline{E}_{rde.apprx}$  (model data) for the battery discharge power  $\underline{P}_{bat\{j\}}$  is defined as:

$$\underline{E}_{rde.apprx\{j\}} = E_{rde0} - a_{rde} \underline{P}_{bat\{j\}} \quad (5.154)$$

The average battery remaining discharge energy  $E_{\text{rde.avg}}$  is defined as the average value of the vector  $\underline{E}_{\text{rde}}$  (reference data):

$$E_{\text{rde.avg}} = \frac{1}{j_{\text{max}}} \sum_{j=1}^{j_{\text{max}}} E_{\text{rde}\{j\}} \quad (5.155)$$

The coefficient of determination  $R^2$  is then defined as [116]:

$$R^2 = 1 - \frac{\sum_{j=1}^{j_{\text{max}}} \left( E_{\text{rde}\{j\}} - E_{\text{rde.apprx}\{j\}} \right)^2}{\sum_{j=1}^{j_{\text{max}}} \left( E_{\text{rde}\{j\}} - E_{\text{rde.avg}} \right)^2} \quad (5.156)$$

The coefficients of determination calculated for each combination of  $n_{\text{soc}}$  and  $n_{\text{pbat}}$  for each battery type are summarized in Tables 5.10, 5.14 and 5.12 and the corresponding calculation times  $dT_{\text{eval}}$  required for the approximation in Tables 5.11, 5.13 and 5.15.

### High Voltage Lithium-Ion Battery

For the approximation of the battery remaining discharge energy as a function of discharge power, the same high voltage battery as in Section 5.6.1 with a nominal capacity  $Q_{\text{bat0}}^{\text{HV}}$  equal to approx. 63 Ah and nominal voltage approx. 355 V is used in this example. For the estimation of the parameters  $E_{\text{rde0}}^{\text{HV}}$  and  $a_{\text{rde}}^{\text{HV}}$  as proposed in Section 5.5.3, the maximum battery discharge power  $P_{\text{bat.max}}^{\text{HV}}$  is set to 70 kW and minimum discharge power  $P_{\text{bat.min}}^{\text{HV}}$  to 0 W. The minimum ( $SoC_{\text{min}}^{\text{HV}}$ ) and initial ( $SoC_0^{\text{HV}}$ ) state of charge values are set to 10% and to 90%, the battery temperature  $T_{\text{bat0}}^{\text{HV}}$  to 25 °C.

For the estimation of the reference data  $\underline{E}_{\text{rde}\{j\}}^{\text{HV}}$  for each discharge power  $\underline{P}_{\text{bat}\{j\}}^{\text{HV}}$ , the algorithm proposed in Section 5.5 with  $n_{\text{soc}} = 1000$  breakpoints is applied. The reference data is calculated for  $j_{\text{max}} = 100$  equally distributed discharge power breakpoints between  $P_{\text{bat.min}}^{\text{HV}}$  and  $P_{\text{bat.max}}^{\text{HV}}$ . The coefficient of determination  $R^2$  for the linear approximation of remaining discharge energy using the assumptions above is given in Table 5.10.

Table 5.10.:  $R^2$  for linear approximation of  $E_{\text{rde}}$  for HV battery.

$R^2$	$n_{\text{pbat}} = 10$	$n_{\text{pbat}} = 20$	$n_{\text{pbat}} = 30$	$n_{\text{pbat}} = 40$	$n_{\text{pbat}} = 50$
$n_{\text{soc}} = 10$	99.944 %	99.948 %	99.949 %	99.949 %	99.950 %
$n_{\text{soc}} = 20$	99.944 %	99.948 %	99.949 %	99.949 %	99.950 %
$n_{\text{soc}} = 30$	99.948 %	99.950 %	99.951 %	99.951 %	99.951 %
$n_{\text{soc}} = 40$	99.948 %	99.951 %	99.951 %	99.951 %	99.951 %
$n_{\text{soc}} = 50$	99.949 %	99.951 %	99.951 %	99.951 %	99.952 %

It can be seen that for all combinations of the numbers of breakpoints in state of charge vector ( $n_{\text{soc}}$ ) and discharge power ( $n_{\text{pbat}}$ ) the corresponding coefficients of determination

( $R^2$ ) are very close to 100%. A slight increase in  $R^2$  can be observed for increasing  $n_{\text{soc}}$  and  $n_{\text{pbat}}$ . The computational time required for the estimation of the linear approximation parameters  $E_{\text{rde0}}^{\text{HV}}$  and  $a_{\text{rde}}^{\text{HV}}$  is given in Table 5.11, which is estimated using the MATLAB functions *tic* and *toc* as the average out of 1000 runs on an Intel i7 CPU. For the estimation of open circuit voltage and internal resistance, a 2D look-up table as a function of state of charge and temperature is used.

Table 5.11.: Calculation time for linear approximation of  $E_{\text{rde}}$  for HV battery.

$dT_{\text{eval}}^{\text{HV}}$	$n_{\text{pbat}} = 10$	$n_{\text{pbat}} = 20$	$n_{\text{pbat}} = 30$	$n_{\text{pbat}} = 40$	$n_{\text{pbat}} = 50$
$n_{\text{soc}} = 10$	101.57 $\mu\text{s}$	104.54 $\mu\text{s}$	119.31 $\mu\text{s}$	125.70 $\mu\text{s}$	131.96 $\mu\text{s}$
$n_{\text{soc}} = 20$	105.12 $\mu\text{s}$	124.95 $\mu\text{s}$	136.66 $\mu\text{s}$	149.63 $\mu\text{s}$	161.58 $\mu\text{s}$
$n_{\text{soc}} = 30$	119.56 $\mu\text{s}$	135.98 $\mu\text{s}$	153.79 $\mu\text{s}$	169.84 $\mu\text{s}$	187.74 $\mu\text{s}$
$n_{\text{soc}} = 40$	126.54 $\mu\text{s}$	149.28 $\mu\text{s}$	170.66 $\mu\text{s}$	193.12 $\mu\text{s}$	217.06 $\mu\text{s}$
$n_{\text{soc}} = 50$	133.30 $\mu\text{s}$	162.17 $\mu\text{s}$	188.88 $\mu\text{s}$	218.89 $\mu\text{s}$	252.38 $\mu\text{s}$

It can be seen that the calculation time increases with the increasing number of breakpoints in state of charge ( $n_{\text{soc}}$ ) and discharge power ( $n_{\text{pbat}}$ ) vectors used for the approximation of parameters  $E_{\text{rde0}}^{\text{HV}}$  and  $a_{\text{rde}}^{\text{HV}}$ . For all combinations a computational time less than 255  $\mu\text{s}$  can be achieved, making the proposed approximation algorithm very well suited the implementation and execution at runtime in embedded systems.

#### 48V Lithium-Ion Battery

For the approximation of the battery remaining discharge energy as a function of discharge power, the same 48V battery as in Section 5.6.1 with a nominal capacity  $Q_{\text{bat0}}^{48\text{V}}$  equal to approx. 300 Ah and nominal voltage approx. 48 V is used. For the estimation of the parameters  $E_{\text{rde0}}^{48\text{V}}$  and  $a_{\text{rde}}^{48\text{V}}$  as proposed in Section 5.5.3, the maximum battery discharge power  $P_{\text{bat.max}}^{48\text{V}}$  is set to 20 kW and minimum discharge power  $P_{\text{bat.min}}^{48\text{V}}$  to 0 W. The minimum ( $SoC_{\text{min}}^{48\text{V}}$ ) and initial ( $SoC_0^{48\text{V}}$ ) state of charge values are set to 15% and to 90%, the battery temperature  $T_{\text{bat0}}^{48\text{V}}$  to 25 °C.

The reference data  $E_{\text{rde}\{j\}}^{48\text{V}}$  for each discharge power  $P_{\text{bat}\{j\}}^{48\text{V}}$  is estimated for  $n_{\text{soc}} = 1000$  breakpoints with the algorithm presented in Section 5.5. It is calculated for  $j_{\text{max}} = 100$  equally distributed discharge power breakpoints between  $P_{\text{bat.min}}^{48\text{V}}$  and  $P_{\text{bat.max}}^{48\text{V}}$ . The coefficient of determination  $R^2$  for the linear approximation of the remaining discharge energy using the assumptions above is given in Table 5.12.

Again, for all combinations of the numbers of breakpoints in state of charge ( $n_{\text{soc}}$ ) and discharge power ( $n_{\text{pbat}}$ ) vector, the corresponding coefficients of determination ( $R^2$ ) are very close to 100%. A slight increase in  $R^2$  can be observed for increasing  $n_{\text{soc}}$  and

Table 5.12.:  $R^2$  for linear approximation of  $E_{rde}$  for 48V battery.

$R^2$	$n_{pbat} = 10$	$n_{pbat} = 20$	$n_{pbat} = 30$	$n_{pbat} = 40$	$n_{pbat} = 50$
$n_{soc} = 10$	99.704 %	99.702 %	99.702 %	99.702 %	99.702 %
$n_{soc} = 20$	99.985 %	99.985 %	99.985 %	99.985 %	99.985 %
$n_{soc} = 30$	99.995 %	99.995 %	99.996 %	99.996 %	99.996 %
$n_{soc} = 40$	99.995 %	99.995 %	99.995 %	99.995 %	99.995 %
$n_{soc} = 50$	99.995 %	99.996 %	99.996 %	99.996 %	99.996 %

$n_{pbat}$ . The computational time required for the estimation of the linear approximation parameters  $E_{rde0}^{48V}$  and  $a_{rde}^{48V}$  is given in Table 5.13, which is estimated using the MATLAB functions *tic* and *toc* as the average out of 1000 runs on an Intel i7 CPU. For the estimation of open circuit voltage, a 2D look-up table as a function of state of charge and temperature is used. For the estimation of internal resistance, a 3D look-up table as a function of state of charge, temperature and battery current is used.

Table 5.13.: Calculation time for linear approximation of  $E_{rde}$  for 48V battery.

$dT_{eval}^{48V}$	$n_{pbat} = 10$	$n_{pbat} = 20$	$n_{pbat} = 30$	$n_{pbat} = 40$	$n_{pbat} = 50$
$n_{soc} = 10$	136.24 $\mu s$	136.21 $\mu s$	159.38 $\mu s$	172.89 $\mu s$	186.76 $\mu s$
$n_{soc} = 20$	136.37 $\mu s$	172.41 $\mu s$	201.97 $\mu s$	231.16 $\mu s$	259.03 $\mu s$
$n_{soc} = 30$	159.11 $\mu s$	201.48 $\mu s$	245.00 $\mu s$	285.14 $\mu s$	327.30 $\mu s$
$n_{soc} = 40$	174.43 $\mu s$	232.03 $\mu s$	285.64 $\mu s$	339.73 $\mu s$	397.50 $\mu s$
$n_{soc} = 50$	189.00 $\mu s$	260.85 $\mu s$	329.73 $\mu s$	398.89 $\mu s$	479.39 $\mu s$

It can be seen that the calculation time increases with the increasing number of breakpoints in state of charge ( $n_{soc}$ ) and discharge power ( $n_{pbat}$ ) vectors used for the approximation of parameters  $E_{rde0}^{48V}$  and  $a_{rde}^{48V}$ . For all combinations a computational time less than 480  $\mu s$  is achieved. The higher computational time compared to the HV battery is caused by the additional dimension in the look-up table for the estimation of battery resistance.

## 12V Lead-Acid Battery

In this example, the same 12V battery as in Section 5.6.1 with a nominal capacity  $Q_{bat0}^{12V}$  equal to approx. 30 Ah and nominal voltage approx. 12 V is used. For the estimation of the parameters  $E_{rde0}^{12V}$  and  $a_{rde}^{12V}$ , the maximum ( $P_{bat,max}^{12V}$ ) and minimum ( $P_{bat,min}^{12V}$ ) battery discharge power is set to 1 kW and 0 W. The minimum ( $SoC_{min}^{12V}$ ) and initial ( $SoC_0^{12V}$ ) state of charge values are set to 30 % and to 90 %, the battery temperature  $T_{bat0}^{48V}$  to 25 °C.

For the estimation of the reference data  $\underline{E}_{rde\{j\}}^{12V}$  for each discharge power  $\underline{P}_{bat\{j\}}^{12V}$ , the algorithm proposed in Section 5.5 with  $n_{soc} = 1000$  breakpoints is applied. The reference

data is calculated for  $j_{\max} = 100$  equally distributed discharge power breakpoints between  $P_{\text{bat.min}}^{12V}$  and  $P_{\text{bat.max}}^{12V}$ . The coefficient of determination  $R^2$  for linear approximation of remaining discharge energy using the assumptions above is given in Table 5.14.

Table 5.14.:  $R^2$  for linear approximation of  $E_{\text{rde}}$  for 12V battery.

$R^2$	$n_{\text{pbat}} = 10$	$n_{\text{pbat}} = 20$	$n_{\text{pbat}} = 30$	$n_{\text{pbat}} = 40$	$n_{\text{pbat}} = 50$
$n_{\text{soc}} = 10$	99.408 %	99.521 %	99.538 %	99.543 %	99.545 %
$n_{\text{soc}} = 20$	99.421 %	99.528 %	99.542 %	99.547 %	99.548 %
$n_{\text{soc}} = 30$	99.423 %	99.528 %	99.543 %	99.547 %	99.548 %
$n_{\text{soc}} = 40$	99.423 %	99.528 %	99.543 %	99.547 %	99.548 %
$n_{\text{soc}} = 50$	99.423 %	99.529 %	99.543 %	99.547 %	99.548 %

Again, for all combinations of the numbers of breakpoints in state of charge vector ( $n_{\text{soc}}$ ) and discharge power ( $n_{\text{pbat}}$ ) the corresponding coefficients of determination ( $R^2$ ) are very close to 100 %. A slight increase in  $R^2$  can be observed for increasing  $n_{\text{soc}}$  and  $n_{\text{pbat}}$ . The computational time required for the estimation of the linear approximation parameters  $E_{\text{rde0}}^{12V}$  and  $a_{\text{rde}}^{12V}$  is given in Table 5.15, which is estimated using the MATLAB functions *tic* and *toc* as the average out of 1000 runs on an Intel i7 CPU. For the estimation of open circuit voltage, a 2D look-up table as a function of state of charge and temperature is used. For the estimation of battery internal resistance, a 3D look-up table as a function of state of charge, temperature and battery current is used.

Table 5.15.: Calculation time for linear approximation of  $E_{\text{rde}}$  for 12V battery.

$dT_{\text{eval}}^{12V}$	$n_{\text{pbat}} = 10$	$n_{\text{pbat}} = 20$	$n_{\text{pbat}} = 30$	$n_{\text{pbat}} = 40$	$n_{\text{pbat}} = 50$
$n_{\text{soc}} = 10$	136.23 $\mu\text{s}$	150.89 $\mu\text{s}$	178.76 $\mu\text{s}$	198.53 $\mu\text{s}$	218.66 $\mu\text{s}$
$n_{\text{soc}} = 20$	151.36 $\mu\text{s}$	197.77 $\mu\text{s}$	238.91 $\mu\text{s}$	280.78 $\mu\text{s}$	319.72 $\mu\text{s}$
$n_{\text{soc}} = 30$	179.88 $\mu\text{s}$	238.71 $\mu\text{s}$	300.12 $\mu\text{s}$	358.68 $\mu\text{s}$	418.12 $\mu\text{s}$
$n_{\text{soc}} = 40$	200.26 $\mu\text{s}$	279.16 $\mu\text{s}$	358.91 $\mu\text{s}$	436.99 $\mu\text{s}$	518.83 $\mu\text{s}$
$n_{\text{soc}} = 50$	220.78 $\mu\text{s}$	320.73 $\mu\text{s}$	419.46 $\mu\text{s}$	520.09 $\mu\text{s}$	631.19 $\mu\text{s}$

It can be seen that the calculation time increases with the increasing number of breakpoints in state of charge ( $n_{\text{soc}}$ ) and discharge power ( $n_{\text{pbat}}$ ) vectors used for the approximation of parameters  $E_{\text{rde0}}^{12V}$  and  $a_{\text{rde}}^{12V}$ . For all combinations the computational time less than 635  $\mu\text{s}$  is achieved. The higher computational time compared to the 48V battery is again caused by the number of iterations required by the look-up function for estimation of battery internal resistance due to the number and structure of breakpoints in the battery current vector.

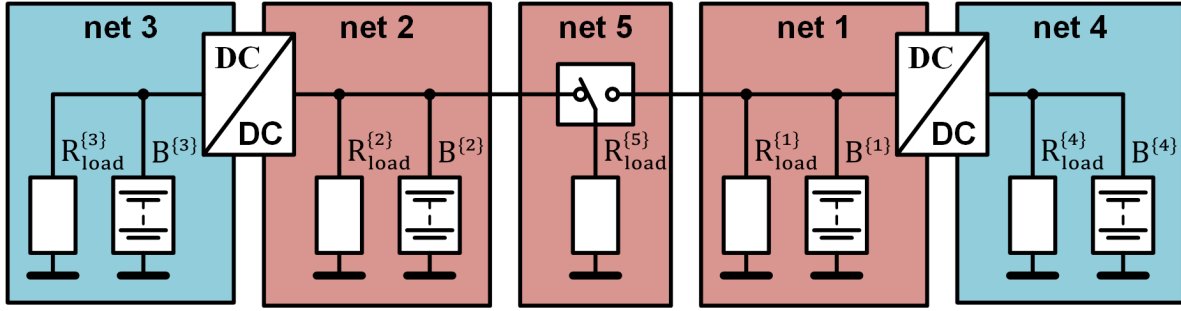


Figure 5.17.: Fail-operational powernet topology with 48V (red) and 12V (blue).

## 5.7. Simulation Results for Energy Distribution

Two different approaches for the energy distribution optimization used for control of the vehicle powernet were proposed in Section 5.1.3 and 5.1.4. By solving the mixed-integer energy distribution optimization problem as defined in the first approach (Version 1), optimal paths for energy distribution as well as the optimal energy amount that should be exchanged between the subpowernets for increasing the overall powernet efficiency are found. By solving the mixed-integer optimization problem as defined in the second approach (Version 2), additionally the discharge efficiency of the batteries is considered and the optimal multiple battery discharge strategy is found. In this section, simulation results exemplifying the functionality of the proposed energy distribution optimization approaches and verifying their capability to be executed at runtime in embedded systems are provided. In Section 5.7.1, the continuous energy distribution for a fail-operational powernet topology consisting of 5 subpowernets using the non-linear and linear programming models according to Section 5.3 are exemplified. In Section 5.7.2, the mixed-integer energy distribution optimization for finding the optimal operating mode vector for powerlinks is exemplified for a fail-operational powernet topology consisting of 4 subpowernets.

### 5.7.1. Example for Continuous Energy Distribution

The fail-operational powernet topology used for the simulation in this section consists of 5 subpowernets as depicted in Fig. 5.17. The level of power supply for subpowernets 1, 2 and 5 is assumed to be 48V and 12V for subpowernets 3 and 4. The 48V loads  $R_{\text{load}}^{\{1\}}$  and  $R_{\text{load}}^{\{2\}}$  are assumed to be symmetrical in energy consumption and functionality, totaling for example 48V propulsion and comfort loads each. If one load fails, the required functionality can be still provided in degraded mode by the other load. The average power consumption  $P_{\text{load}}^{\{1\}}$  and  $P_{\text{load}}^{\{2\}}$  of  $R_{\text{load}}^{\{1\}}$  and  $R_{\text{load}}^{\{2\}}$  for the analysis in this subsection is assumed to be 4000W. The load  $R_{\text{load}}^{\{5\}}$  of the 48V subpowernet 5 models an asymmetrical high power comfort load, e.g. air conditioning, which can be supplied by either traction battery

$B^{\{1\}}$  or  $B^{\{2\}}$  and does not require redundancy in functionality. Therefore, for enabling the functionality in case of a failure in subpowernet 1 or 2 and for state of charge balancing of the batteries  $B^{\{1\}}$  and  $B^{\{2\}}$ , the load  $R_{\text{load}}^{\{5\}}$  is supplied via a toggle switch, which can be also operated in PWM. The efficiency  $\eta_{\text{pl}}^{\{1,5\}}$  of the energy flow from subpowernet 1 to 5 is assumed to be constant and equal to 90 %, and the efficiency  $\eta_{\text{pl}}^{\{2,5\}}$  from subpowernet 2 to 5 is equal to 80 %.

The 12 V loads  $R_{\text{load}}^{\{3\}}$  and  $R_{\text{load}}^{\{4\}}$  are also assumed to be symmetrical in energy consumption and functionality, totaling for example safety-critical 12 V braking and steering loads. If one load fails, the required functionality can be still provided in degraded mode by the other load. The average power consumption  $P_{\text{load}}^{\{3\}}$  and  $P_{\text{load}}^{\{4\}}$  of  $R_{\text{load}}^{\{3\}}$  and  $R_{\text{load}}^{\{4\}}$  for the analysis in this subsection is set to 1200 W. The loads  $R_{\text{load}}^{\{3\}}$  and  $R_{\text{load}}^{\{4\}}$  can be supplied by the traction battery  $B^{\{1\}}$  and  $B^{\{2\}}$  via the DC/DC converters and also directly from the batteries  $B^{\{3\}}$  and  $B^{\{4\}}$ , which can be used for voltage stability in the corresponding subpowernets and which maintain the degraded functionality of safety-critical loads  $R_{\text{load}}^{\{3\}}$  and  $R_{\text{load}}^{\{4\}}$  in case of a failure in subpowernets 1 and 2, which can be decoupled by the corresponding DC/DC converters. The efficiency  $\eta_{\text{pl}}^{\{1,3\}}$  of the energy flow from subpowernet 1 to 3 and  $\eta_{\text{pl}}^{\{2,4\}}$  from 2 to 4 is assumed to be constant and equal to 95 %.

The capacity of the 48 V lithium-ion traction batteries  $B^{\{1\}}$  and  $B^{\{2\}}$  is assumed to be approx. 300 Ah and 30 Ah for the 12 V lead-acid batteries  $B^{\{3\}}$  and  $B^{\{4\}}$ . Due to the limited energy of  $B^{\{3\}}$  and  $B^{\{4\}}$ , the energy for the 12 V subpowernets is not provided to 48 V subpowernets, so the DC/DC converters can be only operated in forward mode, transmitting the energy from 48 V to 12 V subpowernets. For all batteries, an initial state of charge equal to 90 % is assumed.

According to the definition in (5.138), the battery remaining discharge energy  $E_{\text{rde}}$  is defined as the energy which is extracted while discharging the battery from the current state of charge  $SoC_0$  to the minimum discharge threshold  $SoC_{\text{min}}$ . For the traction batteries  $B^{\{1\}}$  and  $B^{\{2\}}$ , the discharge threshold  $SoC_{\text{min}}$  is set to 10 %, for voltage stability batteries  $B^{\{3\}}$  and  $B^{\{4\}}$  to 30 %.

In case of the discharge of a battery, the electrochemical energy is converted into electrical energy at the battery output. The discharge efficiency can be defined as the ratio of battery output power to electrochemical power [29]. Using (5.143), the remaining electrochemical energy of a battery can be estimated for a discharge power equal to 0. In the example powernet topology presented above, the sum of electrochemical energies  $E_{\text{rde0}}^{\{k\}}(t = t_0)$  with  $k \in \{1..4\}$  is equal to 23.8763 kWh. For the following simulation results a driving mission with the duration  $dT_{\text{ssl}}^*$  equal to 0.5 h is assumed.

### Example for Fault-Free Operation

As already mentioned above, both DC/DC converters can be operated in forward mode only, transmitting the energy from the 48 V subpowernet to 12 V loads. The case of DC/DC converters operating in off mode is modeled by the corresponding output power equal to 0 W. Also one operating mode for the toggle switch is assumed, since in PWM mode, the energy can be transferred from both subpowernets 1 and 2. Therefore, only one possible combination of powerlink operating modes  $\underline{M}_{pl}^*$  for this example can be assumed. Since the assumed remaining energy resources are greater than the total energy demand, no degradation will be required. The mixed-integer energy flow optimization can be therefore reduced to the continuous optimization problem with constant operating modes ( $\underline{M}_{pl} = \underline{M}_{pl}^*$ ) and constant degradation step ( $i_{ds} = 1$ ). For fault-free operation, it is assumed that all components have no failures. The results obtained by solving the energy distribution optimization problem as defined in Section 5.2.1 (Version 1) are given in the following Table 5.16.

Table 5.16.: Continuous energy distribution (Version 1) for fault-free operation.

powerlinks output power		battery output power		state of charge at destination		battery resistance scaling factor	
$P_{out}^{\{1,3\}}$	833.4 W	$P_{bat}^{\{1\}}$	7055.6 W	$SoC_{end}^{\{1\}}$	66.70 %	$C_{bat.rin}^{\{1\}}$	1
$P_{out}^{\{2,4\}}$	833.4 W	$P_{bat}^{\{2\}}$	4833.4 W	$SoC_{end}^{\{2\}}$	74.37 %	$C_{bat.rin}^{\{2\}}$	1
$P_{out}^{\{1,5\}}$	2222.2 W	$P_{bat}^{\{3\}}$	408.3 W	$SoC_{end}^{\{3\}}$	30.00 %	$C_{bat.rin}^{\{3\}}$	1
$P_{out}^{\{2,5\}}$	0.0 W	$P_{bat}^{\{4\}}$	408.3 W	$SoC_{end}^{\{4\}}$	30.00 %	$C_{bat.rin}^{\{4\}}$	1

For the prediction of the remaining discharge energy for the 48 V batteries, a constant discharge power  $P_{bat}^{\{1/2\}} = 10$  kW is assumed. For the 12 V batteries, a constant discharge with  $P_{bat}^{\{3/4\}} = 0.3$  kW is assumed. Since in Version 1 of energy distribution no battery discharge efficiency is considered, the energy from the battery for the supply of loads in the same powernet is considered to be the "cheapest" by the solver. Therefore, both 12 V batteries are fully discharged and the state of charge at the end of the driving mission ( $SoC_{end}^{\{3\}}$  and  $SoC_{end}^{\{4\}}$ ) equals to the minimum allowed threshold  $SoC_{min} = 30$  %.

The remaining discharge energy estimated for 12 V batteries using the assumptions above equals to 0.204 14 kWh. As already explained above, the energy from other subpowernets to a subpowernet containing a battery is only transmitted, if the energy demand of the loads in this subpowernet exceeds the available resources. If a battery is fully discharged, the average discharge power can be calculated as the ratio of the predicted remaining discharge energy to the driving duration. In this example, a driving duration equal to 0.5 h is assumed, which results in the average discharge power for 12 V batteries equal to 408.3 W.



Assuming a shorter driving duration, e.g. 0.1 h, the batteries would be discharged with a much higher power equal to  $\frac{0.20414 \text{ kWh}}{0.1 \text{ h}} = 2.04 \text{ kW}$ , since the maximum battery output power is not limited in this version of the energy distribution optimization. For avoiding this effect, a preprocessing of the available energy resources can be done. For a given maximum discharge power  $P_{\text{bat.max}}^{\{k\}}$  of the battery  $k$ , the remaining discharge energy  $E_{\text{rde}}^{\{k\}}$  used as input for the energy distribution optimization considering the remaining driving duration  $dT_{\text{ssl}}$  can be limited to:

$$E_{\text{rde}}^{\{k\}} = \min \left( E_{\text{rde}}^{\{k\}}, P_{\text{bat.max}}^{\{k\}} dT_{\text{ssl}} \right) \quad (5.157)$$

The remaining discharge energy required for the supply of 12 V loads ( $1200 \text{ W} - 408.3 \text{ W} = 791.7 \text{ W}$ ) is transmitted from the subpowernets via the DC/DC converters with the efficiency 95 %, resulting in 833.4 W at the outputs of subpowernets 1 ( $P_{\text{out}}^{\{1,3\}}$ ) and 2 ( $P_{\text{out}}^{\{2,4\}}$ ). Since the energy flow efficiency from subpowernet 1 to 5 is higher than from 2 to 5, the entire energy for the supply of the load  $R_{\text{load}}^{\{5\}}$  is transferred from subpowernet 1, leading to an asymmetrical discharge of the batteries  $B^{\{1\}}$  and  $B^{\{2\}}$ . The sum of the remaining electrochemical energies  $E_{\text{rde0}}^{\{k\}}(t = t_{\text{end}})$  with  $k \in \{1..4\}$  at the end of driving mission equals to 17.3267 kWh, so the sum of consumed electrochemical energies equals to 6.5497 kWh.

In the second version of the energy distribution optimization as defined in Section 5.2.2, the maximum output energy of the batteries is considered with a constraint. For this example, it is assumed that the output energy of traction batteries is limited to  $P_{\text{bat.max}}^{\{1/2\}} = 10 \text{ kW}$  and to  $P_{\text{bat.max}}^{\{3/4\}} = 0.3 \text{ kW}$  for the 12 V batteries. The results obtained by solving the energy distribution optimization problem as defined in Section 5.2.2 (Version 2) are given in the following Table 5.17.

Table 5.17.: Continuous energy distribution (Version 2) for fault-free operation.

powerlinks output power		battery output power		state of charge at destination		battery resistance scaling factor	
$P_{\text{out}}^{\{1,3\}}$	947.4 W	$P_{\text{bat}}^{\{1\}}$	7169.6 W	$SoC_{\text{end}}^{\{1\}}$	66.30 %	$c_{\text{bat.rin}}^{\{1\}}$	1
$P_{\text{out}}^{\{2,4\}}$	947.4 W	$P_{\text{bat}}^{\{2\}}$	4947.4 W	$SoC_{\text{end}}^{\{2\}}$	73.98 %	$c_{\text{bat.rin}}^{\{2\}}$	1
$P_{\text{out}}^{\{1,5\}}$	2222.2 W	$P_{\text{bat}}^{\{3\}}$	300.0 W	$SoC_{\text{end}}^{\{3\}}$	46.36 %	$c_{\text{bat.rin}}^{\{3\}}$	1
$P_{\text{out}}^{\{2,5\}}$	0.0 W	$P_{\text{bat}}^{\{4\}}$	300.0 W	$SoC_{\text{end}}^{\{4\}}$	46.36 %	$c_{\text{bat.rin}}^{\{4\}}$	1

The results obtained with this version are similar to the results presented above, with the main difference that the output power of the 12 V batteries is now limited to 300 W, resulting in higher energy transferred from subpowernet 1 and 2 to subpowernets 3 and 4. The sum of the remaining electrochemical energies  $E_{\text{rde0}}^{\{k\}}(t = t_0)$  with  $k \in \{1..4\}$  at the end of the driving mission equals to 17.3215 kWh, resulting in the total consumed

electrochemical energy equal to 6.5548 kWh. This value is slightly higher than the one achieved with the first version of the energy distribution optimization, which is the result of the limitation of the output power of 12 V batteries to 300 W. With the assumptions made above, also considering the discharge efficiencies of the batteries, it is more energy efficient to supply the 12 V loads  $R_{\text{load}}^{\{3\}}$  and  $R_{\text{load}}^{\{4\}}$  directly from the batteries  $B^{\{1\}}$  and  $B^{\{2\}}$ .

Using the MATLAB function *linprog* for solving the continuous energy distribution optimization problem (Version 1) in non-linear programming form as presented in Section 5.3.1, an average computational time out of 1000 runs on a Intel i7 CPU with the MATLAB functions *tic* and *toc* of approx. 50.1 ms is observed. The average computational time for solving the optimization problem (Version 1) in the form as presented in Section 5.3.2 with MATLAB function *fmincon* is approx. 3.4 ms. The computational time for the second approach of the energy distribution optimization (Version 2) using *fmincon* and *linprog* solvers as presented in Section 5.3.3 and 5.3.4 are approx. 70.9 ms and 3.4 ms. Therefore, the proposed optimization models using the MATLAB function *linprog* are very well suited for the implementation and execution at runtime in embedded systems. In the next example, two proposed approaches for the energy distribution optimization are exemplified and compared for failure case operation.

### Example for Failure Case Operation

For the imitation of a failure case operation, a battery fault increasing the internal resistance of the 12 V lead-acid battery  $B^{\{3\}}$  is injected by using the scaling factor  $c_{\text{bat.rin}}^{\{3\}}$ . An additional change to the example presented above is the limitation of the battery discharge power for both 12 V lead-acid batteries to 300 W using (5.157) for the first approach of the energy distribution optimization. The results are summarized in Table 5.18.

Table 5.18.: Continuous energy distribution (Version 1) for failure case operation.

powerlinks output power		battery output power		state of charge at destination		battery resistance scaling factor	
$P_{\text{out}}^{\{1,3\}}$	947.4 W	$P_{\text{bat}}^{\{1\}}$	7169.6 W	$SoC_{\text{end}}^{\{1\}}$	66.30 %	$c_{\text{bat.rin}}^{\{1\}}$	1
$P_{\text{out}}^{\{2,4\}}$	947.4 W	$P_{\text{bat}}^{\{2\}}$	4947.4 W	$SoC_{\text{end}}^{\{2\}}$	73.98 %	$c_{\text{bat.rin}}^{\{2\}}$	1
$P_{\text{out}}^{\{1,5\}}$	2222.2 W	$P_{\text{bat}}^{\{3\}}$	300.0 W	$SoC_{\text{end}}^{\{3\}}$	33.53 %	$c_{\text{bat.rin}}^{\{3\}}$	5
$P_{\text{out}}^{\{2,5\}}$	0.0 W	$P_{\text{bat}}^{\{4\}}$	300.0 W	$SoC_{\text{end}}^{\{4\}}$	46.35 %	$c_{\text{bat.rin}}^{\{4\}}$	1

It can be seen that despite the reduced discharge efficiency of the battery  $B^{\{3\}}$  due to the increased internal resistance, the energy from the battery for the supply of the internal loads is still considered to be the "cheapest" by the solver. Both 12 V batteries are discharged with the maximum allowed power. The state of charge  $SoC_{\text{end}}^{\{3\}}$  of battery  $B^{\{3\}}$  at

the end of the driving mission is lower than  $SoC_{\text{end}}^{\{4\}}$  of battery  $B^{\{4\}}$  due to the decreased discharge efficiency of  $B^{\{3\}}$ . After the completion of the driving cycle, the sum of the remaining electrochemical energies  $E_{\text{rde0}}^{\{k\}}(t = t_{\text{end}})$  with  $k \in \{1..4\}$  equals to 17.2752 kWh, resulting in total consumed electrochemical energy equal to 6.6011 kWh. The average discharge efficiency of the batteries can be calculated as a ratio of total output energy of batteries to total electrochemical energy depleted from the batteries. With the total output energy of the batteries (sum of  $E_{\text{bat}}^{\{k\}}$  with  $k \in \{1..4\}$ ) equal to 6.3585 kWh, the average discharge efficiency equal to 96.32% is obtained. In addition to the battery losses, also the losses in powerlink components must be considered. The average powernet efficiency can be defined as the ratio of the total electrochemical energy depleted from the batteries to the total energy demand of the loads (sum of  $E_{\text{load}}^{\{k\}}$  with  $k \in \{1..4\}$ ). The average powernet efficiency in the failure case equal to 93.92% is obtained with the first approach of the energy distribution optimization.

In the second approach for the energy distribution optimization, also the battery discharge efficiency is considered. The results for this approach are summarized in Table 5.19.

Table 5.19.: Continuous energy distribution (Version 2) for failure case operation.

powerlinks output power		battery output power		state of charge at destination		battery resistance scaling factor	
$P_{\text{out}}^{\{1,3\}}$	1263.2 W	$P_{\text{bat}}^{\{1\}}$	7485.4 W	$SoC_{\text{end}}^{\{1\}}$	65.20 %	$c_{\text{bat.rin}}^{\{1\}}$	1
$P_{\text{out}}^{\{2,4\}}$	947.4 W	$P_{\text{bat}}^{\{2\}}$	4947.4 W	$SoC_{\text{end}}^{\{2\}}$	73.98 %	$c_{\text{bat.rin}}^{\{2\}}$	1
$P_{\text{out}}^{\{1,5\}}$	2222.2 W	$P_{\text{bat}}^{\{3\}}$	0.0 W	$SoC_{\text{end}}^{\{3\}}$	90.00 %	$c_{\text{bat.rin}}^{\{3\}}$	5
$P_{\text{out}}^{\{2,5\}}$	0.0 W	$P_{\text{bat}}^{\{4\}}$	300.0 W	$SoC_{\text{end}}^{\{4\}}$	46.35 %	$c_{\text{bat.rin}}^{\{4\}}$	1

It can be seen that due to the increased internal resistance of  $B^{\{3\}}$  the load  $R_{\text{load}}^{\{3\}}$  is supplied by the traction battery  $B^{\{1\}}$  via the DC/DC converter, which in this case becomes more energy efficient. After the completion of the driving cycle, the sum of the remaining electrochemical energies  $E_{\text{rde0}}^{\{k\}}(t = t_{\text{end}})$  with  $k \in \{1..4\}$  equals to 17.3084 kWh, leading to a total consumed electrochemical energy equal to 6.5679 kWh. With the total output energy of batteries (sum of  $E_{\text{bat}}^{\{k\}}$  with  $k \in \{1..4\}$ ) equal to 6.3664 kWh, the average discharge efficiency in this example is increased to 96.93% compared with the first approach. Also the overall average powernet efficiency is increased to 94.40%.

Due to the higher energy flow efficiency of the toggle switch between the pins connecting subpowernet 1 and 5 (90%) compared to the connection to subpowernet 2, in all examples above the load  $R_{\text{load}}^{\{2\}}$  was always supplied by the battery  $B^{\{1\}}$ . As a result, the batteries  $B^{\{1\}}$  and  $B^{\{2\}}$  were discharged asymmetrically, which might be unfavorable for fail-operational applications requiring approximately the same driving range in case

of a breakdown of one battery. In the following subsection, a solution for balancing of the remaining discharge energy with the proposed energy distribution optimization is exemplified.

### Example for Battery Remaining Discharge Energy Balancing

With the first approach for the energy distribution optimization proposed in Section 5.1.3, automated energy flow path selection with the best efficiency and automated fault reactions can be implemented. An optimal discharge strategy of multiple traction batteries considering discharge efficiency as well as state of charge or remaining discharge energy balancing is not covered by this approach. If, for example, symmetrical discharge of traction batteries  $B^{\{1\}}$  and  $B^{\{2\}}$  in the powernet topology depicted in Fig. 5.17 would be required, no direct control parameter would be available, but could be still achieved using the penalty function  $f_{\text{edo,pen,pl}}$  for customizing the energy output of powerlinks. In this example, the penalization of the energy flow from subpowernet 1 to 5 ( $E_{\text{out}}^{\{1,5\}}$ ) and from 2 to 5 ( $E_{\text{out}}^{\{2,5\}}$ ) as a function of remaining discharge energy of batteries  $B^{\{1\}}$  and  $B^{\{2\}}$  could be used for this aim. Similar to the approach proposed in (5.28a) and (5.28b), the greater the difference in remaining discharge energies between  $B^{\{1\}}$  and  $B^{\{2\}}$ , the more costly becomes the energy flow  $E_{\text{out}}^{\{1,5\}}$  or  $E_{\text{out}}^{\{2,5\}}$  via the corresponding powerlink outputs. For the remaining discharge balancing of the 12 V lead-acid batteries  $B^{\{3\}}$  and  $B^{\{4\}}$ , this approach would not work, since no direct relationship between the powerlink output energies and battery discharge can be established for this example.

Therefore, in the second approach for the energy distribution optimization proposed in Section 5.1.4, additionally a penalty function  $f_{\text{edo,pen,bat}}$  for customization of battery output energies was introduced. A possible parametrization for the penalty factors is proposed in (5.28a) and (5.28a) and will be used for the remaining discharge energy balancing of the batteries  $B^{\{1\}}$  and  $B^{\{2\}}$  in this example. The parameters for powernet components as well as the initial conditions are the same as assumed for the first example in this section. The curve of the remaining discharge energy delta  $\Delta E_{\text{rde}21}$  between  $B^{\{1\}}$  and  $B^{\{2\}}$  for different scaling factors  $\gamma_{\text{rde}}$  is depicted in Fig. 5.18.

For all factors  $\gamma_{\text{rde}}$  it can be seen that  $\Delta E_{\text{rde}21}$  is first increasing due to the higher energy flow efficiency between subpowernet 1 and 5 and the load  $R_{\text{load}}^{\{5\}}$  is supplied by  $B^{\{1\}}$  only. Depending on the sensitivity of the balancing algorithm, which is increased with higher  $\gamma_{\text{rde}}$ , the remaining discharge energy balancing is activated after the value of the penalty function  $f_{\text{edo,pen,bat}}$  becomes higher than the losses resulting in supply of  $R_{\text{load}}^{\{5\}}$  by  $B^{\{2\}}$ . After the activation, the supply of  $R_{\text{load}}^{\{2\}}$  is continued in PWM mode, accepting the higher losses for the supply of  $R_{\text{load}}^{\{5\}}$  from  $B^{\{2\}}$ , which results in a decrease of the value of the

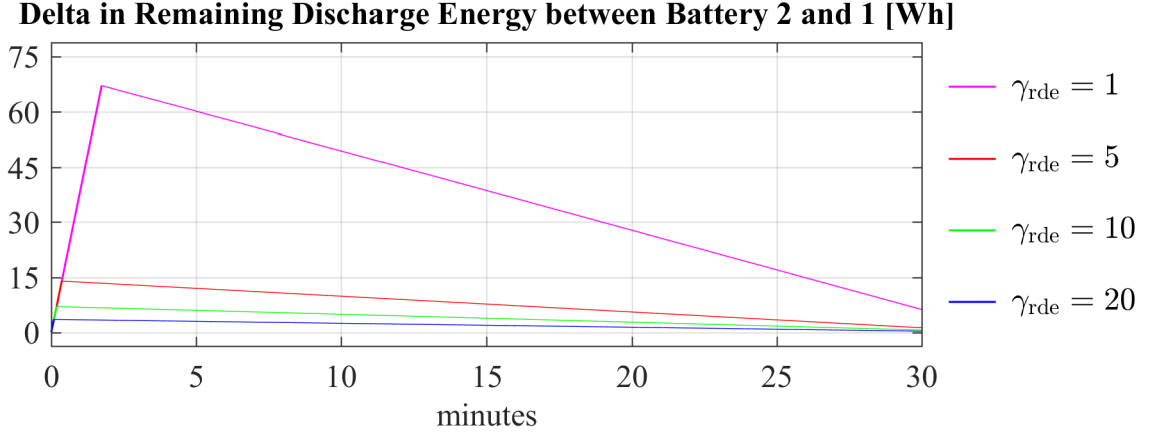


Figure 5.18.: Balancing of batteries remaining discharge energy.

objective  $f_{\text{edo.loss.opt}}$  describing the sum of all remaining energy resources at the end of a given driving cycle. Since the penalty function  $f_{\text{edo.pen.bat}}$  used for remaining discharge energy balancing is weighted to the objective  $f_{\text{edo.loss.opt}}$ , it becomes more significant with decreasing  $f_{\text{edo.pen.bat}}$ . Therefore, as depicted in Fig. 5.18, the  $\Delta E_{\text{rde}21}$  decreases with time. The state of charge  $SoC_{\text{end}}^{\{1/2\}}$  of the traction batteries  $B^{\{1\}}$  and  $B^{\{2\}}$  at the end of the driving mission for different factors  $\gamma_{\text{rde}}$  is summarized in Table 5.20

Table 5.20.: State of charge of batteries  $B^{\{1\}}$  and  $B^{\{2\}}$  at the end of driving mission.

$\gamma_{\text{rde}}$	0	1	5	10	20
$SoC_{\text{end}}^{\{1\}}$	66.305 %	69.890 %	69.906 %	69.907 %	69.908 %
$SoC_{\text{end}}^{\{2\}}$	73.978 %	69.930 %	69.914 %	69.912 %	69.911 %

It can be seen that without remaining discharge energy balancing ( $\gamma_{\text{rde}} = 0$ ) the traction batteries are discharged asymmetrically. With increasing  $\gamma_{\text{rde}}$  the delta in state of charge between both batteries decreases. The examples presented in this subsection were constructed in a way that the optimization of the powerlink operating modes  $\underline{M}_{\text{pl}}$  as well as load degradation was not required, since the operation of the powernet with one combination of  $\underline{M}_{\text{pl}}$  was possible and the available energy resources are higher than the total energy demand of powernet loads, reducing so the mixed-integer problem to a continuous energy distribution optimization. In the next subsection, both the optimization of the powerlink operating modes  $\underline{M}_{\text{pl}}$  as well as the load degradation are exemplified.

### 5.7.2. Example for Mixed-Integer Energy Distribution Optimization

For the examples in this subsection a fail-operational powernet topology consisting of 4 subpowernets as depicted in Fig. 5.19 is assumed. Due to its simplicity and extendability to the state-of-the-art powernet topologies, it was proposed for the usage in highly

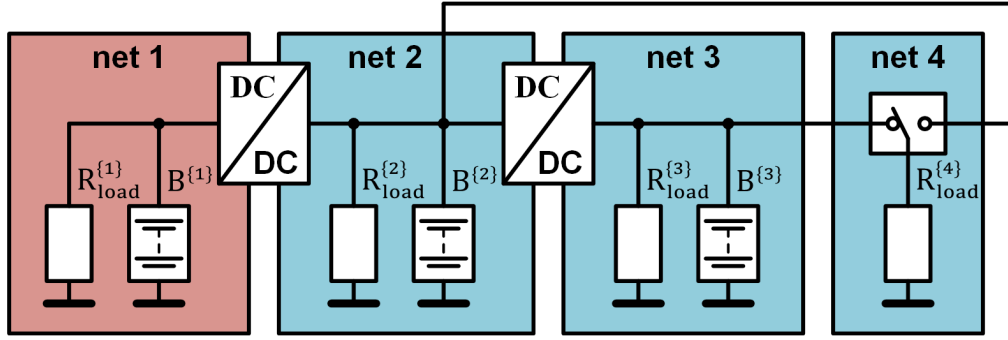


Figure 5.19.: Fail-operational powernet topology with HV (red) and 12V (blue).

automated driving systems in [8, 9, 11] for fulfilling high reliability requirements. Subpowernet 1 is supplied by a HV battery  $B^{\{1\}}$  and contains propulsion and comfort loads, both combined to  $R_{load}^{\{1\}}$  in Fig. 5.19. Subpowernet 2 receives the energy for the supply of the low voltage (12 V) load  $R_{load}^{\{2\}}$  via a DC/DC converter from the battery  $B^{\{1\}}$ . In addition, a voltage stability battery  $B^{\{2\}}$  is used for covering the transient power peaks of  $R_{load}^{\{2\}}$  for avoiding under- or overvoltage conditions in subpowernet 2 due to the power limitations of the DC/DC converter. Also in case subpowernet 1 fails, the load  $R_{load}^{\{2\}}$  can be supplied for a short period of time solely from the battery  $B^{\{2\}}$ , enabling the functionality of safety-critical loads for the duration of the vehicle transition to a safe state.

The load  $R_{load}^{\{2\}}$  totals the 12 V comfort loads and safety-critical subsystems, e.g. braking or steering. Subpowernet 1 and 2 build a typical powernet of a non-automated vehicle. Due to higher reliability requirements for automated vehicles, this basic powernet is extended by an additional 12 V subpowernet 3, which is supplied from subpowernet 2 via a DC/DC converter. Similarly to subpowernet 2, also a voltage stability battery  $B^{\{3\}}$  is used. The load  $R_{load}^{\{3\}}$  represents the safety-critical loads, which are redundant to the loads contained in  $R_{load}^{\{2\}}$ . A fourth subpowernet can be used for the supply of safety-critical subsystems  $R_{load}^{\{4\}}$ , which are considered to be highly reliable. For avoiding malfunction of  $R_{load}^{\{4\}}$  due to power supply breakdown, these loads can be either supplied by subpowernet 3 or 4 using a toggle switch as depicted in Fig. 5.19. With this powernet topology as proposed in [8, 9, 11], the fail-operability of steering and braking subsystems required for the vehicle transition to a safe state can be guaranteed. However, since the traction components ( $R_{load}^{\{2\}}$ ) and their supply ( $B^{\{1\}}$ ) are designed without redundancy, only a limited driving range using the kinetic energy of the vehicle in case of a failure in these components is available.

Due to the redundancy used in the fail-operational powernet as depicted in Fig. 5.19, new degrees of freedom arise for its control. For the supply of the loads, several paths with different energy flow efficiencies might exist. In the following subsection, an example is

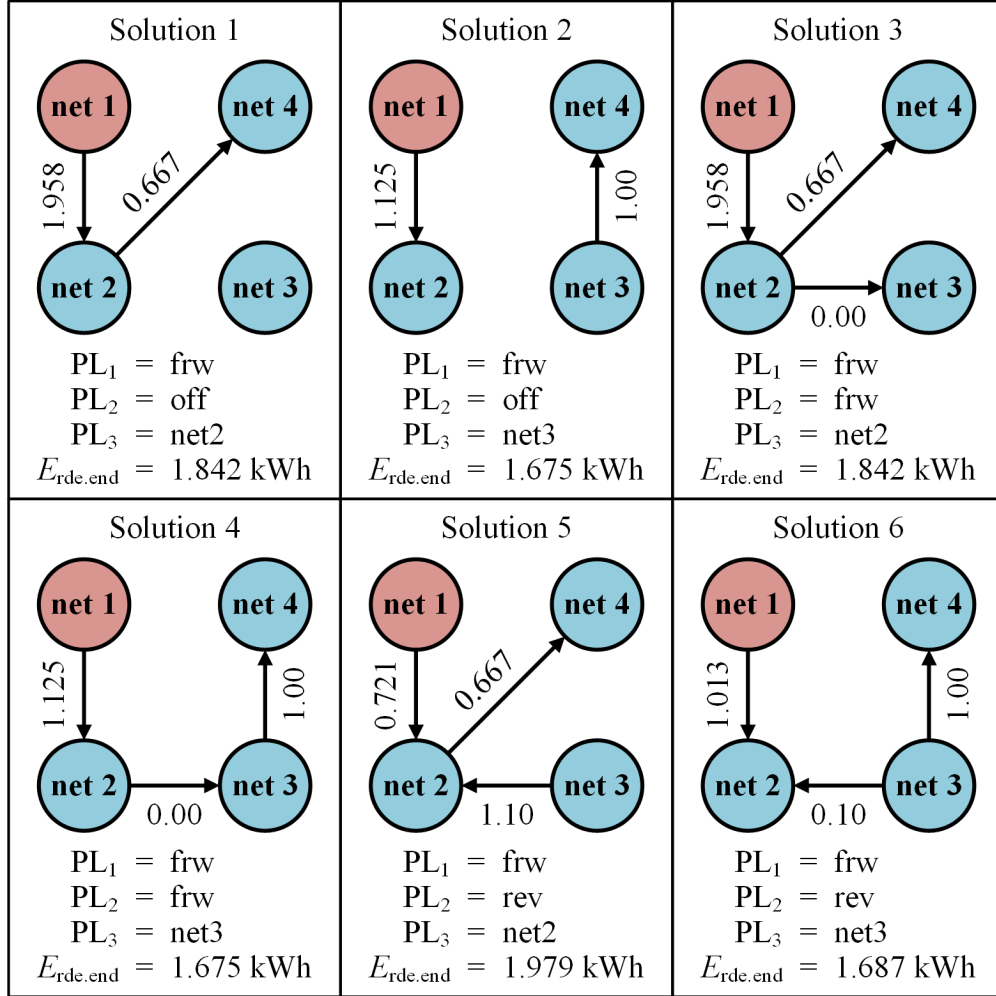


Figure 5.20.: Example of mixed-integer energy distribution optimization.

used for the explanation of the automated energy flow path selection using the energy distribution optimization proposed in this work.

### Automated Selection of Energy Flow Paths

In the powernet topology illustrated in Fig. 5.19, the four subpowernets are interconnected using three powerlinks, namely two DC/DC converters and one toggle switch. Each DC/DC converter can be operated in three modes as explained in Section 5.4 and for the toggle switch two operating modes are assumed, switching the energy supply of  $R_{load}^{4\}}$  between subpowernet 2 and 3. In total,  $3 \times 3 \times 2 = 18$  combinations of the powerlink operating modes are possible in this topology.

It is assumed that the remaining discharge energy  $E_{rde}^{\{1\}}$  of battery  $B^{\{1\}}$  equals to 5.8 kWh,  $E_{rde}^{\{2\}}$  of  $B^{\{2\}}$  to 1.7 kWh and  $E_{rde}^{\{3\}}$  of  $B^{\{3\}}$  to 1.5 kWh. The energy demand  $E_{load}^{\{1\}}$  required for the supply of  $R_{load}^{\{1\}}$  is assumed with 3.1 kWh,  $E_{load}^{\{2\}}$  with 2.6 kWh,  $E_{load}^{\{3\}}$  with 0.4 kWh

and  $E_{\text{load}}^{\{4\}}$  with 0.6 kWh.

The forward (frw) mode efficiency  $\eta_{\text{pl}}^{\{1,2\}}$  of the DC/DC converter for the energy transfer from subpowernet 1 and 2 and the reverse mode (rev) efficiency  $\eta_{\text{pl}}^{\{2,1\}}$  are set to 80 %. The energy from subpowernet 2 to 3 can be transferred using the second DC/DC converter in forward mode with corresponding efficiency  $\eta_{\text{pl}}^{\{2,3\}}$  set to 80 % and in the reverse direction with efficiency  $\eta_{\text{pl}}^{\{3,2\}}$  equal to 90 %. For the energy transfer from subpowernet 2 to 4 an efficiency  $\eta_{\text{pl}}^{\{2,4\}}$  equal to 90 % is assumed and  $\eta_{\text{pl}}^{\{3,4\}}$  equal to 60 % for the energy flow from subpowernet 3 to 4.

As depicted in Fig. 5.20, only for 6 out of 18 combinations of powerlink operating modes a valid solution for the energy distribution according to the optimization problem defined in (5.15) exists. Since the overall energy resources exceed the energy demand, no degradation of powernet loads is required. In this theoretical example it can be seen that the optimal solution for the energy distribution is solution 5, since the total remaining discharge energy  $E_{\text{rde, end}}$  after completing a driving mission is maximum for this example. If the powernet state remains stable, meaning that no failure in components happens, this solution is not expected to be changed. In case of any change, this solution might not be optimal any more and the adaptation of the energy distribution to the current powernet state is required. In the following subsection, the adaptation of the energy distribution strategy to the changes of powernet state is exemplified using fault injection in a simulation.

### Automated Adaption of Energy Distribution to Changing Powernet State

For the simulation in this example, a high voltage lithium-ion battery  $B^{\{1\}}$  with a nominal capacity  $Q_{\text{bat0}}^{\{1\}}$  of approx. 63 Ah and nominal voltage of approx. 355 V is assumed. The initial battery state of charge  $SoC_0^{\{1\}}$  is set to 30 %. For both low voltage batteries  $B^{\{2\}}$  and  $B^{\{3\}}$  a lead-acid battery with a nominal capacity  $Q_{\text{bat0}}^{\{2/3\}}$  equal to approx. 30 Ah and nominal voltage of approx. 12 V is assumed. The initial state of charge  $SoC_0^{\{2/3\}}$  of the low voltage batteries is set to 90 % and the output power  $P_{\text{bat.max}}^{\{2/3\}}$  is limited to 300 W. The temperature for all batteries is set to 25 °C. An average power demand  $P_{\text{load}}^{\{1\}} = 2.0$  kW for load  $R_{\text{load}}^{\{1\}}$ ,  $P_{\text{load}}^{\{2\}} = 1.2$  kW for  $R_{\text{load}}^{\{2\}}$ ,  $P_{\text{load}}^{\{3\}} = 0.6$  kW for  $R_{\text{load}}^{\{3\}}$  and  $P_{\text{load}}^{\{4\}} = 0.2$  kW for  $R_{\text{load}}^{\{4\}}$  is assumed. It is further assumed that the average power demand of all loads can be decreased in 10 equal degradation steps  $i_{\text{ds}}$  starting from 100 % for  $i_{\text{ds}} = 1$  to 10 % for  $i_{\text{ds}} = 10$ . In total, three different faults in powernet components are injected in this example. The simulation results are depicted in Fig. 5.21. The duration  $dT_{\text{ssl}}$  of the driving mission is assumed to be 1 h.

During the entire simulation, the efficiency  $\eta_{\text{pl}}^{\{1,2\}}$  of energy flow from subpowernet 1 to 2 is kept constant at 95 % as well as  $\eta_{\text{pl}}^{\{2,3\}}$  at 90 % for the energy flow from subpowernet 2



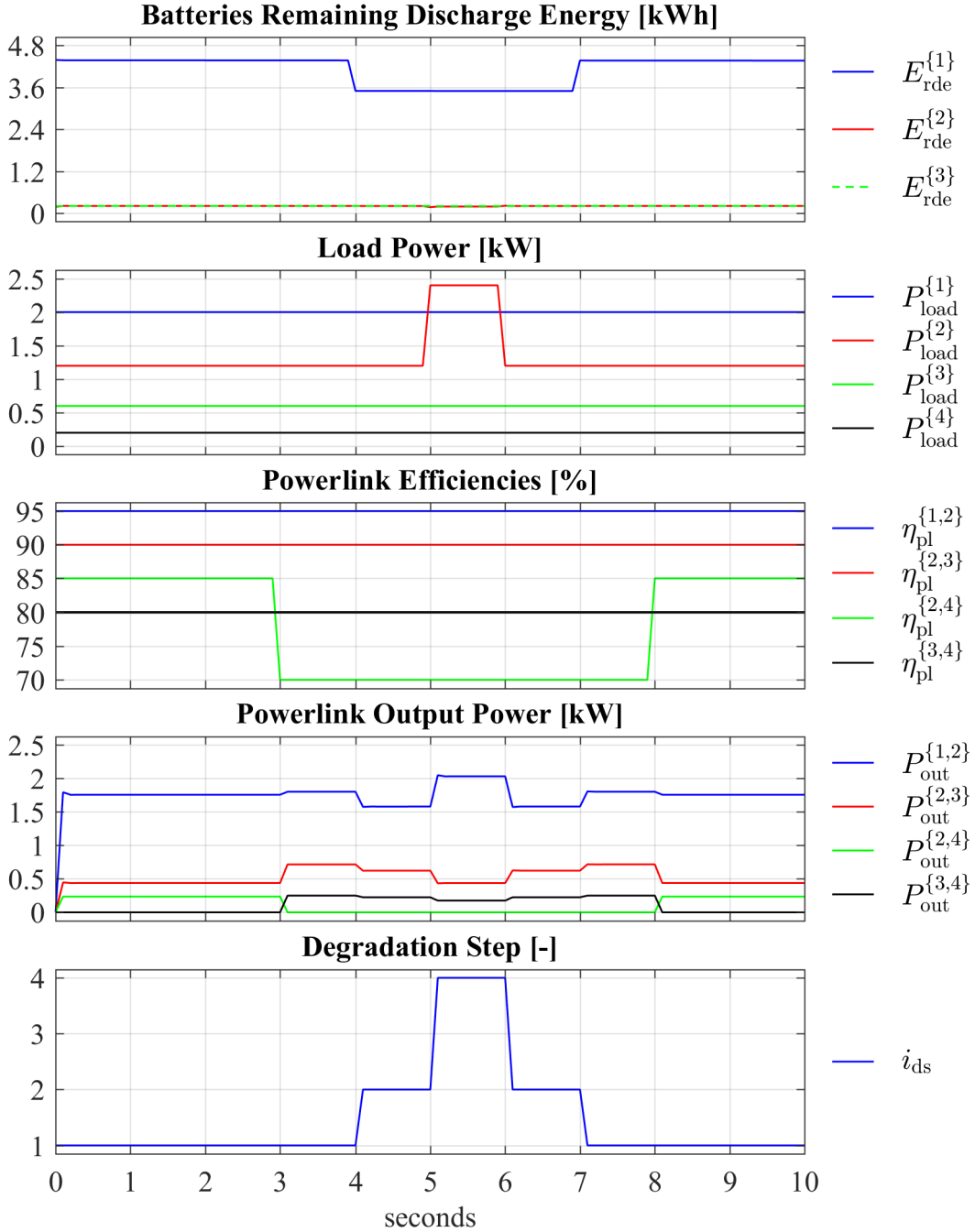


Figure 5.21.: Simulation results for energy distribution with fault injection.

to 3. At the beginning of the simulation ( $t = 0$  s), the efficiency  $\eta_{pl}^{\{2,4\}}$  of energy flow from subpowernet 2 to 4 is assumed with 85 %, which is better compared to  $\eta_{pl}^{\{3,4\}}$  set to 80 % throughout the simulation. Due to this, as it can be seen in Fig. 5.21, the load  $R_{load}^{\{4\}}$  is supplied by subpowernet 2 with the average output power  $P_{out}^{\{2,3\}}$ . At  $t = 3$  s, the energy flow efficiency  $\eta_{pl}^{\{2,4\}}$  is decreased from 85 % to 70 %. A decreased energy flow efficiency of the toggle switch could be for example detected by measuring the output current and

the voltage drop between the input and output. As a fault reaction, the supply of  $R_{\text{load}}^{\{4\}}$  is switched to subpowernet 3, since also due to additional losses in the DC/DC converter connecting subpowernets 2 and 3, this path becomes more energy efficient.

At  $t = 4$  s, a fault in a battery is injected and the battery capacity is reduced by 20 %, using the scaling factor  $c_{\text{bat},q0}^{\{1\}}$ . This fault could be for example caused by a short circuit to ground in one of the parallel battery's branches, which could be detected and disconnected by the battery management system. As a fault reaction, the EMS increases the degradation step  $i_{\text{ds}}$  by 1, which results in reduction of power demand of the loads by 10 %. At  $t = 5$  s, the next fault is injected and the power demand of  $R_{\text{load}}^{\{2\}}$  is increased from 1.2 kW to 2.4 kW. As a fault reaction, the power demand of the loads must be further reduced. For degradation step  $i_{\text{ds}}$  a solution is found in this example.

The transient increase of power demand of  $R_{\text{load}}^{\{2\}}$  is recovered after 1 s. It becomes again possible to activate more loads and as a reaction, the degradation step  $i_{\text{ds}}$  is set again to 2. At  $t = 7$  s, also the battery failure is recovered, and again the full battery capacity is available. As a reaction, the EMS decreases the degradation step to  $i_{\text{ds}} = 1$  (no active degradation). At  $t = 8$  s also the energy flow efficiency  $\eta_{\text{pl}}^{\{2,4\}}$  is set again to 85 %, so the supply of  $R_{\text{load}}^{\{4\}}$  from subpowernet 2 becomes again more energy efficient. Therefore, as a reaction, the supply of  $R_{\text{load}}^{\{4\}}$  is switched again to subpowernet 2.

As it was demonstrated with the simulation examples above, using the proposed energy distribution optimization for the control of a vehicle powernet, the overall energy efficiency can be increased and the fault reactions can be automated. With the proposed optimal, adaptive and real-time approach for the energy management, the reliability of automated vehicles can be significantly increased, allowing the passengers to arrive at the safest possible position in normal and failure case operation. One of the prerequisites for the functionality of the proposed algorithm is accurate prediction of the propulsion energy required for completing a given driving mission. A concept and real-time algorithms allowing accurate prediction of the propulsion energy for powertrain topologies with one and multiple traction motors based on the electronic horizon is proposed in the next chapter of this work.

## Chapter 6.

# Powertrain Control and Propulsion Energy Prediction

The optimal energy distribution for safety-based range extension proposed in this work requires predictive estimation of available energy resources and energy demand of safety-critical, comfort and propulsion loads. For the safety-based range extension, the available resources are then compared with the energy demand and the entire energy flow within the vehicle powernet and powertrain is optimized increasing the overall driving efficiency. Depending on the delta between the energy resources and demands, a three level degradation concept can be applied, degrading the load profile, driving profile and driving destination. An overestimated energy demand would result in unnecessary degradation. An underestimated energy demand could result in a vehicle breakdown, since the energy resources might be insufficient for completing a driving mission. Therefore, accurate prediction of energy demand is one of the prerequisites for the functionality of the proposed EMS for safety-based range extension.

Propulsion energy required for completing a given driving mission is strongly dependent on the route to be driven, traffic conditions, powertrain topology and its state. The power demand of the propulsion components is highly dynamic and appropriate prediction is required for its accurate estimation. Also failures in propulsion components might effect the power demand, requiring appropriate failure reactions. Therefore, for enabling short reaction times, the prediction of the propulsion energy should be executed online avoiding a high computational burden. In Section 6.1, an appropriate powertrain model used for the prediction of propulsion energy considering also component failures is presented.

In Section 6.2, a concept and algorithm for the prediction of the driving trajectory at runtime from the current vehicle position to the driving destination is presented, which is then used for model predictive estimation of the propulsion energy required for completing

the driving mission. The propulsion energy estimation is first exemplified on a powertrain topology with a single traction motor in Section 6.3 with simulation results verifying the accuracy and suitability for online execution of the proposed algorithm.

In fail-operational powertrain topologies, more than one traction motor is available. The total propulsion energy required for completing a driving mission with fail-operational powertrain is strongly dependent on the control strategy splitting the torque request between the individual motors. In Section 6.4, a new optimal and adaptive control strategy for the control of a fail-operational powertrain with multiple motors is proposed, which is then embedded in the propulsion energy prediction.

## 6.1. Powertrain Model

With an appropriate powertrain model, the propulsion energy required for completing a given driving mission can be predicted. In this section, mathematical models of the components used in powertrain topologies of an electric vehicle are presented, namely a gearbox with constant transmission ratio, electrical machine, traction battery as well as a vehicle model describing the longitudinal vehicle dynamics. Also possible failure modes of powertrain components are defined.

### 6.1.1. Failure Modes of Powertrain Components

One of the main goals of the control strategy for the powertrain in this work is to increase the driving range and the availability of the vehicle motion also in case of a failure. For this, the control of the powertrain must be adapted to possible faults in powertrain subsystems. The powertrain model presented in this section contains three subsystems: (1) gearbox, (2) traction motor and (3) traction battery. For the further analysis it is assumed that each powertrain component (subsystem) builds an FCR. In the following, the failure modes considered in this work for these three subsystems of a powertrain are defined.

#### **Gearbox**

A gearbox transmits mechanical power from a mechanical source to a mechanical sink and transforms the rotational speed and output torque of a source with a defined transmission ratio. Depending on the mechanical friction losses, the gearbox transmission efficiency can be defined. In this work it is assumed that a gearbox remains functional during the entire lifespan, which should be ensured by design. Only one failure mode with impact on the propulsion energy consumption is considered, which covers faults (e.g. scuffing [117])

resulting in a *decreased transmission efficiency*. This fault is considered to be permanent and progressive. The operation of the gearbox in this failure mode leads to an increased propulsion energy in motor mode and to a reduced recuperation in generator mode.

### Electric Motor

An electric motor converts electrical power into mechanical power (motor mode) and vice versa (generator mode). Depending on the mechanical and electrical losses [118], the motor efficiency can be estimated for both, motor and generator mode. Different motor faults influence the motor performance and are either of instant or progressive nature [119]. In this work, two different failure classes with impact on the propulsion energy consumption and maximum motor performance are considered, namely (1) *decreased efficiency* in motor and generator mode and (2) *decreased maximum torque* in motor and generator mode. These failure modes are assumed to be either transient (e.g. due to motor overheating) or permanent (e.g. due to motor aging or spontaneous component faults). The operation of a motor with *decreased efficiency* increases the required electrical energy in motor mode and decreases the recuperated energy in generator mode, leading also to an increased operating temperature. The operation of a motor with *decreased maximum torque* might influence the vehicle motion performance and require an adaption of the torque distribution strategy in powertrain topologies with multiple traction motors.

### Traction Battery

For a traction battery, the same three failure modes as already defined in Section 5.1.2 are assumed, namely (1) *decreased battery capacity*, (2) *increased internal resistance* and (3) *internal short circuit to ground*.

In the following subsections, first a vehicle model describing the longitudinal vehicle dynamics and used for the model predictive powertrain control is introduced, followed by gearbox, electric motor and traction battery model considering both, normal and failure case operation.

#### 6.1.2. Vehicle Model

For the prediction of the propulsion energy required for completing a given driving mission, a vehicle model based on a differential equation describing the longitudinal vehicle dynamics is used [29]:

$$F_t(t) = m_v a_v(t) + \frac{\rho A_f c_d v_v^2(t)}{2} + m_v g c_r \cos(\alpha_{rd}(t)) + m_v g \sin(\alpha_{rd}(t)) \quad (6.1)$$

The vehicle traction force  $F_t(t)$  is composed of four subforces. The first summand describes the force required for the acceleration of a vehicle with a mass  $m_v$  and given acceleration  $a_v$ . The vehicle speed profile is denoted by  $v_v$ . The second summand describes the aerodynamic friction. The vehicle frontal area is denoted by  $A_f$ , aerodynamic drag coefficient by  $c_d$  and the ambient air density by  $\rho$ . The third summand describes the rolling friction. The gravitational acceleration is denoted by  $g$ , rolling friction coefficient by  $c_r$  and road angle by  $\alpha_{rd}$ . The last summand describes the component of the gravitational force parallel to the road. By denoting the wheel radius by  $r_w$ , the relationship between the traction force  $F_t$  and the wheel torque  $T_w$  as well as between the vehicle speed  $v_v$  and the angular wheel speed  $\omega_w$  can be defined as [29]:

$$T_w(t) = r_w F_t(t) \quad (6.2a)$$

$$\omega_w(t) = r_w^{-1} v_v(t) \quad (6.2b)$$

Using the quasistatic approach [29], the average traction force  $F_t^{[i]}$  within the time interval  $i$  with  $t \in [t_0^{[i]}, t_0^{[i]} + dT^{[i]})$  required for vehicle acceleration with  $a_v^{[i]}$  can be calculated. The average traction force can be defined as:

$$F_t^{[i]} = \frac{1}{dT^{[i]}} \int_{t=t_0^{[i]}}^{t_0^{[i]}+dT^{[i]}} F_t(t) dt \quad (6.3)$$

Assuming the interval start velocity  $v_0^{[i]}$ , the velocity profile within the time interval  $i$  can be approximated as:

$$v_v^{[i]}(t) \approx v_0^{[i]} + a_v^{[i]} (t - t_0^{[i]}) \quad (6.4)$$

The relationship between the road angle  $\alpha_{rd}^{[i]}$  and road slope  $sl^{[i]}$  within the time interval  $i$  is defined as:

$$\alpha_{rd}^{[i]}(t) = \arctan(sl^{[i]}) \quad (6.5)$$

Using the definitions above, the average traction force  $F_t^{[i]}$  within the time interval  $i$  can be approximated as:

$$F_t^{[i]} \approx m_v a_v^{[i]} + \frac{\rho A_f c_d}{2} \left( v_0^{[i]} + \frac{a_v^{[i]} dT^{[i]}}{2} \right)^2 + \frac{m_v g (c_r + sl^{[i]})}{\sqrt{(sl^{[i]})^2 + 1}} \quad (6.6)$$

The average wheel torque  $T_w^{[i]}$  and angular wheel speed  $\omega_w^{[i]}$  within the time interval  $i$  can be calculated as:

$$T_w^{[i]} = r_w F_t^{[i]} \quad (6.7a)$$

$$\omega_w^{[i]} = r_w^{-1} \left( v_0^{[i]} + \frac{a_v^{[i]} dT^{[i]}}{2} \right) \quad (6.7b)$$

Depending on the powertrain topology, the requested wheel torque can be provided by either one axle or distributed between front and rear axle. By introducing a **f**ront/**r**ear (fr) torque distribution factor  $\alpha_{fr}^{[i]}$  with  $\alpha_{fr}^{[i]} \in [0..1]$ , the wheel torque for front ( $T_{wf}^{[i]}$ ) and rear ( $T_{wr}^{[i]}$ ) axle for the time interval  $i$  with  $t \in [t_0^{[i]}, t_0^{[i]} + dT^{[i]})$  can be defined as:

$$T_{wf}^{[i]} = \alpha_{fr}^{[i]} T_w^{[i]} \quad (6.8a)$$

$$T_{wr}^{[i]} = (1 - \alpha_{fr}^{[i]}) T_w^{[i]} \quad (6.8b)$$

### 6.1.3. Gearbox Model

For the propulsion energy prediction in this thesis it is assumed that the gearboxes in investigated powertrain topologies have only one transmission gear with a constant transmission ratio  $\gamma_{gb}$  and transmission efficiency  $\eta_{gb}$ . For modeling possible gearbox failures resulting in a decrease of transmission efficiency, a time dependent factor  $c_{gb,eff}^{[i]}$  ( $c_{gb,eff}^{[i]} \in (0..1)$ ) is introduced:

$$\eta_{gb}^{[i]} = c_{gb,eff}^{[i]} \eta_{gb} \quad \text{with} \quad c_{gb,eff}^{[i]} \in (0..1) \quad (6.9)$$

The torque and the angular speed at the gearbox input shaft are denoted by  $T_{gb,in}^{[i]}$  and  $\omega_{gb,in}^{[i]}$ , at the output shaft by  $T_{gb,out}^{[i]}$  and  $\omega_{gb,out}^{[i]}$ . In propulsion mode ( $T_{gb,out}^{[i]} \geq 0$ ), the mechanical energy flows from gearbox input shaft to the output shaft, connected to the vehicle axle via a differential. In recuperation mode ( $T_{gb,out}^{[i]} < 0$ ), the mechanical energy flows from gearbox output shaft to the input shaft. The relationship between the torque at the input and output shaft by neglecting the gearbox idle losses can be defined as [29]:

$$T_{gb,in}^{[i]} = \begin{cases} \frac{1}{\eta_{gb}^{[i]}} \frac{T_{gb,out}^{[i]}}{\gamma_{gb}}, & T_{gb,out}^{[i]} \geq 0 \\ \eta_{gb}^{[i]} \frac{T_{gb,out}^{[i]}}{\gamma_{gb}}, & T_{gb,out}^{[i]} < 0 \end{cases} \quad (6.10)$$

The relationship between the angular speed at the gearbox input and output shaft can be defined as [29]:

$$\omega_{gb,in}^{[i]} = \gamma_{gb} \omega_{gb,out}^{[i]} \quad (6.11)$$

In case two motors can be connected to the gearbox input shaft, e.g. from left and right side, the total required torque  $T_{\text{gb.in}}^{[i]}$  at the input shaft can be distributed between the torque  $T_{\text{gbl.in}}^{[i]}$  provided at the left and torque  $T_{\text{gbr.in}}^{[i]}$  at the right input using the left/right (lr) torque distribution factor  $\alpha_{\text{lr}}^{[i]}$  with  $\alpha_{\text{lr}}^{[i]} \in [0..1]$  as:

$$T_{\text{gbl.in}}^{[i]} = \alpha_{\text{lr}}^{[i]} T_{\text{gb.in}}^{[i]} \quad (6.12a)$$

$$T_{\text{gbr.in}}^{[i]} = (1 - \alpha_{\text{lr}}^{[i]}) T_{\text{gb.in}}^{[i]} \quad (6.12b)$$

### 6.1.4. Electric Motor Model

Depending on the operating mode, an electrical machine can be used for the conversion of electrical into mechanical power and vice versa. In motor mode, by requesting a positive torque  $T_{\text{em}}^{[i]}$  at the electrical machine output shaft, the electrical power from the battery is converted to mechanical power, which then flows from the output shaft to the wheels via the gearbox. The efficiency  $\eta_{\text{em.mot}}^{[i]}$  of the electrical machine in motor mode can be then defined as the ratio of mechanical power  $P_{\text{em.mech}}^{[i]}$  to electrical power  $P_{\text{em}}^{[i]}$  [29]:

$$\eta_{\text{em.mot}}^{[i]} = \frac{P_{\text{em.mech}}^{[i]}}{P_{\text{em}}^{[i]}} = \frac{\omega_{\text{em}}^{[i]} T_{\text{em}}^{[i]}}{V_{\text{em}}^{[i]} I_{\text{em}}^{[i]}} \quad \text{with} \quad T_{\text{em}}^{[i]} \geq 0 \quad \text{and} \quad I_{\text{em}}^{[i]} > 0 \quad (6.13)$$

The motor angular speed is denoted by  $\omega_{\text{em}}^{[i]}$ , the motor supply voltage and current by  $V_{\text{em}}^{[i]}$  and  $I_{\text{em}}^{[i]}$ . In generator mode, the mechanical power flows from the wheels to the electrical machine output shaft via the gearbox. By requesting a negative torque  $T_{\text{em}}^{[i]}$  at the output shaft, the mechanical power is converted to electrical and flows to the battery. The efficiency  $\eta_{\text{em.gen}}^{[i]}$  of the electrical machine in generator mode can be then defined as the ratio of electrical power  $P_{\text{em}}^{[i]}$  to mechanical power  $P_{\text{em.mech}}^{[i]}$  [29]:

$$\eta_{\text{em.gen}}^{[i]} = \frac{P_{\text{em}}^{[i]}}{P_{\text{em.mech}}^{[i]}} = \frac{V_{\text{em}}^{[i]} I_{\text{em}}^{[i]}}{\omega_{\text{em}}^{[i]} T_{\text{em}}^{[i]}} \quad \text{with} \quad T_{\text{em}}^{[i]} < 0 \quad \text{and} \quad I_{\text{em}}^{[i]} < 0 \quad (6.14)$$

The maximum positive torque  $T_{\text{em.lim.mot}}^{[i]}$  in motor mode and maximum negative torque  $T_{\text{em.lim.gen}}^{[i]}$  in generator mode which can be provided at the output shaft of the electrical machine can be modeled as a function of the electrical machine angular speed  $\omega_{\text{em}}^{[i]}$  and supply voltage  $V_{\text{em}}^{[i]}$  using a 2D-look-up table function.

$$T_{\text{em.lim.mot}}^{[i]} = c_{\text{em.trq}}^{[i]} LUT_{\text{em.lim.mot}}(\omega_{\text{em}}^{[i]}, V_{\text{em}}^{[i]}) \quad \text{with} \quad T_{\text{em}}^{[i]} \geq 0 \quad (6.15a)$$

$$T_{\text{em.lim.gen}}^{[i]} = c_{\text{em.trq}}^{[i]} LUT_{\text{em.lim.gen}}(\omega_{\text{em}}^{[i]}, V_{\text{em}}^{[i]}) \quad \text{with} \quad T_{\text{em}}^{[i]} < 0 \quad (6.15b)$$

An additional time-dependent coefficient  $c_{\text{em.trq}}^{[i]}$  ( $c_{\text{em.trq}}^{[i]} \in [0..1]$ ) modeling possible electric



motor faults resulting in a decreased maximum torque is introduced. The torque at the output shaft of the electrical machine based on the requested torque  $T_{\text{em.req}}^{[i]}$  is defined as:

$$T_{\text{em}}^{[i]} = \begin{cases} \min(T_{\text{em.req}}^{[i]}, T_{\text{em.lim.mot}}^{[i]}) & \text{with } T_{\text{em.req}}^{[i]} \geq 0 \\ \max(T_{\text{em.req}}^{[i]}, T_{\text{em.lim.gen}}^{[i]}) & \text{with } T_{\text{em.req}}^{[i]} < 0 \end{cases} \quad (6.16)$$

The efficiency of the electrical machine in motor ( $\eta_{\text{em.mot}}^{[i]}$ ) and generator ( $\eta_{\text{em.gen}}^{[i]}$ ) mode can be modeled as a function of output torque  $T_{\text{em}}^{[i]}$ , electrical machine angular speed  $\omega_{\text{em}}^{[i]}$  and supply voltage  $V_{\text{em}}^{[i]}$  using a 3D-look-up table function:

$$\eta_{\text{em.mot}}^{[i]} = LUT_{\text{em.eff.mot}}(T_{\text{em.loss.mot}}^{[i]}, \omega_{\text{em.loss.mot}}^{[i]}, V_{\text{em}}^{[i]}) \quad \text{with } T_{\text{em}}^{[i]} \geq 0 \quad (6.17a)$$

$$\eta_{\text{em.gen}}^{[i]} = LUT_{\text{em.eff.gen}}(T_{\text{em.loss.gen}}^{[i]}, \omega_{\text{em.loss.gen}}^{[i]}, V_{\text{em}}^{[i]}) \quad \text{with } T_{\text{em}}^{[i]} < 0 \quad (6.17b)$$

For the efficiency look-up in motor mode it is assumed that  $n_{\text{eff.mot.trq}}$  breakpoints for torque and  $n_{\text{eff.mot.rot}}$  breakpoints for angular speed are stored in increasing order in the  $n_{\text{eff.mot.trq}}$ -by-1 torque vector  $\underline{T}_{\text{em.eff.mot}}$  and  $n_{\text{eff.mot.rot}}$ -by-1 speed vector  $\underline{\omega}_{\text{em.eff.mot}}$ . For the efficiency look-up in generator mode  $n_{\text{eff.gen.trq}}$  breakpoints for torque and  $n_{\text{eff.gen.rot}}$  breakpoints for angular speed are stored in increasing order in the  $n_{\text{eff.gen.trq}}$ -by-1 torque vector  $\underline{T}_{\text{em.eff.gen}}$  and  $n_{\text{eff.gen.rot}}$ -by-1 speed vector  $\underline{\omega}_{\text{em.eff.gen}}$ . The losses of the electrical machine basically consist of copper, iron and friction losses [15]. For modeling the power losses in low torque and/or motor speed regions with no valid breakpoints in the look-up table, the power losses in these regions are assumed to be constant. This approach also approximates the power losses in case of no load ( $T_{\text{em}}^{[i]} = 0$ ). The torque  $T_{\text{em.loss.mot}}^{[i]} / T_{\text{em.loss.gen}}^{[i]}$  and motor speed  $\omega_{\text{em.loss.mot}}^{[i]} / \omega_{\text{em.loss.gen}}^{[i]}$  for the calculation of the power losses in motor / generator are then defined as:

$$T_{\text{em.loss.mot}}^{[i]} = \max(T_{\text{em}}^{[i]}, \underline{T}_{\text{em.eff.mot}\{1\}}) \quad \text{with } T_{\text{em}}^{[i]} \geq 0 \quad (6.18a)$$

$$\omega_{\text{em.loss.mot}}^{[i]} = \max(\omega_{\text{em}}^{[i]}, \underline{\omega}_{\text{em.eff.mot}\{1\}}) \quad \text{with } T_{\text{em}}^{[i]} \geq 0 \quad (6.18b)$$

$$T_{\text{em.loss.gen}}^{[i]} = \min(T_{\text{em}}^{[i]}, \underline{T}_{\text{em.eff.gen}\{n_{\text{eff.gen.trq}}\}}) \quad \text{with } T_{\text{em}}^{[i]} < 0 \quad (6.18c)$$

$$\omega_{\text{em.loss.gen}}^{[i]} = \max(\omega_{\text{em}}^{[i]}, \underline{\omega}_{\text{em.eff.gen}\{1\}}) \quad \text{with } T_{\text{em}}^{[i]} < 0 \quad (6.18d)$$

In motor mode, if the electrical machine torque  $T_{\text{em}}^{[i]} \geq 0$  is smaller than the first torque breakpoint  $\underline{T}_{\text{em.eff.mot}\{1\}}$  for efficiency look up, then the power losses are calculated in this breakpoint. In the generator mode, if the electrical machine torque  $T_{\text{em}}^{[i]} < 0$  is greater than the last torque breakpoint  $\underline{T}_{\text{em.eff.gen}\{n_{\text{eff.gen.trq}}\}}$  for efficiency look up, then the power losses are calculated in this breakpoint. A similar procedure is also applied to the angular speed of the electrical machine.

For modeling possible failures resulting in the decrease of the efficiency of the electrical machine, a time dependent factor  $c_{\text{em,eff}}^{[i]}$  ( $c_{\text{em,eff}}^{[i]} \in [0..1]$ ) is introduced. The efficiency  $\eta_{\text{em}}^{[i]}$  of the electrical machine can be then defined as:

$$\eta_{\text{em}}^{[i]} = \begin{cases} c_{\text{em,eff}}^{[i]} \eta_{\text{em,mot}}^{[i]} & \text{with } T_{\text{em}}^{[i]} \geq 0 \\ c_{\text{em,eff}}^{[i]} \eta_{\text{em,gen}}^{[i]} & \text{with } T_{\text{em}}^{[i]} < 0 \end{cases} \quad (6.19)$$

Using the definitions above, the power losses of the electrical machine can be calculated as:

$$P_{\text{em,loss}}^{[j]} = \begin{cases} \omega_{\text{em,loss,mot}}^{[i]} T_{\text{em,loss,mot}}^{[i]} \left( \frac{1}{\eta_{\text{em}}^{[i]}} - 1 \right) & \text{with } T_{\text{em}}^{[i]} \geq 0 \\ \omega_{\text{em,loss,gen}}^{[i]} T_{\text{em,loss,gen}}^{[i]} (\eta_{\text{em}}^{[i]} - 1) & \text{with } T_{\text{em}}^{[i]} < 0 \end{cases} \quad (6.20)$$

The electrical power  $P_{\text{em}}^{[i]}$  of the electrical machine can be then calculated as the sum of mechanical power  $P_{\text{em,mech}}^{[i]}$  and power losses  $P_{\text{em,loss}}^{[j]}$ :

$$P_{\text{em}}^{[i]} = P_{\text{em,mech}}^{[i]} + P_{\text{em,loss}}^{[j]} = \omega_{\text{em}}^{[i]} T_{\text{em}}^{[i]} + P_{\text{em,loss}}^{[j]} \quad (6.21)$$

According to the definition in (6.20) the power losses are always positive. In motor mode, the mechanical power is positive and smaller than the electrical power. In generator mode, the mechanical power is negative and greater than the electrical power flowing to the battery. Assuming that the electrical machine started its operation at interval  $j = 1$ , the energy losses dissipated at the end of interval  $j = i$  can be defined as:

$$E_{\text{em,loss}}^{[i]} = \sum_{j=1}^i dT^{[j]} \quad (6.22)$$

### 6.1.5. Traction Battery Model

The battery model used for the prediction of propulsion energy required for completing a given driving mission is based on the equivalent circuit diagram consisting of a voltage source modeling the battery open circuit voltage  $V_{\text{bat,oc}}$  and output resistance modeling the battery internal resistance  $R_{\text{bat,in}}$ . It was already presented in Section 5.5.1 and the equations for the quasistatic calculation are summarized in the following.

The battery output voltage  $V_{\text{bat}}^{[i]}$  for a given output power  $P_{\text{bat}}^{[i]}$  within the time interval  $i$  with  $t \in [t_0^{[i]}, t_0^{[i]} + dT^{[i]})$  is defined as:

$$V_{\text{bat}}^{[i]} = \frac{V_{\text{bat,oc}}^{[i]}}{2} + \frac{\sqrt{(V_{\text{bat,oc}}^{[i]})^2 - c_{\text{bat,rin}}^{[i]} R_{\text{bat,in}}^{[i]} P_{\text{bat}}^{[i]}}}{2} \quad (6.23)$$

The battery open circuit voltage and internal resistance at time instant  $t_0^{[i]}$  are denoted by  $V_{\text{bat.oc}}^{[i]}$  and  $R_{\text{bat.in}}^{[i]}$  and are evaluated at battery state of charge  $SoC^{[i]}$  at the beginning of the time interval  $i$ . The scaling factor  $c_{\text{bat.rin}}^{[i]}$  models possible battery failures resulting in an increase of internal resistance. The battery output current within the time interval  $i$  with  $t \in [t_0^{[i]}, t_0^{[i]} + dT^{[i]})$  is then defined as:

$$I_{\text{bat}}^{[i]} = \frac{V_{\text{bat.oc}}^{[i]} - \sqrt{(V_{\text{bat.oc}}^{[i]})^2 - c_{\text{bat.rin}}^{[i]} R_{\text{bat.in}}^{[i]} P_{\text{bat}}^{[i]}}}{2 c_{\text{bat.rin}}^{[i]} R_{\text{bat.in}}^{[i]}} \quad (6.24)$$

The battery state of charge  $SoC^{[i+1]}$  at the end of the time interval  $i$ , which is used as the initial condition for the calculation in the time interval  $i + 1$  can be defined as:

$$SoC^{[i+1]} = SoC^{[i]} - \frac{I_{\text{bat}}^{[i]} dT^{[i]}}{c_{\text{bat.q0}}^{[i]} Q_{\text{bat0}}} \quad (6.25)$$

The scaling factor  $c_{\text{bat.q0}}^{[i]}$  models possible battery failures resulting in a decrease of battery nominal capacity  $Q_{\text{bat0}}$ . The internal battery losses  $P_{\text{bat.loss}}^{[i]}$  can be modeled as the ohmic losses at the battery resistance:

$$P_{\text{bat.loss}}^{[i]} = c_{\text{bat.rin}}^{[i]} R_{\text{bat.in}}^{[i]} (I_{\text{bat}}^{[i]})^2 \quad (6.26)$$

Assuming that the battery started its operation at interval  $j = 1$ , the energy losses dissipated at the end of interval  $j = i$  can be defined as:

$$E_{\text{bat.loss}}^{[i]} = \sum_{j=1}^i P_{\text{bat.loss}}^{[j]} dT^{[j]} \quad (6.27)$$

Using the powertrain model as presented in this section, the propulsion energy required for completing a given driving trajectory can be estimated. In the next section, a concept and algorithm for the prediction of the driving trajectory at runtime based on electronic horizon is presented.

## 6.2. Driving Trajectory Prediction

For the prediction of propulsion energy required for completing a given driving mission, the knowledge about the route to a destination and about the traffic conditions is required. As shown in Section 2.7, based on digital map data, the electronic horizon describing the route ahead can be provided to vehicle applications [14, 39, 13]. For the transmission of map data to vehicle applications several protocols, e.g. ADASIS or ETSI LDM, exist

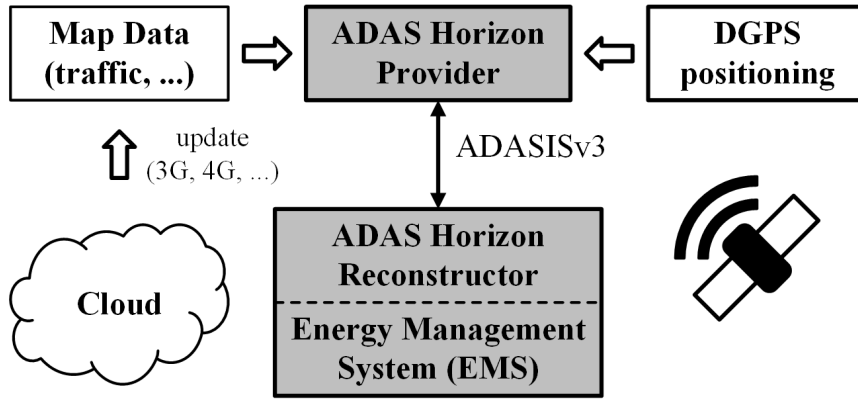


Figure 6.1.: Overview of system architecture for connected energy management.

[14, 42]. In the ADASIS protocol the ADAS horizon provider builds the interface to the control unit storing the map data. On the application side, the ADAS horizon reconstructor builds the interface and is responsible for receiving, unpacking and storing the map data. The transmission of the static map data in the second version of the protocol (ADASISv2) will be extended to the transmission of dynamic map data [41] in the third version (ADASISv3). This dynamic cloud-based map data can be frequently updated over a mobile network [120].

Depending on the level of map data usage, the vehicle applications can be classified into three categories: non-map, map-enhanced and map-enabled applications [40]. While non-map applications do not require map data for their functionality, map-enhanced applications can be improved by using the map data [40]. Map-enabled applications require map data as basic input for their functionality [40]. In the following subsection, a concept for the prediction of the driving trajectory required by the EMS for the control of powertrain and powertrain based on electronic horizon is proposed.

### 6.2.1. Concept for Driving Trajectory Prediction

The EMS proposed in this thesis adapts the power demand of powertrain loads, driving profile and driving destination with the main goal of safety-based range extension. Accurate prediction of the propulsion energy required for completing a given driving mission as well as the driving duration for the prediction of energy required for the supply of powertrain loads is of high importance for the functionality of the proposed EMS, which is a map-enabled application. The overview of the proposed energy management architecture is depicted in Fig. 6.1.

The ADAS horizon provider receives the information about the route to the vehicle destination via the cloud connection as well as the current vehicle position via the DGPS

positioning module. The data is then transmitted using the ADASISv3 protocol to the energy management application, which is received by the corresponding ADAS horizon reconstructor module.

The overall propulsion energy required for completing a given driving mission depends on the velocity, acceleration and slope profile as defined in Section 6.1. The duration of a driving mission is additionally dependent on the number of stops on the way to a destination with the corresponding stop times. Therefore, for the prediction of propulsion energy and of driving time, the electronic horizon profiles as depicted in Fig. 6.2 are used. Each electronic horizon profile consists of two arrays storing the distance offsets and the corresponding requested route data. The offset value describes the position of the route relative to its beginning ( $offset = 0$ ), at which the profile entry becomes valid. It is assumed that the profile value between two offsets is constant.

The proposed EMS can degrade the driving profile for reducing the required propulsion energy by changing the driving velocity and acceleration. Therefore, lower and upper bounds for velocity and acceleration for each segment of the route to a destination should be defined, which are stored in the  $eh_{lim}$  profile. The upper bound  $v_{max}^{[i]}$  for velocity describes the road speed limit. Using the cloud-based map data, the upper limit can be also defined as a function of daytime describing the expected average velocity on the route segment due to the traffic condition.

The lower bound  $v_{min}^{[i]}$  for the velocity can be defined as a minimum tolerated velocity on a specific road type, e.g. urban or highway. Depending on the use case and required vehicle dynamics, lower bound  $a_{min}^{[i]}$  and upper bound  $a_{max}^{[i]}$  for acceleration can be defined. By introducing two variables  $dpdv$  (**d**rivering **p**rofile **d**egradation **v**elocity (dpdv)) and  $dpda$  (**d**rivering **p**rofile **d**egradation **a**cceleration (dpda)), the set velocity  $v_{ems}^{[i]}$  and acceleration  $a_{ems}^{[i]}$  for each segment  $i$  of the route can be defined as:

$$v_{ems}^{[i]} = v_{min}^{[i]} + dpdv (v_{max}^{[i]} - v_{min}^{[i]}), \quad \text{with } dpdv \in [0..1] \quad (6.28a)$$

$$a_{ems}^{[i]} = a_{min}^{[i]} + dpda (a_{max}^{[i]} - a_{min}^{[i]}), \quad \text{with } dpda \in [0..1] \quad (6.28b)$$

The slope profile  $eh_{slope}$  stores the information about the road slope. The stops profile  $eh_{stops}$  stores the position of the stops on the way to the destination with the corresponding average stop time  $dT_{stop}$ . At a stop position, the propulsion energy is assumed to be zero. Since the powernet loads are generally not switched off at an intermediate stop, the average waiting time at a stop position influences the overall vehicle energy consumption.

Additionally to the electronic horizon profiles depicted in Fig. 6.2, a profile containing the

velocity/acceleration limit profile					slope profile		stops profile	
offset	$v_{\min}$	$v_{\max}$	$a_{\min}$	$a_{\max}$	offset	$sl$	offset	$dT_{\text{stop}}$
[km]	[km/h]	km/h	[m/s <sup>2</sup> ]	[m/s <sup>2</sup> ]	[km]	[%]	[km]	[s]
0	60	120	0.5	2.7	0	2.3	0	20
3.4	20	30	0.5	1.5	1.2	4	0.8	15
...	...	...	...	...	...	...	...	...
56.7	70	100	1.2	2.4	45.3	-2	48.9	30

Figure 6.2.: Electronic horizon profiles used for connected energy management.

position of safe stop locations for the degradation of the driving destination as proposed in Fig. 4.1 is required. For a given set of degradation variables for driving profile and destination, a driving trajectory can be estimated. An algorithm for the online prediction of the driving trajectory based on the electronic horizon is presented in the next subsection.

### 6.2.2. Algorithm for Online Driving Trajectory Prediction

The proposed algorithm for the prediction of the driving trajectory consists basically of three main steps. In the first step the received electronic horizon profiles are preprocessed and combined to a single profile allowing a simplified estimation of the required propulsion energy. In the second step the boundary conditions for the velocity at segment start and end are estimated for each segment  $i$ . In the last step, the velocity profile is estimated and stored in a format consisting of entries with constant acceleration, slope and corresponding duration.

According to the definition in (6.6) the average traction force within time interval  $i$  is a function of initial vehicle velocity  $v_0^{[i]}$ , road slope  $sl^{[i]}$  and required vehicle acceleration  $a_v^{[i]}$ . For constant velocity phases with  $a_v^{[i]}$  equal to 0, the required traction force is constant according to (6.6). The goal of the preprocessing step is therefore to merge the electronic horizon profiles  $\underline{eh}_{\text{lim}}$  for velocity and acceleration bounds,  $\underline{eh}_{\text{slope}}$  for slope and  $\underline{eh}_{\text{stops}}$  for stops to a combined profile  $\underline{eh}_{\text{comb}}$ . As depicted in Fig. 6.3 each entry  $i$  of the combined profile consists of constant values for the set velocity  $v_{\text{ems}}^{[i]}$  and acceleration  $a_{\text{ems}}^{[i]}$  calculated as defined in (6.28a) and (6.28b), slope value  $sl^{[i]}$  and the corresponding segment length  $ds^{[i]}$ . Only relevant values between the current vehicle position  $s_0$  and destination  $s_{\text{ssl}}$  ( $s_{\text{ssl}}$ , save stop location) are extracted.

After merging the electronic horizon profiles  $\underline{eh}_{\text{lim}}$  and  $\underline{eh}_{\text{slope}}$ , it is assumed that the combined electronic horizon profile  $\underline{eh}_{\text{comb}}$  consists of  $n_{\text{seg}}$  segments. Also stops are considered to be segments with length, set velocity and acceleration equal to zero. The  $n_{\text{stops}}$  entries

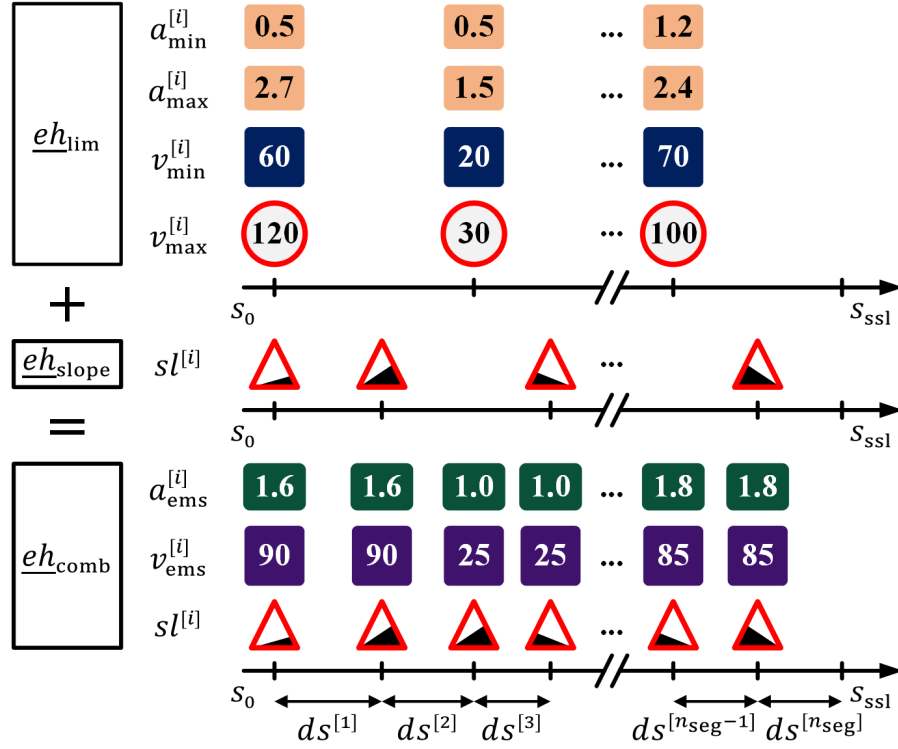


Figure 6.3.: Preprocessing of electronic horizon profiles.

from the stops profile  $\underline{eh}_{stops}$  are inserted into the combined profile  $\underline{eh}_{comb}$ . After inserting the stops, the combined profile  $\underline{eh}_{comb}$  has  $m_{seg}$  segments in total with  $m_{seg} \leq n_{seg} + 2n_{stops}$ .

The set velocity varies from segment to segment and the velocity profile should be calculated considering the changes from one segment to the next. Due to a given set acceleration  $a_{ems}^{[i]}$  and segment length  $ds^{[i+1]}$  it cannot be ensured that the set velocity  $v_{ems}^{[i]}$  within the segment  $i$  will be reached. Assuming a higher set velocity  $v_{ems}^{[i]}$  in segment  $i$  compared to  $v_{ems}^{[i+1]}$  in segment  $i+1$ , it might come to a case that after reaching  $v_{ems}^{[i]}$  in segment  $i$  it would not be possible to decelerate to  $v_{ems}^{[i+1]}$  in segment  $i+1$  with the given deceleration value  $a_{ems}^{[i]}$  in segment  $i$  due to the limited segment length  $ds^{[i+1]}$ .

Therefore, considering the segment length  $ds^{[i]}$  and given segment acceleration and deceleration  $|a_{ems}^{[i]}|$ , the segment start  $v_{start}^{[i]}$  and end velocity  $v_{end}^{[i]}$  for each segment should be estimated taking into account the required velocity changes between the segments. A two-stage iterative approach based on forward and reverse calculation for estimation of velocity boundary conditions for each segment is proposed as depicted in Fig. 6.4.

At first, starting with the current vehicle velocity  $v_0$ , the maximum possible start velocity  $v_{start,max}^{[i]}$  for each segment  $i$  is estimated in an iterative forward calculation. The value  $v_{start,max}^{[i]}$  describes the maximum velocity that can be reached at the end of segment  $i-1$  with the set acceleration  $a_{ems}^{[i-1]}$  starting from the initial segment velocity  $v_{start,frw}^{[i-1]}$

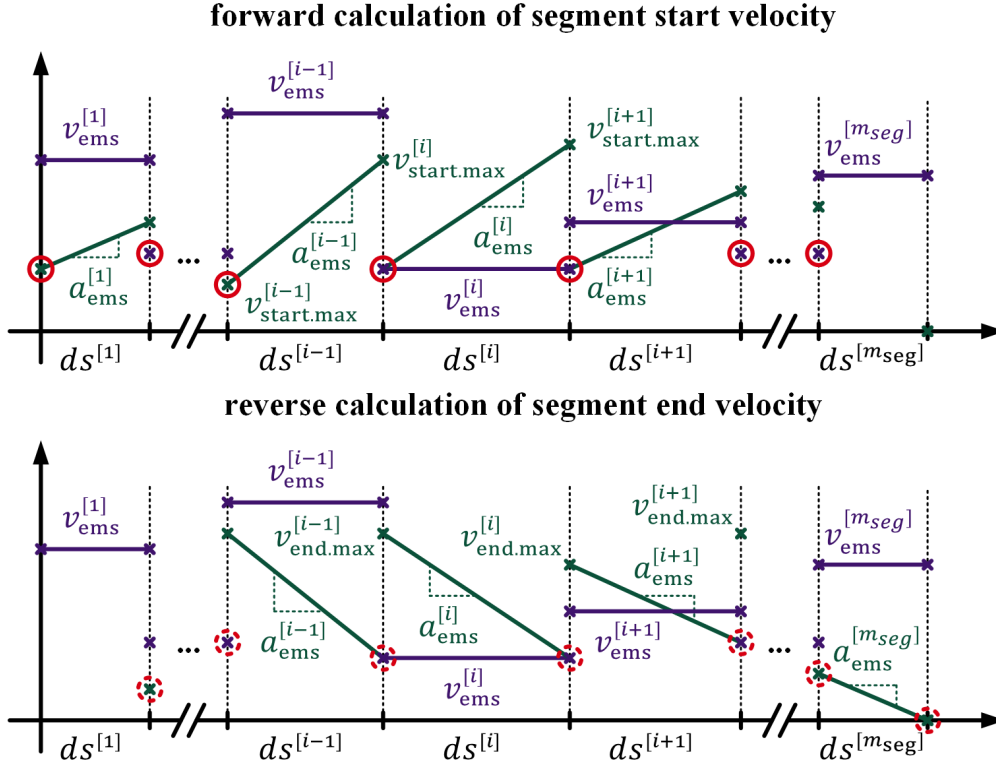


Figure 6.4.: Estimation of velocity bounds for driving trajectory segments.

estimated in the last iteration. Using the length  $ds^{[i-1]}$ , set acceleration  $a_{\text{ems}}^{[i-1]}$  and start velocity  $v_{\text{start.frw}}^{[i-1]}$  of the segment  $i - 1$ , the maximum start velocity  $v_{\text{start.max}}^{[i]}$  for segment  $i$  can be calculated as:

$$v_{\text{start.max}}^{[i]} = \sqrt{(v_{\text{start.frw}}^{[i-1]})^2 + 2 a_{\text{ems}}^{[i-1]} ds^{[i-1]}} \quad (6.29)$$

The start velocity for interval  $i$  estimated in the forward calculation can be then defined as the minimum out of the maximum possible start velocity  $v_{\text{start.max}}^{[i]}$  for segment  $i$  and set velocities  $v_{\text{ems}}^{[i-1]}$  for the preceding segment and  $v_{\text{ems}}^{[i]}$  for the current segment:

$$v_{\text{start.frw}}^{[i]} = \begin{cases} \min(v_{\text{start.max}}^{[i]}, v_{\text{ems}}^{[i-1]}, v_{\text{ems}}^{[i]}), & \text{with } i \in \{2..m_{\text{seg}}\} \\ v_0, & \text{with } i = 1 \end{cases} \quad (6.30)$$

In the same way, the maximum end velocity  $v_{\text{end.max}}^{[i]}$  for each segment starting with velocity equal to zero at the end of a driving mission can be estimated in an iterative reverse calculation. The value  $v_{\text{end.max}}^{[i]}$  describes the maximum velocity at the end of segment  $i$ , from which a deceleration to the end velocity  $v_{\text{end.rev}}^{[i+1]}$  of the segment  $i + 1$  estimated in the last iteration is possible with the set deceleration value  $a_{\text{ems}}^{[i+1]}$ . Using the length  $ds^{[i+1]}$ , set deceleration  $a_{\text{ems}}^{[i+1]}$  and end velocity  $v_{\text{end.rev}}^{[i+1]}$  of the segment  $i + 1$ , the maximum end



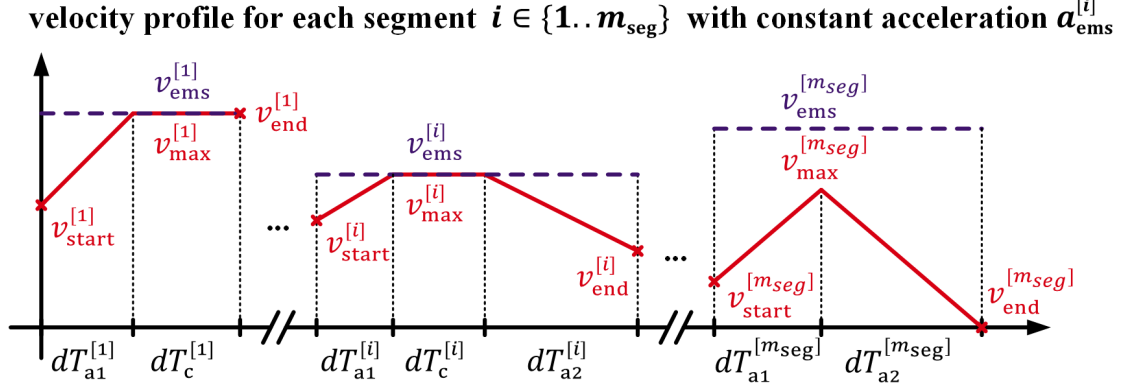


Figure 6.5.: Estimation of velocity profile.

velocity  $v_{\text{end.max}}^{[i]}$  for segment  $i$  can be calculated as:

$$v_{\text{end.max}}^{[i]} = \sqrt{(v_{\text{end.rev}}^{[i+1]})^2 + 2 a_{\text{ems}}^{[i+1]} ds^{[i+1]}} \quad (6.31)$$

The end velocity for interval  $i$  estimated in the reverse calculation can be then defined as the minimum out of the maximum possible end velocity  $v_{\text{end.max}}^{[i]}$  for segment  $i$  and set velocities  $v_{\text{ems}}^{[i]}$  for the current segment and  $v_{\text{ems}}^{[i+1]}$  for the subsequent segment:

$$v_{\text{end.rev}}^{[i]} = \begin{cases} \min(v_{\text{end.max}}^{[i]}, v_{\text{ems}}^{[i]}, v_{\text{ems}}^{[i+1]}), & \text{with } i \in \{1..m_{\text{seg}} - 1\} \\ 0, & \text{with } i = m_{\text{seg}} \end{cases} \quad (6.32)$$

The start velocity  $v_{\text{start}}^{[i]}$  for segment  $i$  can be then calculated as the minimum out of the start velocity  $v_{\text{start.frw}}^{[i]}$  estimated in forward calculation for segment  $i$  and the end velocity  $v_{\text{end.rev}}^{[i-1]}$  estimated in reverse calculation for segment  $i - 1$ :

$$v_{\text{start}}^{[i]} = \begin{cases} \min(v_{\text{start.frw}}^{[i]}, v_{\text{end.rev}}^{[i-1]}), & \text{with } i \in \{2..m_{\text{seg}}\} \\ v_0, & \text{with } i = 1 \end{cases} \quad (6.33)$$

The end velocity  $v_{\text{end}}^{[i]}$  for segment  $i$  can be calculated as the minimum out of the start velocity  $v_{\text{start.frw}}^{[i+1]}$  estimated in forward calculation for segment  $i + 1$  and the end velocity  $v_{\text{end.rev}}^{[i]}$  estimated in reverse calculation for segment  $i$ :

$$v_{\text{end}}^{[i]} = \begin{cases} \min(v_{\text{start.frw}}^{[i+1]}, v_{\text{end.rev}}^{[i]}), & \text{with } i \in \{1..m_{\text{seg}} - 1\} \\ 0, & \text{with } i = m_{\text{seg}} \end{cases} \quad (6.34)$$

After the velocity boundary conditions are determined, a velocity profile can be derived for each segment  $i$ . For this, as depicted in Fig. 6.5, each segment is divided into three phases:

(1) acceleration phase with duration  $dT_{a1}^{[i]}$ , (2) constant velocity phase with duration  $dT_c^{[i]}$  and (3) deceleration phase with duration  $dT_{a2}^{[i]}$ .

The duration of acceleration ( $dT_{a1}^{[i]}$ ), constant velocity ( $dT_c^{[i]}$ ) and deceleration ( $dT_{a2}^{[i]}$ ) phase is estimated in a way, that the integral of the segment velocity profile equals to the segment length  $ds^{[i]}$  by considering the boundary conditions for segment start ( $v_{start}^{[i]}$ ) and end ( $v_{end}^{[i]}$ ) velocity. As illustrated for the segment  $m_{seg}$  in Fig. 6.5, if the segment length  $ds^{[i]}$  is too short, it might come to a case that the set velocity  $v_{ems}^{[i]}$  cannot be reached with the set acceleration  $a_{ems}^{[i]}$ . Therefore, without considering the set velocity, a peak velocity  $v_{peak}^{[i]}$  is calculated first with the assumption, that the velocity profile of segment  $i$  consists of acceleration (from  $v_{start}^{[i]}$  to  $v_{peak}^{[i]}$ ) and deceleration (from  $v_{peak}^{[i]}$  to  $v_{end}^{[i]}$ ) phase only. For a given length  $ds^{[i]}$ , start velocity  $v_{start}^{[i]}$ , end velocity  $v_{end}^{[i]}$  and acceleration/deceleration  $|a_{ems}^{[i]}|$ , the peak velocity  $v_{peak}^{[i]}$  for the segment  $i$  can be calculated as:

$$v_{peak}^{[i]} = \sqrt{a_{ems}^{[i]} ds^{[i]} + \frac{(v_{start}^{[i]})^2 + (v_{end}^{[i]})^2}{2}} \quad (6.35)$$

The maximum velocity  $v_{max}^{[i]}$  that will be reached within the segment  $i$  can be then calculated as:

$$v_{max}^{[i]} = \min(v_{ems}^{[i]}, v_{peak}^{[i]}) \quad (6.36)$$

The duration of acceleration phase  $dT_{a1}^{[i]}$  is then calculated as:

$$dT_{a1}^{[i]} = \begin{cases} \frac{v_{max}^{[i]} - v_{start}^{[i]}}{a_{ems}^{[i]}}, & \text{for } v_{max}^{[i]} > v_{start}^{[i]} \\ 0, & \text{for } v_{max}^{[i]} = v_{start}^{[i]} \end{cases} \quad (6.37)$$

The duration of deceleration phase  $dT_{a2}^{[i]}$  is then calculated as:

$$dT_{a2}^{[i]} = \begin{cases} \frac{v_{max}^{[i]} - v_{end}^{[i]}}{a_{ems}^{[i]}}, & \text{for } v_{max}^{[i]} > v_{end}^{[i]} \\ 0, & \text{for } v_{max}^{[i]} = v_{end}^{[i]} \end{cases} \quad (6.38)$$

The duration of constant velocity phase  $dT_c^{[i]}$  is then calculated as:

$$dT_c^{[i]} = \frac{1}{2} \left( \frac{2 ds^{[i]} - dT_{a1}^{[i]} v_{start}^{[i]} - dT_{a2}^{[i]} v_{end}^{[i]}}{v_{max}^{[i]}} - dT_{a1}^{[i]} - dT_{a2}^{[i]} \right) \quad (6.39)$$

The predicted driving trajectory from the vehicle current position  $s_0$  to the destination  $s_{ss1}$

driving trajectory

$i$	$dT_{\text{seg}}^{[i]}$	$a_{\text{ems}}^{[i]}$	$sl^{[i]}$
[-]	[s]	[m/s <sup>2</sup> ]	[%]
1	1.2	0.7	2.0
...	...	...	...
$i-1$	1.4	-0.5	-1.5
$i$	0.8	0.0	0.5
$i+1$	1.7	1.0	-1.0
...	...	...	...
$n_{\text{traj}}$	1.1	-0.5	-2.5

Figure 6.6.: Format of predicted driving trajectory.

consists then out of entries with constant acceleration and slope value with corresponding duration as depicted in Fig. 6.6. Since only the acceleration, constant velocity and deceleration phases with a duration greater zero are relevant, the total amount of entries in the predicted driving trajectory equals  $n_{\text{traj}}$  with  $n_{\text{traj}} \leq 3 n_{\text{seg}}$ . The time  $dT_{\text{ssl}}$  required for completing the driving mission can be calculated as:

$$dT_{\text{ssl}} = \sum_{i=1}^{n_{\text{traj}}} dT_{\text{seg}}^{[i]} \quad (6.40)$$

Depending on the powertrain topology, the propulsion energy required for completing the predicted driving trajectory can be estimated. In Section 6.3, an algorithm for the estimation of the propulsion energy for a powertrain topology with a single traction motor is presented. This algorithm is then extended to the prediction of the propulsion energy for powertrain topologies with multiple traction motors under consideration of optimal torque distribution in Section 6.4.

### 6.3. Prediction for Powertrain with Single Motor

After predicting a driving trajectory from the current vehicle position to the destination as presented in Section 6.2, the propulsion energy required for completing it can be estimated. Several approaches for the prediction of driving range and corresponding propulsion energy based on geographical information like speed limits, weather conditions and driver behavior exist. In [121], a smartphone application is presented estimating the possible driving range and proposing eco routes using the basic battery data like state of charge or by measuring the battery current and voltage for calculation of energy consump-

tion. The authors of [98] propose an algorithm for the range prediction based on route information clustered in homogeneous segments with constant parameters influencing the power losses by applying stochastic methods. The segments are divided into representative groups and based on the learned data for energy losses estimated while driving a tour, a look-up table with normalized energy losses for each group is created, which is then used for range prediction. In [97, 96], a trip management is proposed estimating the optimal velocity and acceleration trajectory based on dynamic programming. While the trip management proposes the optimal velocity limits online, optimal acceleration and recuperation profiles are estimated offline and stored in a look-up table. The described algorithms are designed for the range prediction in fault-free operation and do not consider powertrain failure states. In the next subsection, an algorithm for the prediction of propulsion energy at runtime required for completing a given driving mission in both, normal and failure case operation, is proposed.

### 6.3.1. Online Propulsion Energy Prediction

The algorithm for estimation of propulsion energy required for completing a given driving mission uses the online diagnostic data of powertrain components and is therefore well suited for range prediction in normal and failure case operation. The propulsion energy is calculated by evaluating the powertrain model as presented in Section 6.1 for each segment of the driving trajectory in the format as depicted in Fig. 6.6. For the calculation, a method based on quasistatic simulation [29] is proposed. Instead of dividing the entire driving trajectory in equal calculation steps  $dT_{\text{calc}}$ , a variable calculation step depending on the segment acceleration is proposed. According to the definition in (6.6), the traction force is a function of velocity. For the set acceleration  $a_{\text{ems}}^{[i]}$  equal to zero, the traction force within the trajectory segment  $i$  remains constant. Taking the segment duration as calculation step for the segments with set acceleration equal zero results in a small calculation error since the battery internal resistance and open circuit voltage depend on state of charge, which is updated only at the end of the segment in this case. By accepting this calculation error, the calculation burden can be reduced significantly, enabling so the online execution of the proposed algorithm.

For acceleration and deceleration phases with required constant acceleration or deceleration  $|a_{\text{ems}}^{[i]}|$ , the vehicle velocity changes within the trajectory segment  $i$ . For increasing the prediction precision, the calculation of propulsion energy in these segments can be divided into  $j_{\text{sub}}^{[i]}$  subintervals. The number of subintervals is set as a function of a minimum defined calculation time step  $dT_{\text{min}}$ . The powertrain state variables required for calculation of propulsion energy are then updated after each subinterval calculation. The

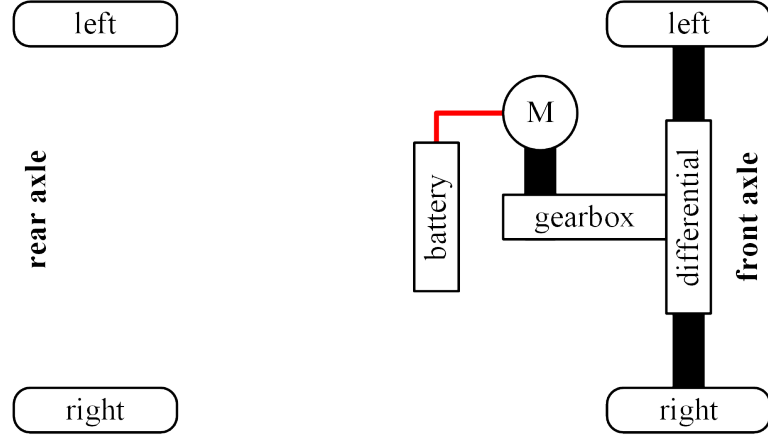


Figure 6.7.: Topology of electric powertrain with single motor.

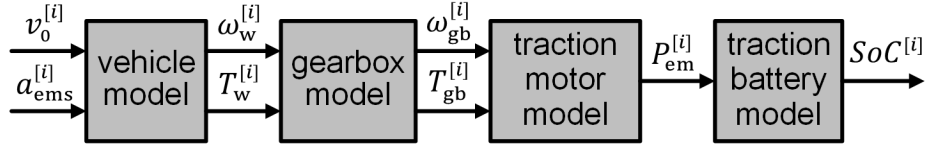


Figure 6.8.: Model of electric powertrain with single motor.

variable calculation time step  $dT_{\text{calc}}^{[i]}$  for the trajectory segment  $i$  with duration  $dT_{\text{seg}}^{[i]}$  can be then defined as:

$$dT_{\text{calc}}^{[i]} = \begin{cases} \frac{dT_{\text{seg}}^{[i]}}{j_{\text{sub}}^{[i]}}, & \text{for } a_{\text{ems}}^{[i]} \neq 0 \text{ and } j_{\text{sub}}^{[i]} = \text{ceil}\left(\frac{dT_{\text{seg}}^{[i]}}{dT_{\text{min}}}\right) \\ dT_{\text{seg}}^{[i]}, & \text{for } a_{\text{ems}}^{[i]} = 0 \end{cases} \quad (6.41)$$

The parameter  $dT_{\text{min}}$  has impact on the overall calculation time as well as on the quality of prediction. Therefore, it should be set depending on the available computational resources and required prediction precision. The total number  $n_{\text{calc}}$  of calculation subintervals or steps for propulsion energy predicted for a given driving trajectory with  $n_{\text{traj}}$  segments is defined as:

$$n_{\text{calc}} = \sum_{i=1}^{n_{\text{traj}}} j_{\text{sub}}^{[i]} \quad (6.42)$$

An exemplary powertrain topology with single traction motor is depicted in Fig. 6.7. It consists of a traction battery, electrical traction motor (M) and a gearbox with constant transmission ratio. The mechanical power provided by the motor at the gearbox input shaft is transmitted to the wheels, which are connected via a differential to the gearbox output shaft. The propulsion energy prediction is based on the powertrain model presented in Section 6.1. The data flow between the model elements is depicted in Fig. 6.11.

The powertrain state variables measured by onboard sensors are taken as initial conditions for the first calculation step  $i$  ( $i \in \{1..n_{\text{calc}}\}$ ). Using the vehicle velocity  $v_0^{[i]}$  at the start of calculation step  $i$  and set acceleration  $a_{\text{ems}}^{[i]}$ , the required wheel torque  $T_{\text{w}}^{[i]}$  and wheel speed  $\omega_{\text{w}}^{[i]}$  are calculated with the vehicle model using (6.7a) and (6.7b). The wheel torque and speed are then used for the calculation of required torque  $T_{\text{gb}}^{[i]}$  and speed  $\omega_{\text{gb}}^{[i]}$  at the gearbox input shaft using (6.10) and (6.11). The electrical power  $P_{\text{em}}^{[i]}$  of the traction motor is estimated with the electrical machine model using (6.21). The battery state of charge  $SoC^{[i+1]}$  at the end of calculation step  $i$  and the battery current  $I_{\text{bat}}^{[i]}$  can be then estimated using (6.25) and (6.24). The predicted powertrain state at the end of calculation step  $i$  is then used as the initial condition for the subsequent calculation step  $i + 1$  and the initial vehicle velocity  $v_0^{[i+1]}$  is set to:

$$v_0^{[i+1]} = v_0^{[i]} + a_{\text{ems}}^{[i]} dT_{\text{calc}}^{[i]} \quad (6.43)$$

In the next subsection, simulation results for the exemplary powertrain topology as depicted in Fig. 6.7 verifying the precision and suitability for online execution of the proposed algorithm are provided.

### 6.3.2. Simulation Results for Powertrain with Single Motor

The prediction of propulsion energy required for completing a given driving cycle consists of two main steps. In the first step, based on the electronic horizon, a driving trajectory from the current vehicle position  $s_0$  to the vehicle destination  $s_{\text{ssl}}$  as a function of degradation variables  $dpdv$  for velocity and  $dpda$  for acceleration is approximated. For the example presented in this section, the vehicle is assumed to be at the beginning of the driving route with  $s_0 = 0$  km and the vehicle destination is set to  $s_{\text{ssl}} = 50$  km. The electronic horizon profile  $eh_{\text{lim}}$  containing the velocity and acceleration bounds for the route ahead consists of 85 entries, the slope profile  $eh_{\text{slope}}$  of 501 and the stops profile  $eh_{\text{stops}}$  of 35 entries. The electronic horizon used for the simulation in this section as well as the vehicle and gearbox parameters are listed in Appendix A. The driving trajectory estimated with the algorithm presented in Section 6.2 using these electronic horizon profiles consists in total of 694 entries.

Two different values, 25 % and 75 % for the degradation variables  $dpdv$  and  $dpda$  are used. The duration of the driving mission for  $dpdv = dpda = 25$  % is approx. 124 min with an average velocity of  $24.2 \frac{\text{km}}{\text{h}}$ . For  $dpdv = dpda = 75$  %, the driving mission is completed after approx. 80 min with an average velocity equal to  $37.5 \frac{\text{km}}{\text{h}}$ . The corresponding velocity ( $v_v$ ), distance ( $s_v$ ) and slope ( $sl$ ) profiles are depicted in Fig. 6.9.

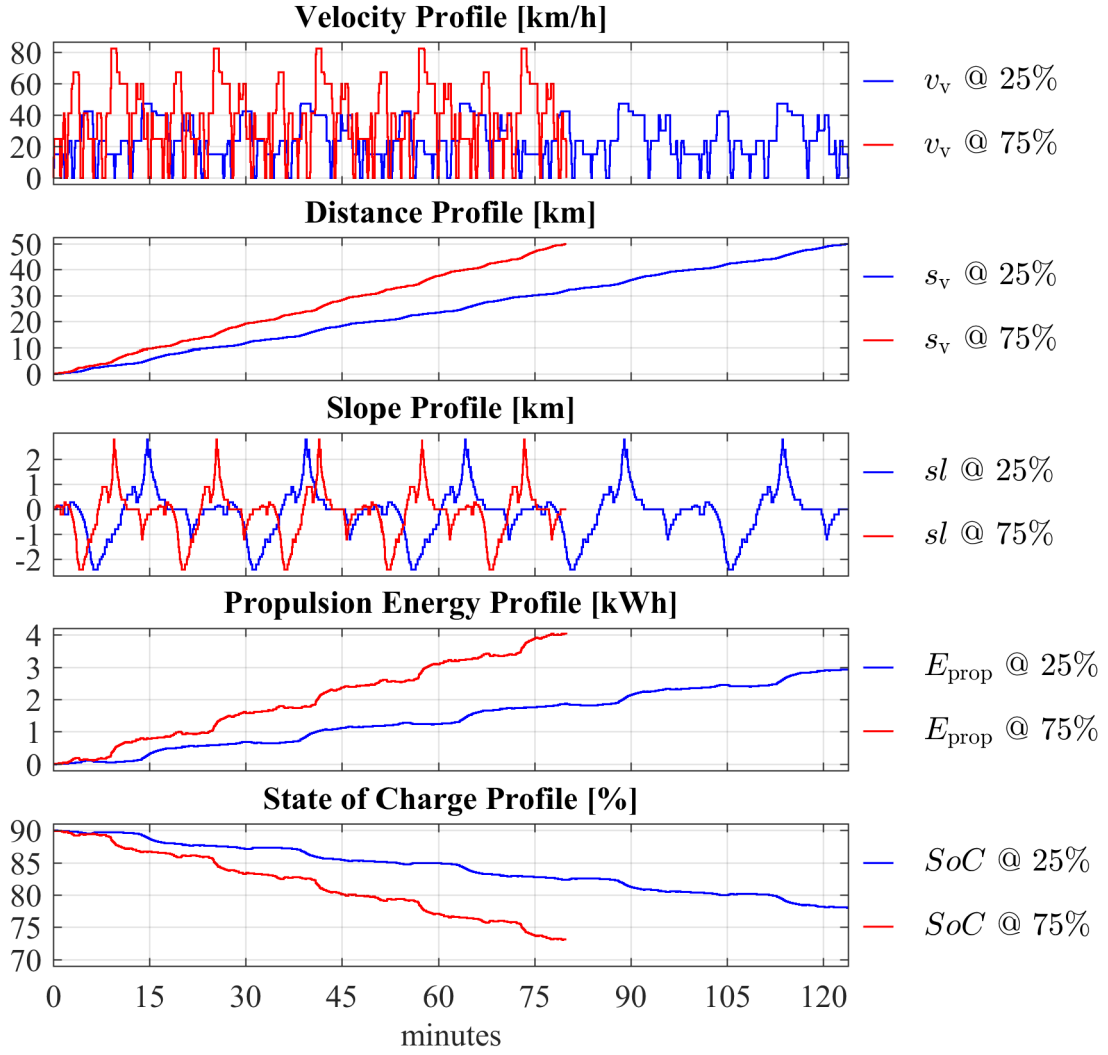


Figure 6.9.: Simulation results for powertrain with single motor.

In the second step of propulsion energy prediction, the powertrain model is calculated for the given driving trajectory as presented in Section 6.3.1. For the example in this section, a lithium-ion battery with a nominal voltage of approx. 355 V and capacity of 63 Ah is assumed. The initial state of charge is set to 90 % and the battery temperature to 25 °C. The battery discharge ( $SoC$ ) and propulsion energy ( $E_{prop}$ ) curve are depicted in Fig. 6.9. For the evaluation of the proposed propulsion energy prediction algorithm, reference values are calculated without applying the variable calculation time step  $dT_{calc}^{[i]}$  as defined in (6.41). Instead, the battery state of charge  $SoC_{qs}$  at the end of the driving mission and total required propulsion energy  $E_{prop,qs}$  are estimated with a time step according to the first case in (6.41), which is similar to a quasistatic simulation. The estimated values with the corresponding evaluation time  $dT_{eval,qs}$  are summarized in Table 6.1.

The evaluation time is measured as an average out of 1000 runs on an Intel i7 CPU using

Table 6.1.: Simulation results using quasistatic approach.

$dpdv$	$dpda$	$E_{\text{prop.qs}}$	$SoC_{\text{qs}}$	$dT_{\text{eval.qs}}$
25 %	25 %	2.929 kWh	78.070 %	19.10 ms
75 %	75 %	4.033 kWh	73.149 %	13.96 ms

the MATLAB functions *tic* and *toc*. The evaluation time covers both, the approximation of the driving trajectory and propulsion energy prediction. Due to the longer driving duration, the calculation time for  $dpdv = dpda = 25\%$  is higher than for degradation variables equal to 25%. Since the average driving velocity is smaller, the total consumed propulsion energy for  $dpdv = dpda = 25\%$  is lower than for 75%. By using the variable time step as proposed in (6.41), the computational time can be significantly reduced while achieving approximately the same results for predicted battery state of charge at the end of the driving mission and consumed propulsion energy.

Simulation results using different minimum calculation time steps  $dT_{\text{min}}$  for  $dpdv = dpda = 25\%$  and 75% are summarized in Tables 6.2 and 6.3. In the second column, the relative deviation  $\Delta E_{\text{prop.qs}}$  of predicted value  $E_{\text{prop}}$  to the consumed propulsion energy  $E_{\text{prop.qs}}$  estimated with the quasistatic approach is given. The relative deviation  $\Delta SoC_{\text{qs}}$  of final battery state of charge and  $\Delta dT_{\text{eval.qs}}$  of time required for evaluation are summarized in the third and fourth columns. The relative deviation  $\Delta a_{\text{qs}}$  of a value  $a_{\text{pred}}$  compared to the value  $a_{\text{qs}}$  estimated with the quasistatic approach is calculated as:

$$\Delta a_{\text{qs}} = \frac{a_{\text{pred}}}{a_{\text{qs}}} - 1 \quad (6.44)$$

With the proposed variable time step, the computational time can be reduced in this example up to 77% for  $dpdv = dpda = 25\%$  and up to 70% for degradation variables equal to 75%, while the prediction precision remains approximately the same. Due to very low computational burden, the proposed energy prediction algorithm is well suited for embedded online execution.

Table 6.2.: Deviation of predicted values for  $dpdv = dpda = 25\%$ .

$dT_{\text{min}}$	$\Delta E_{\text{prop.qs}}$	$\Delta SoC_{\text{qs}}$	$\Delta dT_{\text{eval.qs}}$
1 s	0.0 %	0.0 %	-66.80 %
5 s	-0.054 %	0.009 %	-75.58 %
10 s	-0.115 %	0.020 %	-77.07 %

The estimation of required propulsion energy for a powertrain topology with a single motor is straightforward, since there is only one actor providing the required torque. In powertrain topologies with multiple traction motors, the powertrain losses and therefore



Table 6.3.: Deviation of predicted values for  $dpdv = dpda = 75\%$ .

$dT_{\min}$	$\Delta E_{\text{prop. qs}}$	$\Delta SoC_{\text{qs}}$	$\Delta dT_{\text{eval. qs}}$
1 s	0.0 %	0.0 %	-56.82 %
5 s	-0.146 %	0.045 %	-67.90 %
10 s	-0.431 %	0.136 %	-70.14 %

also the predicted driving range depend on the torque distribution strategy between the individual motors. In the next section, an algorithm for range extension and prediction of propulsion energy in powertrain topologies with multiple traction motors based on the theory of optimal control is proposed.

## 6.4. Prediction for Fail-Operational Powertrain with Multiple Motors

With introduction of automated driving systems, the individual mobility is expected to be changed. According to a technical report published by Roland Berger, approximately one third of worldwide driven kilometers in 2030 will be accomplished by robocabs [1]. Since no driver is expected to be present in robocabs, these automated driving systems must be able to cope with all driving situations without passenger interaction in defined use cases for high driving automation and in all use cases for full driving automation [6]. The concept of safety-based range extension was introduced in Section 4.1, meaning the optimization of powertrain and powernet control in a way allowing to arrive at the safest possible location for the passengers also in case of a failure. In powertrain topologies with a single traction motor, the propulsion functionality might not be provided in case of a single failure, e.g. if the traction motor or the traction battery fails. This would result in limited possibilities for safe stop locations that can be reached, since only coasting would be available. In best case, assuming no uphill road, the rightmost lane could be reached with functional braking and steering.

For the use of robocabs as a mobility service, a certain degree of fail-operability might be expected by the customers. A fail-operational powertrain topology would not only increase the acceptance of automated driving systems like robocabs, but would also provide increased safety for the passengers, since also in case of a single failure, at least degraded propulsion functionality would be still available. In this case a vehicle breakdown at an unsecured location, e.g. in the middle of a crossroads or on a highway, could be avoided.

A fail-operational system provides a minimum level of service required for safety also in case of failures [100], which is achieved by fault tolerance. For fail-operability of a

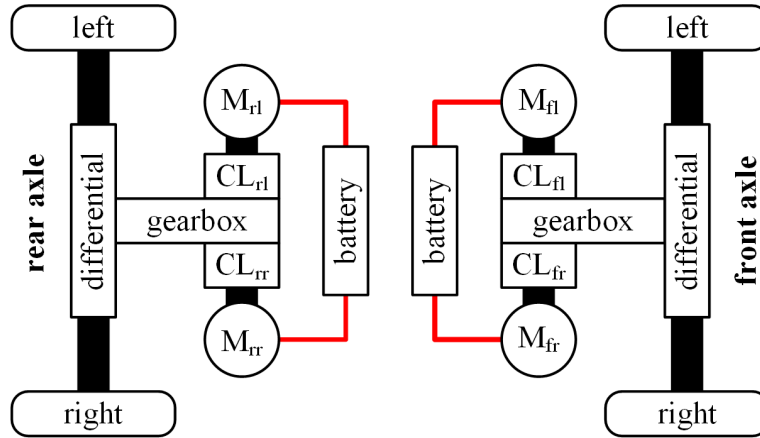


Figure 6.10.: Topology of fail-operational electric powertrain with multiple motors.

propulsion system in an electric vehicle, redundant traction motors and batteries are required. The fail-operational powertrain topology used for further analysis in this work is depicted in Fig. 6.10. It consists of two independent electric axles. Each axle has two traction motors which are connected via clutches to a dual input shaft of a gearbox with constant transmission ratio (one speed gearbox). The traction motors at each axle are supplied by an independent traction battery, which makes the powertrain system tolerant to battery failures. In case of a motor failure, each motor can be disengaged with a corresponding clutch and the traction provided by the remaining functional motors.

In addition to fail-operability of a powertrain topology with multiple traction motors, also the overall driving efficiency can be increased, since new degrees of freedom arise for the powertrain control due to redundancy in components. The authors of [15] proposed a control strategy for a front- and rear-wheel driven electric vehicle improving the driving efficiency by appropriate torque distribution between the front and rear motor. In high torque regions, the requested torque is distributed equally between the motors. In low torque regions, it is checked online whether the powertrain losses, calculated with the motor efficiency map, can be reduced by disengaging one of the motors. With a similar approach, a control strategy for an axle individually propelled powertrain topology increasing the driving efficiency is proposed in [16, 82]. Using offline optimization for minimization of powertrain losses, a look-up table containing optimal torque distribution factor between front and rear axle as a function of motor speed and requested torque is generated, which is then used for online optimal control increasing the energy efficiency and comfort [16]. In addition, for avoiding frequent disengaging of one motor with a clutch, what also results in power losses, a penalty function for disengaging is introduced. Further control strategies for different types of powertrain topologies with the main goal of driving efficiency increase were proposed. The authors of [86] consider for example a

three motor powertrain topology with two in-wheel motors at the rear and one motor at the front axle. Control strategies for powertrain topologies with four in-wheel motors can be found e.g. in [85, 84, 83]).

The referenced control strategies for torque distribution between multiple traction motors have in common that they are designed for the normal operation, while the operation in failure case is not covered. Additionally, only a single traction battery as a source for power supply of traction motors is considered, making the control not tolerant to failures of traction battery. Three main contributions proposed in this work are presented in the following sections. New requirements and control goals of fail-operational powertrain for automated driving are discussed in Section 6.4.1. In Section 6.4.2, a concept for the propulsion energy prediction based on the proposed control strategy for fail-operational powertrain is introduced. An algorithm suitable for online execution of the control strategy combined with the propulsion energy prediction is presented in Section 6.4.3. Simulation results verifying the functionality and suitability for online execution of the proposed algorithm for the powertrain control and propulsion energy prediction are provided in Section 6.4.4 and 6.4.5.

### 6.4.1. Optimal Control Strategy for Fail-Operational Powertrain

The strategy proposed for the control of a fail-operational powertrain is based on the concept of safety-based range extension. The main goal is to adapt the control strategy to the current powertrain state and to enable the transition of the automated driving system to the safest possible position. As already explained in the introduction to this section, the powertrain losses can be minimized by appropriate torque distribution, extending so the driving range. Therefore, the first goal for the control of the fail-operational powertrain is to minimize the overall driving efficiency.

In the powertrain topology as depicted in Fig. 6.10, both traction batteries are independent and not connected electrically to each other. It is assumed that one traction motor, e.g.  $M_{\text{fl}}$ , has the best efficiency compared to the remaining motors. Therefore, the minimization of powertrain losses will result in increased operation of motor  $M_{\text{fl}}$ . Since the traction batteries do not have an electrical connection, the front battery will be discharged in this case more than the rear battery. In extreme cases, depending on the efficiency map of the individual traction motors, the minimization of powertrain losses can result in the case that the battery supplying the motors with better efficiency will be discharged, while the other battery remains fully charged as long as the first battery is not fully empty. In this hypothetical example, a breakdown of the fully charged battery would result in a breakdown of the automated driving system, since no energy resources would be available

for the propulsion. Therefore, to ensure approximately the same driving range in case of a breakdown of one battery, the independent traction batteries should be discharged approximately symmetrically during the entire driving mission, which is the second goal of the proposed control strategy.

It is again assumed that the traction motor  $M_{fl}$  has the best efficiency compared to the other motors. Considering only the minimization of power losses would again result in increased operation of motor  $M_{fl}$ . This would also lead to increased heating of this motor, which could result in faster aging. Therefore, it is proposed to balance the energy dissipated by each motor, ensuring so approximately equal heating and aging of the traction motors. The balancing of the motor losses can be applied between the left and right traction motors as well as between the front and rear axle. With a similar argumentation, considering the heating and aging of the traction batteries, balancing of the energy dissipated by each traction battery is also proposed as the goal for the control of fail-operational powertrain.

Summing up the argumentation presented above, five objectives for the control of fail-operational powertrain are proposed:

- 1<sup>st</sup> objective: increase of powertrain efficiency
- 2<sup>nd</sup> objective: symmetrical discharge of independent traction batteries
- 3<sup>rd</sup> objective: balancing of energy losses dissipated by left and right traction motor
- 4<sup>th</sup> objective: balancing of energy losses dissipated by motors at front and rear axle
- 5<sup>th</sup> objective: balancing of energy losses dissipated by independent traction batteries

For achieving these objectives, a control strategy for the fail-operational powertrain based on the theory of optimal control is proposed. Using the powertrain model as presented in Section 6.1, for each goal an objective function can be defined. The overview of the model used for the fail-operational powertrain topology depicted in Fig. 6.10 is given in Fig. 6.11 with the data flow between the component models within time interval  $i$  with  $t \in [t_0^{[i]}, t_0^{[i]} + dT^{[i]}]$ .

Using the initial vehicle velocity  $v_0^{[i]}$  at the beginning of the interval  $i$  and the required acceleration  $a_{ems}^{[i]}$ , wheel speed  $\omega_w^{[i]}$  and required wheel torque  $T_w^{[i]}$  are calculated using (6.7b) and (6.7a) with the vehicle model presented in Section 6.1.2. The required wheel torque  $T_w^{[i]}$  can be distributed between the front and rear axle using the torque distribution factor  $\alpha_{fr}^{[i]}$ . The required torque  $T_{wf}^{[i]}$  at the output shaft of front and  $T_{wr}^{[i]}$  of rear gearbox is calculated with (6.8a) and (6.8b).

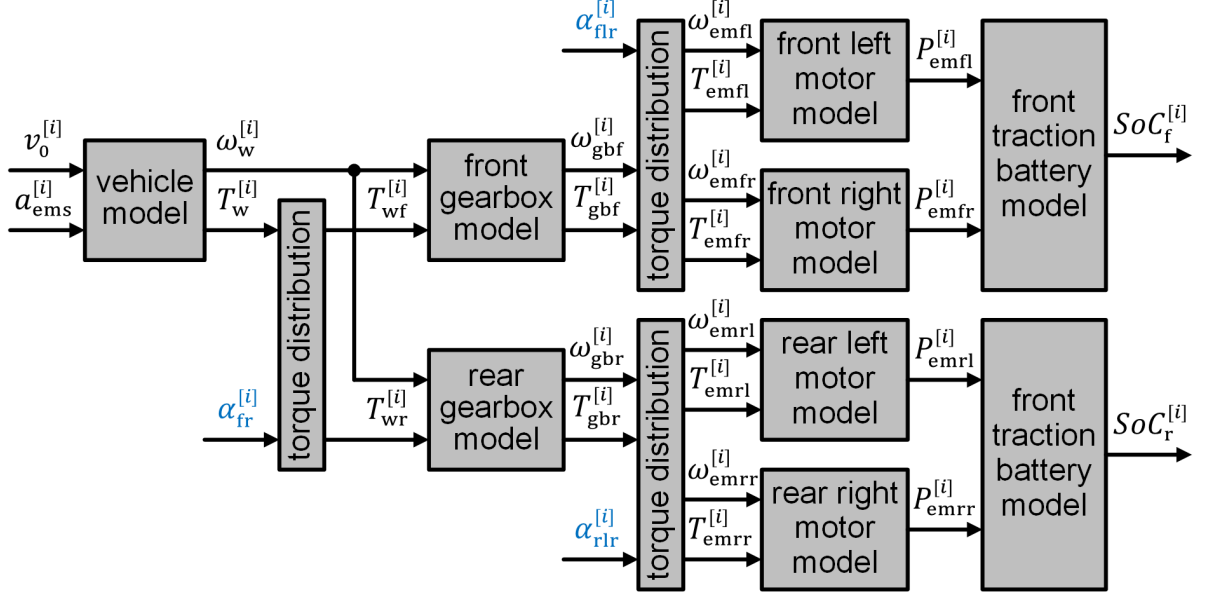


Figure 6.11.: Model of fail-operational electric powertrain with multiple motors.

The gearbox torque  $T_{gb\{x\}}^{[i]}$  required at the output shaft of axle  $x$  (with  $x = f$  for front and  $x = r$  for rear axle) can be distributed between the left and right side traction motor with the torque distribution factor  $\alpha_{\{x\}lr}^{[i]}$  as defined in (6.12a) and (6.12b). Using the corresponding clutches, the traction motors can be disengaged for switching off the idling losses if the requested motor torque  $T_{em\{xy\}}^{[i]}$  equals zero with  $x$  denoting the axle ( $x = f$  for front and  $x = r$  for rear axle) and  $y$  the motor side ( $y = l$  for left and  $y = r$  for right side). The motor speed  $\omega_{em\{xy\}}^{[i]}$  is then defined as:

$$\omega_{em\{xy\}}^{[i]} = \begin{cases} \omega_{gb\{x\}}^{[i]} & \text{with } T_{em\{xy\}}^{[i]} \neq 0 \\ 0 & \text{with } T_{em\{xy\}}^{[i]} = 0 \end{cases} \quad (6.45)$$

Using the model of an electrical machine as presented in Section 6.1.4, the electrical power  $P_{em\{xy\}}^{[i]}$  as well as power losses  $P_{em\{xy\}.loss}^{[i]}$  for each motor can be calculated with (6.21) and (6.20). By denoting the power provided by the battery for the supply of auxiliary loads with  $P_{bat\{x\}.load}^{[i]}$ , the required battery power  $P_{bat\{x\}}^{[i]}$  at the axle  $x$  ( $x = f$  for front and  $x = r$  for rear axle) is then defined as:

$$P_{bat\{x\}}^{[i]} = P_{em\{x\}l}^{[i]} + P_{em\{x\}r}^{[i]} + P_{bat\{x\}.load}^{[i]} \quad (6.46)$$

Using the battery model as presented in Section 6.1.5, the battery state of charge  $SoC_{\{x\}}^{[i+1]}$  at the end of the time interval  $i$  as well as the battery power losses  $P_{bat\{x\}.loss}^{[i]}$  can be calculated with (6.25) and (6.26). The first objective of the proposed control strategy is to increase the overall driving efficiency. The powertrain topology as depicted in Fig. 6.10

is an over-actuated system and the requested wheel torque  $T_w^{[i]}$  can be provided in different ways by varying the torque distribution variables  $\alpha_{fr}^{[i]}$  for front/rear,  $\alpha_{flr}^{[i]}$  and  $\alpha_{rlr}^{[i]}$  for left/right torque distribution at front and rear axle. Since the power losses of an electrical machine are a function of motor speed and torque, they can be also expressed as a function of the torque distribution variables. The overall powertrain losses can be minimized by maximizing the sum of the batteries' state of charge at the end of the interval  $i$ . Therefore, the first objective  $f_{obj1}^{[i]}$  for the control of the fail-operational powertrain can be defined as:

$$f_{obj1}^{[i]}(\alpha_{fr}^{[i]}, \alpha_{flr}^{[i]}, \alpha_{rlr}^{[i]}) = SoC_f^{[i+1]}(\alpha_{fr}^{[i]}, \alpha_{flr}^{[i]}) + SoC_r^{[i+1]}(\alpha_{fr}^{[i]}, \alpha_{rlr}^{[i]}) \quad (6.47)$$

By assuming that the batteries have the same capacity that does not change due to possible failures, the symmetrical discharge as required by the second objective can be achieved by minimizing the delta between front and rear battery state of charge at the end of the interval  $i$ . The second objective  $f_{obj2a}^{[i]}$  for the powertrain control can be defined as:

$$f_{obj2a}^{[i]}(\alpha_{fr}^{[i]}, \alpha_{flr}^{[i]}, \alpha_{rlr}^{[i]}) = \left| SoC_f^{[i+1]}(\alpha_{fr}^{[i]}, \alpha_{flr}^{[i]}) - SoC_r^{[i+1]}(\alpha_{fr}^{[i]}, \alpha_{rlr}^{[i]}) \right| \quad (6.48)$$

If the traction batteries at the front and rear axle have different capacities or the capacity can change due to failures, but nearly the same driving range (approx. half of the driving range available if both batteries are functional) is required in normal and failure case operation, the symmetrical battery discharge can be achieved by minimizing the delta between front and rear battery remaining discharge energy  $E_{rde\{x\}}^{[i]}$ . The battery remaining discharge energy can be calculated as presented in Section 5.5.2 either for a battery output power equal to zero, which would correspond to balancing of remaining chemical energy, or for battery output power equal to the average traction power. The second objective  $f_{obj2b}^{[i]}$  for the powertrain control can be then alternatively defined as:

$$f_{obj2b}^{[i]}(\alpha_{fr}^{[i]}, \alpha_{flr}^{[i]}, \alpha_{rlr}^{[i]}) = \left| E_{rdef}^{[i]}(\alpha_{fr}^{[i]}, \alpha_{flr}^{[i]}) - E_{rder}^{[i]}(\alpha_{fr}^{[i]}, \alpha_{rlr}^{[i]}) \right| \quad (6.49)$$

The cumulative energy losses  $E_{em\{xy\}.loss}^{[i]}$  dissipated by each traction motor at the end of the interval  $i$  starting at the beginning of operation can be calculated using (6.22). The balancing of the energy losses between the left and right motor as required by the third objective can be achieved by minimizing the delta in dissipated energy. The third objective  $f_{obj3}^{[i]}$  for the control of fail-operational powertrain can be then defined as:

$$\begin{aligned} f_{obj3}^{[i]}(\alpha_{fr}^{[i]}, \alpha_{flr}^{[i]}, \alpha_{rlr}^{[i]}) = & \left| c_{emfl} E_{emfl.loss}^{[i]}(\alpha_{fr}^{[i]}, \alpha_{flr}^{[i]}) - c_{emfr} E_{emfr.loss}^{[i]}(\alpha_{fr}^{[i]}, \alpha_{flr}^{[i]}) \right| \\ & + \left| c_{emrl} E_{emrl.loss}^{[i]}(\alpha_{fr}^{[i]}, \alpha_{rlr}^{[i]}) - c_{emrr} E_{emrr.loss}^{[i]}(\alpha_{fr}^{[i]}, \alpha_{rlr}^{[i]}) \right| \end{aligned} \quad (6.50)$$

The time independent factor  $c_{em\{xy\}}$  is used for modeling the different sizes of the traction motors, since the thermal resistance of a motor is also dependent on the geometric dimensions and cooling concept. In a similar way the balancing of the energy losses between front and rear axle as required by the fourth objective can be achieved by minimizing the delta in energy losses dissipated at each axle. The fourth objective can be defined as:

$$f_{obj4}^{[i]}(\alpha_{fr}^{[i]}, \alpha_{flr}^{[i]}, \alpha_{rlr}^{[i]}) = \left| c_{emfl} E_{emfl.loss}^{[i]}(\alpha_{fr}^{[i]}, \alpha_{flr}^{[i]}) + c_{emfr} E_{emfr.loss}^{[i]}(\alpha_{fr}^{[i]}, \alpha_{flr}^{[i]}) \right. \\ \left. - c_{emrl} E_{emrl.loss}^{[i]}(\alpha_{fr}^{[i]}, \alpha_{rlr}^{[i]}) + c_{emrr} E_{emrr.loss}^{[i]}(\alpha_{fr}^{[i]}, \alpha_{rlr}^{[i]}) \right| \quad (6.51)$$

The cumulative energy losses  $E_{bat\{x\}.loss}^{[i]}$  dissipated by each traction battery at the end of the interval  $i$  starting at the beginning of operation can be calculated using (6.27). The balancing of the energy losses between the front and rear battery as required by the fifth objective can be achieved by minimizing the delta in dissipated energy. The fifth objective  $f_{obj5}^{[i]}$  for the control of fail-operational powertrain can be then defined as:

$$f_{obj5}^{[i]}(\alpha_{fr}^{[i]}, \alpha_{flr}^{[i]}, \alpha_{rlr}^{[i]}) = \left| c_{batf} E_{batf.loss}^{[i]}(\alpha_{fr}^{[i]}, \alpha_{flr}^{[i]}) - c_{batr} E_{batr.loss}^{[i]}(\alpha_{fr}^{[i]}, \alpha_{rlr}^{[i]}) \right| \quad (6.52)$$

As by the traction motors, the time independent factor  $c_{bat\{x\}}$  is used for modeling the different sizes of the traction batteries, since the thermal resistance of a battery is also dependent on the geometric dimensions and cooling concept. For the sake of simplified notation, the three torque distribution variables  $\alpha_{fr}^{[i]}$ ,  $\alpha_{flr}^{[i]}$  and  $\alpha_{rlr}^{[i]}$  are summarized in the vector torque distribution variable  $\underline{\alpha}^{[i]}$ . Using the definitions above, the multi objective function  $f_{obj}^{[i]}$  for the control of fail-operational powertrain can be defined as:

$$f_{obj}^{[i]}(\underline{\alpha}^{[i]}) = \begin{bmatrix} \beta_1 \\ -\beta_2 \\ -\beta_3 \\ -\beta_4 \\ -\beta_5 \end{bmatrix}^T \cdot \begin{bmatrix} f_{obj1}^{[i]}(\underline{\alpha}^{[i]}) \\ f_{obj2}^{[i]}(\underline{\alpha}^{[i]}) \\ f_{obj3}^{[i]}(\underline{\alpha}^{[i]}) \\ f_{obj4}^{[i]}(\underline{\alpha}^{[i]}) \\ f_{obj5}^{[i]}(\underline{\alpha}^{[i]}) \end{bmatrix} \quad (6.53)$$

The positive scaling factors  $\beta_{1..5}$  are used for weighting the control goals. By maximizing the objective function  $f_{obj}^{[i]}$ , the optimal torque distribution factors  $\underline{\alpha}_{opt}^{[i]}$  for achieving the five control goals defined above can be estimated and used for the powertrain control. While maximizing the objective function, powertrain system constraints must be considered.

Three constraints considering each traction battery can be defined. The components supplied by the traction battery at each axle are generally designed for operation within a

specified voltage range. If the supply voltage exceeds these limits, a correct functionality of these components cannot be guaranteed. Therefore, by optimizing the torque distribution, it should be considered that the output voltage  $V_{\text{bat}\{x\}}^{[i]}$  of the traction battery at each axle lies within the minimum  $V_{\text{bat}\{x\}.\text{min}}$  and maximum  $V_{\text{bat}\{x\}.\text{max}}$  allowed voltage for avoiding under- and overvoltage in the subpowernet containing the traction battery.

While discharging the battery in motor mode or charging the battery in generator mode, the minimum  $SoC_{\{x\}.\text{min}}$  and maximum  $SoC_{\{x\}.\text{max}}$  thresholds for the specified state of charge must be considered for each battery, ensuring that the current state of charge  $SoC_{\{x\}}^{[i]}$  remains within these specified limits. Similarly, the battery output current  $I_{\text{bat}\{x\}}^{[i]}$  should not exceed the maximum allowed discharge  $I_{\text{bat}\{x\}.\text{dcha.max}}$  and charge  $I_{\text{bat}\{x\}.\text{chrg.max}}$  current, which is negative due to the definition of the battery model in Section 6.1.5.

Also for each traction motor three constraints are considered. The output torque  $T_{\text{em}\{xy\}}^{[i]}$  of each electrical machine as presented in Section 6.1.4 that can be provided in motor mode is limited to a motor speed dependent threshold  $T_{\text{em}\{xy\}.\text{lim.mot}}^{[i]}$  and to  $T_{\text{em}\{xy\}.\text{lim.gen}}^{[i]}$  in generator mode, which is negative due to the electric motor model definition. Therefore, while optimizing the torque distribution between the motors, it should be ensured that the output motor torque  $T_{\text{em}\{xy\}}^{[i]}$  lies within these thresholds. In a similar way, also the electrical power  $P_{\text{em}\{xy\}}^{[i]}$  of each motor can be limited to motor speed dependent thresholds for maximum power  $P_{\text{em}\{xy\}.\text{lim.mot}}^{[i]}$  in motor and to  $P_{\text{em}\{xy\}.\text{lim.gen}}^{[i]}$  in generator mode, which is again negative due to the electric motor model definition. For avoiding unnecessary heating, the operation of the motor can be limited to the efficiency map regions with motor efficiency  $\eta_{\text{em}\{xy\}}^{[i]}$  greater than a specified efficiency limit  $\eta_{\text{em}\{xy\}.\text{lim}}$ .

Using the definitions above and by denoting the lower and upper bounds for torque distribution vector  $\underline{\alpha}^{[i]}$  by  $\underline{\alpha}_{\text{min}}^{[i]}$  and  $\underline{\alpha}_{\text{max}}^{[i]}$ , the optimization problem for estimation of the optimal torque distribution variable  $\underline{\alpha}^{[i]}$  can be defined as:

$$\begin{aligned}
 & \max_{\underline{\alpha}^{[i]}} f_{\text{obj}}^{[i]}(\underline{\alpha}^{[i]}) \\
 & \text{s.t.} \quad \left\{ \begin{array}{l}
 V_{\text{bat}\{x\}.\text{min}} \leq V_{\text{bat}\{x\}}^{[i]}(\underline{\alpha}^{[i]}) \leq V_{\text{bat}\{x\}.\text{max}} \\
 SoC_{\{x\}.\text{min}} \leq SoC_{\{x\}}^{[i+1]}(\underline{\alpha}^{[i]}) \leq SoC_{\{x\}.\text{max}} \\
 I_{\text{bat}\{x\}.\text{chrg.max}} \leq I_{\text{bat}\{x\}}^{[i]}(\underline{\alpha}^{[i]}) \leq I_{\text{bat}\{x\}.\text{dcha.max}} \\
 T_{\text{em}\{xy\}.\text{lim.gen}}^{[i]} \leq T_{\text{em}\{xy\}}^{[i]}(\underline{\alpha}^{[i]}) \leq T_{\text{em}\{xy\}.\text{lim.mot}}^{[i]} \\
 P_{\text{em}\{xy\}.\text{lim.gen}}^{[i]} \leq P_{\text{em}\{xy\}}^{[i]}(\underline{\alpha}^{[i]}) \leq P_{\text{em}\{xy\}.\text{lim.mot}}^{[i]} \\
 \eta_{\text{em}\{xy\}.\text{lim}} \leq \eta_{\text{em}\{xy\}}^{[i]}(\underline{\alpha}^{[i]}) \\
 \underline{\alpha}_{\text{min}}^{[i]} \leq \underline{\alpha}^{[i]} \leq \underline{\alpha}_{\text{max}}^{[i]}
 \end{array} \right. \quad (6.54)
 \end{aligned}$$



By solving the optimization problem as defined in (6.54), the optimal torque distribution variable  $\underline{\alpha}^{[i]}$  for the time interval  $i$  satisfying the defined goals for the control of the fail-operational powertrain can be estimated. The proposed optimal control strategy can be also applied to powertrain topologies without clutches by setting the lower bounds  $\underline{\alpha}_{\min}$  for torque distribution vector  $\underline{\alpha}$  greater zero and upper bounds  $\underline{\alpha}_{\max}$  smaller one. In this case it becomes impossible for the controller to request a disengagement of individual traction motors, since due to the definition in (6.8a), (6.8b), (6.12a) and (6.12b) the torque request for each motor can be zero only in case of zero wheel torque request. Based on the proposed control strategy for a powertrain with multiple traction motors, an algorithm for accurate estimation of propulsion energy required for completing a given driving cycle is presented in the next subsection.

### 6.4.2. Propulsion Energy Prediction for Fail-Operational Powertrain

For the concept of safety-based range extension as well as for the predictive energy distribution within the vehicle powertrain accurate prediction of driving range is required. Assuming equal torque distribution between the traction motors, the propulsion energy required for completing a given driving cycle can be calculated with a similar approach as presented in 6.3.1. Since the driving efficiency of an electric vehicle with multiple traction motors can be increased by applying an appropriate torque distribution strategy [15, 16], using this approach for powertrain topologies with multiple traction motors would result in higher required propulsion energy compared to optimal torque distribution, leading so to inaccuracy of driving range prediction. Therefore, for accurate range prediction, a torque distribution profile should be estimated for the entire driving mission.

As proposed in Section 6.2 for the prediction of the driving trajectory to the vehicle destination, the entire trajectory is divided into  $n_{\text{traj}}$  segments. For each segment  $i$  ( $i \in \{1..n_{\text{seg}}\}$ ), the acceleration  $a_{\text{ems}}^{[i]}$  and slope value  $sl^{[i]}$  are constant and each segment  $i$  can be classified either as acceleration/deceleration phase for  $a_{\text{ems}}^{[i]} \neq 0$  or constant velocity phase with  $a_{\text{ems}}^{[i]} = 0$ . For the prediction of the propulsion energy it is proposed to estimate the optimal torque distribution by solving the optimization problem according to (6.54) for each segment  $i$  as depicted in Fig. 6.12. Similar to the acceleration and slope profile, also the torque distribution factors  $\alpha_{\text{fr}}^{[i]}$ ,  $\alpha_{\text{flr}}^{[i]}$  and  $\alpha_{\text{rlr}}^{[i]}$  modeling the torque distribution between front and rear axle as well as left and right side motor for each axle are kept constant within one segment  $i$ .

From the optimization point of view this simplification may result in suboptimal solutions on the one hand. On the other hand, frequent engaging and disengaging of motors would result in additional switching losses. Therefore, by keeping the torque distribution

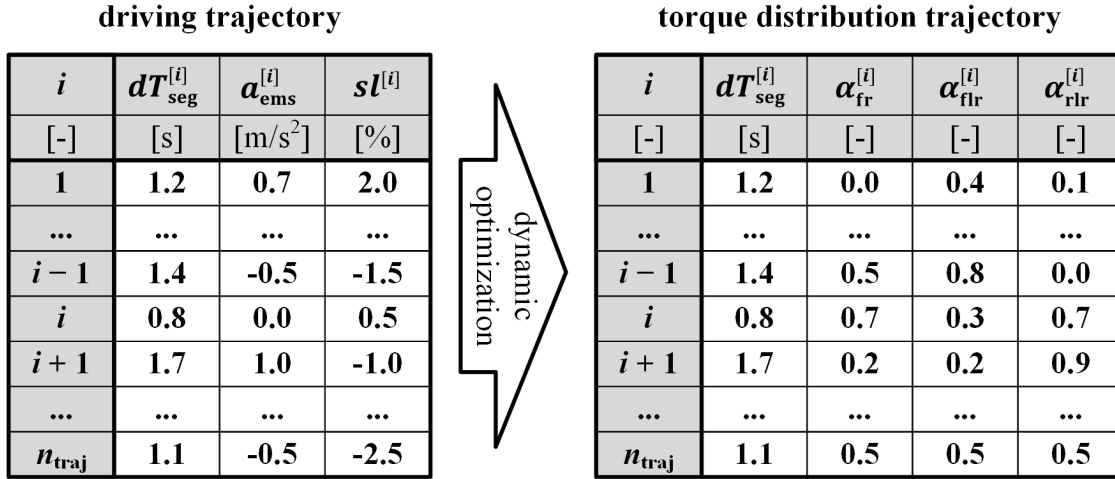


Figure 6.12.: Format of predicted driving and torque distribution trajectory.

parameters constant within one trajectory segment, the total operation of clutches as well as corresponding switching losses can be reduced. The time dependent wheel torque and speed profile within acceleration or deceleration phases would result in a time dependent optimal torque distribution profile. Since the duration of acceleration and deceleration phases is normally short, the deviation between energy consumption with optimal time dependent and approximated constant torque distribution can be neglected compared to total required propulsion energy for the entire driving mission.

For the phases with constant velocity and road slope, the required wheel torque and speed can be considered to be constant according to (6.6). Therefore, also for these phases, approximated constant torque distribution factors would lead to a solution which is close to the optimum. With these arguments, the estimation of the optimal torque distribution profile requiring the solution of a dynamic optimization problem, which can be obtained e.g. by computationally intensive dynamic programming algorithms, can be reduced to the estimation of a discrete-time torque distribution profile as depicted in Fig. 6.12.

The objective function of the optimization problem proposed for the control of the fail-operational powertrain as defined in (6.54) is a nonlinear function, which should be maximized under nonlinear constraints for  $n_{\text{traj}}$  segments. Using state of the art solvers for nonlinear optimization would result in high computational effort, violating so the requirement for online execution of control with short failure reaction times. Therefore, an algorithm with low computational effort for solving the optimization problem at runtime defined in (6.54) estimating the discrete-time torque distribution profiles is required. An approach based on discretization of optimization variables for torque distribution between the motors, which combines the optimization problem solving and propulsion energy prediction is presented in the following subsection.

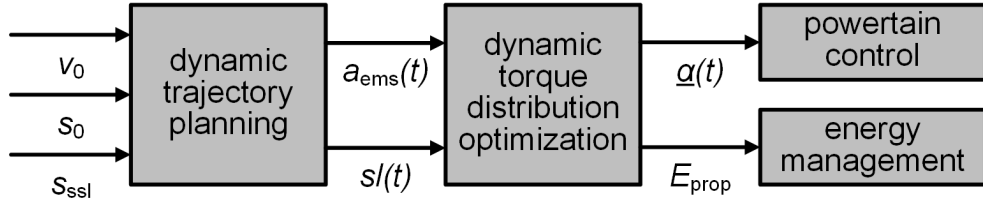


Figure 6.13.: Overview of propulsion energy prediction and powertrain control.

### 6.4.3. Algorithm for Online Torque Distribution Optimization

In powertrain topologies with multiple motors, the overall driving efficiency is dependent on the torque distribution between the traction motors. An adaptive control strategy for fail-operational powertrain topologies based on the torque distribution optimization was proposed in Section 6.4.1 and the corresponding optimization problem was defined in (6.54). As input for the dynamic torque distribution optimization an approximated driving trajectory from the current vehicle position  $s_0$  to the destination  $s_{ssl}$  as depicted in Fig. 6.13 is required, which is estimated using the current vehicle velocity and electronic horizon describing the route ahead. For a given acceleration profile  $a_{ems}(t)$  and slope profile  $s_l(t)$ , an optimal torque distribution profile  $\underline{\alpha}(t)$  is estimated by solving the optimization problem as defined in (6.54).

As already mentioned, for reducing the computational effort, estimation of time-discrete profiles as depicted in Fig. 6.12 is proposed. The first entry of the time-discrete torque distribution profile can be then used as a reference and set value for the control of a powertrain with multiple traction motors. As it will be shown in the following, while estimating the torque distribution profile, also the corresponding propulsion energy  $E_{prop}$  required for completing a given driving trajectory can be calculated, which is then used as input for the energy distribution optimization and safety-based range extension based on the three level degradation concept.

For the maximization of the nonlinear objective function  $f_{obj}(\underline{\alpha})$ , in the first step an approximation of battery state of charge  $SoC_{\{x\}}$  (with  $x = f$  for front and  $x = r$  for rear axle) (or alternatively remaining discharge energy  $E_{rde\{x\}}$ ) as well as of battery losses  $E_{bat\{x\}.loss}$  and motor losses  $E_{em\{xy\}.loss}$  (with  $y = l$  for left and  $y = r$  for right side) as a function of torque distribution variables is required. Since the battery and motor model parameters, as presented in Section 6.1, are data based (look-up tables) and may be updated over time using diagnostic methods, the approximation of the objective function should be done for each optimization cycle, resulting so in additional computational effort. Also for the optimization constraints the same argumentation is valid. Therefore, for solving the optimization problem with the state of the art solvers, e.g. with *fmincon* in

MATLAB, two computationally intensive steps for the approximation of the objective function and constraints as well as for solving it afterwards would be required.

Instead, for reducing the computational time, it is proposed to iteratively calculate the objective function at the end of the driving mission using the model of powertrain as presented in Section 6.1 for different discrete combinations of the factors  $\alpha_{fr}$ ,  $\alpha_{flr}$  and  $\alpha_{rlr}$ , describing the torque distribution between front and rear axle as well as between left and right side motors for each axle. A flow chart of the proposed algorithm combining torque distribution optimization and propulsion energy prediction is depicted in Fig. 6.14.

In the first step, the currently predicted driving trajectory consisting of  $n_{traj}$  entries in the format as depicted in Fig. 6.12 is read. The powertrain model presented in Section 6.1 also incorporates the current diagnostic state of traction motors, batteries and gear boxes, which can be estimated using diagnostic methods and is required for the model predictive estimation of propulsion energy. The current powertrain state defined by the battery state of charge and accumulated energy losses for motors and batteries is used as the initial condition for the further prediction.

The outer loop of the depicted flow chart is used for the iteration of driving trajectory segments  $i$  ( $i \in \{1..n_{traj}\}$ ). As already proposed in (6.41), for increasing the prediction accuracy, each segment  $i$  with duration  $dT_{seg}^{[i]}$  can be divided into  $j_{sub}^{[i]}$  subintervals with duration  $dT_{calc}^{[i]}$  depending on the segment's acceleration  $a_{ems}^{[i]}$  and minimum defined calculation time step  $dT_{min}$ . For the segment  $i$  the average vehicle speed vector  $\underline{v}_{avg}^{[i]}$  is calculated with the  $j$ -th element  $\underline{v}_{avg\{j\}}^{[i]}$  containing the average vehicle velocity in subinterval  $j$  of segment  $i$  and defined as:

$$\underline{v}_{avg\{j\}}^{[i]} = v_{start}^{[i]} + j \frac{a_{ems}^{[i]}}{dT_{calc}^{[i]}}, \quad \text{with } j \in \{1..j_{sub}^{[i]}\} \quad (6.55)$$

The velocity at the start of segment  $i$  is denoted by  $v_{start}^{[i]}$  and by  $v_{end}^{[i]}$  at the end, whereby the following relationship is valid:

$$\begin{aligned} v_{end}^{[i]} &= v_{start}^{[i]} + a_{ems}^{[i]} dT_{seg}^{[i]}, & \text{for } i \in \{1..n_{traj}\} \\ v_{start}^{[i]} &= v_0, & \text{for } i = 1 \\ v_{start}^{[i]} &= v_{end}^{[i-1]}, & \text{for } i \in \{2..n_{traj}\} \end{aligned} \quad (6.56)$$

Using the average velocity vector  $\underline{v}_{avg}^{[i]}$  and the velocity bounds  $v_{start}^{[i]}$  and  $v_{end}^{[i]}$ , the corresponding average required wheel torque vector  $\underline{T}_w^{[i]}$ , wheel speed vector  $\underline{\omega}_w^{[i]}$  and required wheel torque and speed at the segment bounds can be calculated using (6.7a) and (6.7b).

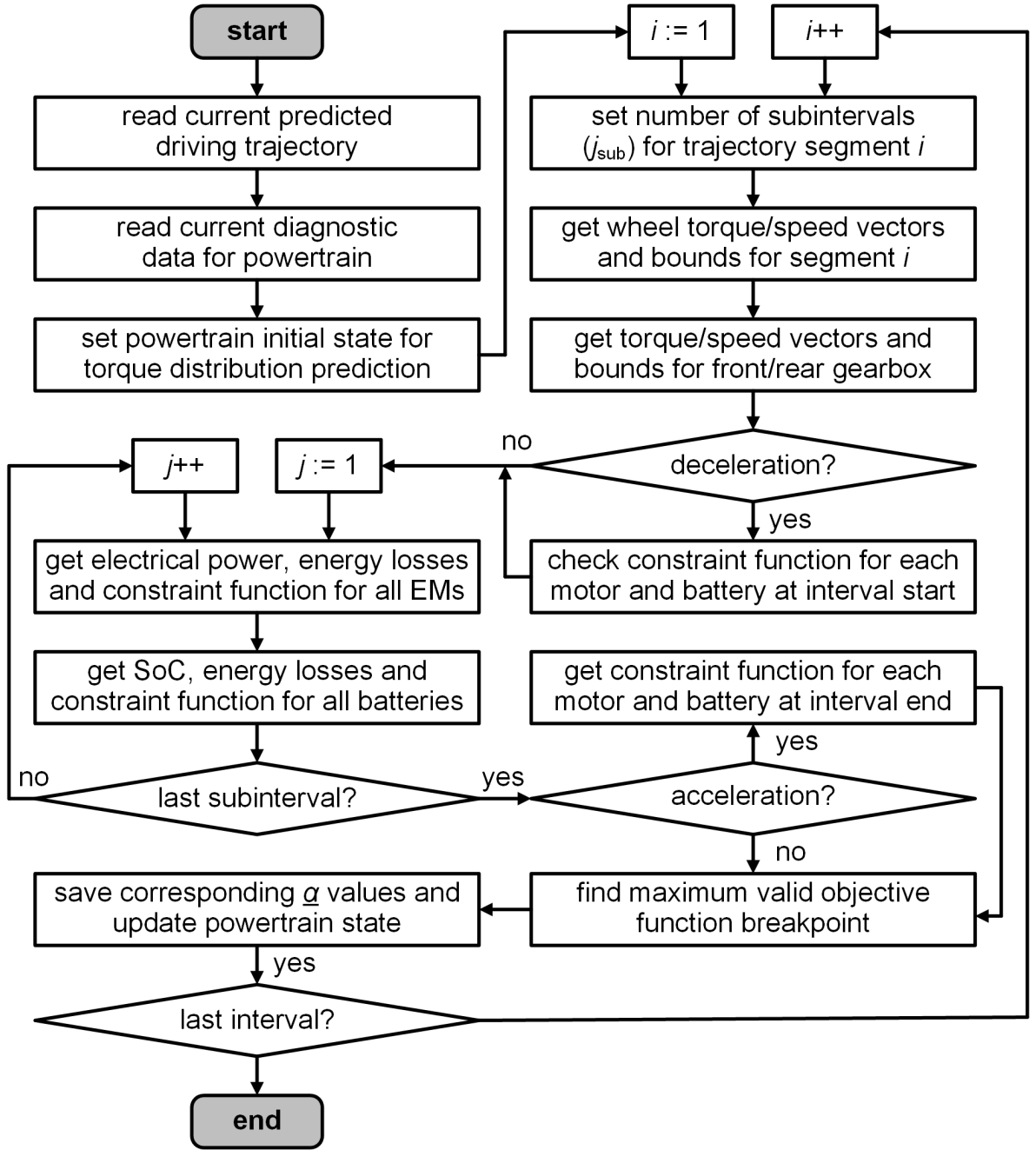


Figure 6.14.: Flow chart of algorithm for dynamic torque distribution optimization.

The  $j$ -th element  $T_{w\{j\}}^{[i]}$  of the torque vector  $T_w^{[i]}$  contains the average torque for the  $j$ -th subinterval of the segment  $i$ . The corresponding wheel speed is stored in the  $j$ -th element  $\omega_{w\{j\}}^{[i]}$  of the wheel speed vector  $\omega_w^{[i]}$ . In a similar way, the average torque vectors, speed vectors and bounds for the front and rear gearbox are calculated in the next step.

As explained above, the objective function is evaluated for a given set  $A_{\text{trq}}$  containing  $n_\alpha$  discrete valued torque distribution vectors  $\underline{\alpha}^{\{k\}}$  with  $\underline{\alpha}^{\{k\}} \in A_{\text{trq}}$  and  $k \in \{1..n_\alpha\}$ . Using the powertrain model as presented in Section 6.1, for each torque distribution vector

$\underline{\alpha}^{\{k\}}$  the objective function at the end of segment  $i$  can be evaluated iteratively in  $j_{\text{sub}}^{[i]}$  calculation steps, indicated with the inner loop of the flow chart depicted in Fig. 6.14. While evaluating the objective function, in parallel the optimization constraints as defined in (6.54) are checked. For this purpose, a Boolean constraint function  $lim_{\{x\}}^{[i]}$  for both, front ( $x = f$ ) and rear ( $x = r$ ) axle is defined and evaluated iteratively in  $j_{\text{sub}}^{[i]}$  steps for each segment  $i$  of the predicted driving trajectory. The Boolean constraint function  $lim_{\{x\}}^{[i]}$  for axle  $x$  is *false*, if none of the constraints defined in (6.54) is violated, and *true* otherwise. For each axle  $x$  the constraints for the left and right side traction motors as well as for the traction battery must be evaluated. For each traction motor at position  $x$  and  $y$  ( $y = l$  for left and  $y = r$  for right side motor), a Boolean constraint function  $lim_{\text{em}\{xy\}}^{[i]}$  can be defined, which is *true* if at least one of the motor related constraints is violated. In a similar way, also a Boolean constraint function  $lim_{\text{bat}\{x\}}^{[i]}$  can be introduced, leading to the following definition of  $lim_{\{x\}}^{[i]}$  as a function of torque distribution vector  $\underline{\alpha}^{[i]}$ :

$$lim_{\{x\}}^{[i]}(\underline{\alpha}^{[i]}) = lim_{\text{bat}\{x\}}^{[i]}(\underline{\alpha}^{[i]}) \vee lim_{\text{em}\{x\}l}^{[i]}(\underline{\alpha}^{[i]}) \vee lim_{\text{em}\{x\}r}^{[i]}(\underline{\alpha}^{[i]}) \quad (6.57)$$

For each electrical machine, three constraints with regard to output torque ( $lim_{\text{em}\{xy}.T}^{[i]}$ ), output power ( $lim_{\text{em}\{xy}.P}^{[i]}$ ) and motor efficiency ( $lim_{\text{em}\{xy}.\eta}^{[i]}$ ) must be considered, resulting in the following definition of  $lim_{\text{em}\{xy\}}^{[i]}$  as a function of torque distribution vector  $\underline{\alpha}^{[i]}$ :

$$lim_{\text{em}\{xy\}}^{[i]}(\underline{\alpha}^{[i]}) = lim_{\text{em}\{xy}.T}^{[i]}(\underline{\alpha}^{[i]}) \vee lim_{\text{em}\{xy}.P}^{[i]}(\underline{\alpha}^{[i]}) \vee lim_{\text{em}\{xy}.\eta}^{[i]}(\underline{\alpha}^{[i]}) \quad (6.58)$$

The output torque limit flag  $lim_{\text{em}\{xy}.T}^{[i]}$  is *true*, if the requested motor torque  $T_{\text{em}\{xy\}}^{[i]}$  exceeds the specified torque range between maximum torque ( $T_{\text{em}\{xy}.lim.gen}^{[i]} < 0$ ) in generator and ( $T_{\text{em}\{xy}.lim.mot}^{[i]} > 0$ ) in motor mode:

$$lim_{\text{em}\{xy}.T}^{[i]}(\underline{\alpha}^{[i]}) = [T_{\text{em}\{xy\}}^{[i]}(\underline{\alpha}^{[i]}) < T_{\text{em}\{xy}.lim.gen}^{[i]}] \vee [T_{\text{em}\{xy\}}^{[i]}(\underline{\alpha}^{[i]}) > T_{\text{em}\{xy}.lim.mot}^{[i]}] \quad (6.59)$$

The output power limit flag  $lim_{\text{em}\{xy}.P}^{[i]}$  is *true*, if the requested motor power  $P_{\text{em}\{xy\}}^{[i]}$  exceeds the specified power range between maximum power ( $P_{\text{em}\{xy}.lim.gen}^{[i]} < 0$ ) in generator and ( $P_{\text{em}\{xy}.lim.mot}^{[i]} > 0$ ) in motor mode:

$$lim_{\text{em}\{xy}.P}^{[i]}(\underline{\alpha}^{[i]}) = [P_{\text{em}\{xy\}}^{[i]}(\underline{\alpha}^{[i]}) < P_{\text{em}\{xy}.lim.gen}^{[i]}] \vee [P_{\text{em}\{xy\}}^{[i]}(\underline{\alpha}^{[i]}) > P_{\text{em}\{xy}.lim.mot}^{[i]}] \quad (6.60)$$

The motor efficiency limit flag  $lim_{\text{em}\{xy}.\eta}^{[i]}$  is *true*, if the motor efficiency  $\eta_{\text{em}\{xy\}}^{[i]}$  at the given operating point is less than the user defined motor efficiency limit ( $\eta_{\text{em}\{xy}.lim}$ ):

$$lim_{\text{em}\{xy}.\eta}^{[i]}(\underline{\alpha}^{[i]}) = [\eta_{\text{em}\{xy\}}^{[i]}(\underline{\alpha}^{[i]}) < \eta_{\text{em}\{xy}.lim}] \quad (6.61)$$

For each traction battery, three constraints with regard to output voltage ( $lim_{bat\{x\}.V}^{[i]}$ ), battery current ( $lim_{bat\{x\}.I}^{[i]}$ ) and state of charge ( $lim_{bat\{x\}.SoC}^{[i]}$ ) must be considered, resulting in the following definition of  $lim_{bat\{x\}}^{[i]}$  as a function of torque distribution vector  $\underline{\alpha}^{[i]}$ :

$$lim_{bat\{x\}}^{[i]}(\underline{\alpha}^{[i]}) = lim_{bat\{x\}.V}^{[i]}(\underline{\alpha}^{[i]}) \vee lim_{bat\{x\}.I}^{[i]}(\underline{\alpha}^{[i]}) \vee lim_{bat\{x\}.SoC}^{[i]}(\underline{\alpha}^{[i]}) \quad (6.62)$$

In a similar way, also the constraints for the battery can be evaluated. The output voltage limit flag  $lim_{bat\{x\}.V}^{[i]}$  is *true*, if the predicted battery output voltage  $V_{bat\{x\}}^{[i]}$  exceeds the specified voltage range between minimum ( $V_{bat\{x\}.min}$ ) and maximum ( $V_{bat\{x\}.max}$ ) voltage:

$$lim_{bat\{x\}.V}^{[i]}(\underline{\alpha}^{[i]}) = [V_{bat\{x\}}^{[i]}(\underline{\alpha}^{[i]}) < V_{bat\{x\}.min}] \vee [V_{bat\{x\}}^{[i]}(\underline{\alpha}^{[i]}) > V_{bat\{x\}.max}] \quad (6.63)$$

The output current limit flag  $lim_{bat\{x\}.I}^{[i]}$  is *true*, if the predicted battery current  $I_{bat\{x\}}^{[i]}$  exceeds the specified current range between maximum charge ( $I_{bat\{x\}.chrq.max} < 0$ ) and discharge ( $I_{bat\{x\}.dcha.max} > 0$ ) current:

$$lim_{bat\{x\}.I}^{[i]}(\underline{\alpha}^{[i]}) = [I_{bat\{x\}}^{[i]}(\underline{\alpha}^{[i]}) < I_{bat\{x\}.chrq.max}] \vee [I_{bat\{x\}}^{[i]}(\underline{\alpha}^{[i]}) > I_{bat\{x\}.dcha.max}] \quad (6.64)$$

The state of charge limit flag  $lim_{bat\{x\}.SoC}^{[i]}$  is *true*, if the state of charge  $SoC_{\{x\}}^{[i+1]}$  at the end of segment  $i$  exceeds the range between minimum specified discharge ( $SoC_{\{x\}.min}$ ) and maximum charge ( $SoC_{\{x\}.max}$ ) threshold:

$$lim_{bat\{x\}.SoC}^{[i]}(\underline{\alpha}^{[i]}) = [SoC_{\{x\}}^{[i+1]}(\underline{\alpha}^{[i]}) < SoC_{\{x\}.min}] \vee [SoC_{\{x\}}^{[i+1]}(\underline{\alpha}^{[i]}) > SoC_{\{x\}.max}] \quad (6.65)$$

After evaluating the objective and corresponding constraint function for the defined discrete valued torque distribution vectors  $\underline{\alpha}^{\{k\}}$  with  $k \in \{1..n_\alpha\}$ , the maximum valid objective function and the corresponding  $\underline{\alpha}^{\{k\}}$  breakpoint are found, which is considered to be the solution of the optimization problem. An objective function breakpoint  $f_{obj}(\underline{\alpha}^{\{k\}})$  is defined to be valid, if none of the constraint functions  $lim_{\{x\}}^{[i]}$  is *true*. As depicted in Fig. 6.14, in addition to the evaluation of constraint function  $lim_{\{x\}}^{[i]}$  in the inner loop, depending on the requested powertrain mode, an additional evaluation is done at the segment bounds. During a deceleration phase the motor is operated in generator mode and the motor speed is maximum at the interval start. While accelerating, the motor mode is required and the maximum motor speed is reached at the interval end. Assuming monotonically decreasing maximum motor torque characteristics as a function of motor speed, the motor would rather be in limitation at the beginning of a deceleration phase or at the end of a motor phase, since the requested power is at a maximum in this operating points. Therefore, in case of deceleration, the constraint function is additionally evaluated

at the interval start and at the interval end in case of acceleration.

The computational effort of the proposed algorithm is dependent on the number  $n_\alpha$  of breakpoints for the torque distribution optimization variable  $\underline{\alpha}$ . Therefore, appropriate selection of the breakpoints for  $\underline{\alpha}$  is required. In the following, two approaches using constant and variable bounds for  $\underline{\alpha}_{\min}$  and  $\underline{\alpha}_{\max}$  for the generation of breakpoints for the torque distribution variable  $\underline{\alpha}$  are proposed.

### Constant Bounds for Torque Distribution Factors

For the generation of torque distribution breakpoints, constant bounds  $\alpha_{\text{fr},\min} = 0$  equal to 0 and  $\alpha_{\text{fr},\max} = 1$  for  $\alpha_{\text{fr}}$  describing the torque distribution between front and rear axle are assumed. In powertrain topologies with clutches disengaging the motors, the lower bound can be set to 0 and the upper bound to 1, meaning that one axle can be disengaged or provide the entire requested torque. Assuming  $n_{\text{fr}}$  equally distributed breakpoints for  $\alpha_{\text{fr}}$  between the lower and upper bound, the  $n_{\text{fr}}$ -by-1 vector  $\underline{eq}_{\text{fr}}$  can be defined as:

$$\underline{eq}_{\text{fr}} = \frac{1}{n_{\text{fr}} - 1} \cdot \left( 0 \quad 1 \quad \dots \quad n_{\text{fr}} - 2 \quad n_{\text{fr}} - 1 \right)^{\text{T}} \quad (6.66)$$

In a similar way, assuming  $n_{\text{lr}}$  breakpoints for the variable  $\alpha_{\{x\}\text{lr}}$  between lower and upper bound with  $\alpha_{\{x\}\text{lr}} \in [0..1]$  describing the torque distribution between left and right side motors for axle  $x$ , the 1-by- $n_{\text{lr}}$  vector  $\underline{eq}_{\text{lr}}$  can be defined as:

$$\underline{eq}_{\text{lr}} = \frac{1}{n_{\text{lr}} - 1} \cdot \left( 0 \quad 1 \quad \dots \quad n_{\text{lr}} - 2 \quad n_{\text{lr}} - 1 \right) \quad (6.67)$$

By denoting a 1-by- $n_{\text{lr}}$  vector with all ones by  $\underline{1}$ , the  $n_{\text{fr}}$ -by- $n_{\text{lr}}$  matrix  $\underline{\alpha}_{\text{em}\{xy\}}$  containing the torque distribution grid points for motor at position  $x$  and  $y$  can be defined as:

$$\begin{aligned} \underline{\alpha}_{\text{emfl}} &= \underline{eq}_{\text{fr}} \cdot \underline{eq}_{\text{lr}} \\ \underline{\alpha}_{\text{emfr}} &= \underline{eq}_{\text{fr}} \cdot \left( \underline{1} - \underline{eq}_{\text{lr}} \right) \\ \underline{\alpha}_{\text{emrl}} &= \left( \underline{1} - \underline{eq}_{\text{fr}} \right) \cdot \underline{eq}_{\text{lr}} \\ \underline{\alpha}_{\text{emrr}} &= \left( \underline{1} - \underline{eq}_{\text{fr}} \right) \cdot \left( \underline{1} - \underline{eq}_{\text{lr}} \right) \end{aligned} \quad (6.68)$$

For each of the torque distribution grid points the powertrain model as presented in Section 6.1 can be calculated for each axle. The  $n_{\text{fr}} \cdot n_{\text{lr}}^2$  breakpoints for the objective function can be then estimated by permutation of state variables for each axle. Depending on the wheel torque request, a high number of objective function breakpoints might become invalid. If, for example, a powertrain topology with symmetrical motors is designed for a given total maximum propulsion power, which is the sum of maximum output powers



of each traction motor, a driving phase with a power request close to specified maximum would lead to valid objective function breakpoints with torque distribution factors close to 0.5 only. Therefore, for increasing the number of valid breakpoints and thereby the accuracy of the solving algorithm, an additional step for the prediction of lower and upper bounds for the torque distribution variables  $\alpha_{fr}$ ,  $\alpha_{fr}$  and  $\alpha_{rlr}$  as proposed in the next subsection can be used for generation of grid points for torque distribution variables.

### Variable Bounds for Torque Distribution Factors

Depending on the driving phase, the lower and upper bounds for the torque distribution variables  $\alpha_{fr}$ ,  $\alpha_{fr}$  and  $\alpha_{rlr}$  can be estimated for each segment  $i$  of the predicted driving trajectory. In an acceleration phase, the motor speed and power are at a maximum at the end of a segment. At this operating point, the maximum torque  $T_{em\{xy\}.lim.mot}^{[i]}$  that can be provided by each motor can be predicted and then used for the estimation of lower and upper bounds for the torque distribution variables. Similarly, in a deceleration phase, the motor speed and regenerative power are at a maximum at the start of a segment. The maximum regenerative torque  $T_{em\{xy\}.lim.gen}^{[i]}$  can be predicted for this operating point and then further processed for bounds estimation. By denoting the maximum torque that can be provided by each motor at position  $x$  and  $y$  without distinction between motor and generator mode by  $T_{em\{xy\}.max}$ , the lower ( $\alpha_{fr.min}^{[i]}$ ) and upper ( $\alpha_{fr.max}^{[i]}$ ) bound for the torque distribution between front and rear axle can be estimated as:

$$\alpha_{fr.min}^{[i]} = \max \left( 1 - \frac{T_{emrl.max}^{[i]} + T_{emrr.max}^{[i]}}{T_{gbr.max}^{[i]}}, 0 \right) \quad (6.69a)$$

$$\alpha_{fr.max}^{[i]} = \min \left( \frac{T_{emfl.max}^{[i]} + T_{emfr.max}^{[i]}}{T_{gbf.max}^{[i]}}, 1 \right) \quad (6.69b)$$

The torque that would be required at the input shaft of gearbox  $x$  to provide the requested wheel torque by this axle only is denoted by  $T_{gb\{x\}.max}^{[i]}$ . The lower bound  $\alpha_{fr.min}^{[i]}$  defines the minimum torque to be provided by the front axle in addition to the rear axle to fulfill the wheel torque request. If the rear axle can provide more torque than required,  $\alpha_{fr.min}^{[i]}$  is limited to 0. The upper bound  $\alpha_{fr.max}^{[i]}$  defines the maximum torque that can be provided by the front axle and it is limited to 1 if it exceeds the requested wheel torque. The  $n_{fr}$ -by-1 vector  $\underline{\alpha}_{fr}^{[i]}$  containing linearly spaced breakpoints for the torque distribution between front and rear axle can be then defined as:

$$\underline{\alpha}_{fr}^{[i]} = \alpha_{fr.min}^{[i]} \cdot \underline{1} + \left( \alpha_{fr.max}^{[i]} - \alpha_{fr.min}^{[i]} \right) \cdot \underline{eq}_{fr} \quad (6.70)$$

For each element  $j$  ( $\alpha_{\text{fr}\{j\}}^{[i]}$ ) of the vector  $\underline{\alpha}_{\text{fr}}^{[i]}$ , the corresponding lower ( $\alpha_{\text{fr.min}\{j\}}^{[i]}$ ) and upper ( $\alpha_{\text{fr.max}\{j\}}^{[i]}$ ) bounds for the front axle can be estimated as:

$$\alpha_{\text{fr.min}\{j\}}^{[i]} = \max \left( 1 - \frac{T_{\text{emfr.max}}^{[i]}}{\alpha_{\text{fr}\{j\}}^{[i]} T_{\text{gbf.max}}^{[i]}}, 0 \right) \quad (6.71a)$$

$$\alpha_{\text{fr.max}\{j\}}^{[i]} = \min \left( \frac{T_{\text{emfl.max}}^{[i]}}{\alpha_{\text{fr}\{j\}}^{[i]} T_{\text{gbf.max}}^{[i]}}, 1 \right) \quad (6.71b)$$

The lower bound  $\alpha_{\text{fr.min}\{j\}}^{[i]}$  defines the minimum torque to be provided by the front left motor in addition to the front right motor to fulfill the front wheel torque request. If the front right motor can provide more torque than required,  $\alpha_{\text{fr.min}\{j\}}^{[i]}$  is limited to 0. The upper bound  $\alpha_{\text{fr.max}\{j\}}^{[i]}$  defines the maximum torque that can be provided by the front left motor and it is limited to 1 if it exceeds the requested front wheel torque. In a similar way, also the lower ( $\alpha_{\text{rlr.min}\{j\}}^{[i]}$ ) and upper ( $\alpha_{\text{rlr.max}\{j\}}^{[i]}$ ) bounds for the rear axle can be estimated for each element  $j$  of ( $\alpha_{\text{fr}\{j\}}^{[i]}$ ) of the vector  $\underline{\alpha}_{\text{fr}}^{[i]}$  as:

$$\alpha_{\text{rlr.min}\{j\}}^{[i]} = \max \left( 1 - \frac{T_{\text{emrr.max}}^{[i]}}{(1 - \alpha_{\text{fr}\{j\}}^{[i]}) T_{\text{gbr.max}}^{[i]}}, 0 \right) \quad (6.72a)$$

$$\alpha_{\text{rlr.max}\{j\}}^{[i]} = \min \left( \frac{T_{\text{emrl.max}}^{[i]}}{(1 - \alpha_{\text{fr}\{j\}}^{[i]}) T_{\text{gbr.max}}^{[i]}}, 1 \right) \quad (6.72b)$$

By denoting a 1-by- $n_{\text{lr}}$  vector with all ones by  $\underline{1}$ , the  $n_{\text{fr}}$ -by- $n_{\text{lr}}$  matrix  $\alpha_{\{x\}\text{lr}}^{[i]}$  containing the grid points for the torque distribution between left and right side motor for axle  $x$  can be then defined as:

$$\alpha_{\{x\}\text{lr}}^{[i]} = \alpha_{\{x\}\text{lr.min}}^{[i]} \cdot \underline{1} + (\alpha_{\{x\}\text{lr.max}}^{[i]} - \alpha_{\{x\}\text{lr.min}}^{[i]}) \cdot \underline{e}q_{\text{lr}} \quad (6.73)$$

Using the definitions above and by denoting 1-by- $n_{\text{lr}}$  vector and  $n_{\text{fr}}$ -by- $n_{\text{lr}}$  matrix with all ones by  $\underline{1}$ , the  $n_{\text{fr}}$ -by- $n_{\text{lr}}$  matrix  $\alpha_{\text{em}\{xy\}}^{[i]}$  containing the torque distribution grid points for motor at position  $x$  and  $y$  can be defined as:

$$\alpha_{\text{emfl}}^{[i]} = (\alpha_{\text{fr}}^{[i]} \cdot \underline{1}) \circ \alpha_{\text{fr}}^{[i]} \quad (6.74a)$$

$$\alpha_{\text{emfr}}^{[i]} = (\alpha_{\text{fr}}^{[i]} \cdot \underline{1}) \circ (\underline{1} - \alpha_{\text{fr}}^{[i]}) \quad (6.74b)$$

$$\alpha_{\text{emrl}}^{[i]} = (\underline{1} - \alpha_{\text{fr}}^{[i]} \cdot \underline{1}) \circ \alpha_{\text{rlr}}^{[i]} \quad (6.74c)$$

$$\alpha_{\text{emrr}}^{[i]} = (\underline{1} - \alpha_{\text{fr}}^{[i]} \cdot \underline{1}) \circ (\underline{1} - \alpha_{\text{rlr}}^{[i]}) \quad (6.74d)$$

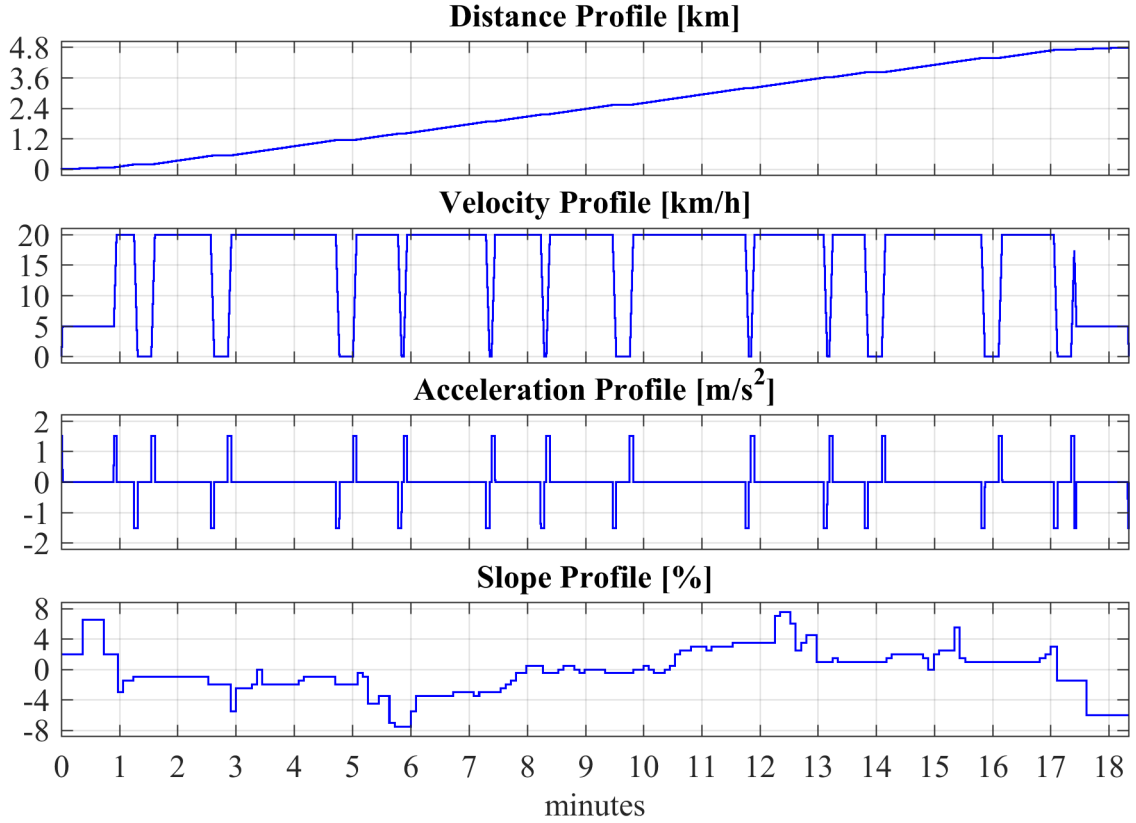


Figure 6.15.: Driving trajectory for torque distribution optimization.

In the following subsections, simulation results exemplifying the functionality of the proposed control strategy and propulsion energy prediction for a fail-operational powertrain and verifying the accuracy and suitability for runtime execution of the proposed algorithm are presented for both, normal and failure case operation.

#### 6.4.4. Simulation Results for Fault-Free Operation

For the control of fail-operational powertrain with multiple motors as depicted in Fig. 6.10 and for accurate prediction of propulsion energy required for completing a given driving mission, an adaptive algorithm with automated fault reactions based on the theory of optimal control is proposed. A MATLAB/Simulink model was implemented for verification of the proposed algorithm and simulation results for an exemplary use case are presented in this section. At simulation start, the vehicle is assumed to be at the beginning of a driving route with  $s_0 = 0$  km and the vehicle destination is set to  $s_{ssl} = 4.8$  km. The electronic horizon profile  $\underline{eh}_{lim}$  containing the velocity and acceleration bounds for the route ahead consists of 3 entries, the slope profile  $\underline{eh}_{slope}$  of 73 and the stops profile  $\underline{eh}_{stops}$  of 12 entries. The electronic horizon used for the simulation in this section as well as the vehicle and gearbox parameters are listed in Appendix B. The driving trajectory estimated with

the algorithm presented in Section 6.2 for these electronic horizon profiles consists in total of 127 entries. The driving trajectory is based on a real logged route and is depicted in Fig. 6.15 for degradation variables  $d\text{pda}$  for acceleration and  $d\text{pdv}$  for velocity equal to 1.

As defined in (6.53), the control of fail-operational powertrain can be customized with 5 parameters  $\beta_1$  to  $\beta_5$ , defining the weight for the individual control goals summarized in Section 6.4.1. For the simulation, a grid generation with constant bounds and 11 ( $n_{\text{fr}} = n_{\text{lr}} = 11$ ) breakpoints for the torque distribution variables was used. For the traction batteries, 48 V lithium-ion batteries with a nominal capacity approx. equal to 300 Ah are assumed with the operating temperature set to 25 °C. The simulation results are provided in each example for equal torque distribution ( $\alpha_{\text{fr}} = \alpha_{\{x\}\text{lr}} = 0.5$ ), which are then used as reference for the comparison with optimized torque distribution. The simulation results for signal  $a$  with equal torque distribution are denoted by  $a^{\text{eq}}$  and by  $a^{\text{opt}}$  for optimized torque distribution.

### Example 1: Increase of Energy Efficiency Only

In this example, the initial condition for the state of charge of front and rear battery is set to 80 % and only two control goals, the increase of energy efficiency ( $\beta_1 = 1$ ) and state of charge balancing ( $\beta_2 = 0.1$ ), are defined. The balancing of motor and battery losses is disabled ( $\beta_{3/4} = \beta_5 = 0$ ). The simulation results are depicted in Fig. 6.16.

With equal torque distribution, the state of charge for front ( $\text{SoC}_{\text{f}}^{\text{eq}}$ ) and rear ( $\text{SoC}_{\text{r}}^{\text{eq}}$ ) battery at the end of the driving cycle are equal to 75.778 %, which corresponds to the average battery discharge  $d\text{SoC}_{\text{avg}}^{\text{eq}}$  of 4.222 %. As the result of a symmetrical powertrain topology with equal motor characteristic and applied equal torque distribution, the delta in motor losses between left and right side for front ( $dE_{\text{emfr.loss}}^{\text{eq}}$ ) and rear ( $dE_{\text{emlr.loss}}^{\text{eq}}$ ) axle is zero. Also the delta in motor losses between front and rear axle ( $dE_{\text{emfr.loss}}^{\text{eq}}$ ) and between front and rear battery ( $dE_{\text{batfr.loss}}^{\text{eq}}$ ) is equal to zero.

Comparing the battery state of charge, it can be seen that by applying optimized torque distribution, the driving efficiency is increased. The state of charge at the end of the driving cycle for front ( $\text{SoC}_{\text{f}}^{\text{opt}}$ ) battery equals to 76.279 % and to 76.284 % for rear ( $\text{SoC}_{\text{r}}^{\text{opt}}$ ) battery. This corresponds to the average battery discharge  $d\text{SoC}_{\text{avg}}^{\text{opt}}$  equal to 3.719 %. By defining the increase of energy efficiency ( $d\eta_{\text{SoC}}$ ) as relative deviation of average discharge with optimized torque distribution compared to equal torque distribution, approx. 11.93 % of efficiency increase is achieved in this example, which is calculated as:

$$d\eta_{\text{SoC}} = \frac{d\text{SoC}_{\text{avg}}^{\text{eq}} - d\text{SoC}_{\text{avg}}^{\text{opt}}}{d\text{SoC}_{\text{avg}}^{\text{eq}}} \quad (6.75)$$

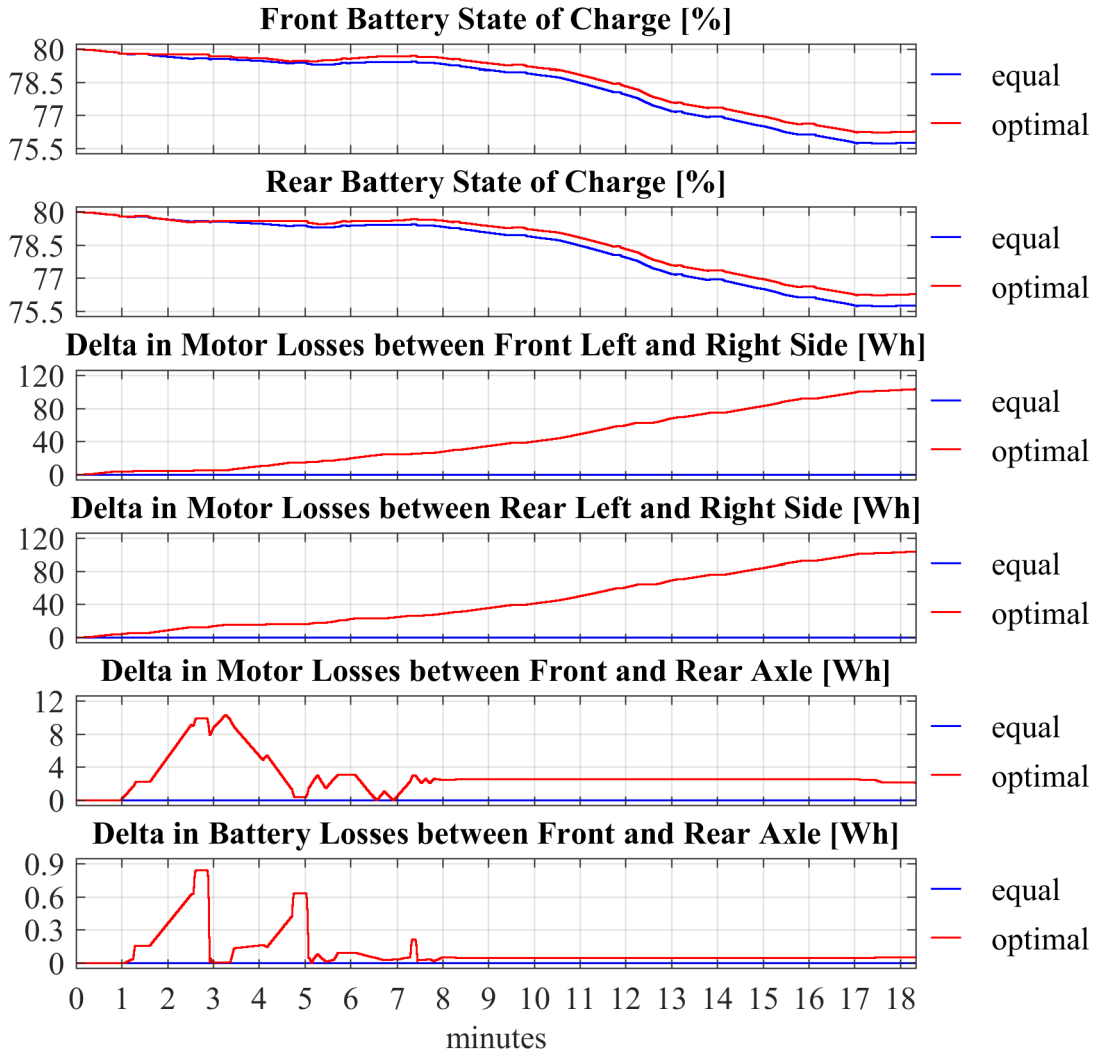


Figure 6.16.: Normal operation with  $\beta_1 = 1$ ,  $\beta_2 = 0.1$ ,  $\beta_{3/4} = 0$  and  $\beta_5 = 0$ .

Due to the optimized torque distribution the motors are not loaded equally anymore, resulting in increased delta in motor losses between the left and right side for the front ( $dE_{emfr.loss}^{opt}$ ) and rear ( $dE_{emrlr.loss}^{opt}$ ) axle. It can be seen in Fig. 6.16 that the left side motors are loaded more than the right side motors in this example. Also the delta in motor losses ( $dE_{emfr.loss}^{opt}$ ) and battery losses ( $dE_{batfr.loss}^{opt}$ ) between the front and rear axle is increased. Due to symmetrical powertrain topology and activated state of charge balancing ( $\beta_2 = 0.1$ ), requiring similarly symmetrical power demand for each axle, the absolute delta in motor and battery energy losses between front and rear axle is much smaller compared to the delta in motor losses between the left and right side.

Due to motor redundancy and high gearbox transmission ratio used in this example, the motors are operated in low torque regions for equal torque distribution in driving phases with constant velocity. By disengaging one motor at each axle, the operating point for

active traction motors can be shifted to higher torque regions with better efficiency, which is consistent with the results provided in [15] and [16]. This behavior explains also the increase of energy efficiency and of delta in motor losses.

For the verification of the prediction accuracy and suitability for runtime execution of the proposed algorithm, the results for the prediction with different combinations of break-points  $n_{fr}$  and  $n_{lr}$  used for torque distribution between the front and rear axle as well as left and right side motors are provided in the Tables 6.4 to 6.7. The corresponding computational time is estimated using the MATLAB functions *tic* and *toc* as an average out of 100 runs on an Intel i7 CPU. For the prediction, both methods with constant and variable bounds for the generation of grid points for the optimization variables are used. The results provided in the following Tables 6.4 to 6.7 are the (static) output of the prediction algorithm executed at the beginning of the driving mission in one optimization cycle, while the simulation results depicted in Fig. 6.16 are the output of a dynamic simulation of a fail-operational powertrain controlled by the proposed algorithm as presented in Section 6.4.2.

 Table 6.4.: Predicted average battery discharge  $dSoC_{avg}$  in [%] for Example 1.

$dSoC_{avg}$	constant bounds for $\underline{\alpha}(t)$				variable bounds for $\underline{\alpha}(t)$			
	$n_{lr} = 1$	$n_{lr} = 3$	$n_{lr} = 5$	$n_{lr} = 11$	$n_{lr} = 1$	$n_{lr} = 3$	$n_{lr} = 5$	$n_{lr} = 11$
$n_{fr} = 1$	4.233	3.804	3.804	3.804	4.233	3.804	3.804	3.804
$n_{fr} = 3$	3.896	3.706	3.706	3.705	3.943	3.719	3.719	3.719
$n_{fr} = 5$	3.968	3.719	3.719	3.719	3.941	3.721	3.721	3.721
$n_{fr} = 11$	3.977	3.719	3.719	3.719	3.972	3.724	3.724	3.724

 Table 6.5.: Predicted increase of energy efficiency  $d\eta_{SoC}$  in [%] for Example 1.

$d\eta_{SoC}$	constant bounds for $\underline{\alpha}(t)$				variable bounds for $\underline{\alpha}(t)$			
	$n_{lr} = 1$	$n_{lr} = 3$	$n_{lr} = 5$	$n_{lr} = 11$	$n_{lr} = 1$	$n_{lr} = 3$	$n_{lr} = 5$	$n_{lr} = 11$
$n_{fr} = 1$	0.0	10.134	10.134	10.135	0.0	10.134	10.134	10.135
$n_{fr} = 3$	7.977	12.465	12.466	12.487	6.860	12.152	12.153	12.153
$n_{fr} = 5$	6.258	12.144	12.144	12.144	6.903	12.091	12.091	12.092
$n_{fr} = 11$	6.053	12.152	12.152	12.153	6.161	12.030	12.030	12.030

 Table 6.6.: Predicted battery state of charge delta  $dSoC_{fr}$  in [%] for Example 1.

$dSoC_{fr}$	constant bounds for $\underline{\alpha}(t)$				variable bounds for $\underline{\alpha}(t)$			
	$n_{lr} = 1$	$n_{lr} = 3$	$n_{lr} = 5$	$n_{lr} = 11$	$n_{lr} = 1$	$n_{lr} = 3$	$n_{lr} = 5$	$n_{lr} = 11$
$n_{fr} = 1$	0.0	0.0	0.0	0.0	0.0	0.0	0.0	0.0
$n_{fr} = 3$	0.615	0.053	0.053	0.046	0.033	0.053	0.053	0.053
$n_{fr} = 5$	0.768	0.037	0.037	0.037	0.790	0.040	0.040	0.040
$n_{fr} = 11$	0.765	0.051	0.051	0.051	0.766	0.046	0.050	0.050

The combination  $n_{fr} = n_{lr} = 1$  corresponds to the equal torque distribution between the traction motors and it is used as reference for the calculation of energy efficiency increase. It can be seen in the Tables above that by applying the optimized torque distribution, the energy efficiency can be increased by up to 12% in this example. For equal torque distribution between the axles ( $n_{fr} = 1$ ), the delta  $dSoC_{fr}$  in battery state of charge is equal to zero due to symmetry in topology and torque request. For all other combinations, a delta less than 1‰ can be achieved.

 Table 6.7.: Average calculation time  $dT_{eval}$  in [ms] for Example 1.

$dT_{eval}$	constant bounds for $\underline{\alpha}(t)$				variable bounds for $\underline{\alpha}(t)$			
	$n_{lr} = 1$	$n_{lr} = 3$	$n_{lr} = 5$	$n_{lr} = 11$	$n_{lr} = 1$	$n_{lr} = 3$	$n_{lr} = 5$	$n_{lr} = 11$
$n_{fr} = 1$	10.04	38.64	35.78	36.57	20.98	50.41	45.83	46.18
$n_{fr} = 3$	36.18	38.48	37.19	42.24	46.14	51.68	48.00	53.10
$n_{fr} = 5$	35.12	36.94	40.34	47.08	43.54	47.91	51.27	58.13
$n_{fr} = 11$	39.73	40.76	45.81	62.49	47.90	51.81	57.01	74.08

Considering the calculation time it can be seen that with increasing number of breakpoints for torque distribution variables, also the calculation time increases. The calculation time for the grid generation using variable bounds is slightly higher due to the additional prediction of the lower and upper bounds for each segment  $i$  of the driving trajectory. For all combinations of  $n_{fr}$  and  $n_{lr}$  a computational time less than 80 ms can be achieved, making the proposed algorithm very well suited for implementation and runtime execution in embedded systems. The example presented in this subsection is extended by additional motor losses balancing in the next subsection.

### Example 2: Increase of Energy Efficiency and Balancing of Motor Losses

In this example, the same assumptions made in Example 1 are valid. In addition to the activated control goal for symmetrical battery discharge ( $\beta_2 = 0.1$ ), also the balancing of the motor losses between left and right side ( $\beta_3 = 0.25$ ) and front and rear axle ( $\beta_4 = 0.25$ ) is activated. The simulation results are depicted in Fig. 6.17.

The results for equal torque distribution are the same as in Example 1. By applying the optimized torque distribution, the state of charge at the end of driving cycle for front ( $SoC_f^{opt}$ ) battery equals to 76.278% and to 76.284% for rear ( $SoC_r^{opt}$ ) battery. This corresponds to the average battery discharge  $dSoC_{avg}^{opt}$  equal to 3.719%. An increase of energy efficiency ( $d\eta_{SoC}$ ) equal to approx. 11.92% is achieved in this example, which is very close to the result in Example 1. Comparing the delta in losses between left and right side motor for front ( $dE_{emfr.loss}^{opt}$ ) and rear ( $dE_{emrlr.loss}^{opt}$ ) axle, it can be seen that the

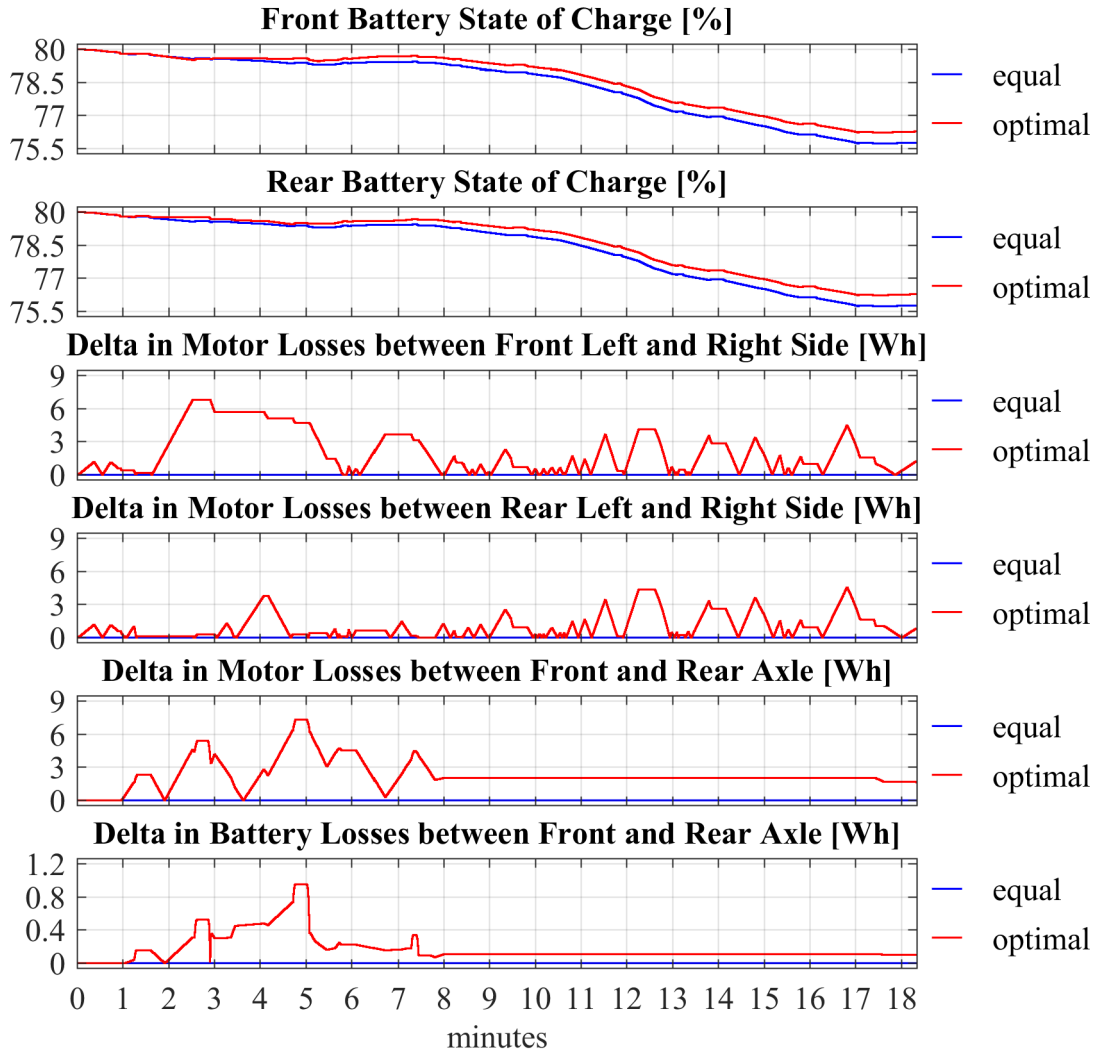


Figure 6.17.: Normal operation with  $\beta_1 = 1$ ,  $\beta_2 = 0.1$ ,  $\beta_{3/4} = 0.25$  and  $\beta_5 = 0$ .

absolute value is reduced by approx. factor 10. Also the delta in motor losses between front and rear axle ( $dE_{emfr.loss}^{opt}$ ) is slightly reduced.

In the following Tables 6.8 to 6.14, again the static simulation results as output of one prediction cycle at the beginning of driving route for different combinations of  $n_{fr}$  and  $n_{lr}$  are summarized. Again, the increase of energy efficiency by up to 12% and symmetry in traction battery discharge less than 1% and calculation time less than 80 ms is achieved.

In addition to results in Example 1, the ratio for losses of front left to right motor ( $R_{emfr.loss}$ ) and of rear left to right motor ( $R_{emlr.loss}$ ) are given, which is close to 1 for all combinations of  $n_{fr}$  and  $n_{lr}$ , meaning approximately the same cumulative energy dissipated by each motor. This is also the case for the losses ratio of front to rear axle motors ( $R_{emfr.loss}$ ). For  $n_{lr} = 1$ , meaning equal torque distribution between left and right side motor,  $R_{em\{x\}lr.loss}$  are exactly 1. Similarly, for  $n_{fr} = 1$ , the ratio  $R_{emfr.loss}$  is exactly 1.



Table 6.8.: Predicted average battery discharge  $dSoC_{\text{avg}}$  in [%] for Example 2.

$dSoC_{\text{avg}}$	constant bounds for $\underline{\alpha}(t)$				variable bounds for $\underline{\alpha}(t)$			
	$n_{\text{lr}} = 1$	$n_{\text{lr}} = 3$	$n_{\text{lr}} = 5$	$n_{\text{lr}} = 11$	$n_{\text{lr}} = 1$	$n_{\text{lr}} = 3$	$n_{\text{lr}} = 5$	$n_{\text{lr}} = 11$
$n_{\text{fr}} = 1$	4.233	3.804	3.804	3.804	4.233	3.804	3.804	3.804
$n_{\text{fr}} = 3$	3.932	3.718	3.718	3.718	3.943	3.719	3.719	3.719
$n_{\text{fr}} = 5$	3.944	3.719	3.719	3.719	3.945	3.719	3.719	3.719
$n_{\text{fr}} = 11$	3.977	3.721	3.721	3.721	3.977	3.719	3.719	3.722

Table 6.9.: Predicted increase of energy efficiency  $d\eta_{\text{SoC}}$  in [%] for Example 2.

$d\eta_{\text{SoC}}$	constant bounds for $\underline{\alpha}(t)$				variable bounds for $\underline{\alpha}(t)$			
	$n_{\text{lr}} = 1$	$n_{\text{lr}} = 3$	$n_{\text{lr}} = 5$	$n_{\text{lr}} = 11$	$n_{\text{lr}} = 1$	$n_{\text{lr}} = 3$	$n_{\text{lr}} = 5$	$n_{\text{lr}} = 11$
$n_{\text{fr}} = 1$	0.0	10.134	10.134	10.134	0.000	10.134	10.131	10.133
$n_{\text{fr}} = 3$	7.107	12.181	12.183	12.182	6.859	12.151	12.149	12.149
$n_{\text{fr}} = 5$	6.822	12.144	12.144	12.147	6.812	12.151	12.150	12.149
$n_{\text{fr}} = 11$	6.057	12.093	12.094	12.093	6.044	12.144	12.143	12.083

Table 6.10.: Predicted battery state of charge delta  $dSoC_{\text{fr}}$  in [%] for Example 2.

$dSoC_{\text{fr}}$	constant bounds for $\underline{\alpha}(t)$				variable bounds for $\underline{\alpha}(t)$			
	$n_{\text{lr}} = 1$	$n_{\text{lr}} = 3$	$n_{\text{lr}} = 5$	$n_{\text{lr}} = 11$	$n_{\text{lr}} = 1$	$n_{\text{lr}} = 3$	$n_{\text{lr}} = 5$	$n_{\text{lr}} = 11$
$n_{\text{fr}} = 1$	0.0	0.0	0.0	0.0	0.0	0.0	0.0	0.0
$n_{\text{fr}} = 3$	0.646	0.056	0.047	0.047	0.061	0.066	0.064	0.066
$n_{\text{fr}} = 5$	0.018	0.042	0.042	0.026	0.024	0.036	0.044	0.043
$n_{\text{fr}} = 11$	0.764	0.046	0.053	0.050	0.757	0.039	0.051	0.050

Table 6.11.: Average calculation time  $dT_{\text{eval}}$  in [ms] for Example 2.

$dT_{\text{eval}}$	constant bounds for $\underline{\alpha}(t)$				variable bounds for $\underline{\alpha}(t)$			
	$n_{\text{lr}} = 1$	$n_{\text{lr}} = 3$	$n_{\text{lr}} = 5$	$n_{\text{lr}} = 11$	$n_{\text{lr}} = 1$	$n_{\text{lr}} = 3$	$n_{\text{lr}} = 5$	$n_{\text{lr}} = 11$
$n_{\text{fr}} = 1$	6.15	33.86	34.61	36.61	16.21	43.50	44.28	46.19
$n_{\text{fr}} = 3$	33.32	35.37	37.24	42.36	41.92	46.40	48.23	53.40
$n_{\text{fr}} = 5$	34.09	36.96	40.51	47.24	42.73	48.17	51.61	58.38
$n_{\text{fr}} = 11$	35.77	40.86	45.73	63.21	44.43	52.16	56.91	74.57

Summing up the results, it can be stated that by using the proposed torque distribution strategy, the overall driving efficiency can be significantly increased. In addition, also symmetrical discharge of traction batteries and balancing of motor losses can be achieved. With calculation time less than 80 ms for dynamic torque distribution optimization and prediction of corresponding propulsion energy required for completing a given driving mission, the proposed algorithm can be used at runtime, enabling also fast reactions to unexpected faults and changes in powertrain state. The adaptivity of the proposed

Table 6.12.: Predicted losses ratio of front left to right motor ( $R_{emfr.loss}$ ) for Example 2.

	constant bounds for $\underline{\alpha}(t)$				variable bounds for $\underline{\alpha}(t)$			
$R_{emfr.loss}$	$n_{lr} = 1$	$n_{lr} = 3$	$n_{lr} = 5$	$n_{lr} = 11$	$n_{lr} = 1$	$n_{lr} = 3$	$n_{lr} = 5$	$n_{lr} = 11$
$n_{fr} = 1$	1.0	0.984	0.983	0.983	1.000	0.984	1.018	0.983
$n_{fr} = 3$	1.0	1.017	1.013	0.986	1.000	1.018	0.982	1.020
$n_{fr} = 5$	1.0	1.019	1.019	1.018	1.000	0.982	1.019	0.983
$n_{fr} = 11$	1.0	0.982	0.982	1.018	1.000	0.987	0.988	1.012

Table 6.13.: Predicted losses ratio of rear left to right motor ( $R_{emrlr.loss}$ ) for Example 2.

	constant bounds for $\underline{\alpha}(t)$				variable bounds for $\underline{\alpha}(t)$			
$R_{emrlr.loss}$	$n_{lr} = 1$	$n_{lr} = 3$	$n_{lr} = 5$	$n_{lr} = 11$	$n_{lr} = 1$	$n_{lr} = 3$	$n_{lr} = 5$	$n_{lr} = 11$
$n_{fr} = 1$	1.0	0.984	0.983	0.983	1.000	0.984	1.018	0.983
$n_{fr} = 3$	1.0	0.988	1.017	1.018	1.000	0.986	1.013	1.012
$n_{fr} = 5$	1.0	0.987	0.987	0.985	1.000	0.987	1.014	1.013
$n_{fr} = 11$	1.0	0.988	0.989	1.013	1.000	1.017	1.018	0.981

Table 6.14.: Predicted losses ratio of front to rear axle motors ( $R_{emfr.loss}$ ) for Example 2.

	constant bounds for $\underline{\alpha}(t)$				variable bounds for $\underline{\alpha}(t)$			
$R_{emfr.loss}$	$n_{lr} = 1$	$n_{lr} = 3$	$n_{lr} = 5$	$n_{lr} = 11$	$n_{lr} = 1$	$n_{lr} = 3$	$n_{lr} = 5$	$n_{lr} = 11$
$n_{fr} = 1$	1.0	1.0	1.0	1.0	1.0	1.0	1.0	1.0
$n_{fr} = 3$	1.101	0.940	0.935	0.935	0.994	0.975	0.974	0.975
$n_{fr} = 5$	0.989	1.001	1.001	0.998	0.993	0.978	0.978	0.978
$n_{fr} = 11$	1.007	0.970	0.970	0.969	1.008	1.004	1.005	0.999

algorithm and automated fault reactions are exemplified in the next subsection.

### 6.4.5. Simulation Results for Failure Case Operation

The proposed algorithm for the control of fail-operational powertrain enables also automated fault reactions. Using the diagnostic data, the control of powertrain is adapted to its current state. Three different scenarios assuming unexpected powertrain state or faults in components are presented in this section. Simulation results are provided for the use case as introduced in Section 6.4.4 and the driving trajectory depicted in Fig. 6.15.

#### Example 1: Asymmetrical Initial Battery State of Charge

For the first example, asymmetrical initial state of charge for batteries is assumed with  $SoC_f$  equal to 60 % for front, and  $SoC_r$  to 80 % for rear axle. Simulation results for this example are depicted in Fig. 6.18.

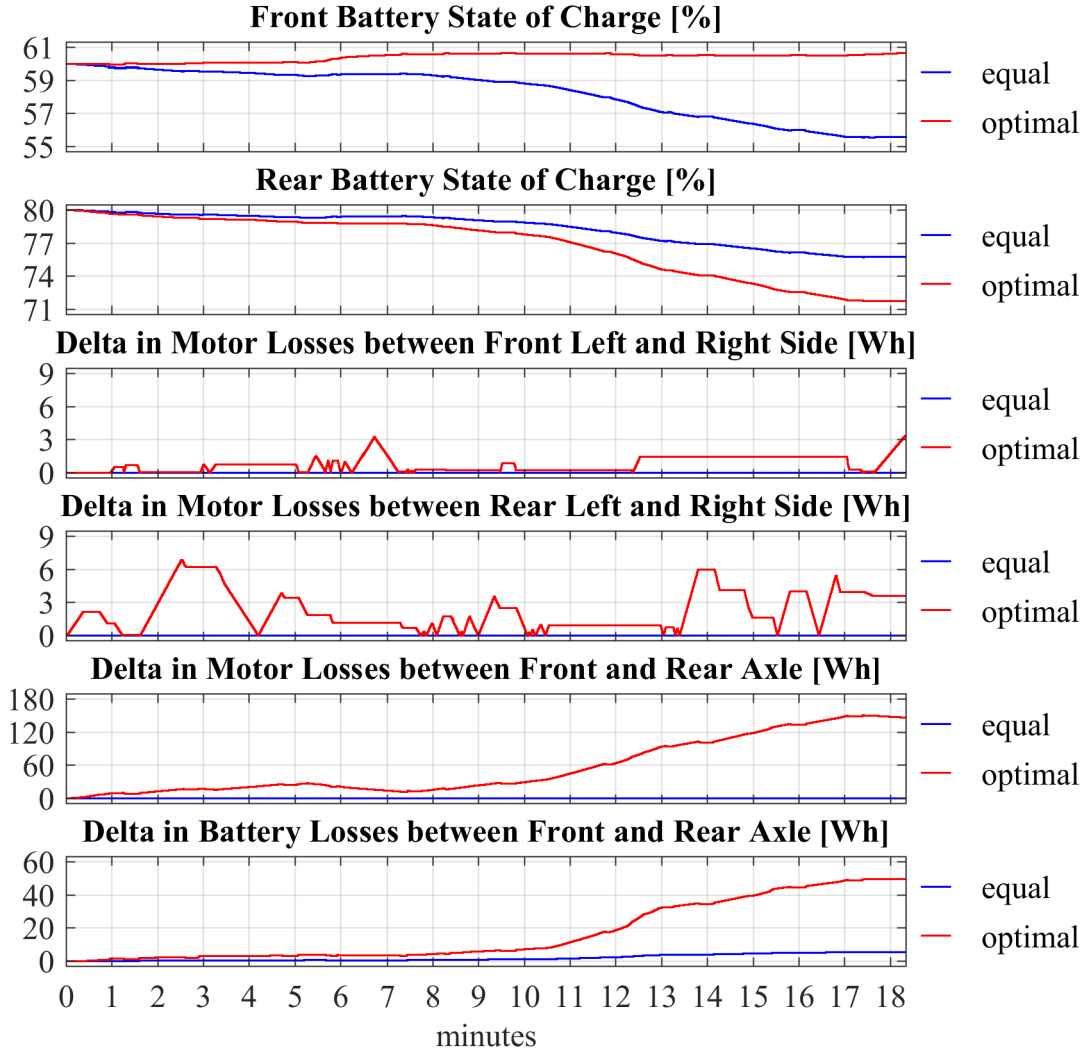


Figure 6.18.: State of charge balancing with  $\beta_1 = 1$ ,  $\beta_2 = 0.1$ ,  $\beta_{3/4} = 0.25$  and  $\beta_5 = 0$ .

By applying equal torque distribution, both batteries are used for propulsion and recuperation equally. The state of charge for front ( $SoC_f^{eq}$ ) and rear ( $SoC_r^{eq}$ ) battery at the end of the driving cycle is equal to 55.607% and 75.778%, what corresponds to the average battery discharge  $dSoC_{avg}^{eq}$  of 4.308%. The initial delta of 20% in battery state of charge is even increased to 20.17% at the end of the driving mission. Since the open circuit voltage of a battery decreases with decreasing state of charge, more battery current is required at the output to provide the same output power, resulting in slightly higher discharge of front battery compared to rear battery. Similarly to examples presented in Section 6.4.4, the delta in motor losses between left and right side for front ( $dE_{emfr.loss}^{eq}$ ) and rear ( $dE_{emlr.loss}^{eq}$ ) axle and between the front and rear axle ( $dE_{emfr.loss}^{eq}$ ) is equal to zero. The delta in battery losses between front and rear axle ( $dE_{batfr.loss}^{eq}$ ) is slightly increased due to asymmetrical output current as a result of asymmetry in battery state of charge.

By applying optimized torque distribution, it can be seen in Fig. 6.18 that the initial delta in battery state of charge can be reduced. The state of charge at the end of the driving mission for front ( $SoC_f^{\text{opt}}$ ) battery equals to 60.651 % and to 71.769 % for rear ( $SoC_r^{\text{opt}}$ ) battery. The state of charge of front battery is even slightly higher at the end of driving mission, which is the result of activated state of charge balancing ( $\beta_2 = 0.1$ ). With optimized torque distribution, the rear axle is used more for propulsion phases, while more energy is recuperated in the front battery. In addition to the state of charge balancing, also the energy efficiency can be increased in this example. The average battery discharge  $dSoC_{\text{avg}}^{\text{opt}}$  equals to 3.790 %, resulting in approx. 12.01 % of efficiency increase compared to equal torque distribution.

With activated balancing of motor losses ( $\beta_3 = \beta_4 = 0.25$ ), also the delta in dissipated energy between left and right side motors for front ( $dE_{\text{emfr.loss}}^{\text{opt}}$ ) and rear ( $dE_{\text{emrr.loss}}^{\text{opt}}$ ) axle is kept small. Since the front axle is used more for recuperation and the rear axle for propulsion, the delta in motor losses ( $dE_{\text{emfr.loss}}^{\text{opt}}$ ) and battery losses ( $dE_{\text{batfr.loss}}^{\text{opt}}$ ) between the axles is higher than in the examples presented in Section 6.4.4. Due to high delta in battery state of charge, the control goal for state of charge balancing becomes more important compared to motor losses balancing. By increasing the weighting factor  $\beta_4$ , the balancing of motor losses between the axles could be enforced to the disadvantage of energy efficiency and symmetry in battery discharge.

### Example 2: Decreased Efficiency of Front Left Motor

For the second example, again a symmetrical initial state of charge for batteries is assumed with  $SoC_f$  and  $SoC_r$  equal to 80 %. A failure in the front left motor resulting in a decrease of motor efficiency by 20 % is used as fault injection by setting the efficiency scaling factor  $c_{\text{emfl.eff}}$  to 0.8 using (6.19). Simulation results for this example are depicted in Fig. 6.19.

By applying equal torque distribution, all motors are used for propulsion and recuperation equally. The state of charge for front ( $SoC_f^{\text{eq}}$ ) and rear ( $SoC_r^{\text{eq}}$ ) battery at the end of the driving cycle is equal to 75.011 % and 75.778 %, which corresponds to the average battery discharge  $dSoC_{\text{avg}}^{\text{eq}}$  of 4.606 %. Since the efficiency of front left motor is decreased, the discharge of the front battery is higher than of rear battery.

The delta in motor losses between left and right side for rear axle ( $dE_{\text{emrr.loss}}^{\text{eq}}$ ) is equal to zero due to symmetry in topology and torque request, while the delta in motor losses between left and side for front axle ( $dE_{\text{emfr.loss}}^{\text{eq}}$ ) and between the front and rear axle ( $dE_{\text{emfr.loss}}^{\text{eq}}$ ) is significantly increased due to the asymmetry in motor efficiencies at front axle. This leads also to asymmetry in battery output current, resulting in slightly increased delta in battery losses between front and rear axle ( $dE_{\text{batfr.loss}}^{\text{eq}}$ ) and delta in battery

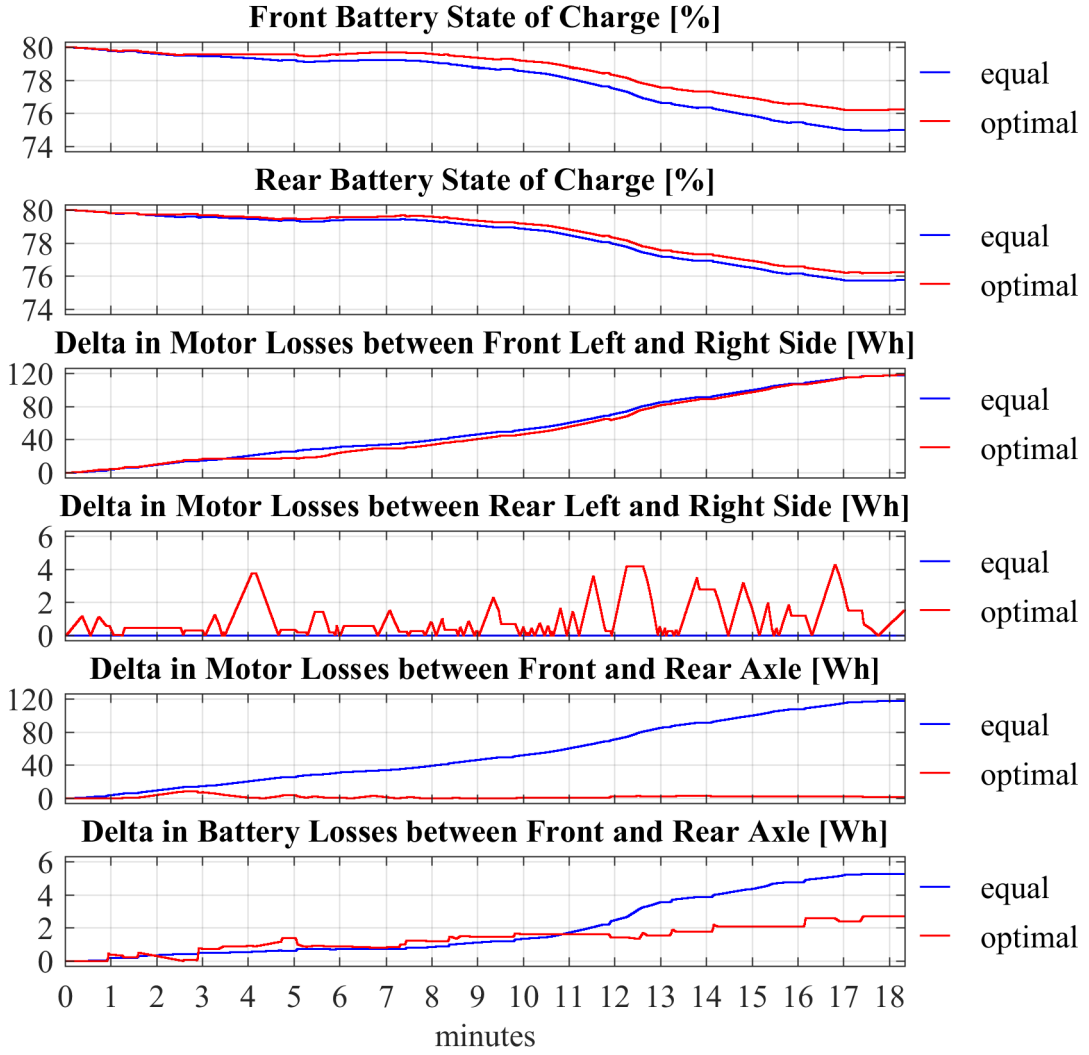


Figure 6.19.: Motor fault injection with  $\beta_1 = 1$ ,  $\beta_2 = 0.1$ ,  $\beta_{3/4} = 0.25$  and  $\beta_5 = 0$ .

state of charge  $dSoC_{fr}^{eq}$  equal to 0.766 %.

By applying optimized torque distribution, it can be seen in Fig. 6.19 that the operation of faulty motor can be reduced, increasing so significantly the energy efficiency. The state of charge at the end of the driving cycle for front ( $SoC_f^{opt}$ ) battery equals to 76.250 % and to 76.249 % for rear ( $SoC_r^{opt}$ ) battery. This results in the average battery discharge  $dSoC_{avg}^{opt}$  equal to 3.751 % and corresponding increase of energy efficiency of approx. 18.56 %. In addition to this automated fault reaction reducing the operation time of faulty motor to a minimum, also the symmetrical battery discharge with  $dSoC_{fr}^{opt}$  equal to 0.008 % can be achieved in contrast to equal torque distribution.

With activated balancing of motor losses ( $\beta_3 = \beta_4 = 0.25$ ), also the delta in dissipated energy between left and right side motors for rear axle ( $dE_{emlr.loss}^{opt}$ ) and between the axles ( $dE_{emfr.loss}^{opt}$ ) is kept small. Since due to the decreased efficiency of the front left motor the

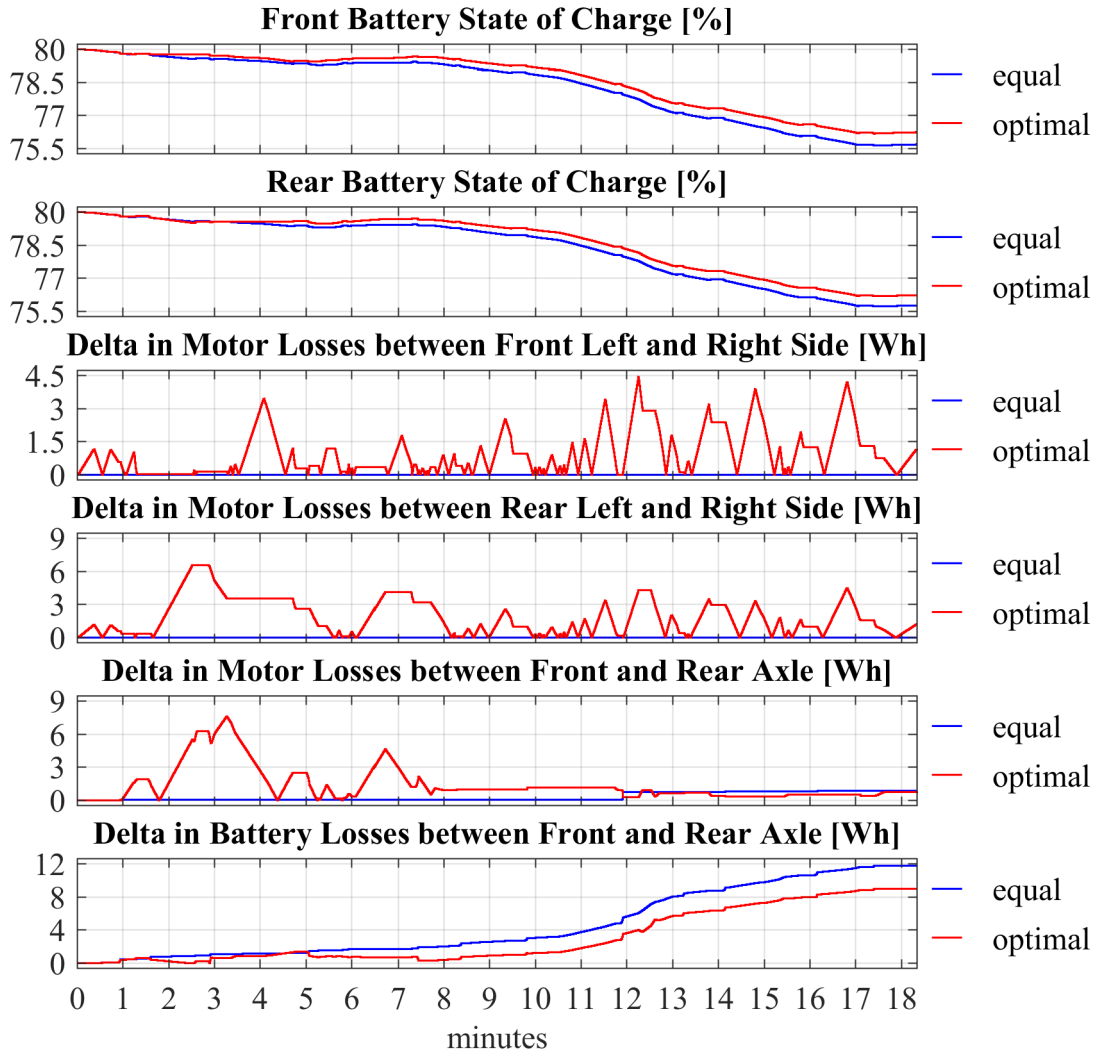


Figure 6.20.: Battery fault injection with  $\beta_1 = 1$ ,  $\beta_2 = 0.1$ ,  $\beta_{3/4} = 0.25$  and  $\beta_5 = 0$ .

balancing of motor losses between left and right side motors for front axle ( $dE_{\text{emfr.loss}}^{\text{opt}}$ ) becomes more costly compared to the increase of energy efficiency, no reduction compared to equal torque distribution is achieved, but could be enforced by using a higher value for the weighting factor  $\beta_3$ . Comparing the battery losses it can be seen that due to activated state of charge balancing, the delta in battery losses ( $dE_{\text{batfr.loss}}^{\text{opt}}$ ) between the axles is reduced compared to equal torque distribution.

### Example 3: Increased Resistance of Front Battery

For the third example, the initial state of charge for both batteries is set to 80%. A fault in the front battery resulting in an increase of internal resistance by 50% is used as fault injection by setting the internal resistance scaling factor  $c_{\text{batf.rin}}$  to 1.5 using (6.26). Simulation results for this example with activated state of charge ( $\beta_2 = 0.1$ ) and motor

losses balancing ( $\beta_3 = \beta_4 = 0.25$ ) are depicted in Fig. 6.20.

By applying equal torque distribution, all motors are used for propulsion and recuperation equally. The state of charge for front ( $SoC_f^{eq}$ ) and rear ( $SoC_r^{eq}$ ) battery at the end of driving cycle is equal to 75.697% and 75.778%, which corresponds to the average battery discharge  $dSoC_{avg}^{eq}$  of 4.263%. Since the internal resistance of front battery is increased, the discharge of the front battery is higher than of rear battery resulting in delta state of charge  $dSoC_{fr}^{eq}$  equal to 0.081%.

The delta in motor losses between left and right side for front ( $dE_{emfr.loss}^{eq}$ ) and rear ( $dE_{emrlr.loss}^{eq}$ ) axle is equal to zero due to symmetry in topology and torque request. Since the internal resistance of batteries is asymmetrical, the delta in battery losses between front and rear axle ( $dE_{batfr.loss}^{eq}$ ) is increased. Additionally, also the supply voltage for motors at front and rear axle becomes asymmetrical. Due to the dependability of motor efficiencies on the supply voltage, the delta in motor losses ( $dE_{emfr.loss}^{eq}$ ) between the axles is slightly greater than 0.

By applying optimized torque distribution, it can be seen in Fig. 6.20 that the operation of faulty battery can be reduced, increasing so the energy efficiency. The state of charge at the end of the driving cycle for front ( $SoC_f^{opt}$ ) battery equals to 76.247% and to 76.244% for rear ( $SoC_r^{opt}$ ) battery. This results in the average battery discharge  $dSoC_{avg}^{opt}$  equal to 3.755% and corresponding increase of energy efficiency of approx. 11.92%. In addition, also the symmetrical battery discharge with  $dSoC_{fr}^{opt}$  equal to 0.036‰ can be achieved in contrast to equal torque distribution.

With activated balancing of motor losses ( $\beta_3 = \beta_4 = 0.25$ ), also the delta in dissipated energy between left and right side motors for front axle ( $dE_{emfr.loss}^{opt}$ ), rear axle ( $dE_{emrlr.loss}^{opt}$ ) and between the axles ( $dE_{emfr.loss}^{opt}$ ) is kept small.

For the balancing of battery losses, also the fifth control goal can be used by defining the weighting factor  $\beta_5$ . The simulation results with additional balancing of battery losses with  $\beta_5$  set to 5 are depicted in Fig. 6.21. Compared to the previous setting with  $\beta_5$  equal to 0, the delta in battery losses between the axles is reduced approx. by factor 2 to the disadvantage of energy efficiency. The state of charge at the end of the driving cycle for front ( $SoC_f^{opt}$ ) battery now equals to 76.242% and to 76.240% for rear ( $SoC_r^{opt}$ ) battery. This results in the average battery discharge  $dSoC_{avg}^{opt}$  equal to 3.759% and corresponding increase of energy efficiency of approx. 11.82%, what is by 0.1% less than without balancing of battery losses.

The adaptivity of the proposed prediction and control algorithm with automated fault reactions is of high importance for the concept of safety-based range extension. By increas-

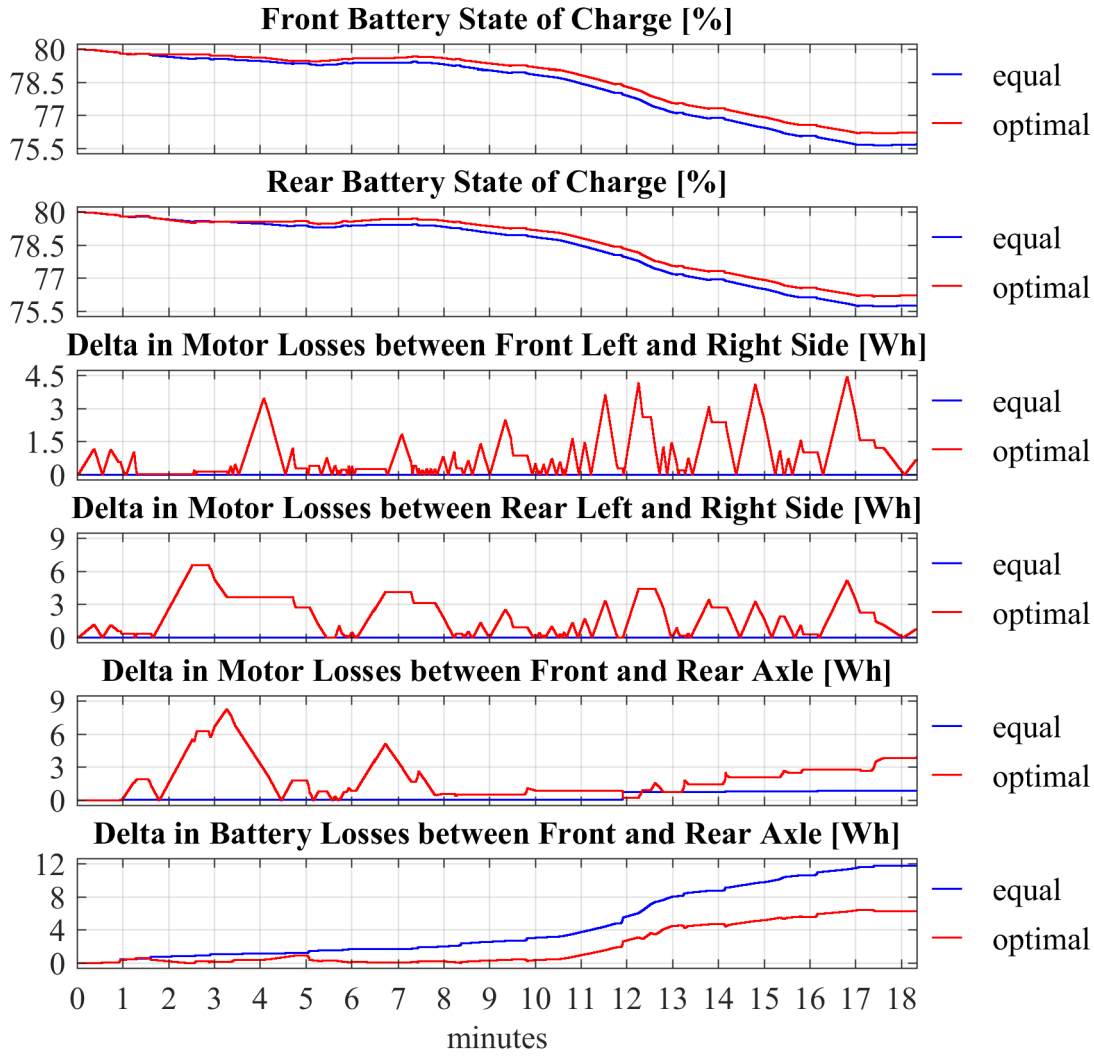


Figure 6.21.: Battery fault injection with  $\beta_1 = 1$ ,  $\beta_2 = 0.1$ ,  $\beta_{3/4} = 0.25$  and  $\beta_5 = 5$ .

ing the energy efficiency, the vehicle driving range in normal and failure case operation can be extended and the predicted propulsion energy can be used by the EMS for accurate energy distribution for the supply of powernet auxiliaries. In the next chapter of this work, two different system architectures for the EMS controlling fail-operational powernet and powertrain with single and multiple motors are proposed.



# Chapter 7.

## Model Predictive Energy Management

The EMS proposed in this work is designed for safety-based range extension with the main goal to optimize the powertrain and powernet control in a way allowing to complete the driving mission at the safest possible position with minimized risks for the passengers as described in Section 4. Four main modules of the model predictive EMS, namely (1) energy distribution optimization, (2) prediction of the remaining discharge energy, (3) prediction of the driving trajectory and (4) prediction of the propulsion energy were presented in Section 5 and 6. The adaptive energy distribution optimization is used for establishing the reliable power supply for the duration of a given driving mission and was presented in Section 5. With an appropriate formulation of the optimization problem based on a generic model of a fail-operational powernet, both normal and failure case operation are covered, allowing also to automate the fault reactions. Therefore, the proposed energy distribution optimization also integrates the automation of fault reactions of a functional safety concept required by ISO 26262 [10] for safety-critical subsystems.

The optimization of the energy distribution is based on predicted remaining energy resources and energy demand required for propulsion and supply of the powernet auxiliaries. A prediction algorithm for the estimation of the remaining discharge energy of batteries was proposed in Section 5.5. Using the parameters  $a_{rde}$  and  $E_{rde0}$  for the linear approximation of the remaining discharge energy as a function of battery output power, also the optimal discharge of multiple batteries was integrated in the energy distribution optimization problem. For an accurate prediction of the energy required for propulsion and supply of powernet auxiliaries, the duration of a given driving mission as well as the corresponding driving trajectory are required.

An approach for the driving trajectory prediction based on electronic horizon was presented in Section 6.2. The entire route to the destination is approximated by dividing it into segments with constant acceleration and slope value. This approximation is then fur-

ther processed by the module for the propulsion energy prediction. Using the quasistatic approach [29] with a variable stepsize, the powertrain model is calculated for each segment of the driving trajectory for the prediction of the propulsion energy required for mission completion. In powertrain topologies with multiple traction motors, also a prediction of the torque distribution profile as presented in Section 6.4 is required, since the driving efficiency and therefore the driving range can be significantly increased by an appropriate torque distribution strategy. In this chapter, these four basic modules are combined to the model predictive EMS, which is then integrated into the vehicle control. Two energy management architectures for the control of a powertrain topology with single and multiple traction motors are introduced and verified with simulation results in Section 7.1. and 7.2.

## 7.1. Energy Management Architecture for Powertrain with Single Motor

As already mentioned in the introduction, one of the main goals of the safety-based range extension is to optimize the control of the powertrain and powernet in a way allowing to arrive at the safest possible location for the passengers. According to Fig. 4.1, different scenarios for the automated vehicle transition to a safe state (standstill) in case of a failure can be defined. Braking in the current driving lane is assumed to be a worst case scenario with a minimum level of safety for the passengers, since the vehicle remains within the active traffic, leading to a hazardous situation for the passengers and the following traffic. A fail-degraded driving to the desired destination (driving home) is considered to be the best case scenario with maximum level of safety for the passengers.

According to Fig. 4.1, an automated transition to a standstill with the scenarios emergency braking (SSL G), comfort stop in current lane (SSL F) and coasting to the rightmost lane (SSL E) might be executed without a fail-operational driving functionality. A powertrain topology with a single traction battery and a single motor can be used for these scenarios, but still requiring a fail-operational powernet for the reliable power supply of the safety-critical subsystems braking and steering. Therefore, a powernet topology with a minimum of three subpowernets can be assumed, one containing a 48 V or HV traction battery and motor (subpowernet 1) and further two (subpowernet 2 and 3) for the redundant supply of the low voltage braking and steering subsystems. For the control of this powertrain and powernet configuration, an EMS architecture depicted in Fig. 7.1 is proposed and explained in Section 7.1.1. Simulation results verifying its functionality for an exemplary powertrain and powernet configuration as depicted in Fig. 6.7 and 7.2 are provided in Section 7.1.2.

### 7.1.1. System Architecture for Powertrain with Single Motor

The EMS architecture as depicted in Fig. 7.1 is a map-enabled application [40] designed for the predictive control of the vehicle powertrain and fail-operational powertrain. The prediction of the driving trajectory from the current vehicle position  $s_0$ , estimated using the DGPS unit, to the destination  $s_{\text{ssl}}$  is based on the electronic horizon. The electronic horizon is transmitted to the EMS using the ADASISv3 protocol by an ADAS horizon provider. The ADAS horizon provider can be for example a part of a navigation system containing static map data or a part of a **C**onnectivity **C**ontrol **U**nit (CCU) with a mobile connection (e.g. 4G/5G) to the cloud, allowing permanent updates of the static map data.

On the energy management side, the ADAS horizon reconstructor receives the electronic horizon and converts it to the three profiles  $\underline{eh}_{\text{lim}}$ ,  $\underline{eh}_{\text{slope}}$  and  $\underline{eh}_{\text{stops}}$  as depicted in Fig. 6.2. The profile  $\underline{eh}_{\text{lim}}$  contains the bounds  $v_{\text{min}}$  and  $v_{\text{max}}$  for the set velocity  $v_{\text{ems}}$  with  $v_{\text{ems}} \in \{v_{\text{min}}..v_{\text{max}}\}$  and the bounds  $a_{\text{min}}$  and  $a_{\text{max}}$  for the set acceleration  $a_{\text{ems}}$  with  $a_{\text{ems}} \in \{a_{\text{min}}..a_{\text{max}}\}$  for each entry  $i$  of the electronic horizon profile. According to the three-level-degradation concept presented in Section 4.1, the EMS can degrade the driving profile for the reduction of the propulsion energy required for completing a given driving cycle to the destination  $s_{\text{ssl}}$ . For this, the driving velocity can be degraded with the variable  $dpdv$  and the acceleration with  $dpda$ , both summarized to the degradation vector  $\underline{dpdx}$  in Fig. 7.1.

The degradation vector  $\underline{dpdx}$  as well as the vehicle destination  $s_{\text{ssl}}$  are the output of the energy distribution optimization, meaning that the EMS is embedded in the motion control of the vehicle. The EMS estimates in this way the vehicle destination  $s_{\text{ssl}}$  and the settings  $\underline{dpdx}$  for the driving profile which are feasible from the energetic point of view. These values can be then used by the superior motion controller for the model predictive vehicle control. Based on the current vehicle velocity  $v_0$ , the driving trajectory to the destination can be approximated according to the algorithm presented in Section 6.2.

The output of the submodule "driving trajectory prediction" contains the remaining driving duration  $dT_{\text{ssl}}$  and the driving trajectory consisting of three  $n_{\text{traj}}$ -by-1 vectors  $\underline{dT}_{\text{seg}}$ ,  $\underline{a}_{\text{ems}}$  and  $\underline{sl}$  in the format as depicted in Fig. 6.6. Each segment  $i$  ( $i \in \{1..n_{\text{traj}}\}$ ) of the driving trajectory is then specified by the corresponding segment duration  $dT_{\text{seg}}^{[i]}$ , segment acceleration  $a_{\text{ems}}^{[i]}$  and segment road slope  $sl^{[i]}$ . Since the driving trajectory is estimated periodically taking into account also the current vehicle velocity with a defined cycle time, e.g. 100 ms, it can be also used as a trajectory feedback control with the set acceleration equal to the first entry  $a_{\text{ems}}^{[1]}$  of the vector  $\underline{a}_{\text{ems}}$ . This feedback control of the velocity profile can be used superimposed to the control of the traction motor.

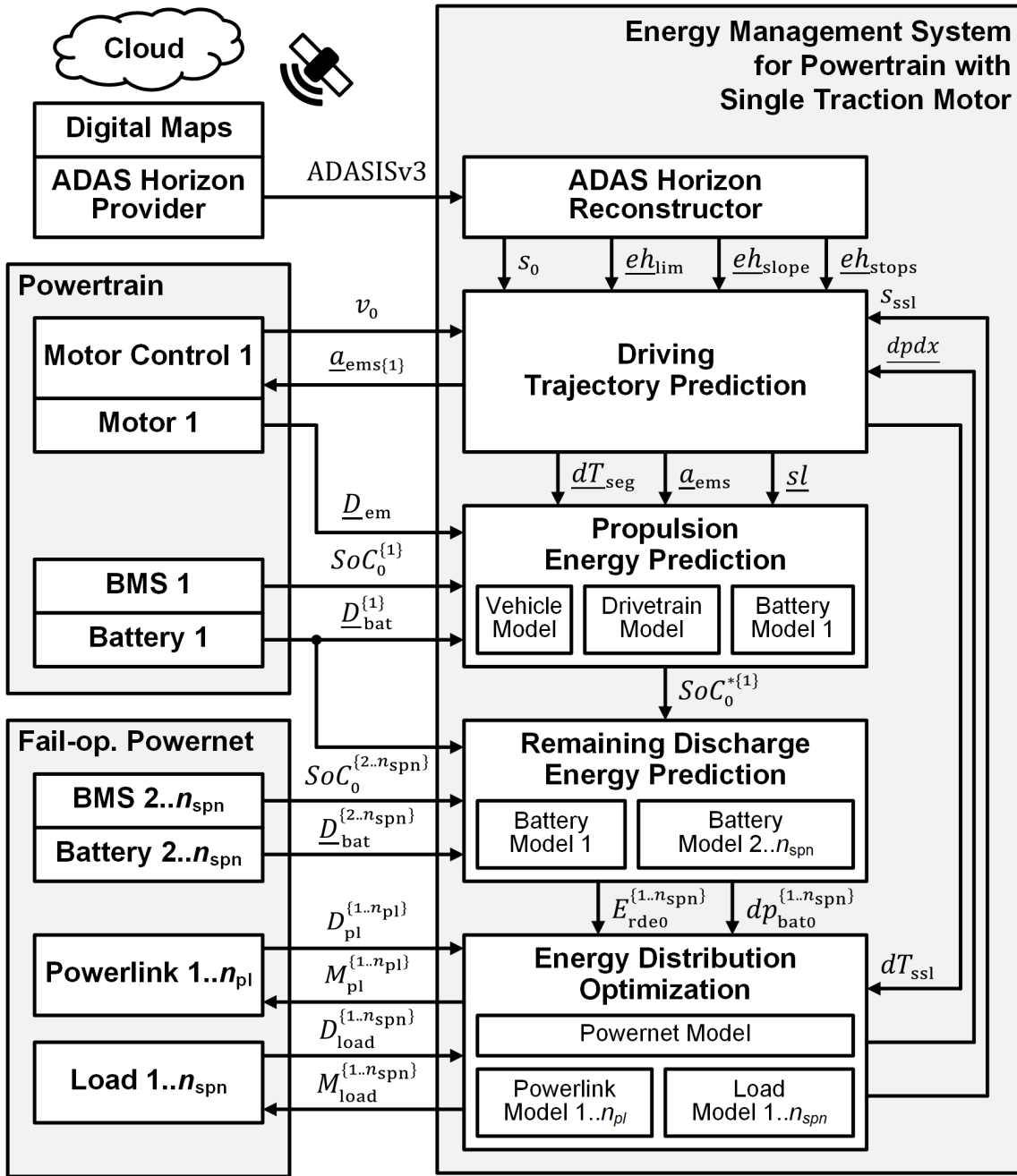


Figure 7.1.: Energy management architecture for powertrain with single motor.

In the next step, the energy required for completing the driving mission at the destination  $s_{ssl}$  with the velocity profile according to the degradation vector  $\underline{dpdx}$  can be predicted using the algorithm as proposed in Section 6.3. This prediction algorithm is based on the models describing the longitudinal vehicle dynamics, traction battery and drivetrain consisting of a traction motor and a gearbox with fixed transmission ratio. In the energy management architecture as depicted in Fig. 7.1, two types of batteries are distinguished. The first battery (Battery 1) is a traction battery, while the remaining batteries (Battery

$2..n_{\text{spn}}$ ), if present, are used for the voltage stability within the corresponding subpowernet. They are also used for the supply of the safety-critical loads for a limited duration in case of a breakdown of the traction battery.

The prediction of the required propulsion energy takes into account the diagnostics of the powertrain components. The diagnostic data of the traction motor (Motor 1) is stored in the vector  $\underline{D}_{\text{em}}$  and consists of the scaling factors  $c_{\text{em.eff}}$  and  $c_{\text{em.trq}}$  describing a decrease in the motor efficiency and in the maximum output torque according to the model of the electrical machine presented in Section 6.1.4. Also the scaling factor  $c_{\text{gb.eff}}$  (not depicted in Fig. 7.1) modeling a decrease of the gearbox efficiency as described in Section 6.1.3 is considered. Similarly, the diagnostic data of the traction battery (Battery 1) is stored in the vector  $\underline{D}_{\text{bat}}^{\{1\}}$  containing the scaling factors  $c_{\text{bat.q0}}$  and  $c_{\text{bat.rin}}$ . As introduced in Section 6.1.5, these factors are used for modeling the battery failures resulting in the decrease of the nominal battery capacity  $Q_{\text{bat0}}$  and in the increase of the internal battery resistance  $R_{\text{bat.in}}$ .

A two stage algorithm was proposed for solving the mixed-integer optimization problem for energy distribution in Section 5.2. The mixed-integer optimization was divided into the continuous energy distribution optimization with a superimposed integer parameter variation. With the algorithm described in Section 5.2.3, the number of valid combinations of mixed-integer variables, for which a continuous optimization is executed, was significantly reduced. For each of these valid combinations, a prediction of the driving trajectory, propulsion energy, remaining driving time and remaining discharge energy is required as input for the energy distribution optimization. For the reduction of the computational burden, an adapted approach is used.

The powernet topology considered in this section has only one traction battery. It can be therefore assumed, that the energy required for the supply of the traction motor is provided by this battery only. As depicted in Fig. 7.1, a virtual state of charge  $SoC_0^{*\{1\}}$  of the traction battery is estimated as the output of the submodule "propulsion energy prediction". This value corresponds to the state of charge of the traction battery after completing the driving mission with all comfort and safety-critical loads switched off. Since all powernet loads, except the traction motor, are switched off, the state of charge of the batteries 2 to  $n_{\text{spn}}$  remains unchanged. The virtual state of charge  $SoC_0^{*\{1\}}$  can be then used as the initial condition for the traction battery in the energy distribution optimization. Since the energy required for the propulsion is already covered by the virtual discharge of the traction battery from  $SoC_0^{\{1\}}$  at the beginning of the driving trajectory ( $t = t_0^{[i]}$ ) to  $SoC_0^{*\{1\}}$  at its end ( $t = t_0^{[i]} + dT_{\text{ssl}}$ ), only the supply of the comfort and safety-critical loads must be considered in the energy distribution optimization. By denoting

the current profile of the traction motor by  $I_{em}(t)$ , the virtual state of charge  $SoC_0^{*\{1\}}$  at the end of the driving mission can be defined as:

$$SoC_0^{*\{1\}} = SoC_0^{\{1\}} - \frac{1}{c_{bat,q0}(t)Q_{bat0}} \int_{t=t_0}^{t_0+dT_{ssl}} I_{em}(t)dt \quad (7.1)$$

The virtual state of charge  $SoC_0^{*\{1\}}$  and accordingly the approximation of the remaining discharge energy of the traction battery must be updated only if the driving destination  $s_{ssl}$  or the degradation vector  $\underline{dpdx}$  is changed. Since the state of charge of the batteries 2 to  $n_{spn}$  remains unchanged, the approximation of the remaining discharge energy for these batteries is required only once per cycle period. As depicted in Fig. 7.1, the prediction of the remaining discharge energy of the batteries 1 to  $n_{spn}$  takes into account the diagnostic data  $\underline{D}_{bat}^{\{1\}}$  to  $\underline{D}_{bat}^{\{n_{spn}\}}$ , which is provided in the same format as described above for the traction battery by the corresponding **B**attery **M**anagement **S**ystem (BMS). The output of the submodule "remaining discharge energy prediction" containing the parameters  $E_{rde0}^{\{i\}}$  and  $dp_{bat}^{\{i\}}$  with  $i \in \{1..n_{spn}\}$  for the linear approximation of the remaining discharge energy of a battery as a function of the discharge power is then used for the energy distribution optimization.

As depicted in Fig. 7.1, the diagnostic state  $D_{pl}^{\{j\}}$  of the powerlink  $j$  with  $j \in \{1..n_{pl}\}$  and the diagnostic state  $D_{load}^{\{i\}}$  with  $i \in \{1..n_{spn}\}$  of the loads are considered in the optimization. The diagnostic state  $D_{pl}^{\{j\}}$  for the powerlink  $j$  corresponds to the model description in Section 5.4. The diagnostic state  $D_{load}^{\{i\}}$  for the load  $i$  in subpowernet  $i$  describes a possible change in the average power demand due to a failure or the operating condition. The operating mode  $M_{pl}^{\{j\}}$  of the powerlink  $j$  as well as  $M_{load}^{\{i\}}$  for the load  $i$  in subpowernet  $i$  are the output of the submodule "energy distribution optimization" and used for their control. The operating mode  $M_{load}^{\{i\}}$  defines the degradation of the load  $i$ . The operating mode  $M_{pl}^{\{j\}}$  for the powerlink  $j$  corresponds to the model description in Section 5.4. Also the driving destination  $s_{ssl}$  and the driving profile degradation vector  $\underline{dpdx}$  are the output of the energy distribution optimization, describing a feasible driving mission from the energetic point of view. For verification of the proposed predictive energy management, a MATLAB/Simulink model for each submodule according to the description in corresponding chapters was implemented. In the next section, simulation results verifying the functionality of the discussed energy management architecture are provided.

### 7.1.2. Simulation Results for Powertrain with Single Motor

The powernet topology with a single traction motor used for the simulation in this section was proposed in [8] and is depicted in Fig. 7.2, which is a detailed version of the

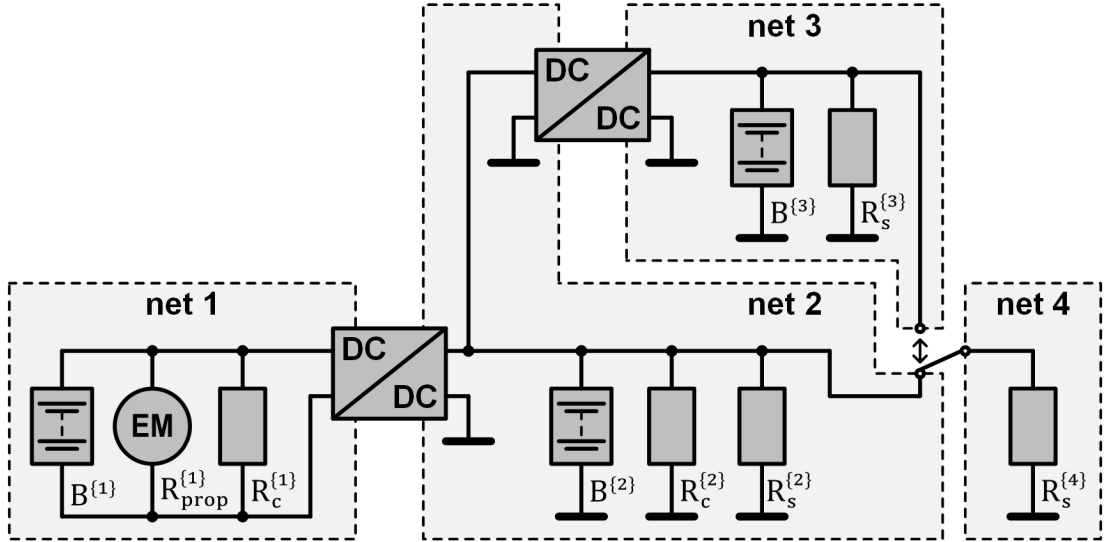


Figure 7.2.: Exemplary powernet topology with single motor.

topology already discussed in Section 5.7.2 and depicted in Fig. 5.19. It consists of one HV subpowernet (net 1) and three low voltage (12 V) subpowernets (net 2 to 4). For the simulation it is assumed that the subpowernet 1 contains a lithium-ion HV battery  $B^{\{1\}}$  with a nominal capacity  $Q_{\text{bat0}}^{\{1\}}$  of 63 Ah and a nominal voltage of 355 V. Both subpowernets 2 and 3 contain a lead-acid battery ( $B^{\{2\}}/B^{\{3\}}$ ) used for the voltage stability with a nominal capacity  $Q_{\text{bat0}}^{\{2/3\}}$  of 30 Ah and a nominal voltage of 12 V.

For the battery  $B^{\{1\}}$  an initial state of charge equal to 45 % and to 90 % for  $B^{\{2\}}$  and  $B^{\{3\}}$  is assumed. The energy from the battery  $B^{\{1\}}$  is transferred to the 12 V loads in subpowernet 1 via the HV/12 V DC/DC converter, which can be operated either in forward (net 1 to 2) or off mode. An additional 12 V/12 V bidirectional DC/DC converter, which can be operated in forward (net 2 to 3), reverse (net 3 to 2) and off mode, couples the subpowernets 2 and 3. Both subpowernets 2 and 3 are required for the redundant supply of the safety-critical loads  $R_s^{\{2\}}$  and  $R_s^{\{3\}}$ , which are assumed to be redundant in the functionality, meaning that a failure in one of these loads can be tolerated. The safety-critical loads  $R_s^{\{4\}}$  in subpowernet 4 can be supplied either by subpowernet 2 or 3.

The average power consumption of the comfort loads  $R_c^{\{1\}}$  and  $R_c^{\{2\}}$  is set to 2500 W and to 1000 W. It is assumed that the power demand of  $R_c^{\{1\}}$  and  $R_c^{\{2\}}$  can be degraded in five ( $n_p = 6$ ) equally distributed steps to 0 W. An average power demand equal to 200 W is set for the safety-critical loads  $R_s^{\{2\}}$  and  $R_s^{\{3\}}$  and 100 W for  $R_s^{\{4\}}$ . In contrast to the comfort loads  $R_c^{\{1\}}$  and  $R_c^{\{2\}}$ , no degradation is assumed for the safety-critical loads  $R_s^{\{2\}}$ ,  $R_s^{\{3\}}$  and  $R_s^{\{4\}}$ . For all powernet components, the operating temperature is set to 25 °C and a fault-free initial state is assumed.

At the beginning of the simulation, the vehicle destination  $s_{\text{ssl}}$  is set to 40 km, which corresponds to the safe stop location "driving home" (SSL A) (refer to Fig. 4.1). For the degradation of the vehicle destination, four further safe stop locations are considered, namely "parking area" (SSL B), "emergency stop bay" (SSL C), "emergency lane" (SSL D), comfort stop in "current lane" (SSL F) and "emergency braking" (SSL G). Since "emergency braking" is the worst case scenario which is executed when no other solution exists (refer to Section 5.2), only the scenarios SSL A, B, C, D and F are used for the degradation concept ( $n_{\text{ssl}} = 5$ ). Starting at the beginning of the route ( $s_0 = 0$  km), it is further assumed that a parking area is available each 10 km, an emergency stop bay each 5 km and an emergency lane each 1 km. For the comfort stop, a coasting distance equal to 0.2 km is assumed. In the simulation, the driving profile can be degraded in four equal steps ( $n_{\text{dp}} = 5$ ). A vehicle configuration and a driving route according to Appendix A are used in the MATLAB/Simulink simulation. The results are depicted in Fig. 7.3 and 7.4.

As depicted in Fig. 7.3, no degradation is active ( $n_{\text{ssl}} = n_{\text{dp}} = n_{\text{p}} = 1$ ) at the beginning of the driving mission ( $t = 0$  min). The energy flow efficiency of both DC/DC converters in forward mode is set to 95 % throughout the simulation ( $\eta_{\text{pl}}^{\{1,2\}}$  and  $\eta_{\text{pl}}^{\{2,3\}}$  in subplot "Powerlink Output Efficiency [%]" of Fig. 7.4). Due to the internal losses in DC/DC converters it becomes more energy efficient to discharge the 12 V lead-acid batteries. For the optimization, the maximum allowed discharge power for the batteries B<sup>{2}</sup> and B<sup>{3}</sup> is set to 250 W ( $P_{\text{bat.max}}^{\{2/3\}}$  in subplot "Battery Output Power [W]" of Fig. 7.4). The remaining discharge energy  $E_{\text{rde0}}^{\{2/3\}}$  at  $t = 0$  min of both 12 V batteries is equal to 0.212 kWh and the remaining driving time  $dT_{\text{ssl}}$  to 0.92 h. The safety-critical loads R<sub>s</sub><sup>{3}</sup> can be fully supplied by B<sup>{3}</sup> for the entire duration of the driving mission, resulting in the average discharge power of B<sup>{3}</sup> equal to 200 W ( $P_{\text{bat}}^{\{3\}}$  in subplot "Battery Output Power [W]" of Fig. 7.4). Also for the supply of the comfort and safety-related loads R<sub>c</sub><sup>{2}</sup> and R<sub>s</sub><sup>{2}</sup> in subpowernet 2 it is more efficient to deplete the energy from the 12 V battery B<sup>{2}</sup>. A maximum discharge of B<sup>{2}</sup> with 250 W would be possible, but is limited by the energy manager to 222.7 W at  $t = 0$  min ( $P_{\text{bat}}^{\{2\}}$  in subplot "Battery Output Power [W]" of Fig. 7.4). This corresponds to the maximum output power completely discharging the battery B<sup>{2}</sup> during the driving time  $dT_{\text{ssl}}$  under consideration of the average power losses  $P_{\text{bat.loss}}^{\{2\}}$  ( $P_{\text{bat.max}}^{\{2\}} = E_{\text{rde0}}^{\{2\}}/dT_{\text{ssl}} - P_{\text{bat.loss}}^{\{2\}}$ ).

The safety-critical load R<sub>s</sub><sup>{4}</sup> in subpowernet 4 can be supplied by either subpowernet 2 or 3. The energy flow efficiency from net 2 to 4 ( $\eta_{\text{pl}}^{\{2,4\}}$ ) and from 3 to 4 ( $\eta_{\text{pl}}^{\{3,4\}}$ ) is set to 90 % and 85 % at the beginning of the simulation (subplot "Powerlink Output Efficiency [%]" of Fig. 7.4). Considering the powerlink and battery losses (with  $dp_{\text{bat}}^{\{1\}} \approx 0.006$  and  $dp_{\text{bat}}^{\{2/3\}} \approx 0.035$ ) it is more efficient to supply R<sub>s</sub><sup>{4}</sup> from subpowernet 1 via subpowernet 2 (assuming that the discharge of B<sup>{2}</sup> is already used for the supply of R<sub>s</sub><sup>{2}</sup> and R<sub>c</sub><sup>{2}</sup>).



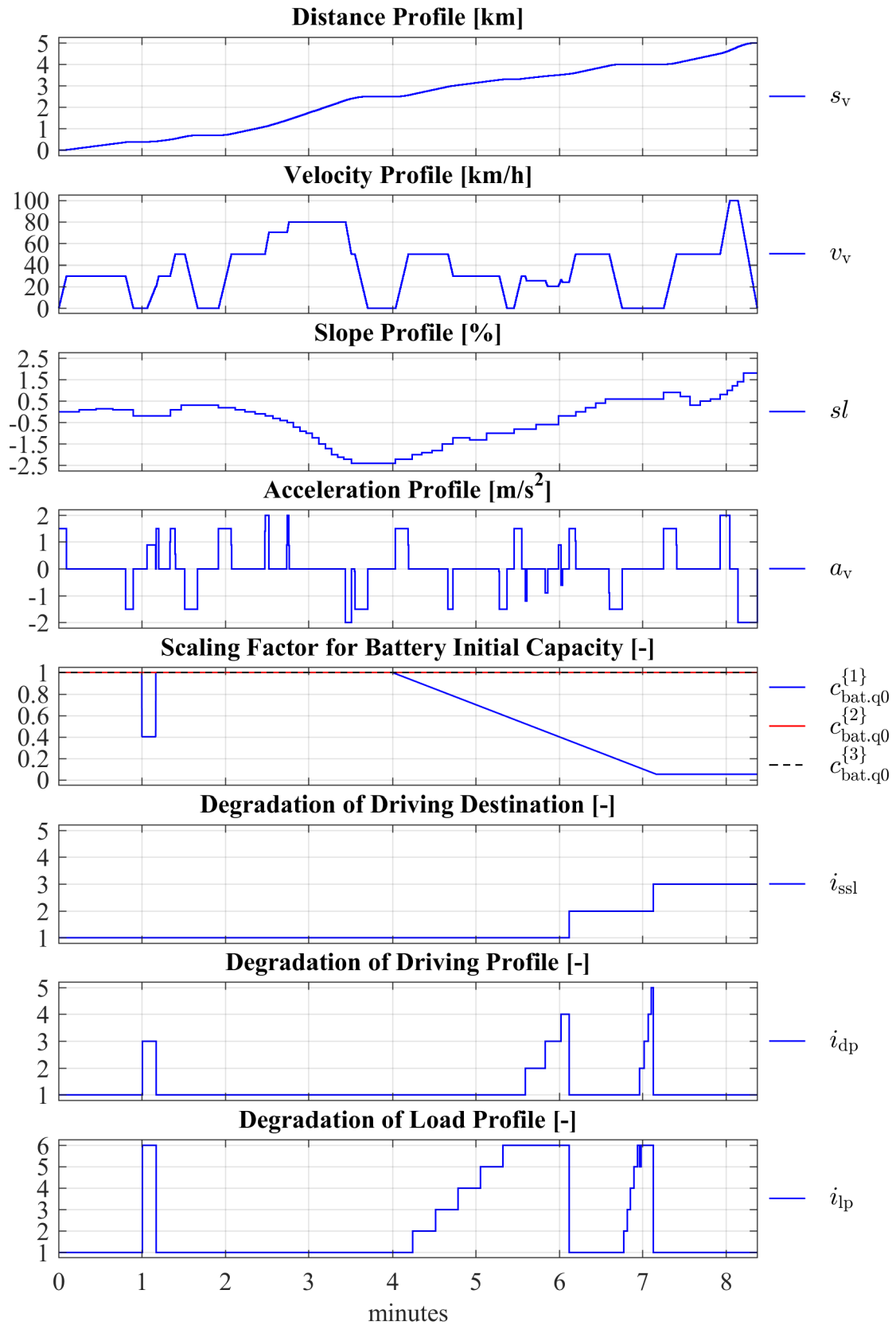


Figure 7.3.: Simulation results for a powertrain topology with single motor (part 1).

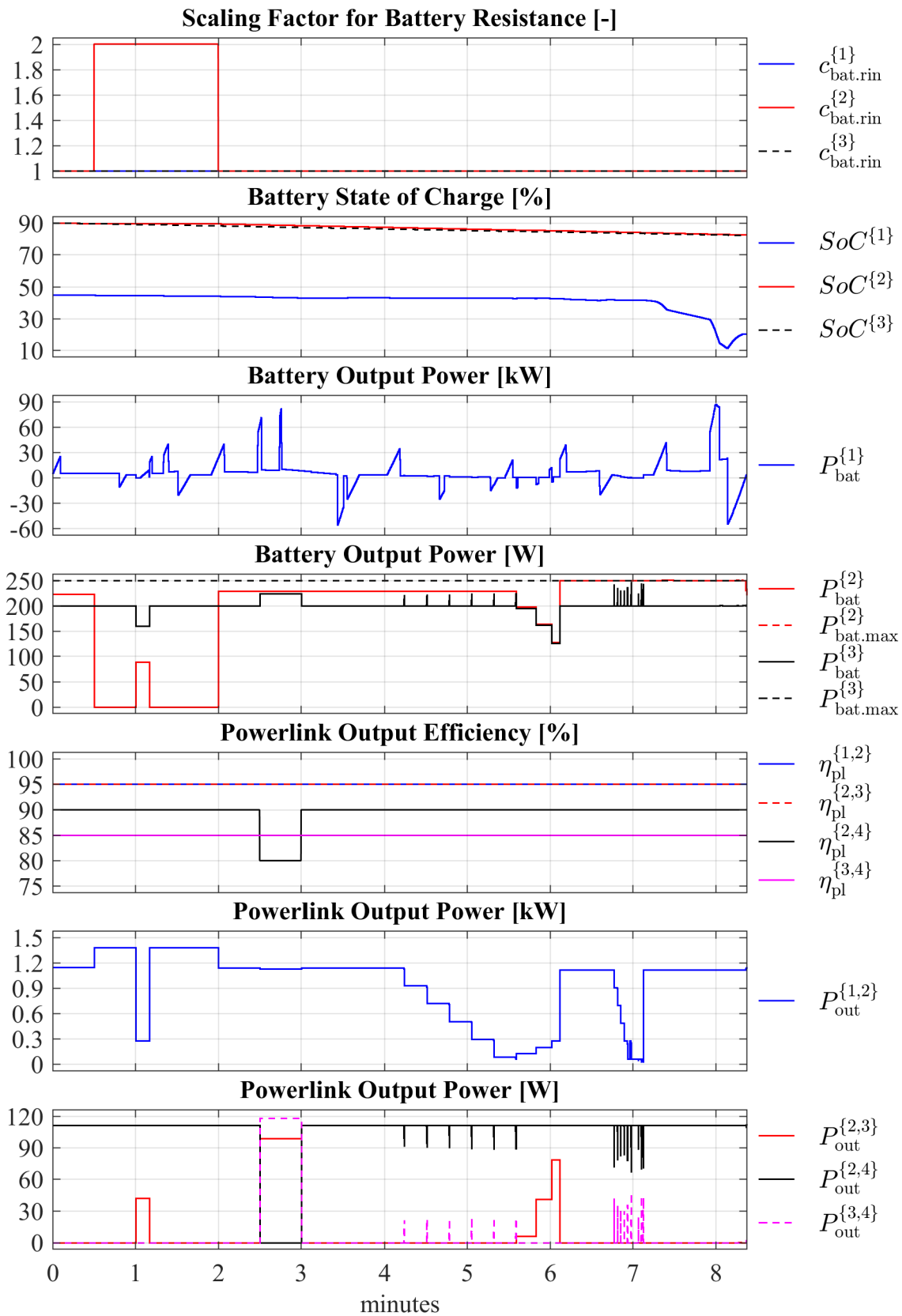


Figure 7.4.: Simulation results for a powernet topology with single motor (part 2).

The operating conditions of powernet components remain stable until the first fault is injected at  $t = 0.5$  min increasing the internal resistance of  $B^{\{2\}}$  by factor 2 ( $c_{\text{bat.rin}}^{\{1\}}$  in subplot "Scaling Factor for Battery Resistance [-]" of Fig. 7.4). The internal resistance of  $B^{\{2\}}$  and  $B^{\{3\}}$  is assumed to be unchanged for the entire simulation. As a fault reaction, the energy manager stops discharging the battery  $B^{\{2\}}$  due to the increased internal losses ( $dp_{\text{bat}}^{\{2\}} \approx 0.077$  at  $t = 0.5$  min). Instead, the entire energy for the supply of  $R_s^{\{2\}}$ ,  $R_c^{\{2\}}$  and  $R_s^{\{4\}}$  is provided by  $B^{\{1\}}$ , resulting in an increase of the output energy from subpowernet 1 to 2 by approx. 234.5 W ( $P_{\text{out}}^{\{1,2\}}$  in subplot "Powerlink Output Power [kW]" of Fig. 7.4).

The second fault is injected at  $t = 1$  min decreasing the initial capacity of  $B^{\{1\}}$  by 60 % ( $c_{\text{bat.q0}}^{\{1\}}$  in subplot "Scaling Factor for Battery Initial Capacity [-]" of Fig. 7.3). The nominal capacity of the batteries  $B^{\{2\}}$  and  $B^{\{3\}}$  is assumed to be unchanged throughout the simulation. As a fault reaction, the energy manager degrades the driving profile to  $i_{\text{dp}} = 3$  and the load profile to  $i_{\text{lp}} = 6$ . With this setting, a degraded driving to the initial destination with  $s_{\text{ssl}} = 40$  km is still possible. Due to the degradation of the driving profile, the remaining driving time also increases ( $dT_{\text{ssl}} \approx 1.26$  h at  $t = 1$  min). This results in a decrease of the average discharge power of  $B^{\{2\}}$  from 200 W by approx. 40.1 W. With the adapted discharge power, the remaining discharge energy  $E_{\text{rde0}}^{\{3\}} = 0.179$  kWh ( $t = 1$  min) would be fully depleted at the end of the driving mission.

For the supply of  $R_s^{\{3\}}$  additional energy must be provided, leading so to the increase of the output power from subpowernet 2 to 3 by approx. 42.2 W at  $t = 1$  min ( $P_{\text{out}}^{\{2,3\}}$  in subplot "Powerlink Output Power [W]" of Fig. 7.4). Due to the reduced available energy in  $B^{\{1\}}$ , the energy manager starts to discharge  $B^{\{2\}}$  also despite of the increased internal losses. For enabling the arrival at  $s_{\text{ssl}} = 40$  km with current degradation ( $i_{\text{dp}} = 3$  and  $i_{\text{lp}} = 6$ ), the discharge of battery  $B^{\{2\}}$  is increased from 0 W to 88.7 W. The remaining energy for the supply of  $R_s^{\{2\}}$ ,  $R_c^{\{2\}}$  and  $R_s^{\{4\}}$  is provided by  $B^{\{1\}}$  via the HV/12 V DC/DC converter ( $P_{\text{out}}^{\{1,2\}}$  in subplot "Powerlink Output Power [kW]" of Fig. 7.4).

At  $t = 1.5$  min, the injected fault reducing the capacity of  $B^{\{3\}}$  is disabled. As a reaction, the energy manager reduces again the degradation of the driving and load profile to no degradation ( $i_{\text{dp}} = i_{\text{lp}} = 1$ ). The operation of the powernet components changes again to the state before the injection of the second fault. Also the first injected fault resulting in the increase of the internal resistance of battery  $B^{\{2\}}$  is disabled at  $t = 2$  min. Again, the energy manager adapts the control of the powernet components similar to the fault-free operation at the beginning of the driving mission.

The third transient fault is injected at  $t = 2.5$  min for the duration of 0.5 min resulting in the decrease of the energy flow efficiency from subpowernet 2 to 4 from 90 % to 80 % ( $\eta_{\text{pl}}^{\{2,4\}}$  in subplot "Powerlink Output Efficiency [%]" of Fig. 7.4). As a fault reaction,

the energy manager toggles the supply of  $R_s^{\{4\}}$  from subpowernet 2 to 3, since this path becomes more energy efficient ( $P_{out}^{\{2,4\}}$  and  $P_{out}^{\{3,4\}}$  in subplot "Powerlink Output Power [W]" of Fig. 7.4). The energy flow from subpowernet 1 to 2 is slightly reduced and the discharge power of the battery  $B^{\{3\}}$  is increased to 223.9 W. Considering the internal losses of  $B^{\{3\}}$  ( $dp_{bat}^{\{3\}} \approx 0.035$ ), this output power would result in a fully discharged battery at the end of the driving mission with  $E_{rde0}^{\{3\}} \approx 0.204$  kWh and  $dT_{ssl} \approx 0.88$  h at  $t = 2.5$  min.

The next fault is injected at  $t = 4$  min resulting in the linear decrease of the nominal capacity of  $B^{\{1\}}$  from 100 % to 5 % within 190 s. As a fault reaction, the energy manager first starts to degrade the load profile from  $i_p = 1$  at  $t \approx 4.24$  min to  $i_p = 6$  at  $t = 5.33$  min. Due to the decreasing available energy of the traction battery it becomes impossible to reach the destination also with all loads degraded. Therefore, the energy manager proceeds with the degradation of the driving profile from  $i_{dp} = 1$  at  $t \approx 5.59$  min to  $i_{dp} = 4$  at  $t \approx 6.02$  min. After finally degrading the driving destination at  $t \approx 6.12$  min to the next parking area (SSL B) at  $s_{ssl} = 10$  km ( $i_{ssl} = 2$ ), it becomes again possible to turn on all loads ( $i_p = 1$ ) and to drive without degradation of driving profile ( $i_{dp} = 1$ ). Similarly, due to the ongoing decrease of the battery capacity, the load profile is degraded again starting from  $i_p = 1$  at  $t \approx 6.78$  min to  $i_p = 6$  at  $t \approx 6.98$  min, followed by the degradation of the driving profile from  $i_{dp} = 1$  at  $t \approx 6.96$  min to  $i_{dp} = 5$  at  $t \approx 7.10$  min. After degrading the driving destination at  $t \approx 7.13$  min to the next emergency bay (SSL C) at  $s_{ssl} = 5$  km ( $i_{ssl} = 3$ ), the degradation of the load and driving profile is disabled again. With the remaining energy resources the driving mission is completed at  $s_{ssl} = 5$  km at  $t \approx 8.37$  min. The corresponding distance ( $s_v$ ), velocity ( $v_v$ ), slope ( $sl$ ) and acceleration profile ( $a_v$ ) are depicted in Fig. 7.3.

The degradation of the load profile, driving profile and driving destination has also an impact on the discharge of the batteries  $B^{\{2\}}$  and  $B^{\{3\}}$ . After degrading the driving destination to the next parking area (SSL B) ( $i_{ssl} = 2$ ) at  $t \approx 6.12$  min, the remaining driving time is also reduced to  $dT_{ssl} \approx 8$  min. Since the discharge of  $B^{\{2\}}$  as explained above is more efficient than transmitting the energy from  $B^{\{1\}}$  via the DC/DC converter,  $B^{\{2\}}$  is discharged with maximum allowed power equal to 250 W. Also in the discharge of the battery  $B^{\{2\}}$  short peaks can be seen. Before degrading the load profile, battery  $B^{\{3\}}$  is temporarily used for the partly supply of  $R_s^{\{4\}}$ , releasing so the energy of  $B^{\{2\}}$  for the supply of  $R_s^{\{2\}}$  and  $R_c^{\{2\}}$ , which is required due to the lack of energy in the traction battery  $B^{\{2\}}$ .

The simulation results presented in this section exemplified and verified the functionality of the adaptive and predictive EMS. Due to the automated fault reactions, the energy manager adapts the control of the fail-operational powernet for arriving at the safest pos-

sible position for the passengers. In the presented example, despite multiple faults, the control of the powernet was optimized, so that the arrival at the next emergency bay at 5 km distance was possible. In the next section, the proposed EMS architecture is extended for the control of fail-operational powertrain and powernet topologies with multiple traction motors by embedding also the predictive torque distribution optimization in the model predictive control.

## 7.2. Energy Management Architecture for Powertrain with Multiple Motors

A powertrain with a single traction motor and a fail-operational powernet with a minimum of three subpowernets can be used for an automated transition to a standstill in case of a failure with the scenarios emergency braking (SSL G), comfort stop in current lane (SSL F) and coasting to the rightmost lane (SSL E). According to Fig. 4.1, a fail-operational drive functionality is required for more complex failure reactions with degraded propulsion functionality enabling to reach an emergency lane (SSL D), next emergency stop bay (SSL C), next parking area (SSL B) or even the desired destination (SSL A). For this, a fail-operational powertrain containing at least two traction motors each supplied by an independent traction battery is required. For establishing reliable power supply for the safety-critical subsystems braking and steering, again a fail-operational powernet is required. Therefore, a powernet configuration with a minimum of four subpowernets can be assumed, two of them (subpowernet 1 and 2) containing a 48 V or high voltage traction battery and motor(s) and further two subpowernets (subpowernet 3 and 4) for the redundant supply of the low voltage braking and steering subsystems. For the control of this powertrain and powernet configuration, an EMS architecture depicted in Fig. 7.5 is proposed and explained in Section 7.2.1. Simulation results verifying its functionality for an exemplary fail-operational powertrain with four EMSs and a powernet with five subpowernets as depicted in Fig. 6.10 and 7.6 are provided in Section 7.2.2.

### 7.2.1. System Architecture for Powertrain with Multiple Motors

The basic structure of the EMS architecture controlling a fail-operational powertrain and powernet is similar to the architecture presented in Section 7.1.1. As depicted in Fig. 7.5 it consists again of four main submodules: (1) "driving trajectory prediction", (2) "torque distribution profile and propulsion energy prediction", (3) "remaining discharge energy prediction" and (4) "energy distribution optimization". The ADAS horizon provider transmits the electronic horizon to the EMS, which is converted to the required format for the

prediction of the driving trajectory by the ADAS horizon reconstructor at the energy management side.

For the powernet topology it is assumed that both traction batteries (Battery 1 and 2) as well as the four traction motors (Motor 1 to 4) are located in the subpowernets 1 and 2. One of the control goals for the predictive torque distribution optimization was the symmetrical discharge of the independent traction batteries. As it will be exemplified in the next subsection, the discharge asymmetry can be also caused by asymmetrical comfort and safety-critical loads in the corresponding subpowernet as well as by asymmetrical supply of other subpowernets (refer e.g. to the powernet topology depicted in Fig. 7.6). Therefore, for ensuring the symmetrical discharge by the torque distribution, first the average power required for the supply of the comfort loads ( $P_{rc}^{\{k,i_p\}}$ ), safety-critical loads ( $P_{rs}^{\{k,i_p\}}$ ) and of other subpowernets ( $\sum_{i=1}^{n_{\text{spn}}} P_{\text{out}}^{\{k,i\}}$ ) must be estimated (for the notation refer to Fig. 5.1). This average power demand, denoted by  $P_{\text{sc}}^{\{k\}}$  in Fig. 7.5, can be then taken into account for the torque distribution optimization. Assuming that the subpowernets 1 and 2 containing the traction batteries cannot receive energy from other subpowernets, the average power demand  $P_{\text{sc}}^{\{k,i_p\}}$  can be defined as:

$$P_{\text{sc}}^{\{k,i_p\}} = P_{\text{rs}}^{\{k,i_p\}} + P_{\text{rc}}^{\{k,i_p\}} + \sum_{i=1}^{n_{\text{spn}}} P_{\text{out}}^{\{k,i\}} \quad \text{with } k = \{1, 2\}, i = \{1..n_{\text{spn}}\} \setminus \{1, 2\} \quad (7.2)$$

At the beginning of each optimization cycle, first the driving trajectory is predicted (analog to the description in Section 7.1.1). In the next step, using the current battery state of charge values ( $SoC_0^{\{1..n_{\text{spn}}\}}$ ) and the current diagnostic state vectors ( $\underline{D}_{\text{bat}}^{\{1..n_{\text{spn}}\}}$ ) (for notation refer to Section 7.1.1), the remaining discharge energy of the traction batteries (Battery 1..2) and voltage stability batteries (Battery 3.. $n_{\text{spn}}$ ) is estimated. In contrast to Section 7.1.1 no virtual state of charge  $SoC_0^{*\{1/2\}}$  after subtracting the propulsion energy is estimated in this version of the EMS. Therefore, the remaining discharge battery is estimated only once per optimization cycle.

After estimation of the remaining driving time  $dT_{\text{ssl}}$  and battery discharge energies modeled with the parameters  $E_{\text{rde0}}^{\{1..n_{\text{spn}}\}}$  and  $dp_{\text{bat}}^{\{1..n_{\text{spn}}\}}$ , the required input for the torque distribution optimization is provided. The energy distribution optimization is then executed under consideration of the current diagnostic vectors for the powerlinks ( $\underline{D}_{\text{pl}}^{\{1..n_{\text{pl}}\}}$ ) and for the loads ( $\underline{D}_{\text{load}}^{\{1..n_{\text{spn}}\}}$ ) (for notation refer to Section 7.1.1) and with the assumption that no energy is required for the propulsion. After optimizing the energy distribution in this way, provided a valid solution exists, sufficient energy resources are allocated for all powernet loads excluding the propulsion loads.

The energy provided by the traction batteries can be divided in two parts. The first part

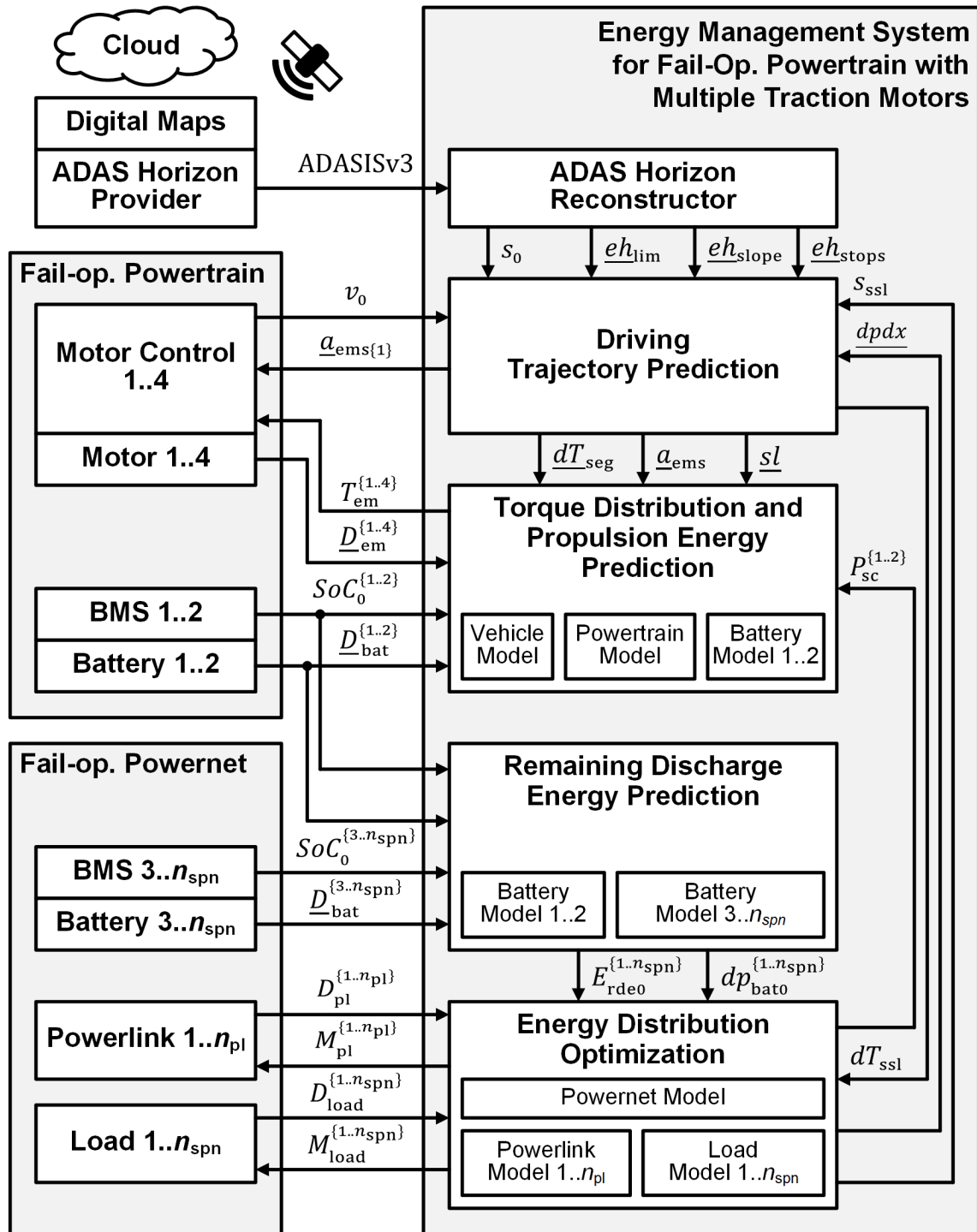


Figure 7.5.: Energy management architecture for powertrain with multiple motors.

is required for the supply of the traction motors. The second part is used for the supply of the safety-critical and comfort loads of the corresponding subpowernet as well as for the supply of other subpowernets, resulting in the average discharge power equal to  $P_{sc}^{\{1/2\}}$  as defined in (7.2), which is estimated as output of the energy distribution optimization. In the next step, the optimal torque distribution profile as well as the corresponding

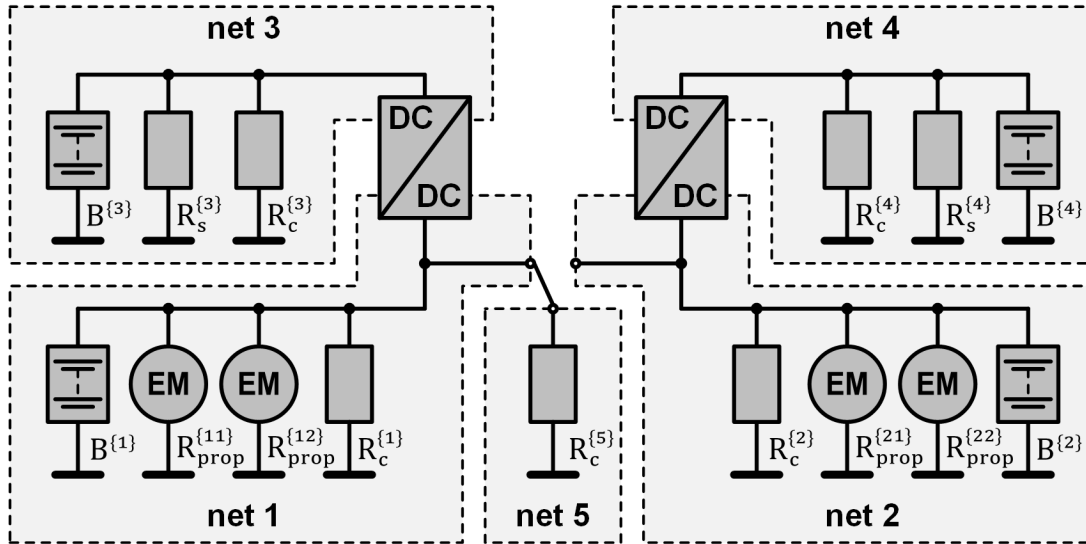


Figure 7.6.: Exemplary powernet topology with multiple motors.

propulsion energy are estimated using the control strategy and algorithms presented in Section 6.4. At the end of the torque distribution and propulsion energy prediction it is checked if the minimum allowed state of charge of at least one of the traction batteries is exceeded. In this case, the energy stored in the traction batteries is not sufficient for the entire driving mission and degradation of overall energy demand is required. This information flag is then transmitted to the energy distribution optimization with the integrated three-level-degradation concept as presented in Section 4.1. The degradation variables for the load profile, driving profile and driving destination are then adapted and this process is repeated until a valid solution is found. In the next section, simulation results verifying and exemplifying the functionality of the discussed energy management architecture in normal (fault-free) and failure case operation are provided.

### 7.2.2. Simulation Results for Powertrain with Multiple Motors

The fail-operational powernet topology with multiple traction motors used for the simulation in this section is depicted in Fig. 7.6, which is a detailed version of the topology already discussed in Section 5.7.1 and depicted in Fig. 5.17. It consists of two 48 V subpowernets (net 1 and net 2) containing each an independent traction battery (B<sup>{1}</sup> and B<sup>{2}</sup>), comfort loads (R<sub>c</sub><sup>{1}</sup> and R<sub>c</sub><sup>{2}</sup>) and two traction motors (R<sub>prop</sub><sup>{11}</sup>/R<sub>prop</sub><sup>{12}</sup> and R<sub>prop</sub><sup>{21}</sup>/R<sub>prop</sub><sup>{22}</sup>). Both subpowernets can supply the third 48 V subpowernet (net 5) via a toggle switch containing a high power comfort load R<sub>c</sub><sup>{5}</sup>, which might be for example an air conditioning system. In this way, the asymmetry in the discharge of the traction batteries B<sup>{1}</sup> and B<sup>{2}</sup> due to the asymmetrical load R<sub>c</sub><sup>{5}</sup> can be avoided. Two independent low voltage (12 V) subpowernets (net 3 and 4) are used for the supply of the safety-critical loads R<sub>s</sub><sup>{3}</sup>



and  $R_s^{\{4\}}$  as well as comfort loads  $R_c^{\{3\}}$  and  $R_c^{\{4\}}$ . The low voltage batteries  $B^{\{3\}}$  and  $B^{\{4\}}$  are used for establishing the voltage stability in subpowernets 3 and 4 in case of high power dynamic load conditions. They are also used for the supply of the safety-critical loads for the duration of automated transition to the safe state in case the main energy source ( $B^{\{1\}}$  for subpowernet 3 and  $B^{\{2\}}$  for subpowernet 4) fails. The safety-critical loads  $R_s^{\{3\}}$  and  $R_s^{\{4\}}$  are assumed to be redundant in the functionality, meaning that a failure in one of these loads can be tolerated.

For the simulation it is assumed that the subpowernet 1 and 2 contain each a lithium-ion battery  $B^{\{1\}}/B^{\{2\}}$  with a nominal capacity  $Q_{\text{bat0}}^{\{1/2\}}$  of 300 Ah and a nominal voltage of 48 V. Both subpowernets 3 and 4 contain a lead-acid battery ( $B^{\{3\}}/B^{\{4\}}$ ) with a nominal capacity  $Q_{\text{bat0}}^{\{3/4\}}$  of 30 Ah and nominal voltage of 12 V. For the batteries  $B^{\{1\}}$  and  $B^{\{2\}}$  an initial state of charge equal to 30 % and to 90 % for the batteries  $B^{\{3\}}$  and  $B^{\{4\}}$  is assumed. The energy from the 48 V batteries  $B^{\{1\}}$  and  $B^{\{2\}}$  is transferred to the 12 V loads in subpowernet 3 and 4 via the 48 V/12 V DC/DC converters, which can be operated either in forward or off mode.

For the comfort loads  $R_c^{\{1\}}$  and  $R_c^{\{2\}}$  in subpowernet 1 and 2 an average power consumption equal to 1000 W is assumed. The average power consumption of the high power comfort load  $R_c^{\{5\}}$  in subpowernet 5 is set to 2000 W and to 1250 W for the low voltage comfort loads  $R_c^{\{3\}}$  and  $R_c^{\{4\}}$ . It is further assumed that the average power demand of all comfort loads can be degraded in five ( $n_{\text{lp}} = 6$ ) equally distributed steps to 0 W. An average power demand equal to 200 W with no degradation is assumed for the safety-critical loads  $R_s^{\{3\}}$  and  $R_s^{\{4\}}$  in subpowernets 3 and 4. For all powernet components, the operating temperature is set to 25 °C and a fault-free initial state is assumed.

At the beginning of the simulation, the vehicle destination is set to 4.8 km, which corresponds to the safe stop location "driving home" (SSL A). For the degradation of the vehicle destination  $s_{\text{ssl}}$ , four further safe stop locations are considered, namely "parking area" (SSL B), "emergency stop bay" (SSL C), "emergency lane" (SSL D), comfort stop in "current lane" (SSL F) and "emergency braking" (SSL G). Since "emergency braking" is the worst case scenario which is executed when no other solution exists (s. Section 5.2), again only the scenarios SSL A, B, C, D and F are used for the degradation concept ( $n_{\text{ssl}} = 5$ ). Starting at the beginning of the route ( $s_0 = 0$  km), a parking area each 1 km, an emergency stop bay each 800 m and an emergency lane each 400 m is assumed. For the coasting distance in case of the comfort stop again 200 m are assumed. In the simulation, the driving profile can be degraded in 4 equal steps ( $n_{\text{dp}} = 5$ ). A vehicle configuration and a driving route according to Appendix B are used in the MATLAB/Simulink simulation. The results are depicted in Fig. 7.7 and 7.8.

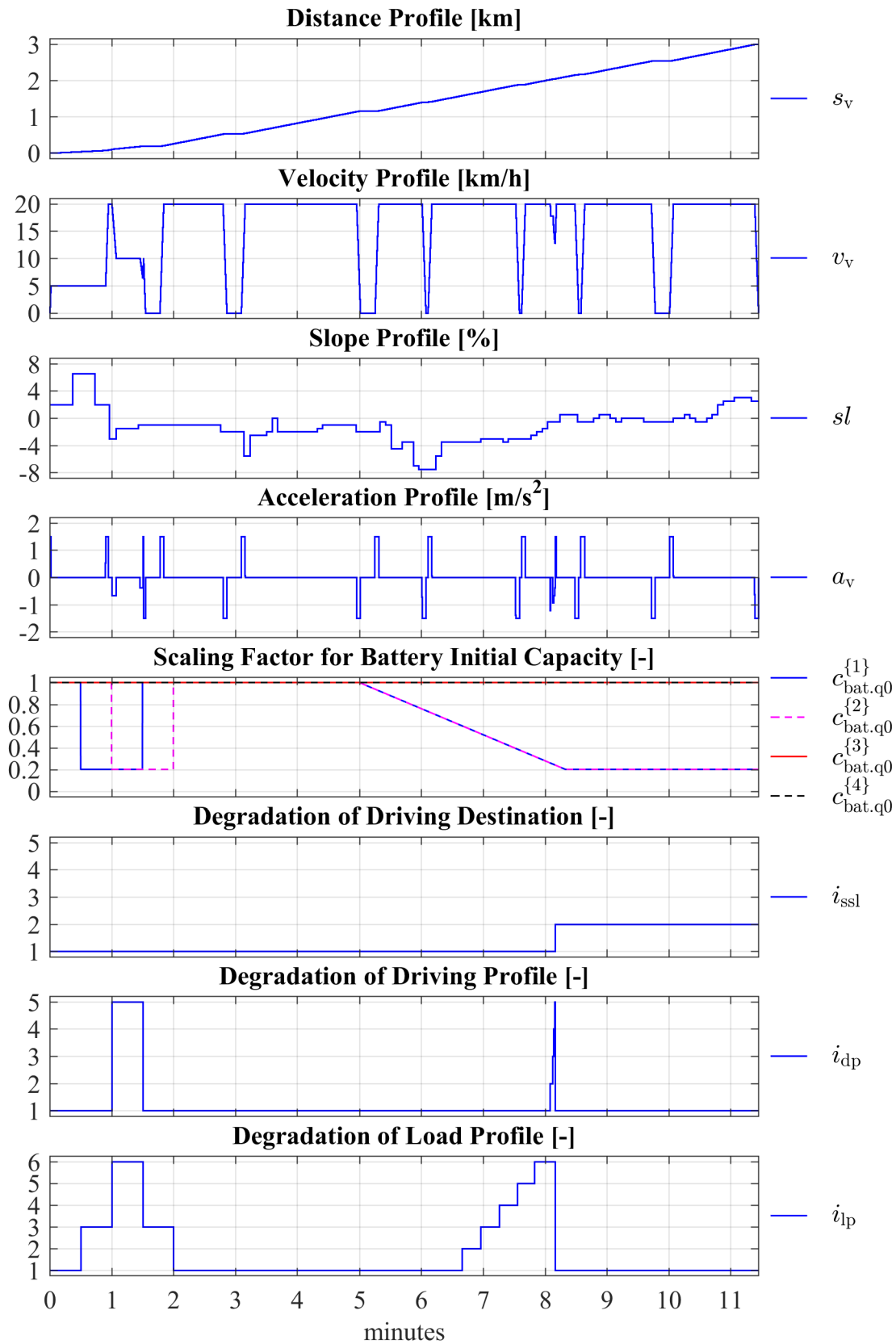


Figure 7.7.: Simulation results for a powernet topology with multiple motors (part 1).

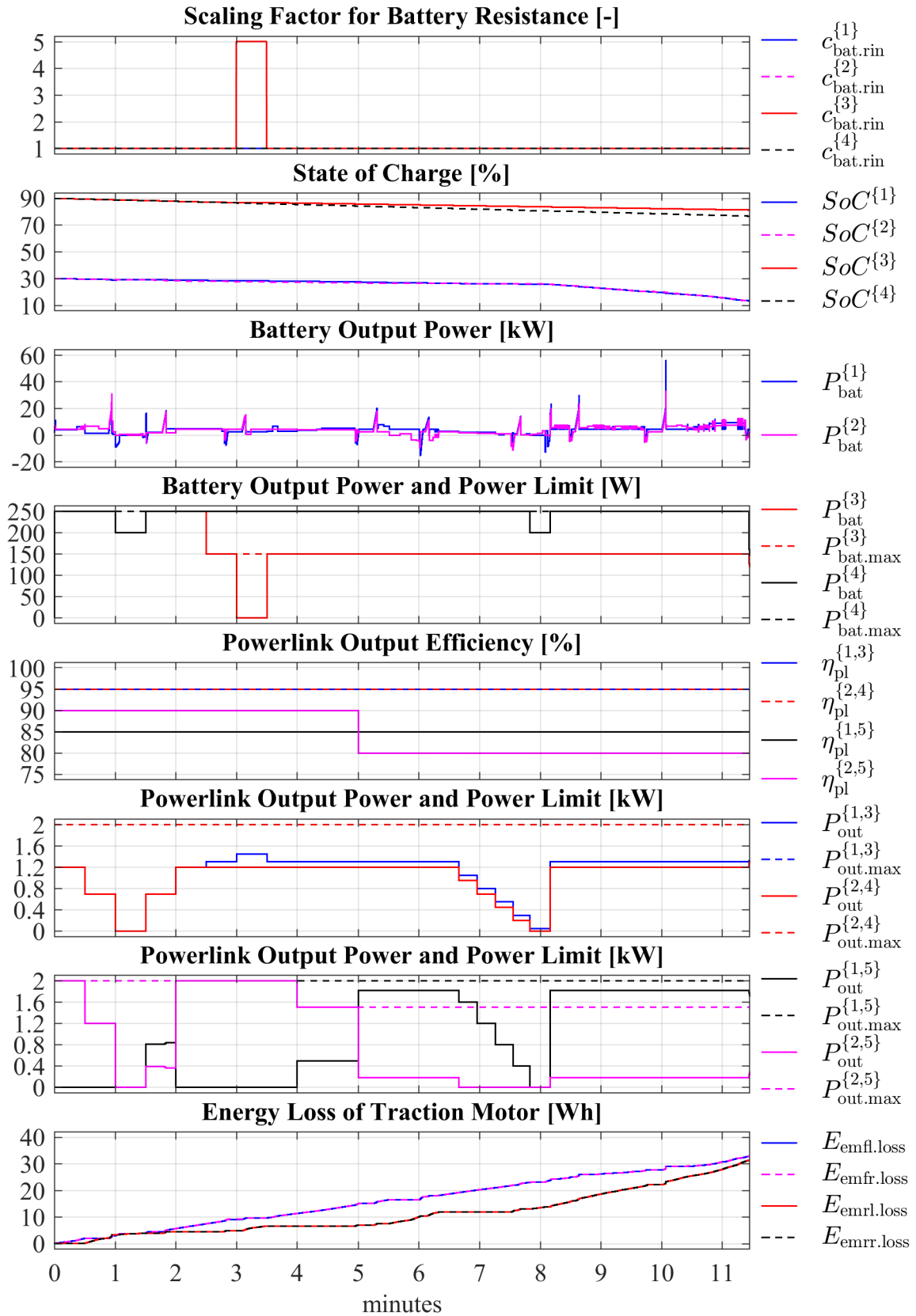


Figure 7.8.: Simulation results for a powernet topology with multiple motors (part 2).

As depicted in Fig. 7.7, no degradation is active ( $n_{\text{ssl}} = n_{\text{dp}} = n_{\text{ip}} = 1$ ) at the beginning of the driving mission ( $t = 0$  min). The energy flow efficiency of both DC/DC converters in forward mode is set to 95 % throughout the simulation ( $\eta_{\text{pl}}^{\{1,3\}}$  and  $\eta_{\text{pl}}^{\{2,4\}}$  in subplot "Powerlink Output Efficiency [%]" of Fig. 7.8). Due to the internal losses in DC/DC converters it becomes more energy efficient to discharge the 12 V lead-acid batteries, which is limited to 250 W ( $P_{\text{bat.max}}^{\{3/4\}}$  and  $P_{\text{bat}}^{\{3/4\}}$  in subplot "Battery Output Power [W]" of Fig. 7.8) at the beginning. The remaining discharge energy of the batteries  $B^{\{3\}}$  and  $B^{\{4\}}$  ( $E_{\text{rde0}}^{\{3/4\}} \approx 0.212$  kWh) is also sufficient for providing the maximum discharge power of 250 W for the entire duration of the driving mission with  $dT_{\text{ssl}} \approx 18.3$  min.

The high power comfort load  $R_c^{\{5\}}$  in subpowernet 5 can be supplied by either subpowernet 1 or 2. The energy flow efficiency from net 1 to 5 ( $\eta_{\text{pl}}^{\{1,5\}}$ ) and from 2 to 5 ( $\eta_{\text{pl}}^{\{2,5\}}$ ) is set to 85 % and 90 % at the beginning of the simulation (subplot "Powerlink Output Efficiency [%]" of Fig. 7.8). Considering the losses of the toggle switch it is more efficient to supply  $R_c^{\{5\}}$  fully from subpowernet 2 ( $P_{\text{out}}^{\{1,5\}}$  and  $P_{\text{out}}^{\{2,5\}}$  in subplot "Powerlink Output Power and Power Limit [kW]" of Fig. 7.8). For the energy distribution optimization, the output power of the DC/DC converters and of the toggle switch is limited to 2 kW ( $P_{\text{out.max}}^{\{1,3\}}$ ,  $P_{\text{out.max}}^{\{2,4\}}$ ,  $P_{\text{out.max}}^{\{1,5\}}$  and  $P_{\text{out.max}}^{\{2,5\}}$  in subplots "Powerlink Output Power and Power Limit [kW]" of Fig. 7.8).

The operating conditions of powernet components remain stable until the first transient fault is injected at  $t = 0.5$  min for the duration of 1 min decreasing the capacity of  $B^{\{1\}}$  by 80 % ( $c_{\text{bat.q0}}^{\{1\}}$  in subplot "Scaling Factor for Battery Initial Capacity [-]" of Fig. 7.7). As a fault reaction, the energy manager degrades the average power consumption of the powernet loads ( $i_{\text{ip}} = 2$ ). Also the capacity of  $B^{\{2\}}$  is reduced to 20 % by a transient fault injected at  $t = 1$  min for the duration of 1 min ( $c_{\text{bat.q0}}^{\{2\}}$  in subplot "Scaling Factor for Battery Initial Capacity [-]" of Fig. 7.7). As a fault reaction, the energy manager further degrades the load profile to the maximum level ( $i_{\text{ip}} = 6$ ). For enabling the arrival at the set destination  $s_{\text{ssl}} = 4.8$  km (SSL A), also the degradation of the driving profile to the maximum level ( $i_{\text{dp}} = 5$ ) is required, resulting in the increased driving time of approx. 32.8 min. Since only the safety-critical loads  $R_s^{\{3\}}$  and  $R_s^{\{4\}}$  are active after degradation, the discharge power of the batteries is reduced for the supply of these loads with 200 W ( $P_{\text{bat}}^{\{3/4\}}$  in subplot "Battery Output Power and Power Limit [W]" of Fig. 7.8).

The first fault is disabled at  $t = 1.5$  min, increasing again the capacity of the traction battery  $B^{\{1\}}$  to 100 %. It becomes again possible to turn on more comfort loads reducing the degradation of load profile to  $i_{\text{ip}} = 2$  and to reduce the driving time by setting the degradation of driving profile to  $i_{\text{dp}} = 1$ , resulting in the remaining driving time of approx. 17.1 min. Both low voltage batteries  $B^{\{3\}}$  and  $B^{\{4\}}$  are discharged again with

the maximum allowed power of 250 W and the remaining power for the supply of loads in subpowernet 3 and 4 is provided by the traction batteries via the DC/DC converters. Also the supply of  $R_c^{\{5\}}$  is activated again, but now taking the energy flow path with lower efficiency (85 % from net 1 to 5), since the capacity of  $B^{\{2\}}$  is still reduced and not enough energy is available for the supply of  $R_c^{\{5\}}$  by subpowernet 2 (90 % from net 2 to 5).

The supply of  $R_c^{\{5\}}$  toggles back to the more energy efficient path from subpowernet 1 to 2 after disabling the second fault increasing again the capacity of the traction battery  $B^{\{2\}}$  to 100 %. It becomes again possible to turn on all the powernet loads by reducing the degradation level of the load profile to  $i_p = 1$ .

At  $t = 2.5$  min a change in the control of the battery  $B^{\{3\}}$  is applied, reducing the maximum allowed discharge power from 250 W to 150 W. The discharge power of the battery  $B^{\{3\}}$  follows this reduction resulting also in the increased energy flow from subpowernet 1 to 3. At  $t = 3$  min, a fault increasing the internal resistance of the battery  $B^{\{3\}}$  by factor 5 is injected, resulting in no discharge of  $B^{\{3\}}$  and the supply of the comfort and safety-critical loads  $R_c^{\{3\}}$  and  $R_s^{\{3\}}$  by the traction battery  $B^{\{1\}}$  via the DC/DC converter, which becomes more energy efficient. After this transient fault is disabled at  $t = 3.5$  min, the battery  $B^{\{3\}}$  is again discharged with maximum allowed 250 W.

At  $t = 4$  min, the next change in the control is applied, reducing the maximum allowed output power of the toggle switch pin connecting subpowernet 2 and 5 to 1.5 kW. The average power consumption of  $R_c^{\{5\}}$  equals to 2000 W at the currently set level for the load profile. Therefore, despite the lower energy flow efficiency, the energy manager transmits the remaining 0.5 kW from subpowernet 1 by operating the toggle switch in PWM mode. At  $t = 5$  min, the next fault is injected resulting in the decrease of the energy flow efficiency from subpowernet 2 to 5 by 10 %. The energy transfer from subpowernet 1 to 5 with efficiency of 85 % becomes now more efficient compared to the path from subpowernet 2 to 5 with 80 % of efficiency. Therefore, the energy manager starts to supply  $R_c^{\{5\}}$  fully from subpowernet 1.

The next fault is injected at  $t = 5$  min resulting in the linear decrease of the nominal capacity of  $B^{\{1\}}$  and  $B^{\{2\}}$  from 100 % to 20 % within 200 s. As a fault reaction, the energy manager first starts to degrade the load profile from  $i_p = 1$  at  $t \approx 6.65$  min to  $i_p = 6$  at  $t = 7.83$  min. Due to the decreasing available energy of the traction batteries it becomes impossible to reach the destination also with all loads degraded. Therefore, the energy manager proceeds with the degradation of the driving profile from  $i_{dp} = 1$  at  $t \approx 8.08$  min to  $i_{dp} = 5$  at  $t \approx 8.15$  min. Since the average driving velocity in this example is already low, the effect of the driving profile degradation to the overall energy reduction remains also low. After finally degrading the driving destination at  $t \approx 8.16$  min to the

next parking area (SSL B) at  $s_{ssl} = 3$  km ( $i_{ssl} = 2$ ), it becomes again possible to turn on all loads ( $i_p = 1$ ) and to drive without degradation of the driving profile ( $i_{dp} = 1$ ). With the remaining energy resources the driving mission is completed at  $s_{ssl} = 3$  km at  $t \approx 11.45$  min. The corresponding distance ( $s_v$ ), velocity ( $v_v$ ), slope ( $sl$ ) and acceleration profile ( $a_v$ ) are depicted in Fig. 7.8.

Despite various injected faults, changes in the system state and in the control settings, also the control goals for the torque distribution optimization could be met. It can be seen that the traction batteries  $B^{\{1\}}$  and  $B^{\{2\}}$  are discharged symmetrically ( $SoC^{\{1\}}$  and  $SoC^{\{2\}}$  in subplot "State of Charge [%]" of Fig. 7.8). With the appropriate torque distribution it becomes also possible to compensate the asymmetrical discharge of the batteries due to the asymmetrical high power load  $R_c^{\{5\}}$ . Considering the balancing of the motor losses it can be also seen that this control goal can be achieved for the balancing between the motors  $M_{fl}/M_{fr}$  at front and the motors  $M_{rl}/M_{rr}$  at rear axle ( $E_{emfl.loss}/E_{emfr.loss}$  for front axle,  $E_{emrl.loss}/E_{emrr.loss}$  for rear axle in subplot "Energy Loss of Traction Motor [Wh]" of Fig. 7.8). For the balancing of the losses between the axles it can be seen that the delta is small at the beginning of the driving mission, but then slightly increases. At the end of the driving mission, the delta of the energy losses between the axles is reduced again.

Summing up the results it can be stated that the proposed EMS architecture manages to adapt the control of the fail-operational powernet and powertrain allowing to arrive at the next parking area at 3 km despite multiple faults and changes in the control settings by additionally enhancing the operation of the powernet and powertrain components.

# Chapter 8.

## Conclusion

With the introduction of automated driving, new safety and reliability requirements arise for the power supply of the safety-critical functions (e.g. braking or steering) involved in the automated vehicle motion and transition to a safe state in case of a failure. Besides new designs for the fail-operational powernet topologies addressing the fulfillment of these requirements, also new strategies and algorithms for their control in fault-free and failure case operation are required. The work presented in this dissertation studied a novel and generic approach for the energy management of fail-operational powernets combining both, the control in fault-free states and the functional safety concept, which is required for all safety-critical functions by ISO 26262, ensuring the reliable power supply for the entire duration of the vehicle transition to a standstill in case of a failure.

As the main control goal, the arrival of the automated vehicle at the safest possible location for the passengers also in case of a failure was defined. For the realization of this safety-based range extension, a model predictive and adaptive approach based on the theory of optimal control was proposed. For the formulation of the optimization problem, a generic mathematical model considering also possible failure states of a fail-operational powernet with up to  $n_{\text{spn}}$  subpowernets interconnected via powerlinks was defined. The ease of adaptation of this model to various powernet topologies by means of parametrization was demonstrated with two examples.

For the allocation of sufficient energy resources for all powernet loads for the entire driving mission, a constraint for the energy distribution optimization problem forcing a positive energy balance for each subpowernet was used, taking into account the predicted values for the available energy resources as well as the trip-based energy consumption of all loads. In case that the energy balance cannot be achieved, meaning that the overall energy consumption exceeds the available resources, a three-level-degradation concept was integrated in the optimization problem by modeling the degradation of the loads with

integer valued optimization variables. As a measure for the reduction of the overall energy demand, the degradation of the comfort loads reducing the average power consumption per time unit was foreseen at the first level. The degradation of the driving profile reducing the average propulsion energy per driven kilometer and the degradation of the driving destination reducing the travel distance was foreseen at the second and third level.

The main goal for the predictive energy distribution is to arrive at the safest possible destination with a minimum of driving time, a maximum of driving comfort and a minimum of energy losses. For achieving these goals, a multi-objective mixed-integer function was defined maximizing the available energy resources at the end of the driving mission (hence minimizing the energy losses) and minimizing the degradation of the driving destination, of the driving profile and of the comfort loads. The losses of the energy distribution in a powernet can be basically divided into two types: (1) internal losses in the powerlink components (coupling elements) due to the energy exchange between the subpowernets and (2) internal losses in the energy storage components (batteries) due to the conversion of the chemical energy into electrical energy. The proposed algorithm for the energy distribution addresses both types of losses by automatically selecting the most efficient paths for the energy transmission as well as by optimizing the discharge strategy of multiple batteries within the powernet. For the selection of the optimal energy flow paths, the operation of the powerlinks in different modes is modeled with integer-valued optimization variables, so that in addition to the average power to be transferred via all powerlink outputs, also the optimal operation mode for each powerlink is estimated. Furthermore, by adding additional constraints to the energy distribution optimization, also the average output power of the powerlinks and the average discharge power of the batteries is limited to the specified maximum rated power.

In the multi-objective cost function used for the mixed-integer energy distribution optimization additional penalty terms were added enabling to customize the energy flow via each powerlink output as well as the discharge of each battery. While the general formulation of the penalty terms leaves room for various customization scenarios, two examples were discussed, namely the balancing of the thermal heating of the powerlinks and the balancing of batteries' state of charge.

The functionality of the proposed EMS for the control of a fail-operational powernet was exemplified and verified on two exemplary powernet topologies with four and five subpowernets. In addition to the control strategy, also runtime optimized algorithms solving the mixed-integer energy distribution problem were proposed, developed and implemented in MATLAB/Simulink. With calculation times in the range of tens of milliseconds implementation of the proposed control strategy in embedded applications becomes feasible.



---

The model predictive energy distribution and control of the fail-operational powertrain requires as basic input precise estimation of the remaining energy resources as well as of the trip-based energy demand for the propulsion and comfort loads. By taking the average power demand of the comfort and safety-critical loads, the total energy consumption can be estimated if the duration of the driving mission is known. The total propulsion energy required for completion of a given driving mission is dependent on the velocity profile, the number and duration of the stops on the way to the destination, on the road slope as well as on the current health state of the powertrain components. For the estimation of the remaining driving time and for the approximation of the velocity profile from the current vehicle position to the destination under consideration of driving profile degradation, an algorithm based on the usage of map data provided by means of electronic horizon was proposed. The entire route was divided into segments with constant acceleration and road slope and the corresponding duration of each segment was estimated. This representation of the driving trajectory was then used for the quasi-static estimation of the propulsion energy required for its completion. The proposed algorithms were runtime optimized enabling the approximation of the driving trajectory and estimation of the propulsion energy for an EV with a single EM in the range of several tens of milliseconds.

With fail-operational powertrain topologies the availability of the automated driving systems can be increased, so that a breakdown of an automated vehicle in hazardous situations, as for example on a highway within the active traffic, can be avoided. For this, powertrain topologies with multiple traction motors and independent power supply must be considered. Furthermore, by appropriate torque distribution between the motors also the overall driving efficiency and therefore the driving range can be significantly increased, which is of high importance for the safety-based range extension. A general approach for the control of a fail-operational powertrain was derived and five main goals enhancing the fail-operability were identified. For the extension of the driving range, the increase of the overall powertrain efficiency by appropriate torque distribution is required. Furthermore, for ensuring approximately the same driving range in case of a breakdown of one axle, the independent traction batteries must be discharged approximately symmetrically. For the control, also the heating of the powertrain components leading possibly to a faster aging and wear must be avoided. For this, three control goals were formulated, ensuring the balancing of energy losses between the EMs at the front axle, at the rear axle as well as between the axles of a fail-operational powertrain. Also a possibility for balancing of energy losses of both independent traction batteries was incorporated in the torque distribution strategy.

For achieving these goals, a torque distribution optimization problem was formulated under consideration of the limitations of the powertrain components as well as their

current health state. With this approach, also the adaptivity to possible abnormalities and failure states with automated fault reactions was achieved. The proposed strategy for the control of the powertrain was implemented and verified in MATLAB/Simulink for an exemplary topology consisting of four EMs and two independent traction batteries. A decrease of the energy losses by approx. 12% for the given powertrain configuration and use case was achieved while also ensuring the symmetrical battery discharge and load of the traction motors.

For the accurate prediction of the propulsion energy in EV drivetrains with multiple EMs, the assumption of equally distributed torque between the motors would enable a computationally efficient estimation of the driving range similarly to the approach used for drivetrains with a single EM. But on the other side the estimated driving range would be pessimistic, leading for example to a decision to degrade the driving destination, which is not in the sense of the safety-based range extension. Therefore, consideration of the torque distribution is of high importance for the prediction of the remaining driving range. A runtime optimized algorithm for the estimation of the torque distribution profile for the entire driving mission based on the optimization problem used for the control of the fail-operational powertrain was developed and combined with the prediction of propulsion energy. A computational time less than 100 ms was achieved for a given use case, making the implementation of the proposed algorithm in embedded applications feasible.

Finally, the application of the main submodules for the model predictive energy management in automated vehicles, namely optimization of the energy distribution, prediction of the remaining energy resources, approximation of the driving trajectory as well as prediction of the torque distribution and propulsion energy was exemplified on two different powertrain and powernet configurations. The benefits of the proposed control strategy were verified with simulation results in fault-free operation as well as by means of fault injection in failure case operation. Despite multiple faults, the proposed EMS was able to find automatically the best suited fault reactions and to establish reliable power supply for the entire duration of the transition to the standstill. With the generic approach used for the design of the proposed model predictive EMS and runtime optimized algorithms, a framework for further implementation in future automated vehicles is provided.

# Appendices



# Appendix A.

## Definition of Use Case 1

### Vehicle and Gearbox Parameters

Table A.1.: Vehicle parameters used in simulation for use case 1.

parameter	description	value	unit
$\rho$	density of ambient air	1.18	$[\frac{kg}{m^3}]$
$g$	acceleration due to gravity	9.80665	$[\frac{m}{s^2}]$
$A_f$	vehicle frontal area	2.0	$[m^2]$
$m_v$	vehicle mass	1474	$[kg]$
$r_w$	wheel radius	28.2	$[cm]$
$c_d$	aerodynamic drag coefficient	0.32	$[-]$
$c_r$	rolling friction coefficient	0.009	$[-]$
$\gamma_{gb}$	gearbox transmission ratio	9.59	$[-]$
$\eta_{gb}$	gearbox transmission efficiency	0.95	$[-]$

### Velocity/acceleration limits profile $e h_{lim}$

Table A.2.: Velocity/acceleration limits profile used in simulation for use case 1.

$i$	$s_{off}$	$v_{min}$	$v_{max}$	$a_{min}$	$a_{max}$
1	0.0	10	30	0.30	1.50
2	0.5	15	50	0.30	1.50
3	1.1	30	70	0.50	2.00
4	1.4	30	80	0.50	2.00
5	2.4	15	50	0.30	1.50
6	3.0	10	30	0.30	1.50
7	3.5	15	50	0.30	1.50
8	4.5	30	100	0.50	2.00
9	5.8	30	80	0.50	2.00

$i$	$s_{off}$	$v_{min}$	$v_{max}$	$a_{min}$	$a_{max}$
44	26.3	30	70	0.50	2.00
45	27.5	15	50	0.30	1.50
46	28.2	30	70	0.50	2.00
47	28.4	20	60	0.30	1.50
48	28.8	30	70	0.50	2.00
49	29.3	10	30	0.30	1.50
50	29.5	15	50	0.30	1.50
51	29.8	10	30	0.30	1.50
52	30.0	10	30	0.30	1.50

$i$	$s_{\text{off}}$	$v_{\text{min}}$	$v_{\text{max}}$	$a_{\text{min}}$	$a_{\text{max}}$	$i$	$s_{\text{off}}$	$v_{\text{min}}$	$v_{\text{max}}$	$a_{\text{min}}$	$a_{\text{max}}$
10	6.3	30	70	0.50	2.00	53	30.5	15	50	0.30	1.50
11	7.5	15	50	0.30	1.50	54	31.1	30	70	0.50	2.00
12	8.2	30	70	0.50	2.00	55	31.4	30	80	0.50	2.00
13	8.4	20	60	0.30	1.50	56	32.4	15	50	0.30	1.50
14	8.8	30	70	0.50	2.00	57	33.0	10	30	0.30	1.50
15	9.3	10	30	0.30	1.50	58	33.5	15	50	0.30	1.50
16	9.5	15	50	0.30	1.50	59	34.5	30	100	0.50	2.00
17	9.8	10	30	0.30	1.50	60	35.8	30	80	0.50	2.00
18	10.0	10	30	0.30	1.50	61	36.3	30	70	0.50	2.00
19	10.5	15	50	0.30	1.50	62	37.5	15	50	0.30	1.50
20	11.1	30	70	0.50	2.00	63	38.2	30	70	0.50	2.00
21	11.4	30	80	0.50	2.00	64	38.4	20	60	0.30	1.50
22	12.4	15	50	0.30	1.50	65	38.8	30	70	0.50	2.00
23	13.0	10	30	0.30	1.50	66	39.3	10	30	0.30	1.50
24	13.5	15	50	0.30	1.50	67	39.5	15	50	0.30	1.50
25	14.5	30	100	0.50	2.00	68	39.8	10	30	0.30	1.50
26	15.8	30	80	0.50	2.00	69	40.0	10	30	0.30	1.50
27	16.3	30	70	0.50	2.00	70	40.5	15	50	0.30	1.50
28	17.5	15	50	0.30	1.50	71	41.1	30	70	0.50	2.00
29	18.2	30	70	0.50	2.00	72	41.4	30	80	0.50	2.00
30	18.4	20	60	0.30	1.50	73	42.4	15	50	0.30	1.50
31	18.8	30	70	0.50	2.00	74	43.0	10	30	0.30	1.50
32	19.3	10	30	0.30	1.50	75	43.5	15	50	0.30	1.50
33	19.5	15	50	0.30	1.50	76	44.5	30	100	0.50	2.00
34	19.8	10	30	0.30	1.50	77	45.8	30	80	0.50	2.00
35	20.0	10	30	0.30	1.50	78	46.3	30	70	0.50	2.00
36	20.5	15	50	0.30	1.50	79	47.5	15	50	0.30	1.50
37	21.1	30	70	0.50	2.00	80	48.2	30	70	0.50	2.00
38	21.4	30	80	0.50	2.00	81	48.4	20	60	0.30	1.50
39	22.4	15	50	0.30	1.50	82	48.8	30	70	0.50	2.00
40	23.0	10	30	0.30	1.50	83	49.3	10	30	0.30	1.50
41	23.5	15	50	0.30	1.50	84	49.5	15	50	0.30	1.50
42	24.5	30	100	0.50	2.00	85	49.8	10	30	0.30	1.50
43	25.8	30	80	0.50	2.00						

**Slope profile**  $eh_{\text{slope}}$

Table A.3.: Slope profile used in simulation for use case 1.

$i$	$s_{\text{off}}$	$sl$	$i$	$s_{\text{off}}$	$sl$	$i$	$s_{\text{off}}$	$sl$	$i$	$s_{\text{off}}$	$sl$
1	0.0	0.0	127	12.6	-2.0	252	25.1	2.4	377	37.6	0.0
2	0.1	0.1	128	12.7	-1.9	253	25.2	2.8	378	37.7	0.0
3	0.2	0.2	129	12.8	-1.8	254	25.3	2.4	379	37.8	0.0
4	0.3	0.1	130	12.9	-1.5	255	25.4	2.1	380	37.9	0.0
5	0.4	-0.2	131	13.0	-1.2	256	25.5	2.4	381	38.0	0.0
6	0.5	0.1	132	13.1	-1.3	257	25.6	2.0	382	38.1	0.0
7	0.6	0.3	133	13.2	-1.0	258	25.7	1.7	383	38.2	0.0
8	0.7	0.2	134	13.3	-0.8	259	25.8	1.5	384	38.3	0.0
9	0.8	0.1	135	13.4	-0.6	260	25.9	1.3	385	38.4	0.0
10	0.9	0.0	136	13.5	-0.2	261	26.0	1.2	386	38.5	0.0
11	1.0	-0.1	137	13.6	0.0	262	26.1	1.1	387	38.6	-0.2
12	1.1	-0.2	138	13.7	0.2	263	26.2	0.9	388	38.7	-0.4
13	1.2	-0.3	139	13.8	0.4	264	26.3	0.8	389	38.8	-0.6
14	1.3	-0.4	140	13.9	0.6	265	26.4	0.6	390	38.9	-1.0
15	1.4	-0.5	141	14.0	0.9	266	26.5	0.5	391	39.0	-1.2
16	1.5	-0.7	142	14.1	0.7	267	26.6	0.4	392	39.1	-1.0
17	1.6	-0.9	143	14.2	0.3	268	26.7	0.4	393	39.2	-0.8
18	1.7	-1.0	144	14.3	0.5	269	26.8	0.4	394	39.3	-0.6
19	1.8	-1.2	145	14.4	0.6	270	26.9	0.4	395	39.4	-0.4
20	1.9	-1.5	146	14.5	0.8	271	27.0	0.4	396	39.5	-0.2
21	2.0	-1.7	147	14.6	1.0	272	27.1	0.4	397	39.6	0.0
22	2.1	-2.0	148	14.7	1.2	273	27.2	0.2	398	39.7	0.0
23	2.2	-2.1	149	14.8	1.4	274	27.3	0.2	399	39.8	0.0
24	2.3	-2.2	150	14.9	1.8	275	27.4	0.0	400	39.9	0.0
25	2.4	-2.4	151	15.0	2.2	276	27.5	0.0	401	40.0	0.0
26	2.5	-2.2	152	15.1	2.4	277	27.6	0.0	402	40.1	0.1
27	2.6	-2.0	153	15.2	2.8	278	27.7	0.0	403	40.2	0.2
28	2.7	-1.9	154	15.3	2.4	279	27.8	0.0	404	40.3	0.1
29	2.8	-1.8	155	15.4	2.1	280	27.9	0.0	405	40.4	-0.2
30	2.9	-1.5	156	15.5	2.4	281	28.0	0.0	406	40.5	0.1
31	3.0	-1.2	157	15.6	2.0	282	28.1	0.0	407	40.6	0.3
32	3.1	-1.3	158	15.7	1.7	283	28.2	0.0	408	40.7	0.2
33	3.2	-1.0	159	15.8	1.5	284	28.3	0.0	409	40.8	0.1
34	3.3	-0.8	160	15.9	1.3	285	28.4	0.0	410	40.9	0.0

$i$	$s_{\text{off}}$	$sl$	$i$	$s_{\text{off}}$	$sl$	$i$	$s_{\text{off}}$	$sl$	$i$	$s_{\text{off}}$	$sl$
35	3.4	-0.6	161	16.0	1.2	286	28.5	0.0	411	41.0	-0.1
36	3.5	-0.2	162	16.1	1.1	287	28.6	-0.2	412	41.1	-0.2
37	3.6	0.0	163	16.2	0.9	288	28.7	-0.4	413	41.2	-0.3
38	3.7	0.2	164	16.3	0.8	289	28.8	-0.6	414	41.3	-0.4
39	3.8	0.4	165	16.4	0.6	290	28.9	-1.0	415	41.4	-0.5
40	3.9	0.6	166	16.5	0.5	291	29.0	-1.2	416	41.5	-0.7
41	4.0	0.9	167	16.6	0.4	292	29.1	-1.0	417	41.6	-0.9
42	4.1	0.7	168	16.7	0.4	293	29.2	-0.8	418	41.7	-1.0
43	4.2	0.3	169	16.8	0.4	294	29.3	-0.6	419	41.8	-1.2
44	4.3	0.5	170	16.9	0.4	295	29.4	-0.4	420	41.9	-1.5
45	4.4	0.6	171	17.0	0.4	296	29.5	-0.2	421	42.0	-1.7
46	4.5	0.8	172	17.1	0.4	297	29.6	0.0	422	42.1	-2.0
47	4.6	1.0	173	17.2	0.2	298	29.7	0.0	423	42.2	-2.1
48	4.7	1.2	174	17.3	0.2	299	29.8	0.0	424	42.3	-2.2
49	4.8	1.4	175	17.4	0.0	300	29.9	0.0	425	42.4	-2.4
50	4.9	1.8	176	17.5	0.0	301	30.0	0.0	426	42.5	-2.2
51	5.0	2.2	177	17.6	0.0	302	30.1	0.1	427	42.6	-2.0
52	5.1	2.4	178	17.7	0.0	303	30.2	0.2	428	42.7	-1.9
53	5.2	2.8	179	17.8	0.0	304	30.3	0.1	429	42.8	-1.8
54	5.3	2.4	180	17.9	0.0	305	30.4	-0.2	430	42.9	-1.5
55	5.4	2.1	181	18.0	0.0	306	30.5	0.1	431	43.0	-1.2
56	5.5	2.4	182	18.1	0.0	307	30.6	0.3	432	43.1	-1.3
57	5.6	2.0	183	18.2	0.0	308	30.7	0.2	433	43.2	-1.0
58	5.7	1.7	184	18.3	0.0	309	30.8	0.1	434	43.3	-0.8
59	5.8	1.5	185	18.4	0.0	310	30.9	0.0	435	43.4	-0.6
60	5.9	1.3	186	18.5	0.0	311	31.0	-0.1	436	43.5	-0.2
61	6.0	1.2	187	18.6	-0.2	312	31.1	-0.2	437	43.6	0.0
62	6.1	1.1	188	18.7	-0.4	313	31.2	-0.3	438	43.7	0.2
63	6.2	0.9	189	18.8	-0.6	314	31.3	-0.4	439	43.8	0.4
64	6.3	0.8	190	18.9	-1.0	315	31.4	-0.5	440	43.9	0.6
65	6.4	0.6	191	19.0	-1.2	316	31.5	-0.7	441	44.0	0.9
66	6.5	0.5	192	19.1	-1.0	317	31.6	-0.9	442	44.1	0.7
67	6.6	0.4	193	19.2	-0.8	318	31.7	-1.0	443	44.2	0.3
68	6.7	0.4	194	19.3	-0.6	319	31.8	-1.2	444	44.3	0.5
69	6.8	0.4	195	19.4	-0.4	320	31.9	-1.5	445	44.4	0.6
70	6.9	0.4	196	19.5	-0.2	321	32.0	-1.7	446	44.5	0.8



$i$	$s_{\text{off}}$	$sl$	$i$	$s_{\text{off}}$	$sl$	$i$	$s_{\text{off}}$	$sl$	$i$	$s_{\text{off}}$	$sl$
71	7.0	0.4	197	19.6	0.0	322	32.1	-2.0	447	44.6	1.0
72	7.1	0.4	198	19.7	0.0	323	32.2	-2.1	448	44.7	1.2
73	7.2	0.2	199	19.8	0.0	324	32.3	-2.2	449	44.8	1.4
74	7.3	0.2	200	19.9	0.0	325	32.4	-2.4	450	44.9	1.8
75	7.4	0.0	201	20.0	0.0	326	32.5	-2.2	451	45.0	2.2
76	7.5	0.0	202	20.1	0.1	327	32.6	-2.0	452	45.1	2.4
77	7.6	0.0	203	20.2	0.2	328	32.7	-1.9	453	45.2	2.8
78	7.7	0.0	204	20.3	0.1	329	32.8	-1.8	454	45.3	2.4
79	7.8	0.0	205	20.4	-0.2	330	32.9	-1.5	455	45.4	2.1
80	7.9	0.0	206	20.5	0.1	331	33.0	-1.2	456	45.5	2.4
81	8.0	0.0	207	20.6	0.3	332	33.1	-1.3	457	45.6	2.0
82	8.1	0.0	208	20.7	0.2	333	33.2	-1.0	458	45.7	1.7
83	8.2	0.0	209	20.8	0.1	334	33.3	-0.8	459	45.8	1.5
84	8.3	0.0	210	20.9	0.0	335	33.4	-0.6	460	45.9	1.3
85	8.4	0.0	211	21.0	-0.1	336	33.5	-0.2	461	46.0	1.2
86	8.5	0.0	212	21.1	-0.2	337	33.6	0.0	462	46.1	1.1
87	8.6	-0.2	213	21.2	-0.3	338	33.7	0.2	463	46.2	0.9
88	8.7	-0.4	214	21.3	-0.4	339	33.8	0.4	464	46.3	0.8
89	8.8	-0.6	215	21.4	-0.5	340	33.9	0.6	465	46.4	0.6
90	8.9	-1.0	216	21.5	-0.7	341	34.0	0.9	466	46.5	0.5
91	9.0	-1.2	217	21.6	-0.9	342	34.1	0.7	467	46.6	0.4
92	9.1	-1.0	218	21.7	-1.0	343	34.2	0.3	468	46.7	0.4
93	9.2	-0.8	219	21.8	-1.2	344	34.3	0.5	469	46.8	0.4
94	9.3	-0.6	220	21.9	-1.5	345	34.4	0.6	470	46.9	0.4
95	9.4	-0.4	221	22.0	-1.7	346	34.5	0.8	471	47.0	0.4
96	9.5	-0.2	222	22.1	-2.0	347	34.6	1.0	472	47.1	0.4
97	9.6	0.0	223	22.2	-2.1	348	34.7	1.2	473	47.2	0.2
98	9.7	0.0	224	22.3	-2.2	349	34.8	1.4	474	47.3	0.2
99	9.8	0.0	225	22.4	-2.4	350	34.9	1.8	475	47.4	0.0
100	9.9	0.0	226	22.5	-2.2	351	35.0	2.2	476	47.5	0.0
101	10.0	0.0	227	22.6	-2.0	352	35.1	2.4	477	47.6	0.0
102	10.1	0.1	228	22.7	-1.9	353	35.2	2.8	478	47.7	0.0
103	10.2	0.2	229	22.8	-1.8	354	35.3	2.4	479	47.8	0.0
104	10.3	0.1	230	22.9	-1.5	355	35.4	2.1	480	47.9	0.0
105	10.4	-0.2	231	23.0	-1.2	356	35.5	2.4	481	48.0	0.0
106	10.5	0.1	232	23.1	-1.3	357	35.6	2.0	482	48.1	0.0

$i$	$s_{\text{off}}$	$sl$	$i$	$s_{\text{off}}$	$sl$	$i$	$s_{\text{off}}$	$sl$	$i$	$s_{\text{off}}$	$sl$
107	10.6	0.3	233	23.2	-1.0	358	35.7	1.7	483	48.2	0.0
108	10.7	0.2	234	23.3	-0.8	359	35.8	1.5	484	48.3	0.0
109	10.8	0.1	235	23.4	-0.6	360	35.9	1.3	485	48.4	0.0
110	10.9	0.0	236	23.5	-0.2	361	36.0	1.2	486	48.5	0.0
111	11.0	-0.1	237	23.6	0.0	362	36.1	1.1	487	48.6	-0.2
112	11.1	-0.2	238	23.7	0.2	363	36.2	0.9	488	48.7	-0.4
113	11.2	-0.3	239	23.8	0.4	364	36.3	0.8	489	48.8	-0.6
114	11.3	-0.4	240	23.9	0.6	365	36.4	0.6	490	48.9	-1.0
115	11.4	-0.5	241	24.0	0.9	366	36.5	0.5	491	49.0	-1.2
116	11.5	-0.7	242	24.1	0.7	367	36.6	0.4	492	49.1	-1.0
117	11.6	-0.9	243	24.2	0.3	368	36.7	0.4	493	49.2	-0.8
118	11.7	-1.0	244	24.3	0.5	369	36.8	0.4	494	49.3	-0.6
119	11.8	-1.2	245	24.4	0.6	370	36.9	0.4	495	49.4	-0.4
120	11.9	-1.5	246	24.5	0.8	371	37.0	0.4	496	49.5	-0.2
121	12.0	-1.7	247	24.6	1.0	372	37.1	0.4	497	49.6	0.0
122	12.1	-2.0	248	24.7	1.2	373	37.2	0.2	498	49.7	0.0
123	12.2	-2.1	249	24.8	1.4	374	37.3	0.2	499	49.8	0.0
124	12.3	-2.2	250	24.9	1.8	375	37.4	0.0	500	49.9	0.0
125	12.4	-2.4	251	25.0	2.2	376	37.5	0.0	501	50.0	0.0
126	12.5	-2.2									

**Stops profile**  $eh_{\text{stops}}$

Table A.4.: Stops profile used in simulation for use case 1.

$i$	$s_{\text{off}}$	$dT_{\text{stop}}$	$i$	$s_{\text{off}}$	$dT_{\text{stop}}$	$i$	$s_{\text{off}}$	$dT_{\text{stop}}$	$i$	$s_{\text{off}}$	$dT_{\text{stop}}$
1	0.40	10	10	12.50	20	19	24.00	30	28	39.60	20
2	0.70	15	11	13.30	5	20	27.70	10	29	40.40	10
3	2.50	20	12	14.00	30	21	29.60	20	30	40.70	15
4	3.30	5	13	17.70	10	22	30.40	10	31	42.50	20
5	4.00	30	14	19.60	20	23	30.70	15	32	43.30	5
6	7.70	10	15	20.40	10	24	32.50	20	33	44.00	30
7	9.60	20	16	20.70	15	25	33.30	5	34	47.70	10
8	10.40	10	17	22.50	20	26	34.00	30	35	49.60	20
9	10.70	15	18	23.30	5	27	37.70	10			

# Appendix B.

## Definition of Use Case 2

### Vehicle and Gearbox Parameters

Table B.1.: Vehicle parameters used in simulation for use case 2.

parameter	description	value	unit
$\rho$	density of ambient air	1.18	$[\frac{kg}{m^3}]$
$g$	acceleration due to gravity	9.80665	$[\frac{m}{s^2}]$
$A_f$	vehicle frontal area	5.5	$[m^2]$
$m_v$	vehicle mass	2800	$[kg]$
$r_w$	wheel radius	27.5	$[cm]$
$c_d$	aerodynamic drag coefficient	0.6	$[-]$
$c_r$	rolling friction coefficient	0.02	$[-]$
$\gamma_{gb}$	gearbox transmission ratio	30.0	$[-]$
$\eta_{gb}$	gearbox transmission efficiency	0.95	$[-]$

### Velocity/acceleration limits profile $eh_{lim}$

Table B.2.: Velocity/acceleration limits profile used in simulation for use case 2.

$i$	$s_{off}$	$v_{min}$	$v_{max}$	$a_{min}$	$a_{max}$
1	0.000	2.5	5	0.38	1.50
2	0.074	10	20	0.38	1.50

$i$	$s_{off}$	$v_{min}$	$v_{max}$	$a_{min}$	$a_{max}$
3	4.726	2.5	5	0.38	1.50

### Slope profile $eh_{slope}$

Table B.3.: Slope profile used in simulation for use case 2.

$i$	$s_{off}$	$sl$
1	0.0	2.0
2	0.0	6.5

$i$	$s_{off}$	$sl$
20	1.4	-7.0
21	1.4	-7.5

$i$	$s_{off}$	$sl$
38	2.5	-0.5
39	2.6	0.0

$i$	$s_{off}$	$sl$
56	3.5	4.5
57	3.6	1.0

$i$	$s_{\text{off}}$	$sl$	$i$	$s_{\text{off}}$	$sl$	$i$	$s_{\text{off}}$	$sl$	$i$	$s_{\text{off}}$	$sl$
3	0.1	2.0	22	1.4	-5.5	40	2.6	0.5	58	3.6	1.5
4	0.1	-3.0	23	1.5	-3.5	41	2.6	0.0	59	3.7	1.0
5	0.1	-1.5	24	1.7	-3.0	42	2.7	-0.5	60	3.8	1.5
6	0.2	-1.0	25	1.8	-3.5	43	2.7	0.0	61	3.9	2.0
7	0.5	-2.0	26	1.8	-3.0	44	2.8	0.5	62	4.1	1.5
8	0.5	-5.5	27	1.9	-2.5	45	2.8	2.0	63	4.1	0.0
9	0.6	-2.5	28	2.0	-2.0	46	2.8	2.5	64	4.1	2.0
10	0.7	-2.0	29	2.0	-1.5	47	2.9	3.0	65	4.1	2.5
11	0.7	0.0	30	2.0	-0.5	48	3.0	2.5	66	4.2	5.5
12	0.7	-2.0	31	2.1	0.5	49	3.0	3.0	67	4.3	1.5
13	0.9	-1.5	32	2.2	-0.5	50	3.1	3.5	68	4.3	1.0
14	1.0	-1.0	33	2.2	0.0	51	3.3	7.0	69	4.6	1.5
15	1.1	-2.0	34	2.3	0.5	52	3.4	7.5	70	4.7	2.0
16	1.2	-0.5	35	2.3	0.0	53	3.4	6.0	71	4.7	3.0
17	1.2	-1.0	36	2.3	-0.5	54	3.5	2.5	72	4.7	-1.5
18	1.2	-4.5	37	2.4	0.0	55	3.5	3.5	73	4.7	-6.0
19	1.3	-3.5									

**Stops profile**  $eh_{\text{stops}}$

Table B.4.: Stops profile used in simulation for use case 2.

$i$	$s_{\text{off}}$	$dT_{\text{stop}}$	$i$	$s_{\text{off}}$	$dT_{\text{stop}}$	$i$	$s_{\text{off}}$	$dT_{\text{stop}}$	$i$	$s_{\text{off}}$	$dT_{\text{stop}}$
1	0.2	14.0	4	1.4	2.0	7	2.5	14.0	10	3.8	14.0
2	0.5	14.0	5	1.9	2.0	8	3.2	2.0	11	4.4	14.0
3	1.2	14.0	6	2.2	2.0	9	3.6	2.0	12	4.7	14.0

# List of Symbols and Notations

## List of Notations

Symbol	Description	Unit
$\underline{0}$	vector or matrix with all elements equal to 0	—
$\underline{1}$	vector or matrix with all elements equal to 1	—
$a_0$	value of $a$ at $t_0$	—
$\underline{a}$	vector or matrix	—
$\underline{a}_{\{i\}}$	$i$ -th element of vector $\underline{a}$	—
$\underline{a}_{\{i,k\}}$	element in the $i$ -th row and $k$ -th column of matrix $\underline{a}$	—
$\underline{a}^{(i)}$	column $i$ of matrix $\underline{a}$	—
$\underline{a}_{(i)}$	row $i$ of matrix $\underline{a}$	—
$a^{\text{eq}}$	value of $a$ with equal torque distribution	—
$a^{\text{opt}}$	value of $a$ with optimal torque distribution	—
$a_{\text{pred}}$	predicted value of $a$	—
$a_{\text{qs}}$	value of $a$ estimated with quasistatic approach	—
$a^*$	value of $a$ at a given set of integer variables	—
$a^{\text{v1}}$	value of $a$ in Version 1 of energy distribution optimization	—
$a^{\text{v2}}$	value of $a$ in Version 2 of energy distribution optimization	—
$d^1 a$	value of $a$ delayed by one sample period with $d^1 a[n] = a[n-1]$	—
$\Delta a_{\text{qs}}$	relative deviation of $a_{\text{pred}}$ from $a_{\text{qs}}$	%
$\underline{I}$	$n_{\text{spn}} \times n_{\text{spn}}$ identity matrix	—

## List of General Symbols

Symbol	Description	Unit
$a$	signal $a$	—
$B^{\{k\}}$	energy storage of subpowernet $k$	—

Symbol	Description	Unit
$dT_{\text{eval}}$	time required for evaluation	s
$i$	index variable	—
$j$	index variable	—
$k$	index variable	—
$M_{\{xy\}}$	motor at position $x$ and $y$	—
$R^2$	coefficient of determination	%
$R_c^{\{k\}}$	comfort components of subpowernet $k$	—
$R_{\text{load}}^{\{k\}}$	load components of subpowernet $k$	—
$R_{\text{prop}}^{\{k\}}$	propulsion components of subpowernet $k$	—
$R_s^{\{k\}}$	safety-critical components of subpowernet $k$	—
$t$	driving time	s
$t_0$	start time	s
$t_{\text{end}}$	end time	s

List of Symbols for Powernet Control

Symbol	Description	Unit
$\underline{A}_{\text{bat.lp}}$	$n_{\text{spn}} \times n_{\text{spn}}^2$ matrix for definition of $\underline{f}_{\text{edo.pen.bat}}$ in LP	—
$\underline{A}_{\text{eq.lp}}$	$n_{\text{spn}}^2 \times n_{\text{spn}}^2$ matrix for linear equality constraints in LP	—
$\underline{A}_{\text{eq.nlp}}$	$n_{\text{spn}} \times n_{\text{spn}}$ matrix for linear equality constraints in NLP	—
$\underline{A}_{\text{espn.lp}}$	$n_{\text{spn}} \times n_{\text{spn}}^2$ matrix for definition of $\underline{E}_{\text{spn.lp}}$ in LP	—
$\underline{A}_{\text{ineq.lp}}$	$3n_{\text{spn}} \times n_{\text{spn}}^2$ matrix for linear inequality constraints in LP	—
$\underline{A}_{\text{ineq.nlp}}$	$n_{\text{spn}} \times n_{\text{spn}}$ matrix for linear inequality constraints in NLP	—
$\underline{A}_{\text{pen.pl.lp}}$	$n_{\text{spn}} \times n_{\text{spn}}^2$ matrix for definition of $\underline{f}_{\text{edo.pen.pl}}$ in LP	—
$a_{\text{rde}}^{\{k\}}$	factor approximating total losses of $B^{\{k\}}$ , stored in $\underline{a}_{\text{rde}}^{n_{\text{spn}} \times 1}$	h
$\underline{b}_{\text{eq.lp}}$	$n_{\text{spn}}^2 \times 1$ vector for linear equality constraints in LP	kWh
$\underline{b}_{\text{eq.nlp}}$	$n_{\text{spn}} \times n_{\text{spn}}$ matrix for linear equality constraints in NLP	kWh
$\underline{b}_{\text{ineq.lp}}$	$3n_{\text{spn}} \times 1$ vector for linear inequality constraints in LP	kWh
$\underline{b}_{\text{ineq.nlp}}$	$n_{\text{spn}} \times n_{\text{spn}}$ matrix for linear inequality constraints in NLP	kWh
$c_{\text{bat.q0}}^{\{k\}}$	scaling factor for capacity $Q_{\text{bat0}}^{\{k\}}$ of $B^{\{k\}}$ , stored in $\underline{D}_{\text{bat}}^{\{k\}}$	—
$c_{\text{bat.rin}}^{\{k\}}$	scaling factor for resistance $R_{\text{bat.in}}^{\{k\}}$ of $B^{\{k\}}$ , stored in $\underline{D}_{\text{bat}}^{\{k\}}$	—
$\underline{c}_{\text{eq.nlp}}$	$n_{\text{spn}} \times n_{\text{spn}}$ nonlinear equality constraints in NLP	kWh
$\underline{c}_{\text{ineq.nlp}}$	$n_{\text{spn}} \times n_{\text{spn}}$ nonlinear inequality constraints in NLP	kWh
$\underline{D}_{\text{bat}}^{\{k\}}$	diagnostic state vector for $B^{\{k\}}$ with $c_{\text{bat.rin}}^{\{k\}}$ and $c_{\text{bat.q0}}^{\{k\}}$	—
$D_{\text{load}}^{\{i\}}$	diagnostic state of load $i$	—
$dp_{\text{bat}}^{\{k\}}$	factor approximating average losses of $B^{\{k\}}$ , stored in $\underline{dp}_{\text{bat}}^{n_{\text{spn}} \times 1}$	—

Symbol	Description	Unit
$D_{pl}^{\{k\}}$	diagnostic state of powerlink $k$ , stored in $\underline{D}_{pl}^{n_{pl} \times 1}$	—
$dT_{dcha}^{\{k\}}$	time for discharge of $B^{\{k\}}$ ( $SoC_0^{\{k\}}$ to $SoC_{min}^{\{k\}}$ )	h
$dT_{dcha.min}^{\{k\}}$	time for discharge of $B^{\{k\}}$ ( $SoC_0^{\{k\}}$ to $SoC_{min}^{\{k\}}$ ) with $P_{bat.max}^{\{k\}}$	h
$E_{bat}^{\{k\}}$	discharge energy of $B^{\{k\}}$ , stored in $\underline{E}_{bat}^{n_{spn} \times 1}$	kWh
$E_{bat.loss}^{\{k\}}$	discharge losses of $B^{\{k\}}$	kWh
$E_{in}^{\{i,k\}}$	energy flow at input $i$ of subpowernet $k$	kWh
$E_{load}^{\{k\}}$	energy demand of $R_{load}^{\{k\}}$ , stored in $\underline{E}_{load}^{n_{spn} \times 1}$	kWh
$E_{out}^{\{i,k\}}$	energy flow at output $k$ of subpowernet $i$ , stored in $\underline{E}_{out}^{n_{spn} \times n_{spn}}$	kWh
$E_{out.max}^{\{i,k\}}$	output energy limit for $E_{out}^{\{i,k\}}$ , stored in $\underline{E}_{out.max}^{n_{spn} \times n_{spn}}$	kWh
$E_{prop}^{\{k\}}$	energy demand of $R_{prop}^{\{k\}}$	kWh
$E_{rc}^{\{k\}}$	energy demand of $R_c^{\{k\}}$	kWh
$E_{rde0}^{\{k\}}$	electrochemical energy of $B^{\{k\}}$ , stored in $\underline{E}_{rde0}^{n_{spn} \times 1}$	kWh
$E_{rde}^{\{k\}}$	remaining discharge energy of $B^{\{k\}}$ , stored in $\underline{E}_{rde}^{n_{spn} \times 1}$	kWh
$E_{rs}^{\{k\}}$	energy demand of $R_s^{\{k\}}$	kWh
$E_{spn}^{\{k\}}$	energy balance of net $k$ , stored in $\underline{E}_{spn}^{n_{spn} \times 1}$	kWh
$\underline{E}_{spn.lp}$	$n_{spn} \times 1$ energy balance vector in LP	kWh
$E_{spn.opt}^{\{k\}}$	energy balance of net $k$ with $E_{bat.loss}^{\{k\}}$ , stored in $\underline{E}_{spn.opt}^{n_{spn} \times 1}$	kWh
$\underline{E}_{spn.opt.lp}$	$n_{spn} \times 1$ energy balance vector with $E_{bat.loss}^{\{k\}}$ in LP	kWh
$f_{edo}$	multi-objective function for energy distribution optimization	kWh
$f_{edo.dp}$	objective for minimization of driving profile degradation	—
$f_{edo.loss.opt}$	objective for minimization of powerlink/battery losses	kWh
$f_{edo.loss.opt.lp}$	objective for minimization of powerlink/battery losses in LP	kWh
$\underline{f}_{edo.loss.opt}$	$n_{spn}^2 \times 1$ vector for minimization of powerlink/battery losses in LP	—
$f_{edo.loss.pl}$	objective for minimization of powerlink losses	kWh
$f_{edo.loss.pl.lp}$	objective for minimization of powerlink losses in LP	kWh
$\underline{f}_{edo.loss.pl}$	$n_{spn}^2 \times 1$ vector for minimization of powerlink losses in LP	—
$f_{edo.lp}$	objective for minimization of load profile degradation	—
$f_{edo.opt}$	multi-objective function for energy distribution and multiple batteries discharge optimization	kWh
$f_{edo.path}$	objective for selection of optimal energy flow paths	kWh
$f_{edo.path.opt}$	objective for selection of optimal energy flow paths with optimal multiple batteries discharge	kWh
$f_{edo.pen.bat}$	penalty function for discharge of batteries	kWh
$f_{edo.pen.bat.lp}$	penalty function for discharge of batteries in LP	kWh
$f_{edo.pen.pl}$	penalty function for energy flow via powerlink outputs	kWh

Symbol	Description	Unit
$f_{\text{edo,pen,pl,lp}}$	penalty function for energy flow via powerlink outputs in LP	kWh
$f_{\text{edo,pen,bat}}$	$n_{\text{spn}}^2 \times 1$ penalization vector for discharge of batteries in LP	—
$f_{\text{edo,pen,pl}}$	$n_{\text{spn}}^2 \times 1$ penalization vector for energy flow via powerlink outputs in LP	—
$f_{\text{edo,ssl}}$	objective for minimization of driving destination degradation	—
$f_{\text{obj,lp}}$	objective vector for optimization in LP formulation	—
$f_{\text{obj,nlp}}$	objective function for optimization in NLP formulation	kWh
$I_{\text{bat}}^{\{x\}}$	output current of $B^{\{k\}}$	A
$i_{\text{dp}}$	degradation step of driving profile with $i_{\text{dp}} \in \{1..n_{\text{dp}}\}$	—
$i_{\text{ds}}$	combined degradation step variable with $i_{\text{ds}} \in \{1..n_{\text{ds}}\}$	—
$i_{\text{lp}}$	degradation step of load profile with $i_{\text{lp}} \in \{1..n_{\text{lp}}\}$	—
$i_{\text{mod}}$	counter variable for valid $\underline{M}_{\text{pl}}$ with $i_{\text{mod}} \in \{1..n_{\text{mod}}\}$	—
$i_{\text{ssl}}$	degradation step of driving destination with $i_{\text{ssl}} \in \{1..n_{\text{ssl}}\}$	—
$\underline{lb}_{\text{lp}}$	$n_{\text{spn}}^2 \times 1$ lower bound vector for $\underline{x}_{\text{lp}}$ in LP	kWh
$\underline{lb}_{\text{nlp}}$	$n_{\text{spn}} \times n_{\text{spn}}$ lower bound matrix for $\underline{x}_{\text{nlp}}$ in NLP	kWh
$M_{\text{load}}^{\{i\}}$	operating mode of load $i$	—
$\underline{M}_{\text{pl}}$	$n_{\text{pl}} \times 1$ powerlink operating mode state vector	—
$M_{\text{pl}}^{\{i\}}$	operating mode of powerlink $i$ , stored in $\underline{M}_{\text{pl}}^{n_{\text{pl}} \times 1}$	—
$n_{\text{dp}}$	number of degradation steps for driving profile	—
$n_{\text{ds}}$	number of degradation steps for $i_{\text{ds}}$	—
$n_{\text{lp}}$	number of degradation steps for load profile	—
$n_{\text{mod}}$	number of valid powerlink operating mode vectors $\underline{M}_{\text{pl}}$	—
$n_{\text{mod}}^{\{i\}}$	number of valid operating modes of powerlink $i$	—
$n_{\text{pbat}}$	number of discharge power breakpoints for prediction of $E_{\text{rde}}^{\{k\}}$	—
$n_{\text{pl}}$	number of powerlinks in powernet	—
$n_{\text{soc}}$	number of SoC breakpoints used for prediction of $E_{\text{rde}}^{\{k\}}$	—
$n_{\text{spn}}$	number of subpowernets	—
$n_{\text{ssl}}$	number of degradation steps for driving destination	—
$P_{\text{bat}}^{\{k\}}$	average discharge power of $B^{\{k\}}$ , stored in $\underline{P}_{\text{bat}}^{n_{\text{spn}} \times 1}$	kW
$P_{\text{bat,loss}}^{\{k\}}$	average discharge power losses of $B^{\{k\}}$ at $P_{\text{bat}}^{\{k\}}$	kW
$P_{\text{bat,loss,max}}^{\{k\}}$	maximum average discharge power losses of $B^{\{k\}}$ at $P_{\text{bat,max}}^{\{k\}}$	kW
$P_{\text{bat,max}}^{\{k\}}$	maximum discharge power of $B^{\{k\}}$ , stored in $\underline{P}_{\text{bat,max}}^{n_{\text{spn}} \times 1}$	kW
$P_{\text{bat,min}}^{\{k\}}$	minimum discharge power of $B^{\{k\}}$ for prediction of $E_{\text{rde}}^{\{k\}}$	kW
$\underline{PL}_{\text{eff}}^{\{i\}}$	vector with current energy flow efficiencies of powerlink $i$	—
$\underline{PL}_{\text{mod}}$	$n_{\text{pl}} \times n_{\text{mod}}$ matrix with the set of valid $\underline{M}_{\text{pl}}$ vectors	—
$\underline{PL}_{\text{mod}}^{\{i\}}$	$n_{\text{mod}}^{\{i\}} \times 1$ vector with the set of valid $M_{\text{pl}}^{\{i\}}$	—



Symbol	Description	Unit
$\underline{PL}_{\text{pin}}^{\{i\}}$	description of powernet connections of powerlink $i$	—
$P_{\text{load}}^{\{k\}}$	average power demand of $R_{\text{load}}^{\{k\}}$	kW
$P_{\text{out}}^{\{i,k\}}$	power flow at output $k$ of subpowernet $i$ , stored in $\underline{P}_{\text{out}}^{n_{\text{spn}} \times n_{\text{spn}}}$	kW
$P_{\text{out.max}}^{\{i,k\}}$	output power limit for $P_{\text{out}}^{\{i,k\}}$ , stored in $\underline{P}_{\text{out.max}}^{n_{\text{spn}} \times n_{\text{spn}}}$	kW
$P_{\text{pl.max}}^{\{i,k\}}$	maximum allowed power at input $i$ of subpowernet $k$	kW
$P_{\text{rc}}^{\{k,i_p\}}$	average power demand of $R_c^{\{k\}}$ at degradation step $i_p$	kW
$P_{\text{rs}}^{\{k,i_p\}}$	average power demand of $R_s^{\{k\}}$ at degradation step $i_p$	kW
$P_{\text{sc}}^{\{k,i_p\}}$	sum of $P_{\text{rc}}^{\{k,i_p\}}$ , $P_{\text{rs}}^{\{k,i_p\}}$ , $P_{\text{out}}^{\{k,i\}}$ with $i \in \{1..n_{\text{spn}}\} \setminus \{k\}$ at $i_p$	kW
$Q_{\text{bat0}}^{\{k\}}$	nominal capacity of $B^{\{k\}}$	Ah
$R_{\text{bat.in}}^{\{k\}}$	internal resistance of $B^{\{k\}}$	$\Omega$
$SNK$	set of subpowernets classified as a sink	—
$SoC^{\{k\}}$	state of charge of battery $k$	%
$SoC_0^{\{k\}}$	state of charge of battery $k$ at $t = t_0$	%
$SoC_{\text{end}}^{\{k\}}$	state of charge of battery $k$ at the end of the driving mission	%
$SoC_{\text{min}}^{\{k\}}$	minimum allowed discharge threshold for battery $k$	%
$S_{\text{out}}^{\{i,k\}}$	state of energy flow $E_{\text{out}}^{\{i,k\}}$ , stored in $\underline{S}_{\text{out}}^{n_{\text{spn}} \times n_{\text{spn}}}$	—
$\underline{S}_{\text{pl}}^{*\{i\}}$	$n_{\text{spn}} \times n_{\text{spn}}$ energy flow activation matrix of powerlink $i$	—
$S_{\text{pl}}^{\{i,k\}}$	activation state of energy flow $E_{\text{out}}^{\{i,k\}}$ , stored in $\underline{S}_{\text{pl}}^{n_{\text{spn}} \times n_{\text{spn}}}$	—
$SRC$	set of subpowernets classified as a source	—
$S_{\text{spn}}^{\{k\}}$	operational state of subpowernet $k$ , stored in $\underline{S}_{\text{spn}}^{n_{\text{spn}} \times 1}$	—
$T_{\text{bat}}^{\{k\}}$	temperature of $B^{\{k\}}$	K
$T_{\text{jun.pl}}^{\{i,k\}}$	junction temperature of powerlink output for $E_{\text{out}}^{\{i,k\}}$	K
$T_{\text{nom.pl}}^{\{i,k\}}$	nominal temperature of powerlink output for $E_{\text{out}}^{\{i,k\}}$	K
$\underline{ub}_{\text{lp}}$	$n_{\text{spn}}^2 \times 1$ upper bound vector for $\underline{x}_{\text{lp}}$ in LP	kWh
$\underline{ub}_{\text{nlp}}$	$n_{\text{spn}} \times n_{\text{spn}}$ upper bound matrix for $\underline{x}_{\text{nlp}}$ in NLP	kWh
$V_{\text{bat}}^{\{x\}}$	output voltage of $B^{\{k\}}$	V
$V_{\text{bat.oc}}^{\{k\}}$	open circuit voltage of $B^{\{k\}}$	V
$\underline{x}_{\text{lp}}$	$n_{\text{spn}}^2 \times 1$ optimization variable vector in LP problem	kWh
$\underline{x}_{\text{nlp}}$	$n_{\text{spn}} \times n_{\text{spn}}$ optimization variable matrix in NLP problem	kWh
$\beta_{\text{bat}}^{\{k\}}$	penalty factor for discharge of $B^{\{k\}}$ , stored in $\underline{\beta}_{\text{pl}}^{n_{\text{spn}} \times 1}$	—
$\beta_{\text{edo.dp}}$	weighting factor for $f_{\text{edo.dp}}$	kWh
$\beta_{\text{edo.lp}}$	weighting factor for $f_{\text{edo.lp}}$	kWh
$\beta_{\text{edo.path}}$	weighting factor for $f_{\text{edo.path}}$	—
$\beta_{\text{edo.ssl}}$	weighting factor for $f_{\text{edo.ssl}}$	kWh
$\beta_{\text{pl}}^{\{i,k\}}$	penalty factor for energy flow $E_{\text{out}}^{\{i,k\}}$ , stored in $\underline{\beta}_{\text{pl}}^{n_{\text{spn}} \times n_{\text{spn}}}$	—
$\gamma_{\text{rde}}$	scaling factor for remaining discharge energy delta in $\beta_{\text{bat}}^{\{k\}}$	h/K

Symbol	Description	Unit
$\gamma_{\text{temp}}$	scaling factor for temperature delta in $\beta_{\text{pl}}^{\{i,k\}}$	h/K
$\eta_{\text{frw}}$	energy flow efficiency of a DC/DC converter in forward mode	%
$\eta_{\text{on}}$	energy flow efficiency of a power switch	%
$\eta_{\text{on1}}$	energy flow efficiency of a toggle switch from pin0 to pin1	%
$\eta_{\text{on2}}$	energy flow efficiency of a toggle switch from pin0 to pin2	%
$\underline{\eta}_{\text{pl}}^{\{i\}}$	$n_{\text{spn}} \times n_{\text{spn}}$ efficiency flow matrix of powerlink $i$	%
$\eta_{\text{pl}}^{\{i,k\}}$	efficiency of energy flow $E_{\text{out}}^{\{i,k\}}$ , stored in $\underline{\eta}_{\text{pl}}^{n_{\text{spn}} \times n_{\text{spn}}}$	%
$\eta_{\text{rev}}$	energy flow efficiency of a DC/DC converter in reverse mode	%

### List of Symbols for Powertrain Control

Symbol	Description	Unit
$A_{\text{f}}$	vehicle frontal area	m <sup>2</sup>
$\underline{A}_{\text{trq}}$	$n_{\alpha} \times 3$ matrix with set of discrete valued $\underline{\alpha}$	—
$c_{\text{bat}\{x\}}$	scaling factor for size of battery at position $x$ in $f_{\text{obj5}}$	—
$c_{\text{d}}$	aerodynamic drag coefficient	—
$c_{\text{em}\{xy\}}$	scaling factor for motor size at position $x$ and $y$ in $f_{\text{obj3}}/f_{\text{obj4}}$	—
$c_{\text{em}\{xy\}.\text{eff}}$	scaling factor for efficiency of motor at position $x$ and $y$	—
$c_{\text{em}\{xy\}.\text{trq}}$	scaling factor for torque limit of motor at position $x$ and $y$	—
$c_{\text{gb}\{x\}.\text{eff}}$	scaling factor for efficiency of gearbox at position $x$	—
$c_{\text{r}}$	rolling friction coefficient	—
$dT^{[i]}$	duration of interval $i$	s
$dE_{\text{batfr}.\text{loss}}$	delta in battery losses between front and rear axle	Wh
$dE_{\text{emfr}.\text{loss}}$	delta in motor losses between front and rear axle	Wh
$dE_{\text{em}\{x\}.\text{lr}.\text{loss}}$	delta in losses between left and right motor at axle $x$	Wh
$\underline{D}_{\text{em}\{xy\}}$	diagnostic state vector for $M_{\{xy\}}$ with $c_{\text{em}\{xy\}.\text{eff}}$ and $c_{\text{em}\{xy\}.\text{trq}}$	—
$dSoC_{\text{avg}}$	average battery discharge	%
$dSoC_{\text{fr}}$	delta in SoC between front and rear battery	%
$dT_{\text{calc}}$	calculation time step for propulsion energy prediction	s
$dT_{\text{min}}$	minimum required calculation time step with $dT_{\text{calc}} \leq dT_{\text{min}}$	s
$d\eta_{\text{SoC}}$	relative reduction in SoC consumption	%
$E_{\text{bat}\{x\}.\text{loss}}$	losses of battery at position $x$	Wh
$E_{\text{em}\{xy\}.\text{loss}}$	losses of motor at position $x$ and $y$	Wh
$\underline{eq}_{\text{fr}}$	$n_{\text{fr}} \times 1$ vector with equally distributed breakpoints for $\alpha_{\text{fr}}$	—
$\underline{eq}_{\text{lr}}$	$1 \times n_{\text{lr}}$ vector with equally distributed breakpoints for $\alpha_{\{x\}\text{lr}}$	—
$E_{\text{rde}\{x\}}$	remaining discharge energy of battery at position $x$	kWh

Symbol	Description	Unit
$f_{obj}$	multi-objective function for optimal torque distribution	—
$f_{obj1}$	objective for minimization of powertrain losses	%
$f_{obj2}$	objective for (a) $SoC_{\{x\}}$ or (b) $E_{rde\{x\}}$ balancing	%
$f_{obj3}$	objective for balancing of losses between left/right motor	Wh
$f_{obj4}$	objective for balancing of losses between front/rear motors	Wh
$f_{obj5}$	objective for balancing of losses between front/rear battery	Wh
$F_t$	vehicle traction force	N
$g$	acceleration due to gravity	m/s <sup>2</sup>
$I_{bat\{x\}}$	output current of traction battery at position $x$	A
$I_{bat\{x\}.chrg.max}$	maximum charge current of battery at position $x$	A
$I_{bat\{x\}.dcha.max}$	maximum discharge current of battery at position $x$	A
$I_{em\{xy\}}$	current of motor at position $x$ and $y$	A
$j_{sub}^{[i]}$	number of subsegments in segment $i$	—
$lim_{bat\{x\}}$	constraint function for battery at position $x$	bool
$lim_{bat\{x\}.I}$	flag for current limitation of battery at position $x$	bool
$lim_{bat\{x\}.SoC}$	flag for SoC limitation of battery at position $x$	bool
$lim_{bat\{x\}.V}$	flag for voltage limitation of battery at position $x$	bool
$lim_{em\{xy\}}$	constraint function for motor at position $x$ and $y$	bool
$lim_{em\{xy\}.P}$	flag for power limitation of motor at position $x$ and $y$	bool
$lim_{em\{xy\}.T}$	flag for torque limitation of motor at position $x$ and $y$	bool
$lim_{em\{xy\}.\eta}$	flag for efficiency limitation of motor at position $x$ and $y$	bool
$lim_{\{x\}}$	constraint function for axle $x$	bool
$m_v$	vehicle mass	kg
$n_{calc}$	number of calculation steps for propulsion energy prediction	—
$n_{eff.gen.rot}$	number of breakpoints in $\underline{\omega}_{em.eff.gen}$	—
$n_{eff.gen.trq}$	number of breakpoints in $\underline{T}_{em.eff.gen}$	—
$n_{eff.mot.rot}$	number of breakpoints in $\underline{\omega}_{em.eff.mot}$	—
$n_{eff.mot.trq}$	number of breakpoints in $\underline{T}_{em.eff.mot}$	—
$n_{fr}$	number of breakpoints for $\alpha_{fr}$	—
$n_{lr}$	number of breakpoints for $\alpha_{\{x\}lr}$	—
$n_{\alpha}$	number of discrete valued $\underline{\alpha}$ in the set $\underline{A}_{trq}$	—
$P_{bat\{x\}}$	output power of traction battery at position $x$	kW
$P_{bat\{x\}.load}$	load power of auxiliaries supplied by battery at position $x$	kW
$P_{bat\{x\}.loss}$	power losses of traction battery at position $x$	W
$P_{em\{xy\}}$	electrical power of motor at position $x$ and $y$	kW
$P_{em\{xy\}.lim.gen}$	power limit of motor at position $x$ and $y$ in generator mode	kW

Symbol	Description	Unit
$P_{em\{xy\}.lim.mot}$	power limit of motor at position $x$ and $y$ in motor mode	kW
$P_{em\{xy\}.loss}$	power losses of motor at position $x$ and $y$	W
$P_{em\{xy\}.mech}$	mechanical power of motor at position $x$ and $y$	kW
$R_{emfr.loss}$	losses ratio of front to rear axle motors	—
$R_{em\{x\}lr.loss}$	losses ratio of front to right motor at axle $x$	—
$r_w$	wheel radius	m
$SoC\{x\}$	state of charge of battery at position $x$	%
$SoC\{x\}.max$	minimum state of charge of battery at position $x$	%
$SoC\{x\}.min$	minimum state of charge of battery at position $x$	%
$\underline{T}_{em. eff. gen}$	$n_{eff.gen.trq} \times 1$ torque vector for look-up of $\eta_{em.gen}$	Nm
$\underline{T}_{em. eff. mot}$	$n_{eff.mot.trq} \times 1$ torque vector for look-up of $\eta_{em.mot}$	Nm
$T_{em.loss.gen}$	torque for calculation of motor losses in generator mode	Nm
$T_{em.loss.mot}$	torque for calculation of motor losses in motor mode	Nm
$T_{em\{xy\}}$	output torque of motor at position $x$ and $y$	Nm
$T_{em\{xy\}.lim.gen}$	torque limit of motor at position $x$ and $y$ in generator mode	Nm
$T_{em\{xy\}.lim.mot}$	torque limit of motor at position $x$ and $y$ in motor mode	Nm
$T_{em\{xy\}.req}$	torque request for motor at position $x$ and $y$	Nm
$T_{gb.in}$	torque at gearbox input shaft (motor side)	Nm
$T_{gb.out}$	torque at gearbox output shaft (wheel side)	Nm
$T_{gb\{x\}}$	total torque required at motor side of gearbox at position $x$	Nm
$T_{gb\{y\}.in}$	torque at gearbox input $y$ (motor side)	Nm
$T_w$	total wheel torque	Nm
$T_{wf}$	front wheel torque	Nm
$T_{wr}$	rear wheel torque	Nm
$V_{bat\{x\}}$	output voltage of traction battery at position $x$	V
$V_{bat\{x\}.max}$	maximum output voltage of battery at position $x$	V
$V_{bat\{x\}.min}$	minimum output voltage of battery at position $x$	V
$V_{em\{xy\}}$	supply voltage of motor at position $x$ and $y$	V
$x$	axle position with $x = f$ for front and $x = r$ for rear axle	—
$y$	motor position with $y = l$ for left and $y = r$ for right side	—
$\underline{\alpha}$	torque distribution vector containing $\alpha_{fr}$ and $\alpha_{\{x\}lr}$	—
$\underline{\alpha}_{em\{xy\}}$	$n_{fr} \times n_{lr}$ torque split matrix for motor at position $x$ and $y$	—
$\alpha_{fr}$	factor for torque split between front and rear axle	—
$\alpha_{fr}.max$	upper bound for $\alpha_{fr}$	—
$\alpha_{fr}.min$	lower bound for $\alpha_{fr}$	—
$\underline{\alpha}_{max}$	upper bounds for torque distribution vector $\underline{\alpha}$	—

Symbol	Description	Unit
$\underline{\alpha}_{\min}$	lower bounds for torque distribution vector $\underline{\alpha}$	—
$\alpha_{\text{rd}}$	road angle	°
$\alpha_{\{x\}\text{lr}}$	factor for torque split between left and right motor at axle $x$	—
$\alpha_{\{x\}\text{lr.max}}$	upper bound for $\alpha_{\{x\}\text{lr}}$	—
$\alpha_{\{x\}\text{lr.min}}$	lower bound for $\alpha_{\{x\}\text{lr}}$	—
$\beta_{\{i\}}$	weighting factor for $f_{\text{obj}\{i\}}$ with $i \in \{1..5\}$ and $u = 1/[f_{\text{obj}\{i\}}]$	u
$\gamma_{\text{gb}}$	gearbox transmission ratio	—
$\eta_{\text{em.gen}}$	efficiency of electric motor in generator mode	%
$\eta_{\text{em.mot}}$	efficiency of electric motor in motor mode	%
$\eta_{\text{em}\{xy\}}$	efficiency of motor at position $x$ and $y$	%
$\eta_{\text{em}\{xy\}.lim}$	lower bound for efficiency of motor at position $x$ and $y$	%
$\eta_{\text{gb}}$	gearbox transmission efficiency	%
$\rho$	density of ambient air	kg/m <sup>3</sup>
$\underline{\omega}_{\text{em.eff.gen}}$	$n_{\text{eff.gen.rot}} \times 1$ torque vector for look-up of $\eta_{\text{em.gen}}$	rpm
$\underline{\omega}_{\text{em.eff.mot}}$	$n_{\text{eff.mot.rot}} \times 1$ torque vector for look-up of $\eta_{\text{em.mot}}$	rpm
$\omega_{\text{em.loss.gen}}$	speed for calculation of motor losses in generator mode	rad/s
$\omega_{\text{em.loss.mot}}$	speed for calculation of motor losses in motor mode	rad/s
$\omega_{\text{em}\{xy\}}$	angular speed of motor at position $x$ and $y$	rad/s
$\omega_{\text{gb.in}}$	angular wheel speed at gearbox input shaft (motor side)	rad/s
$\omega_{\text{gb.out}}$	angular wheel speed at gearbox output shaft (wheel side)	rad/s
$\omega_{\text{gb}\{x\}}$	angular speed (motor side) of gearbox at position $x$	rad/s
$\omega_{\text{w}}$	angular wheel speed	rad/s

### List of Symbols for Driving Trajectory Prediction

Symbol	Description	Unit
$a_{\text{ems}}$	acceleration of driving trajectory, stored in $\underline{a}_{\text{ems}}^{n_{\text{traj}} \times 1}$	m/s <sup>2</sup>
$a_{\text{max}}$	upper bound for acceleration degradation	m/s <sup>2</sup>
$a_{\text{min}}$	lower bound for acceleration degradation	m/s <sup>2</sup>
$a_{\text{v}}$	vehicle acceleration	m/s <sup>2</sup>
$dpda$	variable for degradation of vehicle acceleration $a_{\text{v}}$	%
$dpdv$	variable for degradation of vehicle velocity $v_{\text{v}}$	%
$\underline{dpdx}$	driving profile degradation vector containing $dpda$ and $dpdv$	%
$ds^{[i]}$	length of segment $i$	km
$dT_{\text{a1}}$	duration of acceleration phase	s
$dT_{\text{a2}}$	duration of deceleration phase	s

Symbol	Description	Unit
$dT_c$	duration of constant velocity phase	s
$dT_{\text{seg}}^{[i]}$	duration of segment $i$ in driving trajectory, stored in $dT_{\text{seg}}^{n_{\text{traj}} \times 1}$	s
$dT_{\text{ssl}}$	remaining driving time	h
$dT_{\text{stop}}$	duration of a vehicle stop	s
$\underline{eh}_{\text{comb}}$	electronic horizon profile combining $\underline{eh}_{\text{lim}}$ , $\underline{eh}_{\text{slope}}$ and $\underline{eh}_{\text{stops}}$	—
$\underline{eh}_{\text{lim}}$	electronic horizon profile for velocity and acceleration bounds	—
$\underline{eh}_{\text{slope}}$	electronic horizon profile containing road slope	—
$\underline{eh}_{\text{stops}}$	electronic horizon profile containing vehicle stops	—
$m_{\text{seg}}$	maximum number of segments in $\underline{eh}_{\text{comb}}$	—
$n_{\text{seg}}$	number of segments after merging $\underline{eh}_{\text{lim}}$ and $\underline{eh}_{\text{slope}}$	—
$n_{\text{stops}}$	number of entries in $\underline{eh}_{\text{stops}}$	—
$n_{\text{traj}}$	maximum number of entries in predicted driving trajectory	—
$s_0$	vehicle position at $t = t_0$	km
$sl$	road slope in driving trajectory, stored in $sl^{n_{\text{traj}} \times 1}$	%
$s_{\text{ssl}}$	vehicle destination	km
$s_v$	vehicle position	km
$v_0$	vehicle start velocity	km/h
$v_{\text{avg}}$	average velocity	km/h
$v_{\text{ems}}$	set velocity	km/h
$v_{\text{end}}$	end velocity	km/h
$v_{\text{end.max}}$	maximum possible end velocity	km/h
$v_{\text{end.rev}}$	end velocity estimated in reverse calculation	km/h
$v_{\text{max}}$	upper bound for velocity degradation	km/h
$v_{\text{min}}$	lower bound for velocity degradation	km/h
$v_{\text{peak}}$	peak velocity assuming no constant velocity phase	km/h
$v_{\text{start}}$	start velocity	km/h
$v_{\text{start.frw}}$	start velocity estimated in forward calculation	km/h
$v_{\text{start.max}}$	maximum possible start velocity	km/h
$v_v$	vehicle velocity	km/h

# List of Publications

1. K. Gorelik, A. Kilic, and R. Obermaisser, “Energy management system for automated driving: Optimal and adaptive control strategy for normal and failure case operation,” in *Annual IEEE International Systems Conference*, April 2017, pp. 597–604.
2. K. Gorelik, A. Kilic, and R. Obermaisser, “Modeling and simulation of optimal and adaptive real-time energy management system for automated driving,” in *IEEE Transportation Electrification Conference and Expo*, June 2017, pp. 356–363.
3. K. Gorelik, A. Kilic, and R. Obermaisser, “Dynamic and route based range prediction for automated electric vehicles: Connected energy management system with range extension for improved safety,” in *IEEE Vehicle Power and Propulsion Conference*, December 2017, pp. 1–6.
4. K. Gorelik, A. Kilic, and R. Obermaisser, “Range prediction and extension for automated electric vehicles with fail-operational powertrain,” in *Annual IEEE International Systems Conference*, April 2018, pp. 120–126, Best Paper Award.
5. K. Gorelik, A. Kilic, and R. Obermaisser, “Optimal, adaptive and predictive real-time control of fail-operational powertrain for automated electric vehicles,” in *IEEE Transportation Electrification Conference and Expo*, June 2018, pp. 977–984.
6. K. Gorelik, A. Kilic, R. Obermaisser, and N. Müller, “Modellprädiktives Energiemanagement mit Steuerung der Fahrzeugführung für automatisiertes Fahren,” *at - Automatisierungstechnik*, vol. 66, no. 9, pp. 735–744, September 2018.
7. K. Gorelik, A. Kilic, and R. Obermaisser, “Connected energy management system for automated electric vehicles with fail-operational powertrain and powernet,” *IEEE Transactions on Vehicular Technology*, 2019.





# Bibliography

- [1] W. Bernhart, J.-P. Hasenberg, M. Winterhoff, and L. Fazel, “A CEO agenda for the (r)evolution of the automotive ecosystem,” *Think Act*, March 2016.
- [2] W. Bernhart, J.-P. Hasenberg, M. Winterhoff, and L. Fazel, “Transformation archetypes,” *Think Act Automotive Insights 2016: Transformation of the Car Industry*, May 2016.
- [3] C. McKerracher, I. Orlandi, M. Wilshire, C. Tryggestad, D. Mohr, E. Hannon, E. Morden, J. T. Nijssen, S. Bouton, S. Knupfer, S. Ramkumar, S. Ramanathan, and T. Moeller, “An integrated perspective on the future of mobility,” McKinsey & Company, Inc. and Bloomberg New Energy Finance, Tech. Rep., October 2016.
- [4] W. Bernhart, H. Kaise, Y. Ohashi, T. Schönberg, and L. Schilles, “Reconnecting the rural - autonomous driving as a solution for non-urban mobility,” *Roland Berger Focus*, March 2018.
- [5] T. Henzelmann, T. Schönberg, C. Neuenhahn, D. Frei, and T. Wunder, “Urbane Mobilität 2030: zwischen Anarchie und Hypereffizienz,” *Roland Berger Focus*, October 2017.
- [6] *Taxonomy and definitions for terms related to driving automation systems for on-road motor vehicles*, SAE Std. J3016, 2016.
- [7] “Automated driving systems 2.0: A vision for safety,” U.S. Department of Transportation (DOT) and National Highway Traffic Safety Administration (NHTSA), Tech. Rep., September 2017.
- [8] J.-L. Augier, T. Huck, A. Kilic, W. Müller, and G. Pieraccini, “Efficient, safe and reliable powernet for AD,” in *Elektrik/Elektronik in Hybrid- und Elektrofahrzeugen und elektrisches Energiemanagement VII*, June 2016, pp. 398–411.
- [9] A. Kilic, T. Shen, and K. Gorelik, “Entwicklung eines fail-operational Bordnetzes für autonomes Fahren,” in *VDI/VDE AUTOREG 2017 - Automatisiertes Fahren und vernetzte Mobilität*, July 2017, pp. 449–460.

- [10] *Road vehicles - Functional safety - Part 3: Concept phase*, ISO Std. 26 262-3:2011, 2011.
- [11] T. Shen, A. Kilic, and K. Gorelik, “Dimensioning of power net for automated driving,” in *The 30th International Electric Vehicle Symposium & Exhibition (EVS30)*, October 2017, pp. 1–11.
- [12] *Road vehicles - Functional safety - Part 5: Product development at the hardware level*, ISO Std. 26 262-5:2011, 2011.
- [13] C. Ress, A. Etemad, D. Kuck, and M. Boerger, “Electronic horizon - supporting ADAS applications with predictive map data,” in *13th World Congress on Intelligent Transport Systems*, October 2006.
- [14] C. Ress, D. Balzer, A. Bracht, S. Durekovic, and J. Löwenau, “ADASIS protocol for advanced in-vehicle applications,” in *15th World Congress on Intelligent Transport Systems*, November 2008, pp. 1–15.
- [15] X. Yuan and J. Wang, “Torque distribution strategy for a front- and rear-wheel-driven electric vehicle,” *IEEE Transactions on Vehicular Technology*, vol. 61, no. 8, pp. 3365–3374, October 2012.
- [16] S. Koehler, A. Viehl, O. Bringmann, and W. Rosenstiel, “Energy-efficient torque distribution for axle-individually propelled electric vehicles,” in *IEEE Intelligent Vehicles Symposium (IVS)*, June 2014, pp. 1109–1114.
- [17] W. Bernhart, M. Winterhoff, C. Hoyes, V. Chivukula, J. Garrelfs, S. Jung, and S. Galander, “Autonomous driving,” *Think Act*, November 2014.
- [18] K. Heineke, P. Kampshoff, A. Mkrtchyan, and E. Shao, “Self-driving car technology: When will the robots hit the road?” *Automotive & Assembly*, May 2017.
- [19] I. Koren and C. M. Krishna, *Fault-Tolerant Systems*, 1st ed. Elsevier, Inc., 2007.
- [20] R. Isermann, *Fault-Diagnosis Systems: An Introduction from Fault Detection to Fault Tolerance*, 1st ed. Springer-Verlag Berlin Heidelberg, 2006.
- [21] H. Kopetz, *Real-Time Systems: Design Principles for Distributed Embedded Applications*, 2nd ed. Springer New York Dordrecht Heidelberg London, 2011.
- [22] H. Kopetz, “Fault containment and error detection in the time-triggered architecture,” in *Proceedings of the Sixth International Symposium on Autonomous Decentralized Systems (ISADS)*, April 2003, pp. 1–8.
- [23] V. Gebhardt, G. M. Rieger, J. Mottok, and C. Gießelbach, *Funktionale Sicherheit*

- nach ISO 26262 - Ein Praxisleitfaden zur Umsetzung, 1st ed. dpunkt.verlag GmbH, 2013.
- [24] *Road vehicles - Functional safety - Part 1: Vocabulary*, ISO Std. 26 262-3:2011, 2011.
- [25] T. P. Kohler, J. Froeschl, C. Bertram, D. Buecherl, and H.-G. Herzog, “Approach of a predictive, cybernetic power distribution management,” *World Electric Vehicle Journal*, vol. 4, no. 1, pp. 22–30, 2010.
- [26] M. Schmidt, “Ein selbstadaptierender, dynamischer Energiemanagementansatz für das elektrische Kraftfahrzeugbordnetz,” Ph.D. dissertation, University of Kassel, Department of Electrical Engineering and Computer Science, Kassel, Germany, 2008.
- [27] S. Büchner, “Energiemanagement-Strategien für elektrische Energiebordnetze in Kraftfahrzeugen,” Ph.D. dissertation, Technical University of Dresden, Department of Transport and Traffic Sciences, Dresden, Germany, 2008.
- [28] *Regulation No 13-H of the Economic Commission for Europe of the United Nations (UN/ECE) - Uniform provisions concerning the approval of passenger cars with regard to braking [2015/2364]*, UN/ECE Std. R13-H, 2015.
- [29] L. Guzzella and A. Sciarretta, *Vehicle Propulsion Systems*, 3rd ed. Springer-Verlag Berlin Heidelberg, 2013.
- [30] S. Cui, S. Han, and C. C. Chan, “Overview of multi-machine drive systems for electric and hybrid electric vehicles,” in *IEEE Conference and Expo Transportation Electrification Asia-Pacific (ITEC Asia-Pacific)*, August 2014, pp. 1–6.
- [31] H. Laitinen, A. Lajunen, and K. Tammi, “Improving electric vehicle energy efficiency with two-speed gearbox,” in *IEEE Vehicle Power and Propulsion Conference (VPPC)*, December 2017, pp. 1–5.
- [32] J. Liebl, M. Lederer, K. Rohde-Brandenburger, J.-W. Biermann, M. Roth, and H. Schäfer, *Energiemanagement im Kraftfahrzeug - Optimierung von CO<sub>2</sub>-Emissionen und Verbrauch konventioneller und elektrifizierter Automobile*, 1st ed. Springer Vieweg, 2014.
- [33] L. Rosario, P. C. K. Luk, J. T. Economou, and B. A. White, “A modular power and energy management structure for dual-energy source electric vehicles,” in *IEEE Vehicle Power and Propulsion Conference (VPPC)*, September 2006, pp. 1–6.
- [34] L. C. Rosario and P. C. K. Luk, “Implementation of a modular power and energy

- management structure for battery-ultracapacitor powered electric vehicles,” in *IET Hybrid Vehicle Conference*, December 2006, pp. 141–156.
- [35] M. Papageorgiou, M. Leibold, and M. Buss, *Optimierung - Statische, dynamische, stochastische Verfahren für die Anwendung*, 4th ed. Springer Vieweg, 2015.
- [36] A. Kleimaier, “Optimale Betriebsführung von Hybridfahrzeugen,” Ph.D. dissertation, Technical University of Munich, Department of Electrical and Computer Engineering, Munich, Germany, 2003.
- [37] The MathWorks, Inc., *MATLAB R2015b Documentation: Optimization Toolbox*, 2015.
- [38] M. Back, “Prädiktive Antriebsregelung zum energieoptimalen Betrieb von Hybridfahrzeugen,” Ph.D. dissertation, University of Karlsruhe, Department of Electrical Engineering and Information Technology, Karlsruhe, Germany, 2005.
- [39] C. Röss, A. Etemad, D. Kuck, and J. Requejo, “Using predictive digital map data to enhance vehicle safety and comfort,” in *Proceedings of the 2nd International Workshop on Intelligent Vehicle Control Systems - Volume 1: IVCS (ICINCO)*, 2008, pp. 40–49.
- [40] S. Durekovic and N. Smith, “Architectures of map-supported ADAS,” in *IEEE Intelligent Vehicles Symposium (IVS)*, June 2011, pp. 207–211.
- [41] J. Ludwig, “Elektronischer Horizont für vorausschauende Kartendaten,” *ATZelektronik*, vol. 9, no. 7, pp. 24–27, October 2014.
- [42] Y. Horita and R. S. Schwartz, “Extended electronic horizon for automated driving,” in *14th International Conference on ITS Telecommunications (ITST)*, December 2015, pp. 32–36.
- [43] J. Requejo, C. Röss, A. Etemad, and D. Kuck, “Using predictive digital map data to enhance vehicle safety and comfort,” in *Proceedings of the 2nd International Workshop on Intelligent Vehicle Control Systems - Volume 1: IVCS (ICINCO)*, 2008, pp. 50–59.
- [44] T. P. Kohler, “Prädiktives Leistungsmanagement in Fahrzeugbordnetzen,” Ph.D. dissertation, Technical University of Munich, Department of Electrical and Computer Engineering and Information Technology, Munich, Germany, 2013.
- [45] M. Koot, J. T. B. A. Kessels, B. de Jager, W. P. M. H. Heemels, P. P. J. van den Bosch, and M. Steinbuch, “Energy management strategies for vehicular electric

- power systems,” *IEEE Transactions on Vehicular Technology*, vol. 54, no. 3, pp. 771–782, May 2005.
- [46] J. T. B. A. Kessels, P. P. J. van den Bosch, M. Koot, and B. de Jager, “Energy management for vehicle power net with flexible electric load demand,” in *IEEE Conference on Control Applications (CCA)*, August 2005, pp. 1504–1509.
- [47] J. T. B. A. Kessels, M. Koot, B. de Jager, P. P. J. van den Bosch, N. P. I. Aneke, and D. B. Kok, “Energy management for the electric powernet in vehicles with a conventional drivetrain,” *IEEE Transactions on Control Systems Technology*, vol. 15, no. 3, pp. 494–505, May 2007.
- [48] J. P. Trovão, V. D. N. Santos, P. G. Pereirinha, H. M. Jorge, and C. H. Antunes, “Comparative study of different energy management strategies for dual-source electric vehicles,” in *World Electric Vehicle Symposium and Exhibition (EVS27)*, November 2013, pp. 1–9.
- [49] J. P. Trovão, P. G. Pereirinha, H. M. Jorge, and C. H. Antunes, “A multi-level energy management system for multi-source electric vehicles – an integrated rule-based meta-heuristic approach,” *Applied Energy*, vol. 105, pp. 304–318, 2013.
- [50] J. P. F. Trovão, V. D. N. Santos, C. H. Antunes, P. G. Pereirinha, and H. M. Jorge, “A real-time energy management architecture for multisource electric vehicles,” *IEEE Transactions on Industrial Electronics*, vol. 62, no. 5, pp. 3223–3233, May 2015.
- [51] J. P. F. Trovão, M.-A. Roux, É. Ménard, and M. R. Dubois, “Energy- and power-split management of dual energy storage system for a three-wheel electric vehicle,” *IEEE Transactions on Vehicular Technology*, vol. 66, no. 7, pp. 5540–5550, July 2017.
- [52] O. Gomofov, J. P. F. Trovão, X. Kestelyn, and M. R. Dubois, “Adaptive energy management system based on a real-time model predictive control with nonuniform sampling time for multiple energy storage electric vehicle,” *IEEE Transactions on Vehicular Technology*, vol. 66, no. 7, pp. 5520–5530, July 2017.
- [53] J. Becker, C. Schaeper, and D. U. Sauer, “Energy management system for a multi-source storage system electric vehicle,” in *IEEE Vehicle Power and Propulsion Conference (VPPC)*, October 2012, pp. 407–412.
- [54] J. Becker, C. Schaeper, S. Rothgang, and D. U. Sauer, “Development and validation of an energy management system for an electric vehicle with a split battery storage

- system,” *Journal of Electrical Engineering & Technology*, vol. 8, no. 4, pp. 920–929, 2013.
- [55] J. T. B. A. Kessels, J. H. M. Martens, P. P. J. van den Bosch, and W. H. A. Hendrix, “Smart vehicle powernet enabling complete vehicle energy management,” in *IEEE Vehicle Power and Propulsion Conference (VPPC)*, October 2012, pp. 938–943.
- [56] T. Eymann, K. Williams, K. Benninger, A. Vikas, and C. Lillie, “Holistic vehicle energy management - moving towards CAFE’s target,” in *SAE World Congress & Exhibition*. SAE International, April 2011, pp. 1–9.
- [57] K. D. Nguyen, E. Bideaux, M. T. Pham, and P. L. Brusq, “Game theoretic approach for electrified auxiliary management in high voltage network of HEV/PHEV,” in *IEEE International Electric Vehicle Conference (IEVC)*, December 2014, pp. 1–8.
- [58] T. C. J. Romijn, M. C. F. Donkers, J. T. B. A. Kessels, and S. Weiland, “A dual decomposition approach to complete energy management for a heavy-duty vehicle,” in *53rd IEEE Conference on Decision and Control (CDC)*, December 2014, pp. 3304–3309.
- [59] T. C. J. Romijn, M. C. F. Donkers, J. T. B. A. Kessels, and S. Weiland, “Complete vehicle energy management with large horizon optimization,” in *IEEE Conference on Decision and Control (CDC)*, December 2015, pp. 632–637.
- [60] T. C. J. Romijn, M. C. F. Donkers, J. T. B. A. Kessels, and S. Weiland, “A distributed optimization approach for complete vehicle energy management,” *IEEE Transactions on Control Systems Technology*, pp. 1–17, 2018.
- [61] H. Chen, J. T. B. A. Kessels, M. C. F. Donkers, and S. Weiland, “Game-theoretic approach for complete vehicle energy management,” in *IEEE Vehicle Power and Propulsion Conference (VPPC)*, October 2014, pp. 1–6.
- [62] H. Chen, J. T. B. A. Kessels, and S. Weiland, “Online adaptive approach for a game-theoretic strategy for complete vehicle energy management,” in *European Control Conference (ECC)*, July 2015, pp. 135–141.
- [63] C. Romijn, T. Donkers, J. Kessels, and S. Weiland, “Real-time distributed economic model predictive control for complete vehicle energy management,” *Energies*, vol. 10, no. 8, pp. 1–28, 2017.
- [64] A. Sciarretta and L. Guzzella, “Control of hybrid electric vehicles,” *IEEE Control Systems Magazine*, vol. 27, no. 2, pp. 60–70, April 2007.
- [65] E. Silvas, T. Hofman, N. Murgovski, L. F. P. Etman, and M. Steinbuch, “Review

- of optimization strategies for system-level design in hybrid electric vehicles,” *IEEE Transactions on Vehicular Technology*, vol. 66, no. 1, pp. 57–70, January 2017.
- [66] H. Banvait, S. Anwar, and Y. Chen, “A rule-based energy management strategy for plug-in hybrid electric vehicle (PHEV),” in *American Control Conference (ACC)*, June 2009, pp. 3938–3943.
- [67] C. Zhang and A. Vahidi, “Route preview in energy management of plug-in hybrid vehicles,” *IEEE Transactions on Control Systems Technology*, vol. 20, no. 2, pp. 546–553, March 2012.
- [68] A. Wilde, “Eine modulare Funktionsarchitektur für adaptives und vorausschauendes Energiemanagement in Hybridfahrzeugen,” Ph.D. dissertation, Technical University of Munich, Department of Electrical and Computer Engineering, Munich, Germany, 2008.
- [69] J. von Grundherr zu Altenthan und Weiherhaus, “Ableitung einer heuristischen Betriebsstrategie für ein Hybridfahrzeug aus einer Online-Optimierung,” Ph.D. dissertation, Technical University of Munich, Department of Mechanical Engineering, Munich, Germany, 2010.
- [70] H.-G. Wahl, “Optimale Regelung eines prädiktiven Energiemanagements von Hybridfahrzeugen,” Ph.D. dissertation, Karlsruhe Institute of Technology (KIT), Department of Mechanical Engineering, Karlsruhe, Germany, 2015.
- [71] M. Stiegeler, “Entwurf einer vorausschauenden Betriebsstrategie für parallele hybride Antriebsstränge,” Ph.D. dissertation, Ulm University, Department of Engineering and Computer Science and Psychology, Ulm, Germany, 2008.
- [72] T. Salcher, “Optimierte Betriebsstrategie hybrider Antriebssysteme für den Serieneinsatz,” Ph.D. dissertation, Technical University of Munich, Department of Electrical and Computer Engineering, Munich, Germany, 2013.
- [73] S. G. Li, S. M. Sharkh, F. C. Walsh, and C. N. Zhang, “Energy and battery management of a plug-in series hybrid electric vehicle using fuzzy logic,” *IEEE Transactions on Vehicular Technology*, vol. 60, no. 8, pp. 3571–3585, October 2011.
- [74] S. J. Moura, H. K. Fathy, D. S. Callaway, and J. L. Stein, “A stochastic optimal control approach for power management in plug-in hybrid electric vehicles,” *IEEE Transactions on Control Systems Technology*, vol. 19, no. 3, pp. 545–555, May 2011.
- [75] S. Stockar, V. Marano, M. Canova, G. Rizzoni, and L. Guzzella, “Energy-optimal

- control of plug-in hybrid electric vehicles for real-world driving cycles,” *IEEE Transactions on Vehicular Technology*, vol. 60, no. 7, pp. 2949–2962, September 2011.
- [76] Z. Chen, C. C. Mi, J. Xu, X. Gong, and C. You, “Energy management for a power-split plug-in hybrid electric vehicle based on dynamic programming and neural networks,” *IEEE Transactions on Vehicular Technology*, vol. 63, no. 4, pp. 1567–1580, May 2014.
- [77] T. Radke, “Energieoptimale Längsführung von Kraftfahrzeugen durch Einsatz vorausschauender Fahrstrategien,” Ph.D. dissertation, Karlsruhe Institute of Technology (KIT), Department of Mechanical Engineering, Karlsruhe, Germany, 2013.
- [78] A. Freuer, “Ein Assistenzsystem für die energetisch optimierte Längsführung eines Elektrofahrzeugs,” Ph.D. dissertation, University of Stuttgart, Department Engineering Design, Production Engineering and Automotive Engineering, Stuttgart, Germany, 2016.
- [79] G. Becker, “Ein Fahrerassistenzsystem zur Vergrößerung der Reichweite von Elektrofahrzeugen,” Ph.D. dissertation, University of Stuttgart, Department Engineering Design, Production Engineering and Automotive Engineering, Stuttgart, Germany, 2016.
- [80] K. Li, A. Bouscayrol, S. Han, and S. Cui, “Comparisons of electric vehicles using modular cascade machines system and classical single drive electric machine,” *IEEE Transactions on Vehicular Technology*, vol. 67, no. 1, pp. 354–361, January 2018.
- [81] X. Yuan, J. Wang, and K. Colomage, “Torque distribution strategy for a front and rear wheel driven electric vehicle,” in *IET International Conference on Power Electronics, Machines and Drives (PEMD)*, March 2012, pp. 1–6.
- [82] S. Koehler, A. Viehl, O. Bringmann, and W. Rosenstiel, “Optimized recuperation strategy for (hybrid) electric vehicles based on intelligent sensors,” in *International Conference on Control, Automation and Systems (CCAS)*, October 2012, pp. 218–223.
- [83] A. M. Dizqah, B. Lenzo, A. Sorniotti, P. Gruber, S. Fallah, and J. D. Smet, “A fast and parametric torque distribution strategy for four-wheel-drive energy-efficient electric vehicles,” *IEEE Transactions on Industrial Electronics*, vol. 63, no. 7, pp. 4367–4376, July 2016.
- [84] Y. Wang, H. Fujimoto, and S. Hara, “Torque distribution-based range extension control system for longitudinal motion of electric vehicles by LTI modeling with gen-



- eralized frequency variable,” *IEEE/ASME Transactions on Mechatronics*, vol. 21, no. 1, pp. 443–452, February 2016.
- [85] L. Guo, X. Lin, P. Ge, Y. Qiao, L. Xu, and J. Li, “Torque distribution for electric vehicle with four in-wheel motors by considering energy optimization and dynamics performance,” in *2017 IEEE Intelligent Vehicles Symposium (IVS)*, June 2017, pp. 1619–1624.
- [86] Y.-P. Yang, Y.-C. Shih, and J.-M. Chen, “Real-time torque-distribution strategy for a pure electric vehicle with multiple traction motors by particle swarm optimization,” *IET Electrical Systems in Transportation*, vol. 6, no. 2, pp. 76–87, May 2016.
- [87] N. Jinrui, S. Fengchun, and R. Qinglian, “A study of energy management system of electric vehicles,” in *IEEE Vehicle Power and Propulsion Conference (VPPC)*, September 2006, pp. 1–6.
- [88] S. G. Wirasingha and A. Emadi, “Classification and review of control strategies for plug-in hybrid electric vehicles,” *IEEE Transactions on Vehicular Technology*, vol. 60, no. 1, pp. 111–122, January 2011.
- [89] C. M. Martinez, X. Hu, D. Cao, E. Velenis, B. Gao, and M. Wellers, “Energy management in plug-in hybrid electric vehicles: Recent progress and a connected vehicles perspective,” *IEEE Transactions on Vehicular Technology*, vol. 66, no. 6, pp. 4534–4549, June 2017.
- [90] Q. Gong, Y. Li, and Z.-R. Peng, “Optimal power management of plug-in HEV with intelligent transportation system,” in *IEEE/ASME International Conference on Advanced Intelligent Mechatronics (AIM)*, September 2007, pp. 1–6.
- [91] Q. Gong, Y. Li, and Z.-R. Peng, “Trip-based optimal power management of plug-in hybrid electric vehicles,” *IEEE Transactions on Vehicular Technology*, vol. 57, no. 6, pp. 3393–3401, November 2008.
- [92] Q. Gong, Y. Li, and Z.-R. Peng, “Trip based power management of plug-in hybrid electric vehicle with two-scale dynamic programming,” in *IEEE Vehicle Power and Propulsion Conference (VPPC)*, September 2007, pp. 12–19.
- [93] Q. Gong, Y. Li, and Z.-R. Peng, “Trip based optimal power management of plug-in hybrid electric vehicles using gas-kinetic traffic flow model,” in *American Control Conference (ACC)*, June 2008, pp. 3225–3230.
- [94] H. Yu, M. Kuang, and R. McGee, “Trip-oriented energy management control strat-

- egy for plug-in hybrid electric vehicles,” *IEEE Transactions on Control Systems Technology*, vol. 22, no. 4, pp. 1323–1336, July 2014.
- [95] D. Karbowski, N. Kim, and A. Rousseau, “Route-based online energy management of a PHEV and sensitivity to trip prediction,” in *IEEE Vehicle Power and Propulsion Conference (VPPC)*, October 2014, pp. 1–6.
- [96] T. J. Boehme, F. Held, M. Schultalbers, and B. Lampe, “Trip-based energy management for electric vehicles: An optimal control approach,” in *American Control Conference (ACC)*, June 2013, pp. 5978–5983.
- [97] T. J. Boehme, F. Held, C. Rollinger, H. Rabba, M. Schultalbers, and B. Lampe, “Application of an optimal control problem to a trip-based energy management for electric vehicles,” *SAE International Journal of Alternative Powertrains*, vol. 2, no. 1, pp. 115–126, April 2013.
- [98] K. Gebhardt, V. Schau, and W. R. Rossak, “Applying stochastic methods for range prediction in e-mobility,” in *15th International Conference on Innovations for Community Services (I4CS)*, July 2015, pp. 1–4.
- [99] A. Basler, “Eine modulare Funktionsarchitektur zur Umsetzung einer gesamtheitlichen Betriebsstrategie für Elektrofahrzeuge,” Ph.D. dissertation, Karlsruhe Institute of Technology (KIT), Department of Mechanical Engineering, Karlsruhe, Germany, 2015.
- [100] R. Isermann, *Fault-Diagnosis Applications - Model-Based Condition Monitoring: Actuators, Drives, Machinery, Plants, Sensors, and Fault-tolerant Systems*, 1st ed. Springer-Verlag Berlin Heidelberg, 2011.
- [101] G. Liu, M. Ouyang, L. Lu, J. Li, and J. Hua, “A highly accurate predictive-adaptive method for lithium-ion battery remaining discharge energy prediction in electric vehicle applications,” *Applied Energy*, vol. 149, pp. 297 – 314, 2015.
- [102] IBM Corporation, *IBM ILOG CPLEX Optimization Studio CPLEX User’s Manual, Version 12 Release 7*, 2016.
- [103] MOSEK ApS, *MOSEK Optimization Suite Release 8.1.0.56*, 2018.
- [104] J. Löfberg, “YALMIP : a toolbox for modeling and optimization in MATLAB,” in *IEEE International Symposium on Computer Aided Control Systems Design (CACSD)*, September 2004, pp. 284–289.
- [105] G. Walla, A. Herkersdorf, A. S. Enger, A. Barthels, and H. U. Michel, “An automotive specific MILP model targeting power-aware function partitioning,” in *Inter-*

- national Conference on Embedded Computer Systems: Architectures, Modeling, and Simulation (SAMOS XIV)*, July 2014, pp. 299–306.
- [106] G. Wu, K. Boriboonsomsin, and M. J. Barth, “Development and evaluation of an intelligent energy-management strategy for plug-in hybrid electric vehicles,” *IEEE Transactions on Intelligent Transportation Systems*, vol. 15, no. 3, pp. 1091–1100, June 2014.
- [107] C. Wouters, E. S. Fraga, A. M. James, and E. M. Polykarpou, “Mixed-integer optimisation based approach for design and operation of distributed energy systems,” in *Australasian Universities Power Engineering Conference (AUPEC)*, September 2014, pp. 1–6.
- [108] J. Guanetti, S. Formentin, and S. M. Savaresi, “Energy management system for an electric vehicle with a rental range extender: A least costly approach,” *IEEE Transactions on Intelligent Transportation Systems*, vol. 17, no. 11, pp. 3022–3034, November 2016.
- [109] M. S. Taha, H. H. Abdeltawab, and Y. A.-R. I. Mohamed, “An online energy management system for a grid-connected hybrid energy source,” *IEEE Journal of Emerging and Selected Topics in Power Electronics*, pp. 1–15, 2018.
- [110] S. Terwen, M. Back, and V. Krebs, “Predictive powertrain control for heavy duty trucks,” *IFAC Proceedings Volumes*, vol. 37, no. 22, pp. 105–110, April 2004.
- [111] P. Elbert, T. Nüesch, A. Ritter, N. Murgovski, and L. Guzzella, “Engine on/off control for the energy management of a serial hybrid electric bus via convex optimization,” *IEEE Transactions on Vehicular Technology*, vol. 63, no. 8, pp. 3549–3559, October 2014.
- [112] N. Murgovski, B. Egardt, and M. Nilsson, “Cooperative energy management of automated vehicles,” *Control Engineering Practice*, vol. 57, pp. 84 – 98, 2016.
- [113] Y. Wang, Z. Chen, and C. Zhang, “On-line remaining energy prediction: A case study in embedded battery management system,” *Applied Energy*, vol. 194, pp. 688–695, 2017.
- [114] M. Ceraolo and G. Pede, “Techniques for estimating the residual range of an electric vehicle,” *IEEE Transactions on Vehicular Technology*, vol. 50, no. 1, pp. 109–115, January 2001.
- [115] M. Ceraolo, “New dynamical models of lead-acid batteries,” *IEEE Transactions on Power Systems*, vol. 15, no. 4, pp. 1184–1190, November 2000.

- [116] J. Welc and P. J. R. Esquerdo, *Applied Regression Analysis for Business*, 1st ed. Springer International Publishing AG, 2018.
- [117] G. Antoni, “On the mechanical friction losses occurring in automotive differential gearboxes,” *The Scientific World Journal*, vol. 2014, pp. 1–11, January 2014.
- [118] A. H. Bonnett and C. Yung, “Increased efficiency versus increased reliability,” *IEEE Industry Applications Magazine*, vol. 14, no. 1, pp. 29–36, January 2008.
- [119] A. J. Bazarro, E. C. Quispe, and R. C. Mendoza, “Causes and failures classification of industrial electric motor,” in *IEEE ANDESCON*, October 2016, pp. 1–4.
- [120] D. Burgstahler, A. Xhoga, C. Peusens, M. Möbus, D. Böhnstedt, and R. Steinmetz, “RemoteHorizon.KOM: Dynamic cloud-based eHorizon,” in *AmE 2016 - Automotive meets Electronics; 7th GMM-Symposium*, March 2016, pp. 1–6.
- [121] P. Conradi, “Reichweitenprognose für Elektromobile,” *ATZelektronik*, vol. 7, no. 3, pp. 186–191, June 2012.